Exploring Plasmonic-Photonic Coupled Systems Using Microcavity-Based Single-Particle Spectroscopy

By
Feng Pan

A dissertation submitted in partial fulfillment
of the requirements for the degree of

Doctor of Philosophy
(Chemistry)

at the
UNIVERSITY OF WISCONSIN-MADISON
2022

Date of final oral examination: February 16, 2022

The dissertation is approved by the following members of the Final Oral Committee:

Randall Goldsmith, Professor, Chemistry

Gilbert Nathanson, Professor, Chemistry

Yang Yang, Assistant Professor, Chemistry

Zongfu Yu, Associate Professor, Electrical & Computer Engineering

This dissertation is dedicated to my wife and son

Acknowledgements

Writing this section reminds me of tremendous number of memories when I worked on my MS thesis back to 2016. I would like to show my gratitude to more and more people along this journey. I would like to first thank my advisor at Texas A&M, Dr. Simon North, who supported me to pursue what really intrigued me for my Ph.D. His passion for science and teaching undoubtedly has huge impact on my career path in terms of research and teaching. I really miss coffee walk per week chatting about science although I did not drink coffee that often, and lunch takeout on Saturdays when we chatted about non-science stuff.

Randy, I really appreciate that you persistently sold your research to me during recruiting weekend and when I joined the department. I have never seen a research group in which people work on so many areas but toward a unified goal before I joined the group. Your eagerness to learn new things and ambition to cook multiple disciplines in one pot are truly amazing. Your attitude toward collaboration among group members and with people outside of the department is inspiring. These spirits would definitely shape my research program when I start an independent career. I like the way how you manage the group and that you are always open for improvements in group management. You have been a role model to me for advising and teaching. If I got another chance, I would join the group again.

I want to thank my committee, Profs. John Wright, Jeremy Rogers, Gil Nathanson, Yang Yang, and Zongfu Yu. John, thank you for taking me in your lab doing summer research in 2016! Your kindness and being knowledgeable about multidimensional

spectroscopy made me enjoy my time in your group. Your encouragement and comments to my RP means a lot to me. Jeremy, thank you for providing your insights into optics and Zemax ray tracing! Your contribution to our collaborative work published in Optics Express is fantastic. Your being knowledgeable about microscopy really fuels my passion to learn about a variety of microscopy techniques. Although you two cannot make it to the end of my Ph.D. journey, I would like to thank you for advice and writing reference letters to support me. Gil, thank you for teaching me 960 seminar class, which stimulates me to keep asking questions and being engaged in seminars. Also, thank you for helping me improve my presentation skills! Yang, thank you for being on my committee from my RP through defense! Your obsession with quantum chemistry and DFT is amazing! I was honored to work with you as a TA for your 562 class and I want to tell you that I learned something new from your class. Also, I want to thank you for accommodating my parent leave for the rest weeks in fall semester of 2019. Zongfu, thank you for having me rotate in your group for 3 weeks in 2016. I really admire your knowledge in electromagnetics and I'm sorry I did not take your nanophotonics class.

I also want to thank my collaborators along this journey. Thank you, Kevin, for contributing to the theory in our paper! I really appreciate that you always got back to me so rapidly with your updates. You are still very responsive to my questions even after graduation. David, thank you for keeping bringing new theoretical aspects to our work. I'm sorry that I haven't got far-field scattering measurement to work for characterizing our hybrid system. Thank you for writing a reference to support my application for a postdoc position in Teri's lab! Kris and Sile, thank you for your collaboration in making bubbles for

my latest work. Jonathan, you are a great resource to ask any questions about bubbles although you don't work with them any longer. Thank you for your wisdom!

I would like to show my sincere gratitude to the former and present colleagues in the Goldsmith group. First, I'm indebted to Kevin for inspiration and help! When I stood in front of the recruiting poster for the Goldsmith group and listened to you speaking for 5 minutes, I had no idea about Fanos but hairy noise on your spectrum. Life is so dramatic that I have been hooked up to this word for almost 4 years! I really like your excitement about talking about science when we rode a bus together and did office chat. Unfortunately, you left the group for your new job at Intel just when I joined group. Notwithstanding, your help is always there when I need it throughout my graduate studies. The asset and impact you left for the photonics subgroup is profound. I was saddened that you chose not to become a professor one day but pursue new science in industry. I'm glad you found what you love to do. Congrats again on your new role in Seattle!

Erik, thank you for training me on photothermal setup in two weeks when I joined the photonics subgroup. Your explanation about PDH locking and resonance dip is straightforward. Thank you for showing me your way of doing optics alignment! You have been so helpful that I selfishly relied on you to resolve any research issues for a while. Your wisdom on tapering, doing photothermal imaging, and comsol simulations really impacts me in my latest two research works.

Kasie, thank you for showing me how to do RCA cleaning on toroid chips and load chips to the setup and do evanescent coupling. Your solid skills for handling tiny devices are quite impressive! I'm grateful for you taking my request for cleaning toroid chips

seriously. I enjoyed fun jokes you made when we took data together. Morgan, thank you for continuing to feed us with your baking goods in the past few years! I was happy to work with you on the PEDOT:PSS project. You are so kind and willing to help everyone in the group as much as you can. Your attitude toward keeping improving presentation skills inspires me to hone mine persistently.

I was happy to work with you in the same subgroup but on different projects over the past few years, Levi! Your passion for outreach activities and maintaining lab safety standards is admirable. I love the jokes and fun facts you talked about during group meetings. Thank you for being helpful and sharing your wisdom about microbubble whenever I need. Also, thanks for being devoted to preparing the celebration for my defense.

Ceci, thank you for cleaning toroid chips and doing XeF_2 etching for me! You have been doing an amazing fab!. Making microrings is very challenging. I think your work will lay the foundation for the group to do single-molecule spectroscopy using resonators in the future. I have been suffering from taper drift issue for almost 5 years and I know how helpful it would be to have an integrated waveguide. Keeping up!

Brandon Mehlenbacher, you are a great software engineer in the group. I'm impressive that you spearheaded renovation of computer-instrument interface in pandemic times and programed all the instrument control and data acquisition using Python for your setup. I know Python as programing language will be the future in the group although I personally like programing the control of instruments with LabView. This is something I hoped to learn when I was in the Wright group. Brandon Hacha, your strong

interest in topological photonics and acoustics is unparalleled. I hope I can learn this stuff as fast as you do. Your contribution to setting up scripts for running FDTD simulations on CHTC and HPC is a great asset to the group. Beau, you are so dedicated to making fiber mirrors. Now you are the master of CO_2 ablation in the group. Alex Fairhall, you are going to be the first person to do “cold” experiments in the group. Your commitment to getting things done is excellent. Julia, thank you for joining the photonics subgroup. I believe you will get really cool data out from microcavity SRS experiments which we have been looking forward to for a long time.

Sudheer, thank you for being the postdoc in the group! You have been a great resource I often reached out to for help on electronics and resonators. I was happy to chat with you about your fiber cavity and brainstorming for my RP on metasurface for imaging. Thanks for talking about Indian food! Mike, I really enjoyed chatting with you about science both in plasmonics and topological photonics. Your ability to build up a new direction from scratch in the group is amazing. I learned a lot from you, and you are one of a few guys I have often bothered for science questions. Hoang, thank you for sharing the setup with me! Your persistence with microcavity SRS experiments is unparalleled. You are one of a few persons in the group I closely worked with. I like talking with you about Vietnamese food. Ruohan, although we did not interact too much due to distant lab locations, I was impressed that you initiated the magnetic tweezer project while being surrounded by a group of biologists. LM, I’m glad you joined the group and contributed to the Raman project. I really appreciate that you keep engaging the group through a variety of social activities. Tzu-Ling, I hope you like the group and learn what you hope to learn for your academic career. Your skill set in Fabry-Perot cavities and PDH locking is very

solid. Thank you for inspiring me in 2019 when we had a chance to interact in cavity-enhanced user meeting so that I decided to replace the notorious Newport lockbox with Vescent box, which is the one being popularly used in the group now. Carlos, thanks for teaching me stuff about microspheres. Your expertise in fiber microcavities will enable the group to leap ambitiously.

Alex Foote, I like your way of presenting science. You are always willing to present resources that might benefit the group, like tricks in LabView programing and CHTC and HPC clusters. I enjoyed your company several times when I worked late in the lab. Brendan and Simi, I have faith in you two in that you will get new stuff out of ABEL trap soon. James, I'm grateful for you answering me tons of questions about microscopy tirelessly in my first two years. Also, thank you and Andrew for feeding us with a big free Chipotle order! Andrew, my work would not make it to the front cover in Nano Lett without your help on the graphical design. Thank you for many fun and random office chats! Veronica, you are a great microscopist now in the group. I really like your group meetings because you present your science in such a lively way and your presentation is filled with fun. Mackinsey, you are an ambitious chemist! I believe you will get beautiful data from ZMWs you made. Ray, thank you for the book you bought for my son two years ago! He can turn pages very quickly now; I don't know if he really perceives those cartoons on the book. Katherine, I was impressed that you built a *k*-space imaging setup from scratch when you are a junior grad. I look forward to images you take using this setup for chiral molecules in your fishnet metamaterials. Daniel, I missed talking with you about organic synthesis which reminded me what I did long time ago. Lydia, thank you for launching ELN in the group to help us organize our data although I sometimes still have a clutter

logging style. Angela, your baked cookies are really good and thank you for being kind to me when I joined the group. David, you are an amazing data scientist! It's mysterious that you can learn EBL and programing so fast while being a biologist. Windy, thank you for being an undergrad researcher in the group. I always think of you as an independent researcher, and you have showed your ability to handle challenge problems on your own. Good luck with your study at Caltech!

Tingting, as my partner and friend, thank you so much for your kindness and support throughout my Ph.D. life in Madison! We interacted for the first time when I rotated in the Schmidt group, and we started to get more and more interactions since then. I was hooked by your passion for baking, running, and playing volleyball. I have never thought I would be mated with another chemist when I started graduate school. Having a family with you is truly a milestone in my life! Thanks for your support in my pursuit of my academic career. Memories with you on century biking and trips in Seattle are still fresh to me. I promise you we will have a honeymoon together. I'm eager to explore the world more with you in our rest of life, like doing road trips, biking, snorkeling, diving, etc. In the meantime, thanks for your endurance and collaboration in raising MQ in pandemic times. I hope there is always a place for me in your heart.

MQ, thank you for coming to this world! Having you in my graduate school is remarkable. I'm very sorry that you spend your early childhood in pandemic times. I know you're NOT a quiet boy and are always ready for exploring the world. As your parents, we are very cautious for your health and development. Yes, we are still learning how to be great parents. Thanks for bringing us tons of joys and smiles and keeping us busy in

the past two years! Also, thank you for letting me rethink about artificial intelligence while watching you learning to walk and speak.

I'm grateful for my mom and dad and my family in law! Thanks to my family in law so much for flying to support us when MQ was born. Your help really eased our burden so that we can move on with our research. Thank you to my mom for flying to support us upon request in pandemic times. It was hard to fly to Singapore first and be in quarantine for two weeks and then fly to Chicago. Your support is critical to me in that I can focus on my research and land two postdoc offers.

Table of Contents

Acknowledgements ii
Table of Contents x
Table of Figures xiv
Table of Tables xvi
Abstract xvii
Thesis overview 1
Chapter 1 Light-matter interactions in cavities 4
Introduction 4
Cavities 6
Defining coupling regimes 8
Weak coupling limit 9
Strong coupling limit 14
References 15
Chapter 2 Plasmonic nanocavities, optical microcavities, and plasmonic-photonic coupled cavities 18
Plasmonic nanocavities 18
Optical microcavities 24
WGM optical microcavities 27
Different types of WGM microcavities 29
Loss mechanisms 30
Coupling methodologies 32
Coupling equations 36
Coupled plasmonic-photonic cavities 38
Spectroscopic investigation of coupled plasmonic-photonic systems 45
References 46
Chapter 3 Elucidating energy pathways through simultaneous measurement of absorption and transmission in a coupled plasmonic-photonic cavity 53
Main text: Abstract 53
Main text: Introduction 54

Main text: Absorption and Two-Sided Transmission 57
Main text: Modeling 62
Main text: Analysis 67
Main text: Methods 75
References 77
Chapter 4 Active control of plasmonic-photonic interactions in a microbubble cavity 83
Main text: Introduction 83
Main text: Embedding method 85
Main text: Spectroscopic study 89
Main text: Determining couplings and optical simulations 94
Main text: Conclusion 101
Main text: Methods 101
Main text: Acknowledgements 103
Supporting information: the effect of changing dielectrics on mode spectrum 103
Supporting information: Optical images for air-filled and chloroform-filled microbubble 105
Supporting information: Fitting method 106
Supporting information: Optical simulations 108
Supporting information: Other results 110
References 113
CHAPTER 5 Single-particle photothermal imaging via inverted excitation through high-Q all-glass toroidal microresonators 116
Main text: Abstract 116
Main text: Introduction 117
Main text: Fabrication and imaging setup 119
Main text: Single-particle photothermal imaging 122
Main text: Low-resolution PSF characterization 124
Main text: Single nanorod PSF characterization 125
Main text: Simulated ray-tracing analysis of astigmatism 128
Main text: Toroid component analysis 131
Main text: Conclusion 131

Appendix A: Device fabrication details 132
Appendix B: Gold nanorod deposition and imaging 132
Appendix C: Zemax ray-tracing analysis 133
Funding 134
Acknowledgments 134
References 135
Chapter 6 Two-dimensional palladium-nanosheet intercalated with gold-nanoparticle for plasmon-enhanced electrocatalysis 139
Main text: Abstract 139
Main text: Introduction 140
Main text: Synthetic method and formation mechanism of 2D AuNP-in-PdNS heterostructure. 145
Main text: Plasmon-enhanced hydrogen evolution and oxygen reduction on Au_xNP-in-PdNS. 150
Main text: Electromagnetic simulations of Au_xNP-in-PdNS 155
Main text: Mechanism discussion 160
Main text: Conclusions 167
Main text: Experimental section 168
Main text: Plasmon-enhanced Electrocatalysis Measurements. 172
Main text: Electromagnetic simulations 175
Main text: Acknowledgements 176
References 177
Chapter 7 Unfinished projects 183
Introduction 183
Project 1: Breaking PEDOT-S aggregates 183
Project 1: pH control of doping level in PEDOT-S 185
Project 2: PDMS coating 189
Project 2: Optical simulations of PDMS-coated microtoroid 193
References 195
Chapter 8 Mingling a nanoscopic world with a microscopic world 197
Introduction 197

Plasmons and their media 197
Photons and whispering-gallery-mode microcavities 199
Whispering-gallery-mode microcavity as a tiny thermometer 202
What we learn from a mingled system 203
Outlook and future directions 208
New optical microcavities toward strongly coupled systems 208
Dark-field scattering measurement 209

Table of Figures

Figure 1.1 A two-level system coupled to electromagnetic field in free space (**A**) and cavity (**B**). 6
Figure 1.2 A Fabry-Perot cavity coupled to a two-level system with a coupling strength (g). 7
Figure 2.1 Excitation of a localized surface plasmon (LSP) in a plasmonic nanoparticle. 19
Figure 2.2 Designs of plasmonic cavities. 20
Figure 2.3 Electric field profile in plasmonic nanocavities and materials interacting with these cavities. 22
Figure 2.4 Fabry-Perot microcavities. 25
Figure 2.5 Whispering-gallery-mode microcavities and photonic crystal microcavity. 27
Figure 2.6 Whispering gallery conceptual representation (**A**) and whispering-gallery-mode (WGM) microcavity (**B**). 28
Figure 2.7 Evanescent coupling mechanism and coupling methods. 34
Figure 2.8 Applications of plasmonic-photonic coupled systems for sensing (**A**), optical trapping (**B**), and emission control (**C**). Reprinted with permission from Ref[80, 82, 85]. 40
Figure 2.9 Fano antiresonance in coupled plasmonic-photonic systems. 40
Figure 2.10 Plasmonic-photonic couplings and spectral signatures in different coupled systems. 42
Figure 2.11 Control of plasmonic-photonic hybridization by tuning LSP resonance. 44
Figure 3.1 Schematic of dissipative coupled AuNR-microresonator system with all parameters ($\omega 0$, $\gamma 0, NR$, $\gamma 0, Rad$, g, $\omega 1$, $\gamma 1, NR$, $\gamma 1, Rad$, $\gamma 1, Fib$) as well as experimental observables 57
Figure 3.2 Experimental setup for simultaneous measurement of absorption and two-sided transmission 59
Figure 3.3 Simultaneous spectral measurements. 61
Figure 3.4 Simultaneous fits to reduced absorption cross-section (top) and transmission cross-section (bottom). 68
Figure 3.5 (a) All fit parameters in log scale (left side) obtained from simultaneous fits to experimental data in well-separated spectral windows indicated by dark dashed lines. 72
Figure 4.1 Schematic of active control via modifying interior dielectric environment in a microbubble cavity 85
Figure 4.2 Fixation of single AuNRs on the interior surface of the microbubble. 88
Figure 4.3 Intermediate-resolution and high-resolution absorption spectra of two single AuNRs in the air-filled (**A** and **C**) and chloroform-filled (**B** and **D**) microbubble. 91
Figure 4.4 LSP parameters determined via simultaneous fits to high-resolution and low-resolution spectra. 93
Figure 4.5 Distributions of g determined in experiments for two single AuNRs (**i** and **ii**) (**A**) and comparison of distributions for reduced g ($g/\gamma 0, Rad/\omega 12$) between experiment and simulation for AuNR **i** (**B**) and AuNR **ii** (**C**). 98
Figure 4.6 Kernel density distributions of V (**A**), J (**B**), and J/V (**C**). 100

Figure 4.7 Mode spectra obtained for air-filled (**top**) and chloroform-filled (**middle**) microbubble and a microtoroid (**bottom**)..... 105
Figure 4.8 Optical images of the microbubble filled with air (**A**) and chloroform (**B**)... 106
Figure 4.9 Analysis of fitting robustness. 107
Figure 4.10 Kernel density plots of J and J/V at different simulated spatial locations along the microbubble stem axis. 109
Figure 4.11 Experimentally determined distributions of g for the rest of single AuNRs. 110
Figure 4.12 Probability distributions of experimental and simulated reduced g $(g/\gamma 0, \mathrm{Rad}/\omega 12)$ for different AuNRs at different simulated spatial locations along the microbubble stem axis (z: 0, 5 ,10, 15, and 20 μm). 111
Figure 4.13 Low-resolution absorption spectra of single AuNRs under air-filled or chloroform-filled conditions. 113
Figure 5.1 Imaging via inverted excitation with thin-substrate toroidal microresonators. 121
Figure 5.2 Comparison of photothermal imaging via topside and inverted excitation. 123
Figure 5.3 Focus progression of PSFs in whole toroid images. 125
Figure 5.4 Experimental and simulated PSF evolution of single nanorods. 127
Figure 5.5 PSF evolution as a function of toroid component. 130
Figure 6.1 Synthesis of 2D AuNP-in-PdNS heterostructure. 144
Figure 6.2 Structural characterization of the 2D Au0.15NP-in-PdNS heterostructure. 149
Figure 6.3 Plasmon-enhanced hydrogen evolution reaction electrocatalysis on 2D AuNP-in-PdNS heterostructure at room temperature. 153
Figure 6.4 Electromagnetic simulations for AuxNP-in-PdNS heterostructure. 159
Figure 6.5 Proposed mechanism for the plasmon-enhanced hydrogen evolution reaction. 165
Figure 7.1 Molecular structure of PEDOT-S (**A**) and PEDOT:PSS (**B**) 184
Figure 7.2 Absorption spectra of PEDOT-S measured by single-particle absorption spectroscopy. 185
Figure 7.3 Thermal treatment of PEDOT-S solution. 186
Figure 7.4 pH control of doping level in PEDOT-S. 187
Figure 7.5 Correlation of electronic structure to ordering of chromophores. 188
Figure 7.6 PDMS coating of a microtoroid via droplet-wetting method. 190
Figure 7.7 Field intensity profiles as a function of the thickness of PDMS layer. 191
Figure 7.8 Narrowing pillar via XeF_2 etching. 192
Figure 7.9 Scanning electron micrographs for PDMS-coated, etched microtoroid. 193
Figure 7.10 Resonance shift (black) and energy fraction (blue) in PDMS as a function of the thickness of PDMS layer. 195
Figure 8.1 Understanding oscillation and plasmon. 198
Figure 8.2 Whispering-gallery waves and microcavities. 199
Figure 8.3 A whispering-gallery microcavity and my experimental scheme. 202
Figure 8.4 Optical difference between a bubble-shape microcavity filled with air and an organic solvent. 205

Table of Tables

Table 2.1 Mode volume and field enhancement in plasmonic cavities. 23
Table 2.2 Parameters in a toroidal microcavity 38
Table 3.1 The mean and standard deviation of the mean for all fit parameters. 73
Table 4.1 Polarization dependence study of single AuNRs. 112

Abstract

Control of light-matter interactions is important for a variety of applications, such as sensing, photocatalysis, and information science, to name a few. Recently, plasmonic-photonic coupled systems, which inherit ultrahigh-quality factor and ultrasmall mode volume from their component cavities, have shown promise in tailoring light-matter interactions. Understanding energy dynamics in such coupled systems which dictate multiple dissipation pathways and couplings, sheds light upon the rational design of optimal coupled systems, for instance, achieving disparity between couplings and dissipations for strong coupling and precisely controlling photon transfer rates between component cavities in photonic circuits. The core of my thesis examines a model system, i.e., a whispering-gallery-mode (WGM) microcavity coupled to a gold nanorod that supports localized surface plasmon (LSP), and addresses two main questions, i.e., how to elucidate system parameters and how to control them. I will present a new way that combines simultaneous measurement of absorption and transmission with theoretical modeling, to pin down eight system parameters spanning up to *9* orders of magnitude. I then demonstrate a solvent-embedding strategy to actively control plasmonic-photonic interactions in a microbubble cavity. Chloroform that has similar refractive index to the material of the microbubble cavity, is chosen to fill the microbubble for increasing the mode overlap between LSP and WGMs. The effect of modulating interior dielectric environment on mode volume and mode overlap is thoroughly interrogated through both experiments and optical simulations. In addition, I will demonstrate two most recent applications under the theme of plasmonics and photonics, i.e., single-particle

photothermal imaging through high-Q all-glass WGM microcavities and plasmonic enhancement for electrocatalysis, respectively.

Thesis overview

This thesis mainly addresses fundamental questions in plasmonics, photonics, as well as the junction between them, i.e., coupled plasmonic-photonic systems. How do we understand light-matter interactions in each of these systems which have implications for control of light-matter interactions, imaging, and catalysis? How do we characterize energy pathways in a coupled system? Can we actively control critical system parameters, such as coupling strength and spectral lineshapes? To answer these questions, this thesis first lays out a foundation for understanding a variety of cavities ranging from nanoscale to microscale, i.e., plasmonic cavity, optical microcavity, and coupled plasmonic-photonic cavity. The thesis then focuses on the discussion of the coupled cavities because they promise strong Purcell enhancement and provide new platforms for control of light-matter interactions.

Chapter 1 introduces light-matter interactions and a critical metric–transition rate–to quantify these interactions. A cavity can be used to manipulate local density of states that governs the transition rate of an interacting system. Upon excitation of a system coupled to a cavity, the relationship between coupling strength and the dominant damping rate in the system dictates the regimes where light interacts matter, i.e., weaking coupling or strong coupling. Since the coupled system discussed in this thesis operates in the weaking coupling regime, the study of strong coupling is beyond the scope of this thesis.

Chapter 2 reviews a variety of plasmonic cavities and optical microcavities and discusses their differences using two figures of merit (quality factor and mode volume).

To further enhance light-matter interactions, the coupled plasmonic-photonic systems that inherits ultrasmall mode volume from plasmon mode and ultrahigh quality factor from photonic mode are studied for emission control, (bio)sensing, label-free detection, and optical trapping. Several methods that characterize these coupled systems are summarized in this chapter.

Chapter 3 demonstrates a new method to elucidate energy pathways in a coupled plasmonic-photonic cavity. A single tapered optical fiber is used to measure both photothermal absorption and two-sided transmission simultaneously. Combining with theoretical modeling, all system parameters are determined, spanning over *9* orders of magnitude. A full description of the coupled system is provided using this method, paving the way for active control of light-matter interactions.

Chapter 4 shows a novel method to actively tune interactions in a coupled system. An organic solvent that fills the microbubble cavity embeds plasmonic nanocavity within an optical microcavity. The effect of tuning dielectric environment on plasmonic-photonic interactions is thoroughly examined, suggesting that both mode volume and mode overlap play significant roles in determining couplings.

Chapter 5 presents a photothermal imaging method in which gold nanorods that are deposited on an all-glass microtoroid are imaged through a thin glass substrate from the backside. An optical astigmatism is studied using ray optics simulations. This study underscores possible optical aberrations that likely occur in non-flat microcavity systems.

Chapter 6 discusses a two-dimensional palladium nanosheet intercalated with gold nanoparticles for plasmon-enhanced electrocatalysis. A considerable electrocatalytic enhancement is achieved on this heterostructure due to excitation of the localized surface plasmon resonance (LSPR). The unique heterostructure and strongly enhanced localized field intensity under LSPR excitation could result in hot electrons concentrated on the surface of palladium nanosheets and direct transfer of plasmonic energy to metal–adsorbate complexes, manifesting as a reduction of the apparent activation barrier in the electrocatalysis. This investigation provides insight into both the design of efficient electrocatalysts and the distinct role of LSPR excitation in plasmon-enhanced electrocatalysis.

Chapter 7 summarizes two unfinished projects in my Ph.D. period. One of them is an addition to the work that demonstrates active tuning of plasmonic-photonic interaction in coupled systems. A polymer-embedding method was implemented to embed plasmonic nanoparticles on the surface of a microtoroid. The other is the study of an as-synthesized single-component polythiophene conductive polymer using single-particle photothermal absorption spectroscopy.

Chapter 8 is intended to present my graduate research to non-scientific audiences through the program of Wisconsin Initiative of Science Literacy at UW-Madison. I focus on conceptual understanding of plasmons and photons in materials and cavities. I then describe the journey to my research goals and the importance of my graduate research to the public.

Chapter 1 Light-matter interactions in cavities

Introduction

Light-matter interactions are ubiquitous throughout many disciplines from atomic, molecular, optical physics, condensed matter physics, to electrical engineering and biology, with light frequencies and length scales spanning many orders of magnitude. These interactions can either act as probes for interrogating matter's properties or modify electromagnetic radiation in multiple degrees of freedom such as phase, frequency, spin, and orbital angular momentum.

Specifically, these interactions, when employed in an analytical method and measured as transmission, reflection, absorption, scattering, or emission signals, can reveal physical and optical properties of the matter in a noninvasive way. The interactions may be strong or weak, depending on whether the process is resonant or not. In order to chase for highly sensitive tools, sophisticated instrumentation, such as interferometric detection[1] and frequency-modulation[2] techniques, a highly sensitive detector[3] or complicated optical alignment, might enable one to keep pushing the limit of detection further. Although weak signal can be gleaned and measured through these efforts, the instrumentation requires a lot of design and construction.

However, this challenge can be remedied alternatively by enhancing light-matter interactions. To understand this enhancement, let us take a two-level system coupled to an electromagnetic field as an example (see **Figure 1.1**). A critical metric that is used to

characterize the interaction is coupling strength ($\hbar g$). It can be quantified by electric dipole interaction $|\mu_{12} \cdot E_{vac}|$, where $\mu_{12} = -e\langle 1|x|2\rangle$ is one of off-diagonal electric transition dipole matrix elements and E_{vac} is the magnitude of the vacuum field. Even though there is no photon in space, there is a zero-point energy ($1/2\hbar\omega$), called vacuum fluctuation energy. Recalling time-average energy in space equally contributed by both electric and magnetic fields, we obtain

$$\langle \varepsilon \rangle = 2 \int \frac{1}{2} \varepsilon_0 |E_{vac}|^2 dV. \qquad 1.1$$

E_{vac} can thus be obtained by equating $\langle \varepsilon \rangle$ to the zero-point energy. If E_{vac} is constant everywhere in free space, $E_{vac} = \sqrt{\frac{\hbar\omega}{2\varepsilon_0 V}}$. Apparently as V goes smaller, E_{vac} becomes larger. Plugging E_{vac} back to electric field dipole interaction we obtain

$$g = \sqrt{\frac{\mu_{12}^2 \omega}{2\varepsilon_0 \hbar V}}. \qquad 1.2$$

For a given transition, g is inversely proportional to $\sqrt{V}$, suggesting that decreasing V enhances this interaction. Note that the local density of states (LDOS) is proportional to V in free space and has no dependence on V in a cavity. For the given transition, increased LDOS is conducive to accelerate transition rate of absorption or emission because transition rate is proportional to LDOS according to Fermi's golden rule.[I] In 1965,

[I] I will talk more about this rule in Purcell enhancement section

Drexhage et al. showed enhanced radiative rate of emitters by studying the distance of emitter layer to a metal (gold, silver, or aluminum) coated mirror.[4] This experiment first demonstrates that modifying LDOS can manipulate light-matter interactions in optical

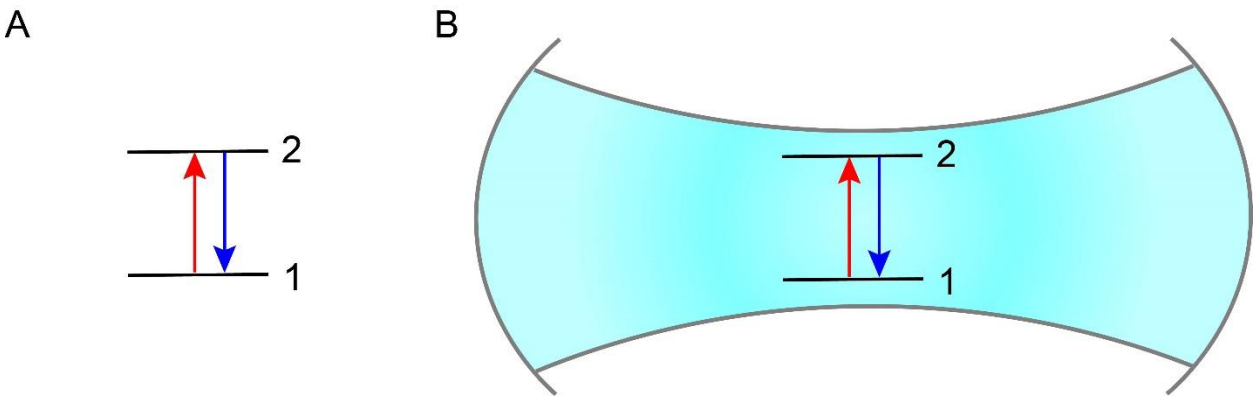

Figure 1.1 A two-level system coupled to electromagnetic field in free space (**A**) and cavity (**B**).

frequencies, although this effect was discovered in radio frequencies by Purcell in 1946 and called Purcell effect.[5] In particular, when these interactions are tightly confined in a finite volume of a resonant structure (**Figure 1.1**), the matter's properties may be modified, such as the change in reactivity and more efficient energy transfer enabled by the half-light and half-matter quasiparticles (or polaritons).

Cavities

Cavities, ranging from the giant Fabry-Perot interferometer (such as LIGO[6]) to extremely small plasmonic picocavity,[7] have been widely studied for the control of light-matter interactions. In principle they modify the photonic environment, which may manifest as electromagnetic enhancement as compared to that in free space in the perturbative limit. The cavities, when driven by external electromagnetic fields, will dump

energy in a variety of pathways. The field is spatially and temporally confined in the cavities, which is characterized by mode volume (V) and quality factor (Q), respectively. Take a Fabry-Perot cavity as an example, after light enters the cavity, light is bounced back and forth for one loop, accumulating a phase shift (φ), as shown in **Figure 1.2**. If φ is equal to $2\pi n$ (n is integer), light is constructively interfered, which we call on resonance. After many times of constructive interference, overall light intensity increases drastically and thus store energy in the cavity. In other words, traveling waves constructively interfere with each other to form a standing wave pattern in the cavity.

The cavity can support different modes (standing wave patterns) resonant with

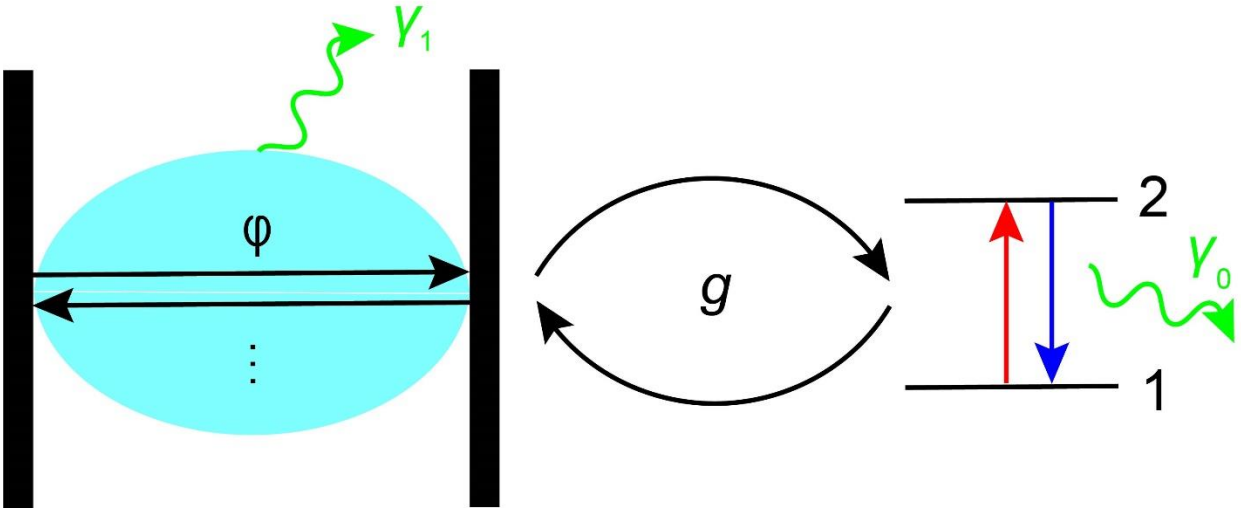

Figure 1.2 A Fabry-Perot cavity coupled to a two-level system with a coupling strength (g). Each component has a certain loss rate (γ_0 and γ_1). A phase shift (φ) is accumulated when light is bounced back and forth in the cavity.

specific photon energies in addition to a fundamental mode. A fundamental mode typically has the smallest mode volume and thus tightly concentrates light. The mode volume is generally calculated by integrating electromagnetic energy over the space and normalized with respect to the maximum electromagnetic energy as shown below,

$$V = \frac{\iiint \varepsilon |E|^2 dV}{\max\left[\varepsilon |E|^2\right]}. \quad 1.3$$

This mode dissipates energy with the slowest rate (P) to the environment and has the highest *Q*-factor when the energy (U) is stored in the cavity with certain angular frequency, resulting in the following relationship,

$$Q = \omega \frac{U}{P}. \quad 1.4$$

However, plasmonic cavities might be understood differently given that mode is confined below diffraction limit and magnetic energy is less than electric energy.[8] Plasmon in plasmonic cavities is typically understood by collective oscillations of electrons. Since an electron has a much shorter De Broglie wavelength than a photon with the same energy does, the mode volume is less than the cubic of excitation wavelength.[I]

Defining coupling regimes

When an atom, a molecule, or an artificial atom (quantum dots, plasmonic nanoparticles, etc.) interacts with electromagnetic field in a cavity, photons in the cavity can be absorbed by an emitter[II] and it can also emit photons back to the cavity. Of particular interest is the interaction where one of the cavity's modes is resonant with

[I] This part will be thoroughly discussed in the section of plasmonic nanocavities in Chapter 2.

[II] Here I use emitter to represent emission process of atoms, molecules, etc.

transition frequency of the emitter. This interaction regime is determined by the relationship among three parameters, i.e., coupling strength (g), cavity's loss rate (γ_1) and emitter's damping rate (γ_0), as seen in **Figure 1.2**. In general, when $g \ll max(\gamma_0, \gamma_1)$, defined as the weak coupling limit, the emitter is weakly coupled to the cavity. Here the emission process of the emitter is irreversible like spontaneous emission in free space. But the emission rate is modified by the cavity, which will be explained more in the section of weak coupling limit. In strong coupling limit where $g \gg max(\gamma_0, \gamma_1)$, the photon emitted by the emitter excites the cavity mode and can be reabsorbed by the emitter and undergo this reversible process many and many times before it is finally lost to the environment. This reversible process is characterized as Rabi oscillation in time domain. The criteria for strong coupling vary in the literature and sometimes are debatable. Typically, the degree to which characteristic Rabi splitting is large relative to loss rates in frequency domain is used to define how strong the coupling is.[9] These two limits presented above generalize two totally different scenarios of light-matter interaction and result in very different behaviors in a spectrum.

Weak coupling limit

In the previous section I present the distinction between weak coupling and strong coupling. In the weak coupling limit, photons are lost faster than characteristic interaction time between the cavity and emitter. Light-matter interaction is typically treated by perturbation theory because the effect of the cavity is small enough but to enhance or suppress transition rate compared to that in a free space. I will use the derivation of

spontaneous emission rate in a cavity to demonstrate how Purcell effect emerges at this limit.[9]

In a free space spontaneous emission, transition rate Γ_{free} is given below according to Fermi's golden rule,

$$\Gamma_{free} = \frac{2\pi}{\hbar^2}|M_{12}|^2\rho(\omega), \quad 1.5$$

where M_{12} is transition matrix element and $\rho(\omega)$ is LDOS. To simplify the calculation, we can assume the transition dipole is positioned in a cavity that has a very large mode volume V_0. V_0 is so large that the transition is barely affected by the chosen volume. M_{12} is defined as the average electric dipole interaction in free space:

$$M_{12} = < \mu_{12} \cdot E >, \quad 1.6$$

where E is vacuum electric field (E_{vac}) that triggers the spontaneous emission. After averaging all possible configurations of transition dipole with respect to the vacuum field polarization, we thus obtain ${M_{12}}^2 = \frac{1}{3}{\mu_{12}}^2{E_{vac}}^2$. LDOS for the defined volume V_0 is $\frac{\omega^2 V_0}{c^3\pi^2}$. After normalizing it with respect to V_0, we obtain

$$\rho_{V_0} = \frac{\omega^2}{c^3\pi^2}. \quad 1.7$$

In a homogeneous medium this normalized density of states scales as ω^2. Substituting both ${M_{12}}^2$ and $\rho(\omega)$ in equation 1.5 we obtain

$$\Gamma_{free} = \frac{{\mu_{12}}^2 \omega^3}{3\pi\varepsilon_0 \hbar c^3}. \quad 1.8$$

Γ_{free} is independent of the chosen V_0. Note that c is the speed of light in vacuum and should be replaced by c/n in a medium with a refractive index n.

For the spontaneous emission rate in a cavity, first, we presume that a single mode in a cavity is coupled to the transition dipole of the emitter, which usually is the fundamental mode. This mode's resonant frequency is ω_c and the mode volume is V. Although there are other high-order modes in the cavity that might be coupled to the transition dipole of the emitter, we assume the couplings are relatively weak and do not consider these modes. When there is no photon in the cavity, we can obtain $E_{vac} = \sqrt{\frac{\hbar\omega_c}{2\varepsilon_0 V}}$ that interacts with the transition dipole of the emitter. LDOS in the cavity is different from that in free space. Since we assume a single mode is coupled to the transition dipole of the emitter, $\rho(\omega)$ must satisfy

$$\int_0^\infty \rho(\omega) d\omega = 1. \quad 1.9$$

If $\rho(\omega)$ takes a Lorentzian line shape, we can obtain

$$\rho(\omega) = \frac{2}{\pi} \cdot \frac{Q}{\omega_c} \cdot \frac{\gamma_1^2}{(\omega - \omega_c)^2 + \gamma_1^2}. \quad 1.10$$

$\rho(\omega)$ derived here is similar to the density of states due to radiative broadening. In reality, there is a nonradiative pathway that contributes to photon loss rate in the cavity. But at

this point the nonradiative and radiative pathways are aggregated in the total loss rate γ_1. Q is defined earlier in the previous section and rewritten here as $Q = \frac{\omega_c}{\Delta\omega_c} = \frac{\omega_c}{2\gamma_1}$,[I] where $\Delta\omega_c$ is the full width at half maximum obtained from the cavity's Lorentzian line shape. Compared to LDOS in a free space, the cavity's LDOS shows a single peak with a line width $2\gamma_1$. Again, if we normalize this LDOS relative to the mode volume, V will be added to the denominator. Taken together, substituting both $\rho(\omega)$ and E_{vac} in equation 1.5 and additional rearrangement give rise to

$$\Gamma_{res} = \frac{2}{\hbar}\xi^2 \frac{{\mu_{12}}^2}{\varepsilon_0}\frac{Q}{V}\frac{\gamma_1^2}{(\omega-\omega_c)^2+\gamma_1^2}, \qquad 1.11$$

where ξ^2 is electric transition dipole orientation factor and equals 1/3 for randomly oriented transition dipole in free space. When the electric transition dipole is aligned with respect to the electric field polarization in the cavity, ξ^2 is 1. The Purcell factor is ratio of transition rates in the cavity and in free space as follows,

$$F_p = \frac{\Gamma_{res}}{\Gamma_{free}} = 6\pi\xi^2\left(\frac{c}{\omega}\right)^3\frac{Q}{V}\frac{\gamma_1^2}{(\omega-\omega_c)^2+\gamma_1^2}. \qquad 1.12$$

Recalling that the dielectric environment in free space is exactly like that in the cavity, thus c should be replaced by c/n in the space with refractive index n. If the emitter is

[I] Note that in our Q-factor measurement we scan the resonance in wavelength and compute Q using wavelength, which includes external loss rate due to fiber coupling to cavity. But here external loss rate is ignored.

tuned to be resonant with the cavity ($\omega_a = \omega_c$) and its transition dipole is aligned perfectly along the electric field, Purcell factor is further simplified to be

$$F_p = \frac{3}{4\pi^2}\left(\frac{\lambda}{n}\right)^3 \frac{Q}{V}, \tag{1.13}$$

where $\frac{\lambda}{2\pi n} = \frac{c}{\omega}$, λ is the incident wavelength and n is the refractive index in the cavity. If $F_p < 1$, the cavity is suppressing emission process, whereas Purcell factor larger than unity implies an enhancement in emission rate. Purcell enhancement is widely seen in various applications, such as label-free sensing[10] and surface-enhanced spectroscopies.[11] Strong Purcell enhancement requires high Q-factor and small mode volume. At the same time, the maximum Purcell enhancement occurs when $\omega_a = \omega_c$ and $\xi^2 = 1$. Making emitter resonant with the cavity can be done by designing the cavity or manipulating emitter's transition frequency via Stark effect. However, it is relatively difficult to control perfect alignment of transition dipole with respect to the cavity's mode field polarization. If we define $\left(\frac{\lambda}{n}\right)^3 \frac{1}{V}$ as mode density D_{mode}, thus QD_{mode} becomes a figure of merit for designing a cavity to achieve desired Purcell effect and tailor light-matter interactions. In plasmonic-enhanced spectroscopy,[11, 12] electromagnetic enhancement sometimes is equivalent to Purcell enhancement, which is defined as

$$F_{EM} = \left|\frac{E_{local}}{E_1}\right|^2, \tag{1.14}$$

where E_{local} is local electric field and E_1 is electric field in free space.

Purcell enhancement through increasing LDOS via a cavity is widely used to tailor light-matter interactions, such as increasing excitation rate,[13] controlling branching ratio of various decay channels,[14] and radiative quantum efficiency,[15] although Purcell enhancement is commonly seen in the case of spontaneous emission of an emitter. Control of light-matter interactions has profound impact on catalysis,[16] label-free sensing,[10, 17] ultralow-threshold lasing,[18] nonlinear optics,[19] ultrafast and bright light-emitting diodes.[20] For instance, accelerating absorption rate can lead to perfect absorbers.[21] This enhanced absorption can efficiently harvest energy for catalysis.[22, 23] Control of spontaneous emission process is important for designing fast single photon sources.[24] Purcell enhancement is beneficial to the development of nanoscale, ultralow threshold lasers because minimum pump power for lasing is proportional to V/Q.[18] Hence, increasing Purcell factor can largely reduce pump power consumption. Cavity-enhanced sensing also benefits a lot from Purcell enhancement, where sensitivity is determined by Q/V.

Strong coupling limit

In strong coupling regime, photons are recycled through light-matter interaction before they are eventually lost to their local environment. This study of reversible light-matter interaction in this regime is called cavity quantum electrodynamics (cQED). In the framework of cQED, light field of a single mode in the cavity is quantized, which is

described by a quantum harmonic oscillator.[I] In this context, vacuum fluctuations are considered to be on the ground state (or Fock state) with zero photon number in quantized light field.[9] Recently it has been believed that vacuum fluctuation plays a critical role in modifying chemical reactivity in cavity-controlled chemistry.[25] Also, phonon heat transfer at the nanoscale might be mediated by vacuum fluctuation under strong coupling regime.[26] The discussion on strong coupling is beyond the scope of this thesis and readers can refer to reviews[16, 25, 27] for more details.

References

1. Hwang, J., Fejer, M. M., et al., "Scanning interferometric microscopy for the detection of ultrasmall phase shifts in condensed matter." *Phys. Rev. A* **2006**, *73*(2): 021802.

2. Moerner, W. E. and Kador, L., "Optical detection and spectroscopy of single molecules in a solid." *Phys. Rev. Lett.* **1989**, *62*(21): 2535-2538.

3. Gol'tsman, G. N., Okunev, O., et al., "Picosecond superconducting single-photon optical detector." *Appl. Phys. Lett.* **2001**, *79*(6): 705-707.

4. Drexhage, K. H., "Influence of a dielectric interface on fluorescence decay time." *J. Lumin.* **1970**, *1-2*: 693-701.

5. Purcell, E. M., "Spontaneous Emission Probabilities at Radio Frequencies." *Phys. Rev.* **1946**, *69*(681).

6. Collaboration, L. S., Virgo, C., et al., "Observation of Gravitational Waves from a Binary Black Hole Merger." *Phys. Rev. Lett.* **2016**, *116*(6): 061102.

7. Benz, F., Schmidt, M. K., et al., "Single-molecule optomechanics in "picocavities"." *Science* **2016**, *354*(6313): 726-729.

8. Brongersma, M. L., Halas, N. J., et al., "Plasmon-induced hot carrier science and technology." *Nat. Nanotechnol.* **2015**, *10*(1): 25-34.

9. Fox, M., "Quantum Optics: An Introduction." **2006**, Oxford University Press.

[I] The second quantization of field theory

10. Jiang, X., Qavi, A. J., et al., "Whispering-Gallery Sensors." *Matter* **2020**, *3*(2): 371-392.

11. Willets, K. A. and Duyne, R. P. V., "Localized Surface Plasmon Resonance Spectroscopy and Sensing." *Annu. Rev. Phys. Chem.* **2007**, *58*(1): 267-297.

12. Itoh, T., Yamamoto, Y. S., et al., "Plasmon-enhanced spectroscopy of absorption and spontaneous emissions explained using cavity quantum optics." *Chem. Soc. Rev.* **2017**, *46*(13): 3904-3921.

13. Krivenkov, V., Samokhvalov, P., et al., "Synergy of Excitation Enhancement and the Purcell Effect for Strong Photoluminescence Enhancement in a Thin-Film Hybrid Structure Based on Quantum Dots and Plasmon Nanoparticles." *J. Phys. Chem. Lett.* **2020**, *11*(19): 8018-8025.

14. Wientjes, E., Renger, J., et al., "Nanoantenna enhanced emission of light-harvesting complex 2: the role of resonance, polarization, and radiative and non-radiative rates." *Phys. Chem. Chem. Phys.* **2014**, *16*(45): 24739-24746.

15. Luo, Y., Ahmadi, E. D., et al., "Purcell-enhanced quantum yield from carbon nanotube excitons coupled to plasmonic nanocavities." *Nat. Commun.* **2017**, *8*(1): 1413.

16. Lather, J., Thabassum, A. N. K., et al., "Cavity catalysis: modifying linear free-energy relationship under cooperative vibrational strong coupling." *Chem. Sci.* **2022**, *13*(1): 195-202.

17. Vollmer, F. and Yang, L., "Review Label-free detection with high-Q microcavities: a review of biosensing mechanisms for integrated devices." *Nanophotonics* **2012**, *1*(3-4): 267-291.

18. Li, Y., Zhang, J., et al., "Room-temperature continuous-wave lasing from monolayer molybdenum ditelluride integrated with a silicon nanobeam cavity." *Nat Nanotechnol* **2017**, *12*(10): 987-992.

19. Kippenberg, T. J. (**2004**). Nonlinear Optics in Ultra-High-Q Whispering-Gallery Optical Microcavities, California Institute of Technology. *Ph.D.*

20. Tsakmakidis, K. L., Boyd, R. W., et al., "Large spontaneous-emission enhancements in metallic nanostructures: towards LEDs faster than lasers [Invited]." *Opt. Express* **2016**, *24*(16): 17916-17927.

21. Akselrod, G. M., Huang, J., et al., "Large-Area Metasurface Perfect Absorbers from Visible to Near-Infrared." *Adv. Mater.* **2015**, *27*(48): 8028-8034.

22. Huang, Q., Canady, T. D., et al., "Enhanced Plasmonic Photocatalysis through Synergistic Plasmonic–Photonic Hybridization." *ACS Photonics* **2020**, *7*(8): 1994-2001.

23. Ding, J., Wang, F., et al., "Two-Dimensional Palladium Nanosheet Intercalated with Gold Nanoparticles for Plasmon-Enhanced Electrocatalysis." *ACS Catal.* **2021**, *11*(21): 13721-13732.

24. Senellart, P., Solomon, G., et al., "High-performance semiconductor quantum-dot single-photon sources." *Nat. Nanotechnol.* **2017**, *12*(11): 1026-1039.

25. Garcia-Vidal, F. J., Ciuti, C., et al., "Manipulating matter by strong coupling to vacuum fields." *Science* **2021**, *373*(6551): eabd0336.

26. Fong, K. Y., Li, H.-K., et al., "Phonon heat transfer across a vacuum through quantum fluctuations." *Nature* **2019**, *576*(7786): 243-247.

27. Hertzog, M., Wang, M., et al., "Strong light–matter interactions: a new direction within chemistry." *Chem. Soc. Rev.* **2019**, *48*(3): 937-961.

Chapter 2 Plasmonic nanocavities, optical microcavities, and plasmonic-photonic coupled cavities

Plasmonic nanocavities

Plasmons initially proposed in 1952[1] describe quantization of classical plasma oscillations, arising from long-range electron-electron correlations, which can be understood as a collective oscillation of free electrons in metallic conductors. Surface plasmons[2] are coherent electron oscillations at the interface of metal and dielectric media upon excitations, which have lower energy than bulk plasmons (**Figure 2.1**). Since the sign in real part of the dielectric function across the interface (metal-dielectric interface) flips from the negative to the positive, surface plasmons' electrical field perpendicular to the surface exponentially decays as a function of distance from the surface, preventing power from propagating to the far field along surface normal axis.[3] Plasmonics, termed by Atwater and Halas, focuses on the study of this light-matter interaction and its various applications,[4] such as biological and chemical sensing,[5] surface-enhanced spectroscopy,[6] surface plasmon resonance microscopy,[7] and plasmonic photocatalysis.[8]

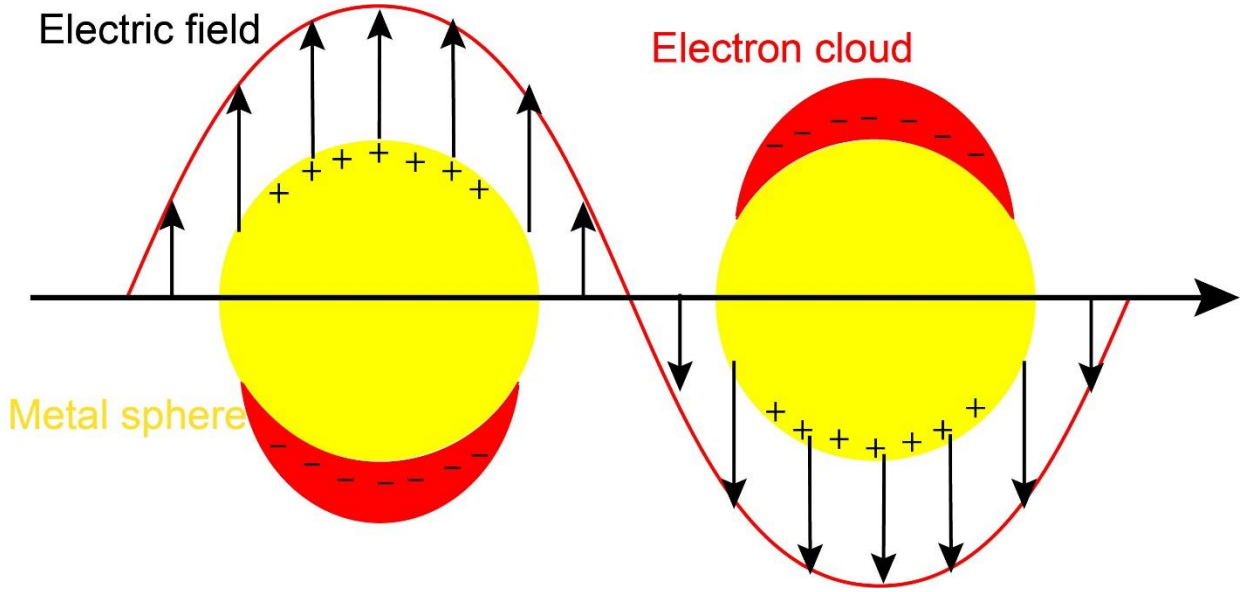

Figure 2.1 Excitation of a localized surface plasmon (LSP) in a plasmonic nanoparticle.

Metallic nanoparticles, for instance, gold nanorods, support localized surface plasmon (LSP) due to their closed surface, featuring a strong enhancement in electric field near the surface and maximum absorption at a plasmon resonant frequency.[9] Dipolar modes have low resonant energy, whereas high order modes are at high resonant frequencies, which are characterized by optically inactive (dark) modes. These dark modes can be measured by near-field techniques, such as scanning near-field optical microscopy,[10] electron energy loss spectroscopy,[11, 12] etc. Only dipolar LSP is discussed in this section and hereafter LSP is used for dipolar LSP mode. LSP's tight confinement effectively reduces its mode volume below the diffraction limit (see **Table 2.1**), whereas the quality factor typically is less than 10^2 due to its considerable absorptive and radiative losses. The ultrasmall mode volume results in high plasmon local density of states, though Q-factors are low, giving rise to a Purcell factor of ~10^2.[13]

When two identical nanoparticles aggregate to form a dimer (**Figure 2.1A**), two gap plasmons are formed by hybridizing dipolar LSP of each individual nanoparticle, similar to bonding and antibonding orbitals in molecules. Typically, the lower-energy gap plasmon is probed, which provides the largest field enhancement. Note that field distribution in the gap is not uniform, with the highest enhancement in the vicinity to the two tips or protrusions of the nanoparticles. The mode volume can be further reduced to 10^{-6} μm^3 in a nanodimer (see **Table 2.1**),[13] as in a bowtie nanostructure (**Figure 2.3A**).[14-17] This bowtie nanostructure can provide up to 100-fold field enhancement compared to the isolated single nanoparticle. Thus, this strong field enhancement or high plasmon LDOS makes this dimer nanostructure desirable for studying strong light-matter interactions. Haran group demonstrated strong coupling of a few quantum dots (QDs) or even single QD to a gold prism nanodimer using dark-field scattering spectroscopy.[17, 18]

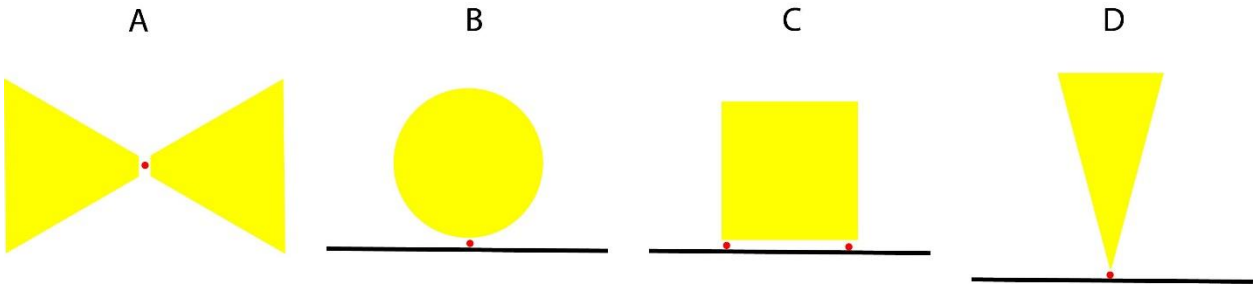

Figure 2.2 Designs of plasmonic cavities. (**A**) bowtie dimer, (**B**) nanosphere and (**C**) nanocube on a mirror, (**D**) tip on a mirror. The red dot indicates an emitter.

Another design to create gap plasmons and thus obtain stronger Purcell enhancement is the scaffold of a metal nanoparticle (nanosphere, nanocube, etc.) on a mirror (NPoM) coated with metallic film (**Figure 2.2B** and **Figure 2.2C**).[19-21] There is a large impedance mismatch between gap plasmons and free space, i.e., the direct

coupling efficiency is very low (10^{-4}).[19] However, the gap plasmons can couple to the plasmonic antenna mode which can be directly excited by free-space light. This unique geometry greatly increases the coupling efficiency. The gap plasmon modes have a very large in-plane wavevector ($k_{\parallel} \approx 100k_0$) and are polarized normal to the mirror surface, like a nanoscopic Fabry-Perot cavity. This NPoM structure has an even smaller mode volume and stronger field enhancement (see **Table 2.1**), largely confining electromagnetic field and consequently enhancing light-matter interaction. The spacing between the nanoparticle and the mirror is precisely controlled by a thin dielectric layer with a few nanometers down to sub-nm[22], such as self-assembled monolayers of short alkyl chain or aromatic thiols, transition metal dichalcogenides, graphene, etc.[19] Baumberg's group examined single QDs,[23, 24] single molecules,[25] and monolayer of transition-metal dichalcogenides[26, 27] sandwiched by this nanostructure (**Figure 2.3D**). They observed a single dye molecule encapsulated in a cucurbituril (CB) macrocyclic molecule is strongly coupled to the gap plasmon (**Figure 2.3B**).[25] This host-guest chemistry of CB:dye preferentially aligns the dye to the polarization direction of the field in the gap and also defines a gap of 0.9 nm. Although both Haran's and Baumberg's groups claimed strong coupling of single QD or single molecule to these nanocavities,

both reproducibility of these experiments and deterministic control of both number and position of QD are a concern.

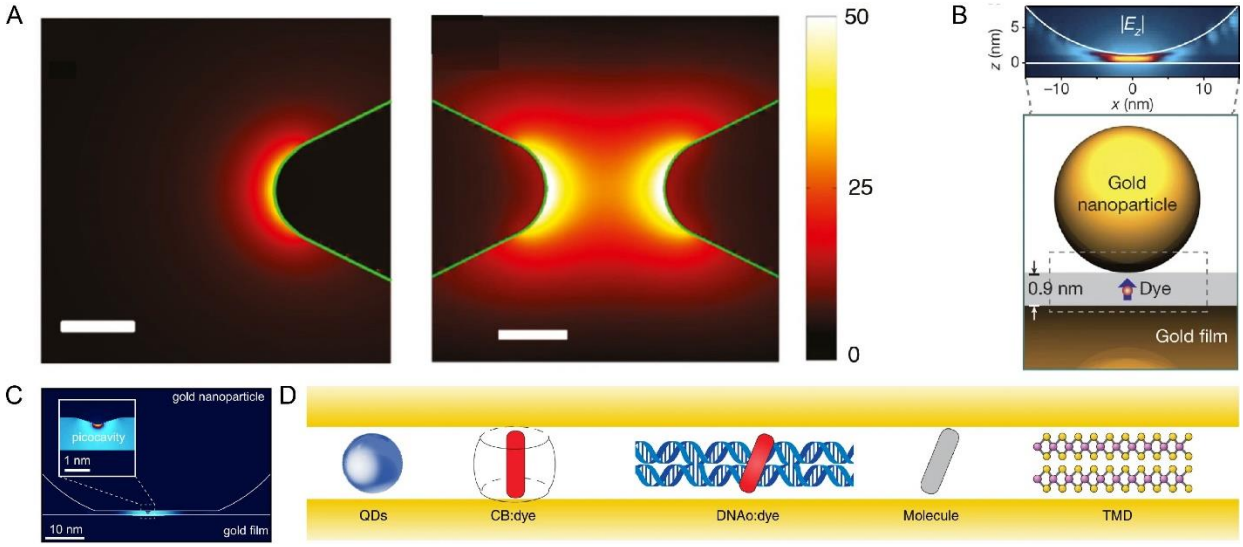

Figure 2.3 Electric field profile in plasmonic nanocavities and materials interacting with these cavities. (**A**) Electric field intensity in a bowtie nanodimer is presented and compared to that in an isolated nanoparticle. (B) NPoM nanocavity. (**C**) Picocavity. (**D**) Different materials sandwiched by the NPoM nanocavity. Reprinted with permission from Ref[18-19, 25, 28].

In addition, Baumberg's group demonstrated a picocavity design formed by a single gold atom and gold film (**Figure 2.3C**),[28] further shrinking the mode volume down to less than 1 nm^3. This picocavity has a short lifetime (a few minutes) even at cryogenic temperatures and can be disassembled by laser irradiation. This extreme optical confinement provides *6* orders of magnitude enhancement of optomechanical coupling between optical field and vibrations of individual molecular bonds. Zhang et al. demonstrated a tip-enhanced scanning tunneling microscopy (TE-STM) of a single organic molecule with a sub-nanometer spatial resolution, using a tip-on-mirror nanocavity (**Figure 2.2D**).[29] Matching the gap plasmon to vibronic transitions of the

molecule strongly enhances Raman process. The sub-nanometer spatial resolution might be attributed to the picocavity formed by atomistic protrusion of the silver tip apex.

Table 2.1 Mode volume and field enhancement in plasmonic cavities. Note that the radius of NP is 15 nm in isolated NS,[30] a gap distance is 2 nm in bowtie nanodimer, $V = \frac{\pi R d^2}{2ln2n_g^2} \approx Rd^2$ and $F_{EM} = 16ln2Qn_g\left(\frac{R}{d}\right)^2$ in NPoM, where R is the radius of NP (40 nm), d is the gap size (0.9 nm), n_g is the refractive index in the dielectric layer, Q = 15.

	Isolated NS[30]	Bowtie nanodimer[30]	NPoM[25]	Picocavity[28]
V (μm^3)	1.3×10^{-5}	~10^{-6}	3.7×10^{-8}	10^{-11}
F_{EM}	~10	~65	4.6×10^5	6.5×10^5

It has been well believed when an emitter is in the vicinity of a metal nanostructure (<10 nm) fluorescence is quenched by higher-order dark modes, although dipolar modes yield high plasmon LDOS, increasing the excitation rate. However, in the nanodimer or NPoM, as the emitter approaches the metal surface closer, fluorescence quenching is strongly suppressed because high-order modes acquire a radiative component due to hybridization of plasmons in these tightly coupled nanostructures.[31] Specifically, the fluorescence quantum yield of an emitter largely increases compared to the cases where the emitter is near the surface of isolated nanoparticles. Alternatively, a dielectric layer can greatly decouple the emitter and the metal and thus suppress fluorescence quenching induced by the metal substrate. Recently, Yang et al. achieved a sub-

nanometer photoluminescence imaging of a single phthalocyanine molecule by attaching three layers of NaCl to the metal substrate in their TE-STM instrument.[32]

In addition to the exploration of these strong light-matter interactions enabled by these nanocavities, plasmonic nanocavities have been widely used for biological and chemical sensing,[5] surface-enhanced Raman spectroscopy (SERS),[6] and more recent advances in the study of strongly coupled plasmon-exciton polaritons and creation of single photon sources.[33] Biological or chemical sensing rely on measuring wavelength shift due to high sensitivity of LSP resonance to the changes in local dielectric environment. SERS pioneered by Van Duyne and his coworkers has thrived for almost two decades and finds wide applications in ultrafast vibrational spectroscopy,[34] sub-diffraction-limit imaging (high-resolution scanning probe SERS), the study of electrochemical reactions at the single-molecule level, etc.[35]

Optical microcavities

Optical microcavities have been widely studied for achieving high Purcell enhancement or strong coupling. These two behaviors have been demonstrated in early examples of planar inorganic semiconductor microcavities, where the active region is made of quantum wells or quantum dots and two mirrors are distributed Bragg reflectors (DBR). In 1998, Lidzey et al. for the first time showed the observation of strong coupling in organic semiconductor microcavities at room temperature (**Figure 2.4A**).[36] These types of microcavities attract a lot attention for the study of exciton-polariton Bose-Einstein Condensation at room temperature and lasing. Interested readers can refer to this

review[37] for more details in this active field. In addition to the open-access feature, these Fabry-Perot microcavities can yield Q-factor up to 10^7, but mode volume is very large

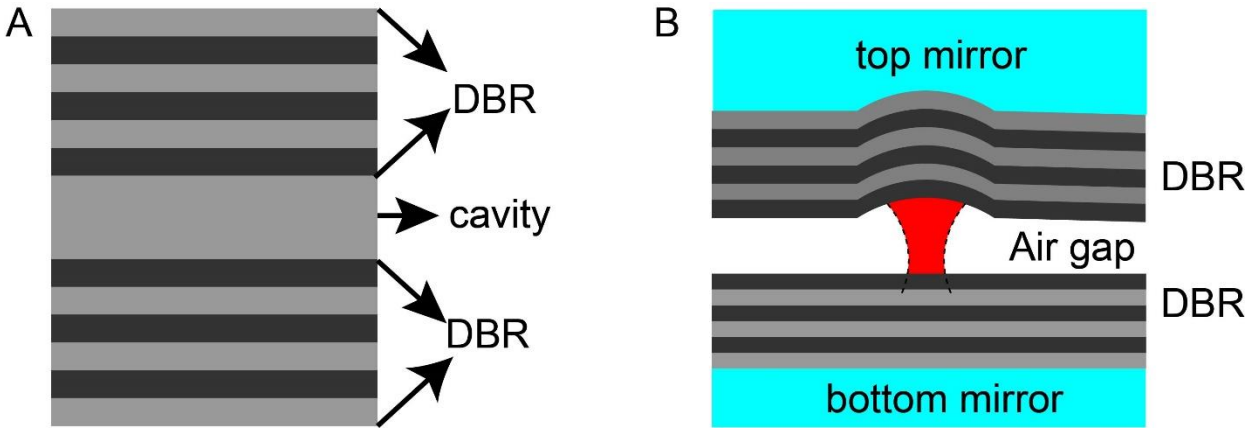

Figure 2.4 Fabry-Perot microcavities. DBR: distributed Bragg reflectors. (**A**) Organic dye molecules are embedded in a host matrix sandwiched the microcavity. (**B**) A scanning fiber based microcavity where the top mirror is a coated fiber mirror and the bottom is supported by a flat glass substrate with high reflectivity.

($10^4\left(\frac{\lambda}{n}\right)^3$). Recently fiber-based Fabry-Perot microcavities have become attractive as the mode volume gets smaller while preserving high Q-factors. Hunger's group invented a scanning Fabry-Perot cavity microscopy technique using a concave-planar geometry,[38-40] where the planar mirror provides the open-access for sample deposition and the concave mirror is supported by a laser-ablated optical fiber (Figure 2.4B).

On the other hand, a variety of whispering-gallery-mode (WGM) microcavities (**Figure 2.5A-C**), such as microsphere,[41] microbottle[42] and microbubble,[43] microtoroid and microdisk,[44] have been fabricated for label-free sensing,[44] single-particle detection,[44] cQED between atoms and microtoroid cavity,[45, 46] Raman lasing,[47, 48] and most recently frequency comb generation,[49] *PT*-symmetric optics,[50, 51] and the study of non-Hermitian physics.[50-52] These microcavities trap light spatially and temporally, with mode volume of

around tens or hundreds of $\left(\frac{\lambda}{n}\right)^3$ and Q-factor of over 10^8. Electron beam lithography makes it possible to fabricate small ring microcavities with integrated waveguides, which yields Q-factor up to 10^6 in silicon nitride rib microring cavities (**Figure 2.5D**).[53] The volume is an order of magnitude smaller than typical silica microtoroid cavities. Another type of micro(nano)cavities is 2D or 1D photonic crystal cavities (PCs).[54-56] The defect is created on purpose in a periodic structure to open modes in a stop band for spatially and temporally trapping light (**Figure 2.5E**). The mode volume has been lowered down to $\left(\frac{\lambda}{2n}\right)^3$, whereas the highest Q-factor that has been demonstrated so far is around ~10^6 in silicon nanobeam PCs.[57] Since this thesis mainly focuses on the interplay between WGM microcavities and plasmonic nanocavities, I will focus only on WGM microcavities in the following sections.

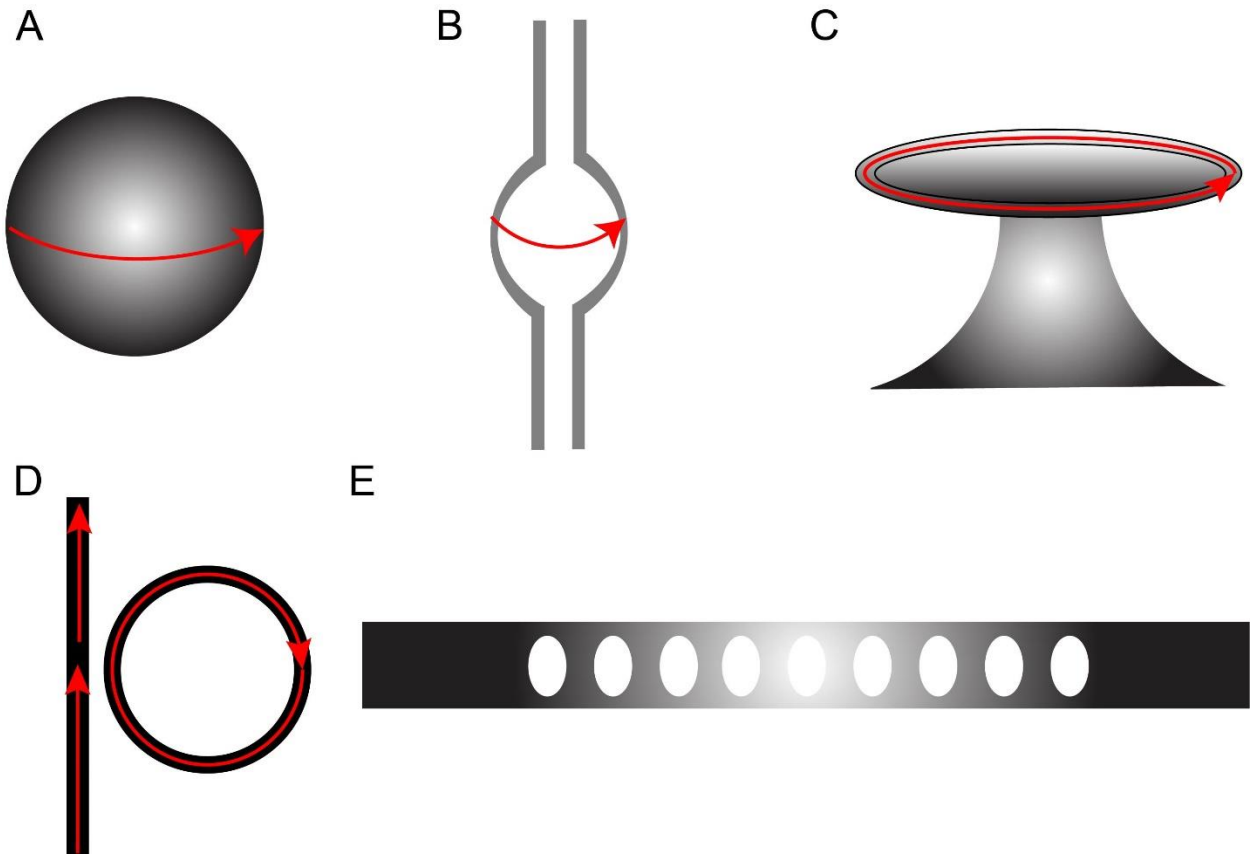

Figure 2.5 Whispering-gallery-mode microcavities and photonic crystal microcavity. (**A**) microsphere, (**B**) microbottle and microbubble, (**C**) microtoroid and microdisk, (**D**) microring, (**E**) One-dimenstional photonic crystal. The red arrows represent light propagation direction.

WGM optical microcavities

WGM optical microcavities inherit their name from acoustic sound wave propagation mechanism in circular resonant structures, for instance, Wisconsin Capitol rotunda (**Figure 2.6A**). Similar to the sound wave propagation in these structures, the way light propagates in WGM optical microcavities can be understood as total internal reflection in a closed-loop optical fiber from the perspective of ray optics (**Figure 2.6B**). The refractive index (n_1) of a microcavity must be higher than that (n_2) in its local

environment to realize total internal reflection. According to Snell's law, at or above a critical angle (θ), light is totally reflected on microcavity's inside wall, as expressed below

$$\theta = \arcsin\left(\frac{n_2}{n_1}\right). \qquad 2.1$$

As we tell from equation 2.1, a high refractive index contrast is desired for confining light propagation in WGM optical microcavities.

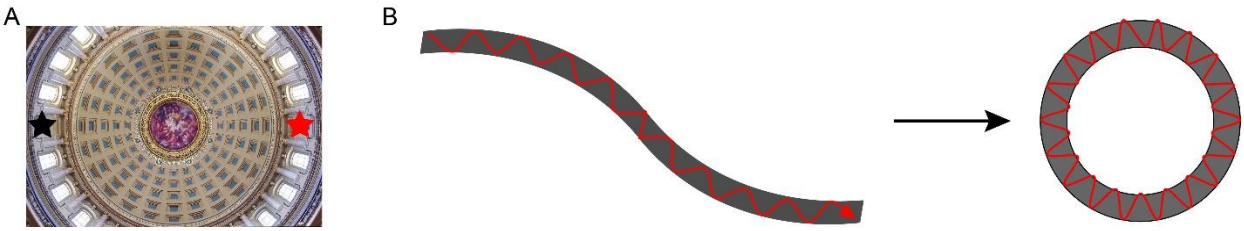

Figure 2.6 Whispering gallery conceptual representation (**A**) and whispering-gallery-mode (WGM) microcavity (**B**). (**A**) Whispering sound can propagate from one position (red star) to another (black star) in Wisconsin Capitol rotunda (credit: Wisconsin Public Television). (**B**) Light propagation in a WGM microcavity (right) is equivalent to that in a closed-loop optical fiber on the left.

Like any other cavities, WGM optical microcavities only allow light with certain wavelength (λ) to propagate inside. The resonant condition, as we recall from the early section in Chapter 1, is written as below for WGM microcavities

$$2\pi R n_1 = m\lambda, \qquad 2.2$$

where R is the radius of the structure and m is an integer number.[I] On resonance, light wave is constructively interfered within the microcavity, storing the energy temporally.

[I] We call it azimuthal mode number in the following section

Otherwise, light wave is destructively interfered, and no energy stored. So, a continuous, broadband light source cannot be coupled into the microcavity.

Different types of WGM microcavities

The first type of WGM microcavities are microsphere cavities, which were fabricated from fused quartz with a diameter of 40-400 μm and a Q-factor above 10^8 by Ilchenko's group in 1980s.[58] And then they demonstrated a Q-factor of 8×10^9 in fused silica microsphere.[41] Microsphere cavities have been used for gas sensing and Raman lasing.[59] Microbottle and microbubble cavities have been demonstrated to be more attractive in solution-phase studies and microfluidics than microspheres due to their unique hollow structures where WGMs are supported by a very thin wall (a few μm or sub-μm).[43] On-chip silica-on-silicon microtoroids were firstly fabricated by Vahala's group with a Q-factor as high as over 10^8.[60] This high Q-factor is attributed to microtoroid's ultra-smooth surface after a CO_2 laser reflow process. Although all-glass microtorids have been fabricated in a similar way but smoothed using a furnace reflow,[61] Q-factors (~10^6) are less comparable to demonstrated Q-factors in silica-on-silicon microtoroids. Microdisk cavities have been reported to yield a Q-factor of ~10^7 even without reflow process.[62] Thanks to geometric confinement in axial direction, there are smaller number of modes in microtoroids than those in microspheres, microbottles or microbubbles. Another great advantage is chip-scale fabrication of microtoroids, which shows applications in label-free sensing, optomechanics, and single-particle photothermal imaging and spectroscopy, and promise in constructing quantum network and integrated optics. The monolithic

fabrication of microring cavities with a comparable Q-factor around 10^6 featuring integrated waveguides are very attractive platforms for single-molecule spectroscopy, topological photonics, and photonic quantum computing.

Loss mechanisms

The stored energy can be lost to the environment in a variety of pathways, such as material absorption loss, scattering loss induced by surface inhomogeneity and surface contamination, bending loss, and external coupling loss. Put it another way, the photon in the cavity has a lifetime determined by the losses which are contributed by these dissipations. The photon lifetime is given by $\tau_{lifetime} = Q/\omega$. To quantify all these loss mechanisms, let us revisit the definition of Q-factor and rewrite it reciprocally

$$\frac{1}{Q} = \frac{P}{\omega U}. \tag{2.3}$$

Although all the losses summarized above originate from the commonly stored energy at resonant frequency, they have their characteristic loss rates and thus can be defined as individual characteristic Q-factors. Based on this understanding, *Q*-factor is a characteristic parameter that quantifies how long energy is stored in the cavity or how fast energy is dissipated to its environment. After we include all the loss rates into equation 2.3, it is now expanded as

$$\frac{1}{Q_{tot}} = \frac{P_{abs}}{\omega U} + \frac{P_{scatt}}{\omega U} + \frac{P_{bend}}{\omega U} + \frac{P_{ext}}{\omega U} = \frac{1}{Q_{abs}} + \frac{1}{Q_{scatt}} + \frac{1}{Q_{bend}} + \frac{1}{Q_{ext}}, \tag{2.4}$$

where Q_{abs} accounts for the material and surface contamination absorption loss, Q_{scatt} is Q factor limited by the scattering loss due to both surface inhomogeneity and contamination, Q_{bend} represents the bending loss due to microcavity's curvature boundary, Q_{ext} describes the loss induced by external coupling.

Material absorption loss is induced by the materials used for fabrication. If we know in what wavelength range the microcavity operates, we can choose transparent materials that barely absorb or absorb less in that range. For instance, although silicon is a common material for integrated photonics, it strongly absorbs ultraviolet and visible light, limiting its operation in this spectrum. In contrast, fused silica is transparent across visible and infrared spectrum with a loss of 0.2 dB/km at 1.5 μm, which corresponds to Q_{abs} of 10^{11}.[63] However, monolayer water absorbed on the surface can limit Q-factor to 2-4×10^8 due to absorption in O-H overtone band.[64] Scattering loss limited Q-factor has a relationship with both microcavity's radius and resonant wavelength. The dependence on the radius can be understood as the mode field has a shorter tail across the surface when the radius becomes smaller. As resonant wavelength goes smaller, scattering effects become dominant due to Rayleigh scattering. Large-size contaminants on the surface can scatter light and limit Q-factor as well. Bending loss will not limit Q-factor with a radius over 15 μm in air[65] and 40 μm in water[66]. It is understandable that light is less likely to make sharp turns along the wall with a large curvature. That's why it is relatively easier to get high Q-factors in large-sized microcavities. Unfortunately, as size goes up, the mode volume also scales up. Since the sensitivity is proportional to *Q*/*V*, there is a trade-off between

ultrahigh-Q-factor and sensitivity. We can aggregate the first three terms in equation 2.4, and define

$$\frac{1}{Q_{int}} = \frac{1}{Q_{abs}} + \frac{1}{Q_{scatt}} + \frac{1}{Q_{bend}}. \quad 2.5$$

In our microtoroid cavities, our measurable Q-factors are around 10^6 to 10^7 and sometimes may reach low 10^8. Both water absorption loss and contaminants-induced absorption and scattering loss are major contributors, preventing from achieving ultrahigh Q-factors.

Coupling methodologies

Far-field photons are not easily coupled into the microcavities. To understand this difficulty, we need to recall that the microcavities' ultrahigh Q-factor makes photons relatively difficult to leak out. We can also think about this difficulty in the manner of time-reversal symmetry, that is, bringing photons back to the microcavities directly from the free space is difficult. Free-space coupling has a relatively low efficiency, although it has been demonstrated in semiconductor microdisk cavities.[67] An efficient coupling requires a phase matching condition, where in-plane wavevectors across the medium-cavity interface remain equal. Above the critical angle of total internal reflection, out-of-plane wavevector ($k_\perp$) in the medium in equation 2.6 becomes imaginary

$$k_\perp = \sqrt{k_0^2 - k_\parallel^2}, \quad 2.6$$

where $k_0 < k_{\parallel}$. As a result, the electromagnetic field exponentially decays from the interface to the medium but will not propagate to the far-field due to energy conservation (**Figure 2.7A**). Now it should be more understandable that far-field photons cannot be coupled to the microcavities because of this near-field feature. Put it another way, any device or coupler that can introduce the near-field feature can efficiently couple photons to the microcavities, i.e., evanescent coupling.

A nano-scatterer[68, 69] near the evanescent wave region of microcavities can, upon far-field excitation, mediate the coupling between free-space photons and microcavities (**Figure 2.7B**). But this coupling might involve a lot of absorptive or scattering loss and thus has low efficiency. The first evanescent coupling methodology is prism-based coupling,[58] which is very stable and relatively easy to set up. However, the prism is bulky

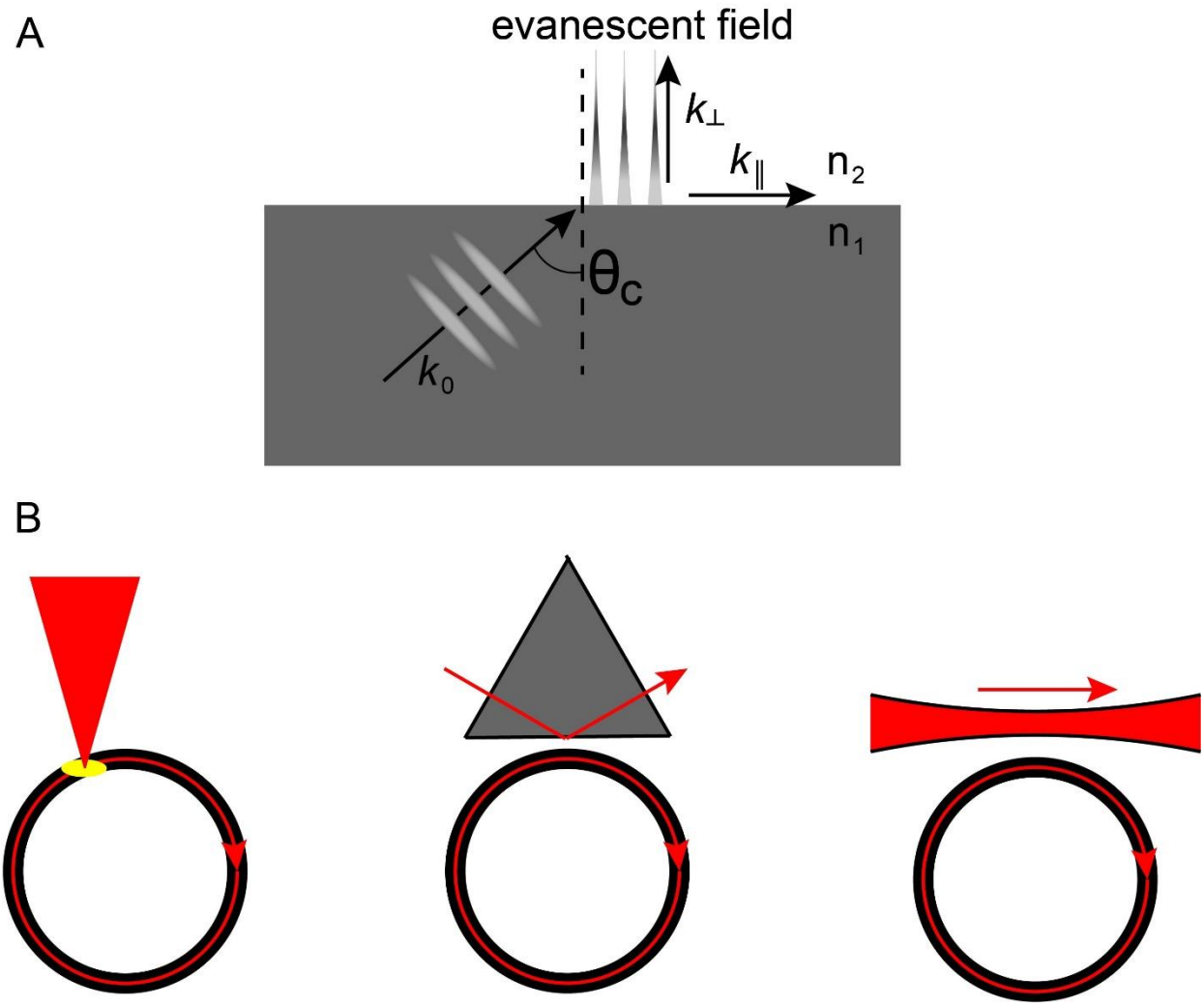

Figure 2.7 Evanescent coupling mechanism and coupling methods. (**A**) Evanescent decay of field in the medium 2 (n_2) when the incident angle in the medium 1 (n_1) is equal or greater than θ_c. (**B**) Evanescent coupling via nano-coupler, prism, and tapered fiber.

compared to the microcavities and is not readily suitable for integrated optics and on-chip devices. Typically, prism-based coupling methodology does not have high coupling efficiency and brings in parasitic loss to total *Q*-factor.

Tapered optical fiber has become the most ubiquitous coupling method since firstly demonstrated in 1997 by Knight et al.,[70] which has a coupling efficiency up to 99%.[71] Tapered optical fiber can be fabricated in multiple ways. Heating a single-mode optical fiber in hydrogen flame or CO_2 laser beam and adiabatically tapering down to sub-wavelength diameter is widely used for making tapered optical fiber. Chemically etching single-mode (SM) optical fiber in HF solution sometimes is adopted but is less reproducible for making reliable fiber tapers. Coupling can be easily manipulated by finely tuning the distance between the fiber taper and a microcavity. However, the taper is sensitive to vibrations and abrupt air flux, easily disrupting coupling of photons to the microcavity. Due to this free-drift feature, this coupling geometry is not suitable for integrated photonics and packaging. To overcome this drawback, on-chip waveguide is fabricated by lithographically patterning with microcavities at the same time. But coupling strength is not easily tunable due to this monolithic fabrication, which might be addressed by fabricating a waveguide on a separate chip and changing the distance between two chips with a nano-positioner. Another concern is input and output of the waveguide. Thus, two grating couplers are fabricated onto the ends of a waveguide for coupling free-space light into the waveguide and collecting transmission photons. This on-chip waveguide has been widely used in microring[72] or photonic crystal cavities.[73]

Coupling equations

Now we have some idea about how to couple photons into the microcavities. But how do we determine intrinsic Q-factor in experiments? How do we characterize intracavity field and intensity that underlies lasing and thermal effects in the microcavities? To answer these questions, I will start with the derivation of transmission coefficient and intracavity field as a function of intrinsic and external loss rates. A tapered optical fiber is used to couple input field (a_{in}) into a microcavity with an external coupling loss rate ($\gamma_{1,ext}$). a is the build-up intracavity field and a_o is the output field. According to the taper-cavity coupled mode theory,[74] time-dependent intracavity field (a) can be written as

$$i\frac{da}{dt} = \left(\omega_1 - \frac{i\gamma_{1,int}}{2} - \frac{i\gamma_{1,ext}}{2}\right)a - i\sqrt{\gamma_{1,ext}}a_{in}, \qquad 2.7$$

where ω_1 is the resonant frequency and $\gamma_{1,int}$ is the intrinsic loss rate. As $a = Ae^{-i\omega t}$, thus $\frac{da}{dt} = -i\omega Ae^{-i\omega t} + \frac{dA}{dt}e^{-i\omega t}$, which works similarly for a_{in}. Further substitution and rearrangement give rise to the following equation

$$\frac{dA}{dt} = \left(i\Delta_\omega - \frac{\gamma_{1,int}}{2} - \frac{\gamma_{1,ext}}{2}\right)A - \sqrt{\gamma_{1,ext}}A_{in}, \qquad 2.8$$

where $\Delta_\omega = \omega - \omega_1$ is the laser detuning. $\sqrt{\gamma_{1,ext}}$ can be understood as coupling coefficient between taper and cavity. Note that $|A|^2$ is normalized to the stored optical energy in the cavity, whereas $|A_{in}|^2$ is normalized to the input optical power through the taper. Solving for the steady-state solution in equation 2.8, we obtain

$$A = \frac{\sqrt{\gamma_{1,ext}}}{i\Delta_\omega - \frac{\gamma_{1,int}}{2} - \frac{\gamma_{1,ext}}{2}} A_{in}. \quad 2.9$$

The output field is the interference between ballistic input field and cavity leakage field,[75] which is expressed as

$$A_o = A_{in} + \sqrt{\gamma_{1,ext}} A. \quad 2.10$$

The transmission coefficient is given by $T = \frac{|A_o|^2}{|A_{in}|^2}$. Substituting equation 2.9 for *A* in equation 2.10, we obtain T as

$$T = 1 - \frac{\gamma_{1,int}\gamma_{1,ext}}{\Delta\omega^2 + \left(\frac{\gamma_{1,int} + \gamma_{1,ext}}{2}\right)^2}. \quad 2.11$$

We can tell from equation 2.11 that transmission coefficient has a Lorentzian lineshape and approach the minimum as laser detuning becomes zero (on resonance). In particular, T approaches zero when $\gamma_{1,int} = \gamma_{1,ext}$, i.e., the critical-coupling condition. Beyond this condition, the taper is either under- or over-coupled to the cavity. Relevant to the intracavity field, a characteristic factor called power build-up factor (*B*) is defined as below,

$$B = \frac{|A|^2/\tau_r}{|A_{in}|^2} = \frac{1}{\tau_r} \frac{\gamma_{1,ext}}{\Delta\omega^2 + \left(\frac{\gamma_{1,int} + \gamma_{1,ext}}{2}\right)^2}. \quad 2.12$$

Note that τ_r is the photon round-trip time ($\tau_r = \frac{2\pi nR}{c}$) which is different from $\tau_{lifetime}$. As shown in **Table 2.2**. $\tau_{lifetime}$ (8.2 ns) is longer than τ_r (0.756 ps) by a factor of 10846 for

a *Q*-factor of 10^7 at 1550 nm. In addition to Q-factor and mode volume defined in Chapter 1, another parameter for characterizing WGM cavities is free spectral range (*FSR*), which is defined as frequency spacing or wavelength spacing between two adjacent modes. Note that these adjacent modes are either neighboring azimuthal or axial modes ($FSR = \frac{\lambda^2}{2\pi nR}$). There are many modes within one *FSR* due to field distribution in radial or polar directions. The mode spectra in microtoroid and microbubble cavities are presented in Chapter 3 and 4 to revisit this topic.

Table 2.2 Parameters in a toroidal microcavity ($R = 25\ \mathrm{nm}$, $Q = 10^7$, $n = 1.4$, $\lambda = 1550\ \mathrm{nm}$).

parameters	$\tau_{lifetime}$	τ_r	*FSR*	*B*	Round trips
values	8.2 ns	0.756 ps	10.9 nm	2558	10846

Coupled plasmonic-photonic cavities

Although both plasmonic cavities and optical microcavities are widely used for a variety of applications (imaging, spectroscopy, sensing, optomechanics, etc.), there is still room for further increasing Purcell factor and therefore enhancing light-matter interactions even more strongly. Hence, alternative methods to confine light more tightly are in great need. One of such alternatives is the combination of plasmonic nanocavities and optical microcavities. When a plasmonic nanocavity is coupled to an optical microcavity, energy is partially stored in the one component while the rest is in the other component upon excitation, thus inheriting characters from individual component cavities. The desirable

features, i.e., ultrasmall volume from the plasmonic nanocavity and ultrahigh Q-factor from the optical microcavity, may be preserved in this way. Hybrids promise even larger or comparable F_p than their component cavities, like SiN nanobeam and Au dimers, respectively.[76]

The coupled cavity system was first experimentally studied in 1999 in a cylindrical microcavity doped with fractal silver nano-aggregates that host dye molecules, showing a low lasing threshold and strongly enhanced Raman scattering.[77] Since then, coupled plasmonic-photonic systems by depositing microcavities' surface with plasmonic nanoparticles have been widely demonstrated in (bio)sensing[78] and label-free detection of a few molecules,[79] single proteins (**Figure 2.8A**),[80] and single metal ions.[81] Furthermore, these coupled systems find numerous applications in optical trapping of nanoparticles[82, 83] or biomolecules[84] due to strong localized field enhancement as opposed to optical tweezers that provide intense light field via a laser (**Figure 2.8B**). More recently, the coupled systems were explored both experimentally and theoretically for the purpose of emission control[85] and study of strong light-matter interactions[86] or strong coupling by engineering very high local DOS (**Figure 2.8C**). The intricacy of the plasmonic-photonic coupled systems is characterized by a phenomenological spectral signature called Fano antiresonance which is indicative of the mutual interaction between distinct plasmonic and photonic modes (**Figure 2.9A** and **Figure 2.9B**). Fano lineshapes (**Figure 2.9C**) are ubiquitously observed in several weakly coupled systems and generally

understood as the interference of broadband (continuum) resonance and narrowband (discrete) resonance under the vein of coupled mode theory.

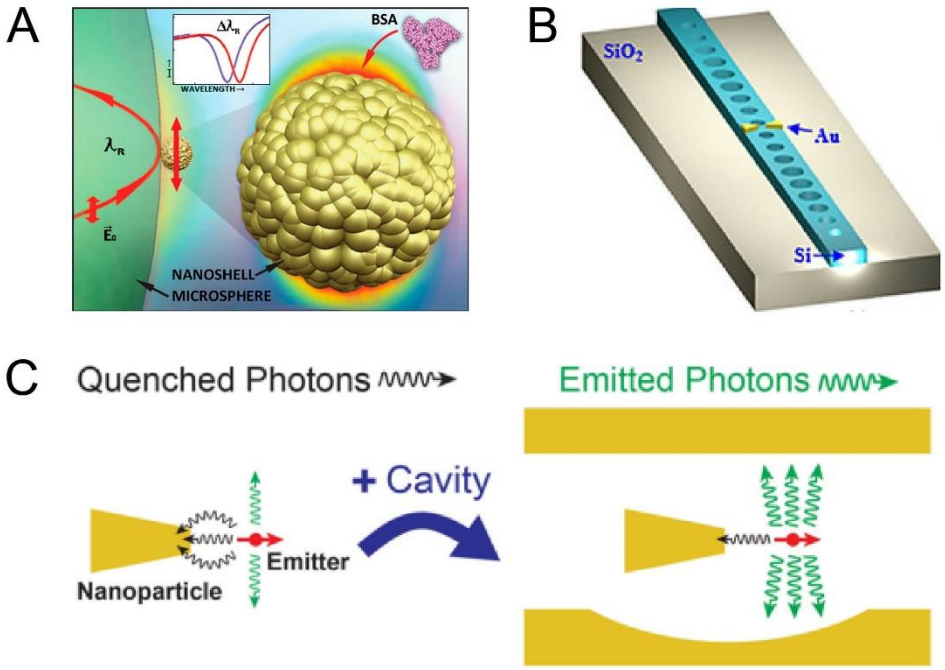

Figure 2.8 Applications of plasmonic-photonic coupled systems for sensing (**A**), optical trapping (**B**), and emission control (**C**). Reprinted with permission from Ref[80, 82, 85].

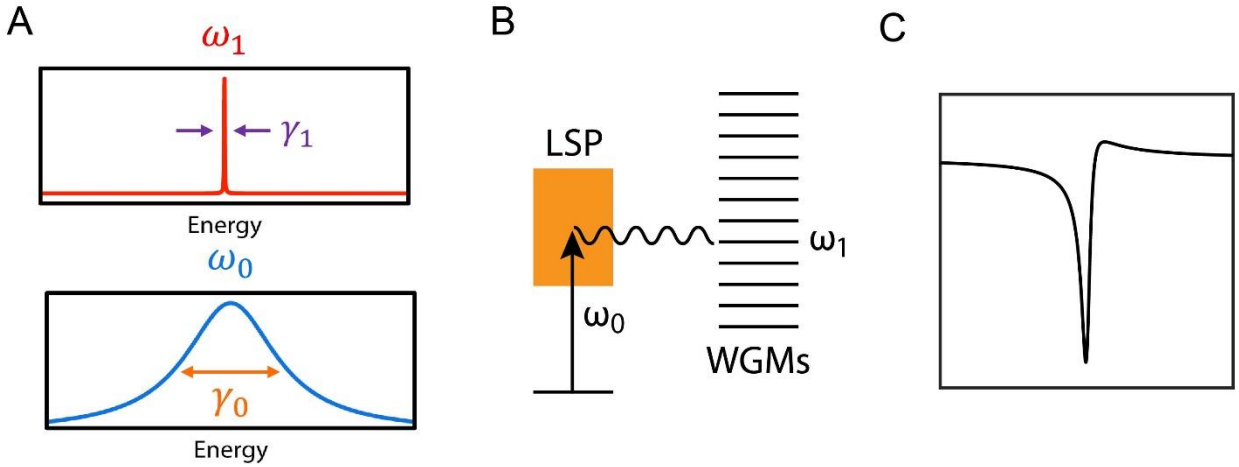

Figure 2.9 Fano antiresonance in coupled plasmonic-photonic systems. (**A**) Spectral lineshapes of a LSP and a WGM. (**B**) Mode interference between LSP continuum and discrete WGMs. (**C**) An example of Fano spectral signature.

Since this thesis mainly focuses on understanding of plasmonic-photonic interactions, I first show most recent thrusts in revealing the intricacy of the coupled systems by our group,[87] Koenderink's group,[88] and Cunningham's group,[89] and then present the recent works from Koenderink's group in local DOS engineering using a coupled microcavity system (**Figure 2.10**).[90] Our group for the first time demonstrated this plasmonic-photonic interaction using a single-particle absorption spectroscopy, featuring very narrow Fano antiresonances (a few tens of μeV).[87] Almost at the same time, Koenderink's group theoretically predicted that a very high Purcell enhancement can be obtained in an antenna-cavity coupled system, which may provide a new way for engineering local DOS around an emitter.[88] Similarly, another theoretical work[85] in which an external Fabry-Perot cavity is used to control radiative and non-radiative properties of an emitter coupled to an antenna shows that non-radiative pathways are inhibited when antenna-cavity is far detuned. Although the two works operate in the weak-coupling regime (or Purcell regime), the coupled system enabled by Fabry-Perot cavity might assist entering the strong-coupling regime. There are several experimental works that evidence this theoretical prediction. In a photonic crystal microcavity platform, a nano-antenna's local field intensity can be amplified even more when coupled to the modest-Q microcavity resonance than in the Fabry-Perot cavity by one order of magnitude.[89] In addition to amplified local field intensity on the nano-antenna, the absorption is amplified, and its amplification is spectrally tunable.[91]

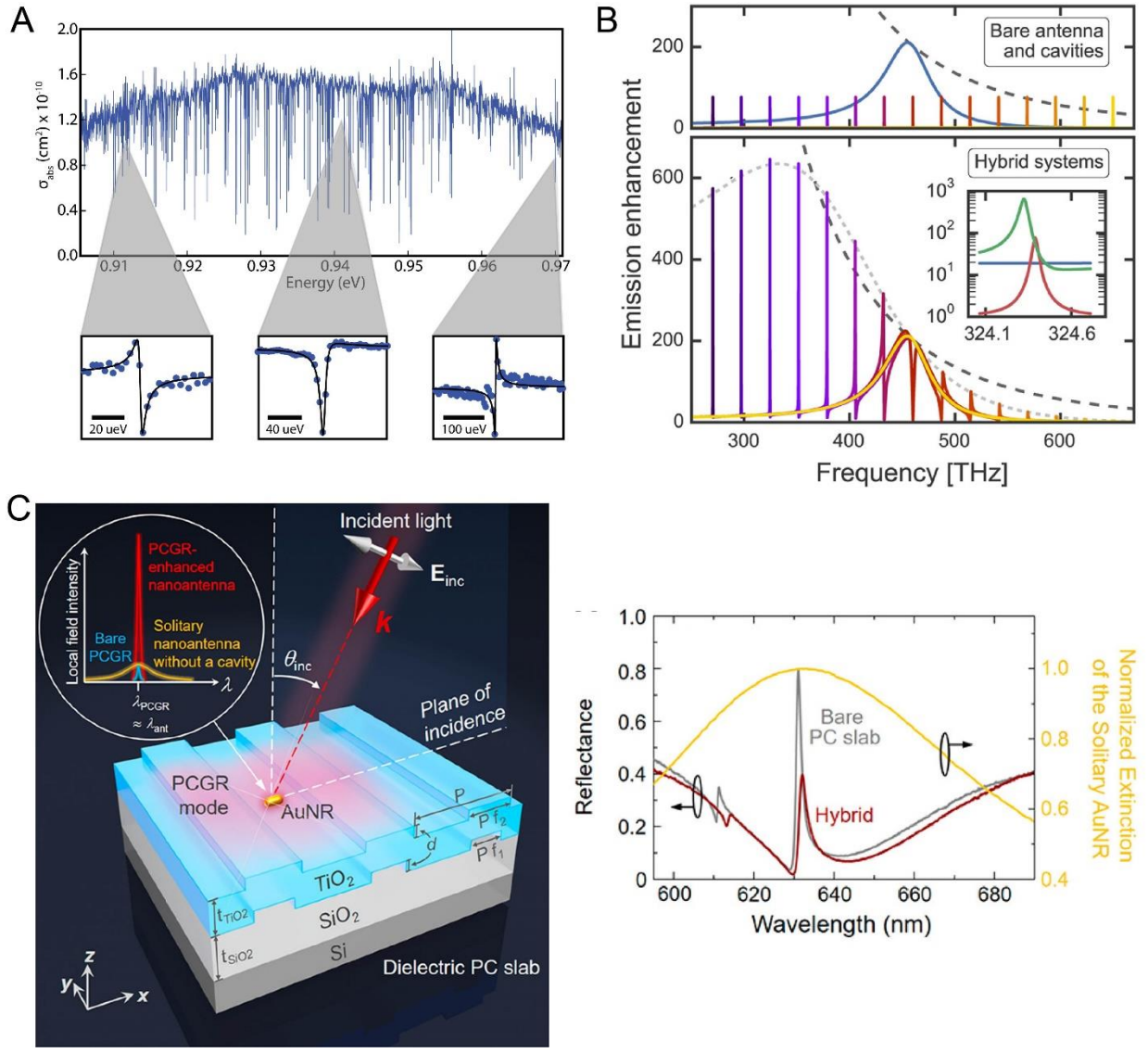

Figure 2.10 Plasmonic-photonic couplings and spectral signatures in different coupled systems. (**A**) Distinct Fano lineshapes are seen at different spectral locations of a broad LSP absorption spectrum. (**B**) Emission enhancement or local DOS is computed for coupled, bare antenna, and bare cavity. (**C**) Multiple AuNRs are coupled to a dielectric photonic crystal slab, resulting in a Fano signature. Reprinted with permission from Ref[87-89].

The plasmonic-photonic hybridization can be well controlled by changing the antenna's aspect ratio.[92] Instead of examining a series of different antenna-cavity samples, single AuNRs are melted on the microcavity via heating the coupled systems

and then assessed by the same microcavity using single-particle absorption spectroscopy. As a result, Fano lineshapes are being sculpted as LSP resonance is blue shifted (**Figure 2.11A**). The beauty of this experiment is to provide the evidence for the control of plasmonic-photonic interactions at the single-particle level. Unfortunately, this heating method may limit its application in emissions control because emitters likely degrade at high temperatures. Computed F_p reaches the maximum when the detuning is zero (**Figure 2.11A**). However, as shown in Koenderink's coupled system,[88] the maximum Purcell factor is obtained only when the antenna resonance is far detuned from the cavity resonance. This distinct prediction might be explained in terms of different theoretical methods in treating quasi-normal modes.

To verify the emission control via a coupled cavity system, quantum dots (QDs) are precisely positioned at the tips of the aluminum nano-antennas which are fabricated on the edge of silicon-nitride microdisk (**Figure 2.11B**).[90] The emission spectrum of QDs is modified in proportion to local DOS governed by the coupled system, shown as distinctive Fano lineshapes on top of an emission envelope of QDs. When the antenna resonance is detuned relative to the cavity resonances, Fano lineshapes on the emission spectrum transform from near Lorentzian peak to a total destructive dip. This behavior is further verified by studying the emission control in single quantum dots. A boost of over

14X local DOS enhancement over bare antenna alone is seen when cavity resonance is red-detuned from antenna resonance.

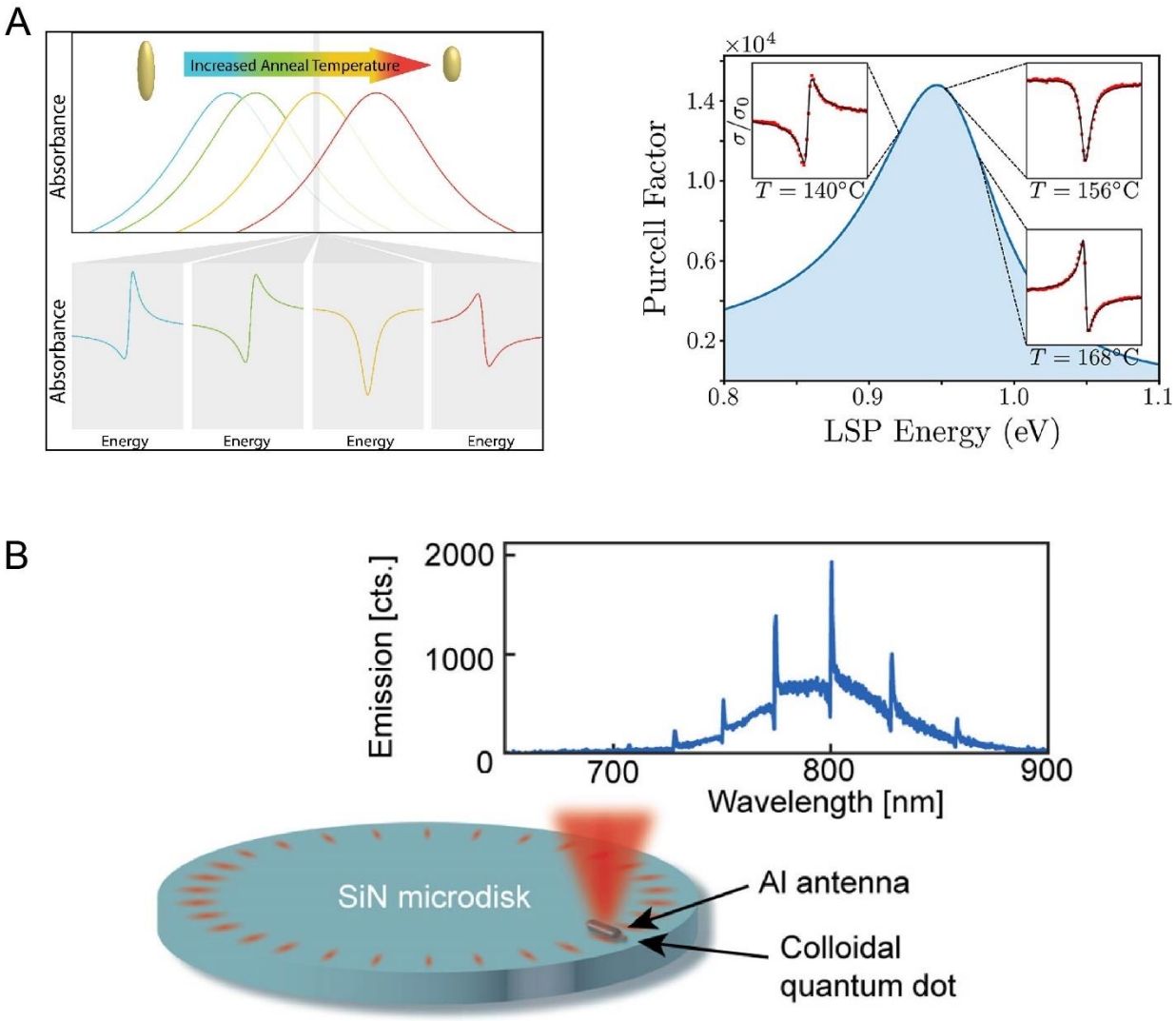

Figure 2.11 Control of plasmonic-photonic hybridization by tuning LSP resonance. (**A**) LSP resonance is blue shifted when the AuNR is melted. When LSP-WGM detuning is zero, a maximum F_p is obtained, as shown on the right. (**B**) QD emission spectrum is modified as a function of local DOS engineered by hybridization of WGMs in a SiN microdisk and LSP in an Al antenna. Reprinted with permission from Ref[92, 90].

Spectroscopic investigation of coupled plasmonic-photonic systems

There are a variety of spectroscopic methods to interrogate plasmonic-photonic coupled systems. When a plasmonic nanoparticle is coupled to a photonic microcavity, the coupling is imprinted into several pathways and subsequent observables that can be used to characterize the interactions. When a localized surface plasmon is excited, the plasmonic nanoparticles absorb and scatter photons efficiently due to large cross sections of ~10^{-10} cm^2. In a coupled plasmonic-photonic system, both absorption and scattering spectra are dressed with characteristic Fano antiresonances. So far, our group have developed a photothermal absorption spectroscopy in which a microtoroid cavity acts as both an absorption spectrometer that reads out absorption and a microcavity that is coupled to single plasmonic nanoparticles. This method will be further discussed in detail in Chapter 3 and 4. Absorption can be also obtained by measuring both transmission and reflection through free-space illumination of the coupled system.[91] But this method requires simultaneous measurement of two observables and careful comparison of two measurements to accurately extract out absorption.

In addition to free-space excitation, a tapered optical fiber that evanescently couples photons to a microcavity can provide the coupling information in both transmission and reflection channels. An in-line optical circulator enables both transmission and reflection photons to be detected. In addition to these two readouts, scattered photons can be collected by an objective at the same time.[93] All these three observables provide information for resonance shifts and broadening and verify that

cavity modes are perturbed by a nano-antenna. Note that the scattered photons can be detected in a darkfield manner when the coupled system is evanescently excited by a tapered optical fiber and essentially background-free scattering is observed.[93] The scattering spectrum features two distinct Fano lineshapes at two different wave vectors, respectively. Another excitation geometry is to deliver a hollow excitation beam through a darkfield objective and then collect scattered photons through the same objective. Unfortunately, the detection might suffer from background scattering due to microcavity's curvature.[94] Flat patterned microcavities, such as ring microcavity and photonic crystal microcavity, may be used to overcome this limitation.

References

1. Pines, D. and Bohm, D., "A Collective Description of Electron Interactions: II. Collective vs Individual Particle Aspects of the Interactions." *Phys. Rev.* **1952**, *85*(2): 338-353.

2. Ritchie, R. H., "Plasma Losses by Fast Electrons in Thin Films." *Phys. Rev.* **1957**, *106*(5): 874-881.

3. Barnes, W. L., Dereux, A., et al., "Surface plasmon subwavelength optics." *Nature* **2003**, *424*(6950): 824-830.

4. Stockman, M. I., Kneipp, K., et al., "Roadmap on plasmonics." *Journal of Optics* **2018**, *20*(4): 043001.

5. Jiang, N., Zhuo, X., et al., "Active Plasmonics: Principles, Structures, and Applications." *Chem. Rev.* **2018**, *118*(6): 3054-3099.

6. Willets, K. A. and Duyne, R. P. V., "Localized Surface Plasmon Resonance Spectroscopy and Sensing." *Annu. Rev. Phys. Chem.* **2007**, *58*(1): 267-297.

7. Zhou, X.-L., Yang, Y., et al., "Surface Plasmon Resonance Microscopy: From Single-Molecule Sensing to Single-Cell Imaging." *Angew. Chem. Int. Ed.* **2020**, *59*(5): 1776-1785.

8. Zhang, X., Chen, Y. L., et al., "Plasmonic photocatalysis." *Rep. Prog. Phys.* **2013**, *76*(4): 046401.

9. Rycenga, M., Cobley, C. M., et al., "Controlling the Synthesis and Assembly of Silver Nanostructures for Plasmonic Applications." *Chem. Rev.* **2011**, *111*(6): 3669-3712.

10. Esteban, R., Vogelgesang, R., et al., "Direct Near-Field Optical Imaging of Higher Order Plasmonic Resonances." *Nano Lett.* **2008**, *8*(10): 3155-3159.

11. Swearer, D. F., Zhao, H., et al., "Heterometallic antenna−reactor complexes for photocatalysis." *Proceedings of the National Academy of Sciences* **2016**, *113*(32): 8916-8920.

12. Bitton, O., Gupta, S. N., et al., "Vacuum Rabi splitting of a dark plasmonic cavity mode revealed by fast electrons." *Nat. Commun.* **2020**, *11*(1): 487.

13. Koenderink, A. F., "On the use of Purcell factors for plasmon antennas." *Opt. Lett.* **2010**, *35*(-24): 4210.

14. Chang, S.-W., Ni, C.-Y. A., et al., "Theory for bowtie plasmonic nanolasers." *Opt. Express* **2008**, *16*(14): 10580-10595.

15. Fromm, D. P., Sundaramurthy, A., et al., "Gap-Dependent Optical Coupling of Single “Bowtie” Nanoantennas Resonant in the Visible." *Nano Lett.* **2004**, *4*(5): 957-961.

16. Sundaramurthy, A., Crozier, K. B., et al., "Field enhancement and gap-dependent resonance in a system of two opposing tip-to-tip Au nanotriangles." *Phys. Rev. B* **2005**, *72*(16): 165409.

17. Bitton, O., Gupta, S. N., et al., "Quantum dot plasmonics: from weak to strong coupling." *Nanophotonics* **2019**, *8*(4): 559.

18. Santhosh, K., Bitton, O., et al., "Vacuum Rabi splitting in a plasmonic cavity at the single quantum emitter limit." *Nat. Commun.* **2016**, *7*(1): 11823.

19. Baumberg, J. J., Aizpurua, J., et al., "Extreme nanophotonics from ultrathin metallic gaps." *Nat. Mater.* **2019**, *18*(7): 668-678.

20. Chikkaraddy, R., Zheng, X., et al., "How Ultranarrow Gap Symmetries Control Plasmonic Nanocavity Modes: From Cubes to Spheres in the Nanoparticle-on-Mirror." *ACS Photonics* **2017**, *4*(3): 469-475.

21. Akselrod, G. M., Argyropoulos, C., et al., "Probing the mechanisms of large Purcell enhancement in plasmonic nanoantennas." *Nat. Photonics* **2014**, *8*(11): 835-840.

22. Zhang, Y., Luo, Y., et al., "Visualizing coherent intermolecular dipole–dipole coupling in real space." *Nature* **2016**, *531*(7596): 623-627.

23. Hoang, T. B., Akselrod, G. M., et al., "Ultrafast spontaneous emission source using plasmonic nanoantennas." *Nat. Commun.* **2015**, *6*(1): 7788.

24. Hoang, T. B., Akselrod, G. M., et al., "Ultrafast Room-Temperature Single Photon Emission from Quantum Dots Coupled to Plasmonic Nanocavities." *Nano Lett.* **2016**, *16*(1): 270-275.

25. Chikkaraddy, R., de Nijs, B., et al., "Single-molecule strong coupling at room temperature in plasmonic nanocavities." *Nature* **2016**, *535*: 127.

26. Akselrod, G. M., Ming, T., et al., "Leveraging Nanocavity Harmonics for Control of Optical Processes in 2D Semiconductors." *Nano Lett.* **2015**, *15*(5): 3578-3584.

27. Huang, J., Akselrod, G. M., et al., "Tailored Emission Spectrum of 2D Semiconductors Using Plasmonic Nanocavities." *ACS Photonics* **2018**, *5*(2): 552-558.

28. Benz, F., Schmidt, M. K., et al., "Single-molecule optomechanics in “picocavities”." *Science* **2016**, *354*(6313): 726-729.

29. Zhang, R., Zhang, Y., et al., "Chemical mapping of a single molecule by plasmon-enhanced Raman scattering." *Nature* **2013**, *498*(7452): 82-86.

30. Yang, Z.-J., Antosiewicz, T. J., et al., "Role of material loss and mode volume of plasmonic nanocavities for strong plasmon-exciton interactions." *Opt. Express* **2016**, *24*(18): 20373-20381.

31. Kongsuwan, N., Demetriadou, A., et al., "Suppressed Quenching and Strong-Coupling of Purcell-Enhanced Single-Molecule Emission in Plasmonic Nanocavities." *ACS Photonics* **2018**, *5*(1): 186-191.

32. Yang, B., Chen, G., et al., "Sub-nanometre resolution in single-molecule photoluminescence imaging." *Nat. Photonics* **2020**.

33. Koenderink, A. F., "Single-Photon Nanoantennas." *ACS Photonics* **2017**, *4*(4): 710-722.

34. Yampolsky, S., Fishman, D. A., et al., "Seeing a single molecule vibrate through time-resolved coherent anti-Stokes Raman scattering." *Nat. Photonics* **2014**, *8*(8): 650-656.

35. Langer, J., Jimenez de Aberasturi, D., et al., "Present and Future of Surface-Enhanced Raman Scattering." *ACS Nano* **2020**, *14*(1): 28-117.

36. Lidzey, D. G., Bradley, D. D. C., et al., "Strong exciton–photon coupling in an organic semiconductor microcavity." *Nature* **1998**, *395*(6697): 53-55.

37. Deng, H., Haug, H., et al., "Exciton-polariton Bose-Einstein condensation." *Rev. Mod. Phys.* **2010**, *82*(2): 1489-1537.

38. Benedikter, J., Moosmayer, T., et al., "Transverse-mode coupling effects in scanning cavity microscopy." *New J. Phys.* **2019**, *21*(10): 103029.

39. Mader, M., Reichel, J., et al., "A scanning cavity microscope." *Nat. Commun.* **2015**, *6*: 7249.

40. Hümmer, T., Noe, J., et al., "Cavity-enhanced Raman microscopy of individual carbon nanotubes." *Nat. Commun.* **2016**, *7*: 12155.

41. Gorodetsky, M. L., Savchenkov, A. A., et al., "Ultimate Q of optical microsphere resonators." *Opt. Lett.* **1996**, *21*(7): 453-455.

42. Senthil Murugan, G., Petrovich, M. N., et al., "Hollow-bottle optical microresonators." *Opt. Express* **2011**, *19*(21): 20773-20784.

43. Sumetsky, M., Dulashko, Y., et al., "Optical microbubble resonator." *Opt. Lett.* **2010**, *35*(7): 898-900.

44. Heylman, K. D., Knapper, K. A., et al., "Optical Microresonators for Sensing and Transduction: A Materials Perspective." *Adv. Mater.* **2017**, *29*(30): 1700037.

45. Aoki, T., Dayan, B., et al., "Observation of strong coupling between one atom and a monolithic microresonator." *Nature* **2006**, *443*: 671.

46. Spillane, S. M., Kippenberg, T. J., et al., "Ultrahigh-Q toroidal microresonators for cavity quantum electrodynamics." *Phys. Rev. A* **2005**, *71*(1): 013817.

47. Li, B.-B., Xiao, Y.-F., et al., "Low-threshold Raman laser from an on-chip, high-Q, polymer-coated microcavity." *Opt. Lett.* **2013**, *38*(11): 1802-1804.

48. Özdemir, Ş. K., Zhu, J., et al., "Highly sensitive detection of nanoparticles with a self-referenced and self-heterodyned whispering-gallery Raman microlaser." *Proceedings of the National Academy of Sciences* **2014**, *111*(37): E3836-E3844.

49. Kippenberg, T. J., Gaeta, A. L., et al., "Dissipative Kerr solitons in optical microresonators." *Science* **2018**, *361*(6402).

50. Peng, B., Özdemir, Ş. K., et al., "Parity–time-symmetric whispering-gallery microcavities." *Nat Phys* **2014**, *10*: 394.

51. Zhao, H. and Feng, L., "Parity–time symmetric photonics." *Nat. Sci. Rev.* **2018**, *5*(2): 183-199.

52. Özdemir, Ş. K., Rotter, S., et al., "Parity–time symmetry and exceptional points in photonics." *Nat. Mater.* **2019**.

53. Gondarenko, A., Levy, J. S., et al., "High confinement micron-scale silicon nitride high Q ring resonator." *Opt. Express* **2009**, *17*(14): 11366-11370.

54. Akahane, Y., Asano, T., et al., "High-Q photonic nanocavity in a two-dimensional photonic crystal." *Nature* **2003**, *425*(6961): 944-947.

55. Quan, Q., Deotare, P. B., et al., "Photonic crystal nanobeam cavity strongly coupled to the feeding waveguide." *Appl. Phys. Lett.* **2010**, *96*(20): 203102.

56. Ohta, R., Ota, Y., et al., "Strong coupling between a photonic crystal nanobeam cavity and a single quantum dot." *Appl. Phys. Lett.* **2011**, *98*(17): 173104.

57. Deotare, P. B., McCutcheon, M. W., et al., "High quality factor photonic crystal nanobeam cavities." *Appl. Phys. Lett.* **2009**, *94*(12): 121106.

58. Braginsky, V. B., Gorodetsky, M. L., et al., "Quality-factor and nonlinear properties of optical whispering-gallery modes." *Phys. Lett. A* **1989**, *137*(7): 393-397.

59. Yang, L. (**2005**). Fabrication and Characterization of Microlasers by the Sol-Gel Method, California Institute of Technology. *Ph.D.*

60. Armani, D. K., Kippenberg, T. J., et al., "Ultra-high-Q toroid microcavity on a chip." *Nature* **2003**, *421*(6926): 925-928.

61. Knapper, K. A., Heylman, K. D., et al., "Chip-Scale Fabrication of High-Q All-Glass Toroidal Microresonators for Single-Particle Label-Free Imaging." *Adv. Mater.* **2016**, *28*(15): 2945-2950.

62. Li, G., Liu, P., et al., "High-Q silica microdisk optical resonators with large wedge angles on a silicon chip." *Photon. Res.* **2015**, *3*(5): 279-282.

63. Pinnow, D. A., Rich, T. C., et al., "Fundamental optical attenuation limits in the liquid and glassy state with application to fiber optical waveguide materials." *Appl. Phys. Lett.* **1973**, *22*(10): 527-529.

64. Rokhsari, H., Spillane, S. M., et al., "Loss characterization in microcavities using the thermal bistability effect." *Appl. Phys. Lett.* **2004**, *85*(15): 3029-3031.

65. Kippenberg, T. J. (**2004**). Nonlinear Optics in Ultra-High-Q Whispering-Gallery Optical Microcavities, California Institute of Technology. *Ph.D.*

66. Armani, A. M., Armani, D. K., et al., "Ultra-high-Q microcavity operation in H2O and D2O." *Appl. Phys. Lett.* **2005**, *87*(15): 151118.

67. Liew, S. F., Ge, L., et al., "Pump-controlled modal interactions in microdisk lasers." *Phys. Rev. A* **2015**, *91*(4): 043828.

68. Zhu, J., Özdemir, Ş. K., et al., "Interfacing whispering-gallery microresonators and free space light with cavity enhanced Rayleigh scattering." *Sci. Rep.* **2014**, *4*: 6396.

69. Shu, F., Jiang, X., et al., "A scatterer-assisted whispering-gallery-mode microprobe." *Nanophotonics* **2018**, *7*(8): 1455-1460.

70. Knight, J. C., Cheung, G., et al., "Phase-matched excitation of whispering-gallery-mode resonances by a fiber taper." *Opt. Lett.* **1997**, *22*(15): 1129-1131.

71. Cai, M., Painter, O., et al., "Observation of Critical Coupling in a Fiber Taper to a Silica-Microsphere Whispering-Gallery Mode System." *Phys. Rev. Lett.* **2000**, *85*(1): 74-77.

72. Shi, W., Wang, X., et al., "Grating-coupled silicon microring resonators." *Appl. Phys. Lett.* **2012**, *100*(12): 121118.

73. Saber, I., Boddeda, R., et al., "Photonic crystal nanobeam cavities with optical resonances around 800 nm." *J. Opt. Soc. Am. B* **2019**, *36*(7): 1823-1828.

74. Haus, H. A., "Waves and Fields in Optoelectronics." **1983**, Prentice Hall.

75. Peng, B., Özdemir, Ş. K., et al., "Loss-induced suppression and revival of lasing." *Science* **2014**, *346*(6207): 328-332.

76. Palstra Isabelle, M., Doeleman Hugo, M., et al. (**2019**). Hybrid cavity-antenna systems for quantum optics outside the cryostat? Nanophotonics. *8***:** 1513.

77. Kim, W., Safonov, V. P., et al., "Fractals in Microcavities: Giant Coupled, Multiplicative Enhancement of Optical Responses." *Phys. Rev. Lett.* **1999**, *82*(24): 4811-4814.

78. Bozzola, A., Perotto, S., et al., "Hybrid plasmonic–photonic whispering gallery mode resonators for sensing: a critical review." *Analyst* **2017**, *142*(6): 883-898.

79. De Angelis, F., Patrini, M., et al., "A Hybrid Plasmonic−Photonic Nanodevice for Label-Free Detection of a Few Molecules." *Nano Lett.* **2008**, *8*(8): 2321-2327.

80. Dantham, V. R., Holler, S., et al., "Label-Free Detection of Single Protein Using a Nanoplasmonic-Photonic Hybrid Microcavity." *Nano Lett.* **2013**, *13*(7): 3347-3351.

81. Baaske, M. D. and Vollmer, F., "Optical observation of single atomic ions interacting with plasmonic nanorods in aqueous solution." *Nat. Photonics* **2016**, *10*(11): 733-739.

82. Conteduca, D., Reardon, C., et al., "Ultra-high Q/V hybrid cavity for strong light-matter interaction." *APL Photonics* **2017**, *2*(8): 086101.

83. Lin, P.-T., Chu, H.-Y., et al., "Trapping particles using waveguide-coupled gold bowtie plasmonic tweezers." *Lab on a Chip* **2014**, *14*(24): 4647-4652.

84. Conteduca, D., Dell'Olio, F., et al., "Rigorous design of an ultra-high Q/V photonic/plasmonic cavity to be used in biosensing applications." *Optics & Laser Technology* **2016**, *77*: 151-161.

85. Gurlek, B., Sandoghdar, V., et al., "Manipulation of Quenching in Nanoantenna–Emitter Systems Enabled by External Detuned Cavities: A Path to Enhance Strong-Coupling." *ACS Photonics* **2018**, *5*(2): 456-461.

86. Peng, P., Liu, Y.-C., et al., "Enhancing Coherent Light-Matter Interactions through Microcavity-Engineered Plasmonic Resonances." *Phys. Rev. Lett.* **2017**, *119*(23): 233901.

87. Heylman, K. D., Thakkar, N., et al., "Optical microresonators as single-particle absorption spectrometers." *Nat. Photonics* **2016**, *10*: 788-795.

88. Doeleman, H. M., Verhagen, E., et al., "Antenna–Cavity Hybrids: Matching Polar Opposites for Purcell Enhancements at Any Linewidth." *ACS Photonics* **2016**, *3*(10): 1943-1951.

89. Liu, J.-N., Huang, Q., et al., "Nanoantenna–Microcavity Hybrids with Highly Cooperative Plasmonic–Photonic Coupling." *Nano Lett.* **2017**, *17*(12): 7569-7577.

90. Doeleman, H. M., Dieleman, C. D., et al., "Observation of Cooperative Purcell Enhancements in Antenna-Cavity Hybrids." *ACS Nano* **2020**.

91. Huang, Q. and Cunningham, B. T., "Microcavity-Mediated Spectrally Tunable Amplification of Absorption in Plasmonic Nanoantennas." *Nano Lett.* **2019**, *19*(8): 5297-5303.

92. Thakkar, N., Rea, M. T., et al., "Sculpting Fano Resonances To Control Photonic–Plasmonic Hybridization." *Nano Lett.* **2017**, *17*(11): 6927-6934.

93. Cognée, K. G., Doeleman, H. M., et al., "Cooperative interactions between nano-antennas in a high-Q cavity for unidirectional light sources." *Light Sci. Appl.* **2019**, *8*(1): 115.

94. Knapper, K. A., Pan, F., et al., "Single-particle photothermal imaging via inverted excitation through high-Q all-glass toroidal microresonators." *Opt. Express* **2018**, *26*(19): 25020-25030.

Chapter 3 Elucidating energy pathways through simultaneous measurement of absorption and transmission in a coupled plasmonic-photonic cavity[l]

Main text: Abstract

Control of light-matter interactions is central to numerous advances in quantum communication, information, and sensing. The relative ease in which interactions can be tailored in coupled plasmonic-photonic systems makes them ideal candidates for investigation. To exert control over the interaction between photons and plasmons, it is essential to identify the underlying energy pathways which influence the system's dynamics and determine the critical system parameters, such as the coupling strength and dissipation rates. However, in coupled systems which dissipate energy through multiple competing pathways, simultaneously resolving all parameters from a single experiment is challenging as typical observables such as absorption and scattering each probe only a particular path. In this work, we simultaneously measure both photothermal absorption and two-sided optical transmission in a coupled plasmonic-photonic resonator consisting of plasmonic gold nanorods deposited on a toroidal whispering-gallery-mode

[l] This chapter is adapted from the published manuscript as Pan, F.*, Smith, K. C.*, et al., "Elucidating Energy Pathways through Simultaneous Measurement of Absorption and Transmission in a Coupled Plasmonic–Photonic Cavity." *Nano Lett.* **2020**, *20*(1): 50-58. * Equal co-first authorship.

optical microresonator. We then present an analytical model which predicts and explains the distinct line shapes observed and quantifies the contribution of each system parameter. By combining this model with experiment, we extract all system parameters with a dynamic range spanning nine orders of magnitude. Our combined approach provides a full description of plasmonic-photonic energy dynamics in a weakly coupled optical system, a necessary step for future applications that rely on tunability of dissipation and coupling.

Main text: Introduction

In 1946 Purcell theoretically demonstrated that the spontaneous emission rate of an emitter can be enhanced by its dielectric environment,[1] prompting the birth of what is now known as cavity quantum electrodynamics (cQED). Following this discovery and its subsequent experimental confirmation,[2] cQED has remained an active area of both theoretical and experimental research and has found application in a variety of fields such as quantum communication and information,[3-10] sensing,[11-14] and cavity-controlled chemistry.[15-22] The development of cQED is intertwined with developments in nanoscience and nanofabrication. In particular, recent years have seen a boom in cQED experiments due to the emergence of sophisticated techniques for fabrication of high-quality-factor, chip-scale optical microcavities[23] and deterministic positioning of “artificial atoms” such as quantum dots and plasmonic nanoparticles on optical microcavities.[24-28]

Whispering-gallery-mode (WGM) microcavities are especially attractive due to the attainable ultrahigh quality factor (up to 10^8)[23, 29] of their optical modes which can allow

for Purcell factors as large as 190.[30] In recent work, it has been predicted that this factor may be improved even further by coupling the cavity modes to the localized surface plasmon (LSP) of a metal nanoparticle, effectively creating a hybrid plasmonic-photonic resonator which inherits the ultrasmall mode volume of the LSP while retaining the large quality factor of the WGMs.[31-37] In order to both understand and leverage the light-matter interactions in such a system, it is imperative to accurately determine the multiple intrinsic damping rates, the LSP-WGM coupling strength, and additional extrinsic dissipation rates introduced through the measurement. However, these quantities can span many orders of magnitude, particularly in weakly coupled systems, making it difficult for a single experiment to capture all of the information.

Many methods have been used to probe light-matter interactions in cavity-matter systems, including far-field detection of emitted or reflected photons,[25, 38-45] measurement of transmitted/reflected photons in a waveguide coupled to the system,[24, 46-49] and single-particle absorption measurements.[31, 50] Specifically, photoluminescence or scattering measurements collect radiated energy in the far field, transmission/reflection measurements using a waveguide detects energy transferred from the WGM to the tapered fiber, and absorption measurements probe nonradiative dissipation. While these techniques are individually capable of revealing spectral signatures of the underlying light-matter interaction, each serves as a readout for only a particular dissipative pathway and cannot simultaneously resolve all parameters that govern energy flow within the system. For example, nonradiative and radiative damping rates can be inferred from absorption and scattering spectra, respectively, while a fiber-based one-sided transmission

experiment inherently depends upon the rate of energy exchange between an optically pumped waveguide and the cavity to which it is coupled. Crucially, the linewidth of any spectral feature contains information about the total dissipation rate of the system but does not distinguish between the various dissipative pathways regardless of the observable. Thus, simultaneous measurement of multiple spectroscopic observables is needed for one to understand how energy is both distributed and dissipated via multiple pathways in a coupled cavity-matter system.

In this work we demonstrate the ability to simultaneously measure both photothermal absorption and optical transmission in a coupled plasmonic-photonic cavity consisting of plasmonic gold nanorods (AuNRs) deposited on a silica toroidal WGM microresonator.[23] Specifically, the transmission is measured in a two-sided[51] manner, where energy is input through a free-space pump laser and output through a fiber to which the LSP-WGM system is coupled. In contrast to previous studies on single AuNRs or quantum dots which have relied on measurements of scattering or photoluminescence, we measure photothermal absorption and two-sided transmission using a single photonic waveguide, where an individual AuNR is optically pumped by a frequency-tunable free-space laser. AuNRs of a high aspect ratio (10:1) are used so that the longitudinal dipolar LSP is efficiently excited by our tunable, narrow-linewidth near-infrared free-space pump laser. Taken together, absorption and transmission encode sufficient information about the individual damping rates and mutual coupling strength of the LSP and WGM such that all relevant system parameters (see **Figure 3.1**) may be determined. **Figure 3.1** illustrates

these system parameters as well as the complete set of observables that both determine and are defined by their specific values.

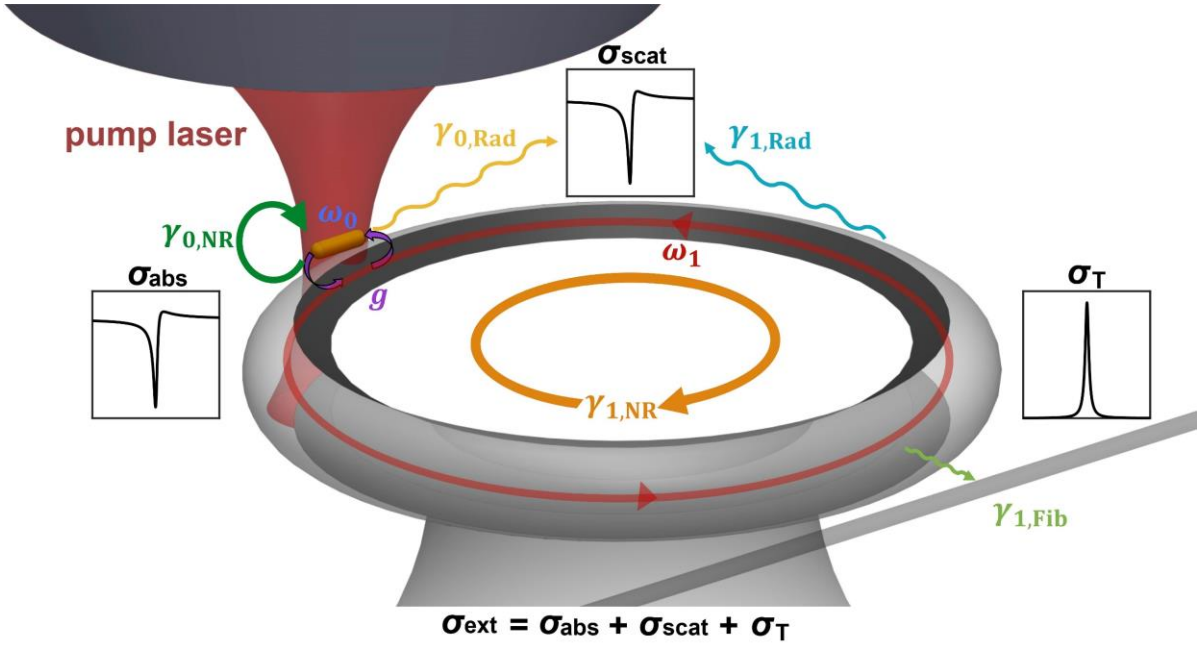

Figure 3.1 Schematic of dissipative coupled AuNR-microresonator system with all parameters (ω_0, $\gamma_{0,NR}$, $\gamma_{0,Rad}$, g, ω_1, $\gamma_{1,NR}$, $\gamma_{1,Rad}$, $\gamma_{1,Fib}$) as well as experimental observables (inset spectra). Energy enters the coupled system via pump laser excitation of the dipolar LSP of the AuNR and is dissipated through various pathways. Once excited, the LSP decays through both radiative ($\gamma_{0,Rad}$) and nonradiative ($\gamma_{0,NR}$) means, and in addition may exchange energy with the microresonator via LSP-WGM coupling (g). The WGM likewise may exchange energy with the LSP or decay via outcoupling to the waveguide ($\gamma_{1,Fib}$) in addition to radiative ($\gamma_{1,Rad}$) and nonradiative ($\gamma_{1,NR}$) dissipation channels. The conservation of energy through these various pathways in the steady state is reflected by the equality between the extinction cross-section (σ_{ext}), which is a measure of the rate at which energy enters the system, and the sum of the absorption (σ_{abs}), scattering (σ_{scat}) and transmission (σ_T) cross-sections (inset equation), each of which probes a particular dissipative pathway.

Main text: Absorption and Two-Sided Transmission

As described previously[31, 50, 52], photothermal absorption spectroscopy is performed with separate pump and probe beams. As shown in the experimental scheme of **Figure 3.2**, a narrow-band tunable probe laser coupled to a tapered optical fiber

interrogates the microresonator WGMs via evanescent coupling. At the other end of the optical fiber is an avalanche photodiode (APD) to allow monitoring of probe beam transmission. The probe beam is phase-modulated at radio frequencies (RF) and locked to the WGM resonance via the Pound-Drever-Hall locking scheme.[50] Simultaneously, a pump beam is focused to a near diffraction-limited spot and overlapped with individual nanoparticles on the microresonator surface. The pump beam is amplitude-modulated at kHz frequencies to maximize the signal-to-noise ratio. This double modulation scheme is capable of resolving resonance shifts down to under one attometer.[50] The amount of resonance shift is then used to compute the power absorbed by the AuNRs with the aid of a FEM (COMSOL) simulation of the steady-state temperature increase within the microresonator.[50] The pump laser is raster-scanned over the microresonator to search for single AuNRs sparsely deposited on the resonator. Once located, an absorption spectrum is obtained by wavelength-scanning the tunable continuous-wave pump laser polarized along the long axis of the AuNR. High-resolution photothermal absorption spectra show distinctive sharp Fano antiresonance line shapes (shown schematically as σ_{abs} in **Figure 3.1**), indicative of mutual interaction between photonic and plasmonic modes.[31, 50, 53]

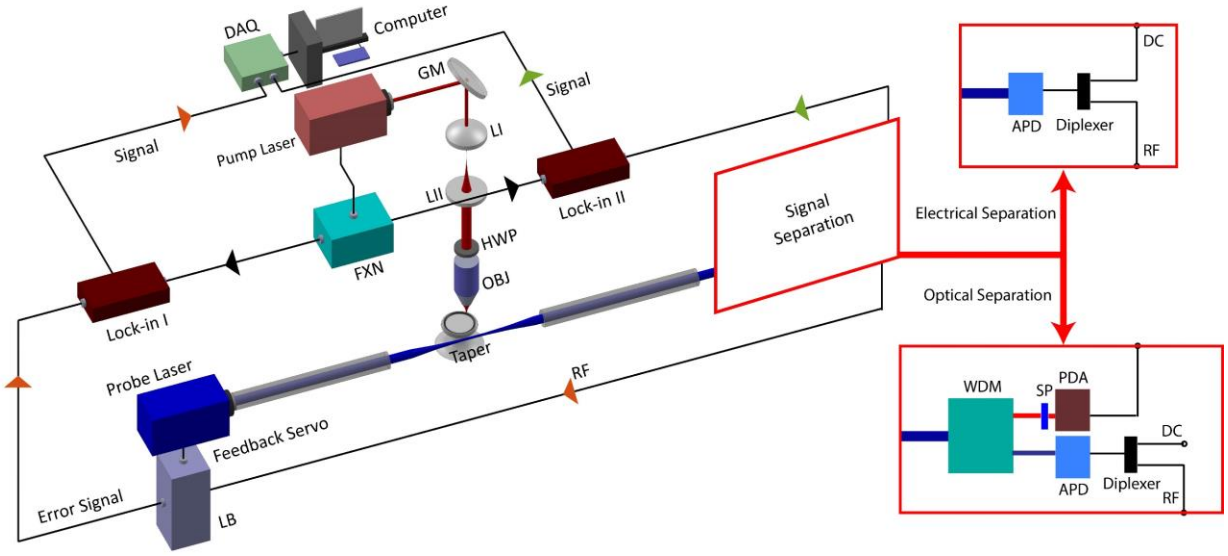

Figure 3.2 Experimental setup for simultaneous measurement of absorption and two-sided transmission. LI: lens I, LII: lens II, GM: galvo mirrors, FXN: function generator, Lock-in: lock-in amplifier, HWP: half-wave plate, OBJ: objective, LB: lock box, WDM: wavelength division multiplexer, SP: short-pass optical filter, PDA: adjustable-gain photodiode detector, APD: avalanche photodiode detector, DAQ: National Instruments LabView data acquisition card, RF: radio-frequency electrical signal generated from APD, DC: kHz to DC electrical signal generated from APD. The red box indicates where either an electrical separation (top) or optical separation (bottom) is implemented. Arrows of different colors represent photothermal absorption (orange) and transmission (green) measurements or references (black).

Concurrent with photothermal absorption, we now measure the two-sided transmission (σ_T in **Figure 3.1**), i.e., the power transmitted from the free-space pump laser through the plasmonic-photonic system and into the same tapered fiber used for the above photothermal measurement. In order to implement the simultaneous measurement of photothermal absorption and two-sided transmission, we first relied on the use of an electrical signal diplexer in an electrical separation scheme that can discriminate RF signal from much slower oscillatory signal (kHz to DC, hereafter called DC), as shown in **Figure 3.2**. Both signals are generated by the APD detector. As above, the photothermal absorption signal is decoded from pump-induced phase shifts in the RF signal through

both the local oscillator used for phase-modulation of the probe beam and a lock-in amplifier. At the same time, the DC signal is directly connected to a second lock-in amplifier for measurement of the kHz-modulated two-sided transmission. This strategy relies on the fact that while the photothermal and two-sided transmission signals are both modulated via the pump beam's (kHz) modulation, only the photothermal signal is additionally modulated at RF frequencies. However, high-resolution spectra collected over several spectral ranges show that signal measured through the DC channel (Figure 3a, middle) closely follows the asymmetric Fano line shapes measured through the RF channel (**Figure 3.3a**, top). In addition, low-resolution spectra measured through the two channels both show broad spectral signatures of the LSP (see Figure S2 in SI). The similar spectral line shapes in absorption and transmission (Figure 3a, top and middle) can be understood by examining the resonance shift induced by photothermal response of the microresonator, shown in **Figure 3.3b**. The DC channel measures the amplitude difference (labeled with $\mathbf{T_{Electrical}}$) in the vertical direction which is proportional to the WGM resonance shift (labeled with **A**) in the horizontal direction due to photothermal effect, and therefore, the DC signal provides a scaled replica of the photothermal absorption spectrum. Thus, this scheme, cannot discriminate the two-sided transmission from the photothermal signal.

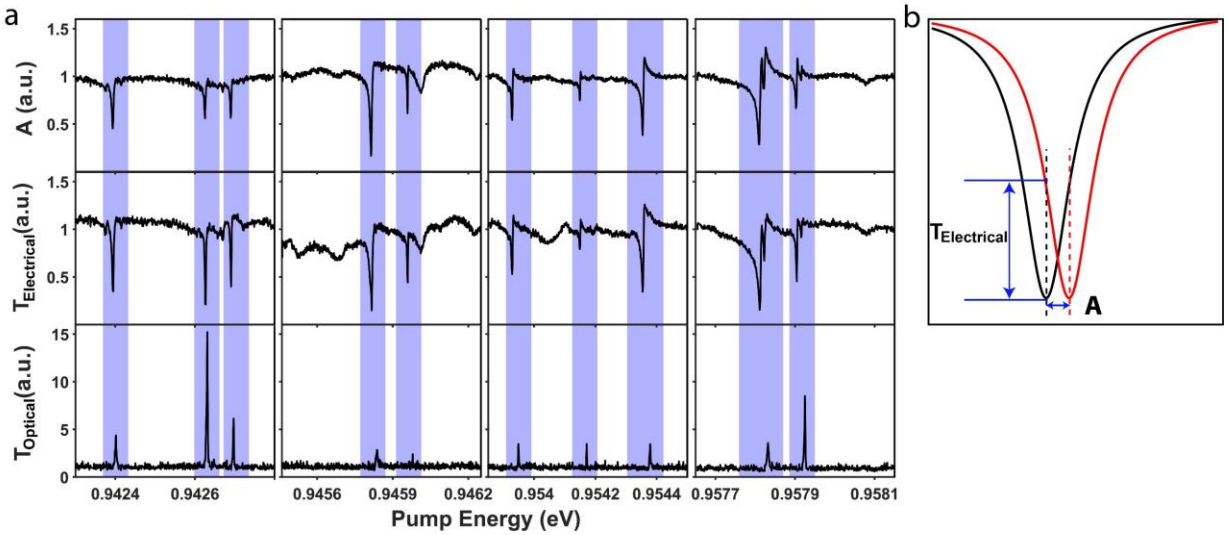

Figure 3.3 Simultaneous spectral measurements. (a) photothermal absorption (**A**) measured through the RF channel from APD (top); transmission ($\mathbf{T_{Electrical}}$) measured through DC channel from APD (middle); transmission ($\mathbf{T_{Optical}}$) measured with the WDM included and detected via the PDA (bottom). Note that the resonance "teeth" of transmission ($\mathbf{T_{Optical}}$) are not exactly lined up with other two observables. In this case, $\mathbf{T_{Electrical}}$ and **A** were measured simultaneously, but $\mathbf{T_{Optical}}$ was measured later and the laser scanning actuator experienced minor motion hysteresis. (b) Schematic illustration of how photothermal and transmission measurements are conveyed through RF and DC channels when the pump laser induces a resonance shift.

In comparison, the simple optical separation scheme shown in **Figure 3.2** enables the distinction between photons transmitted through the coupled plasmonic-photonic cavity system from the pump beam (λ = 1275-1355 nm) and those photons originating in the probe beam (λ = 1550-1570 nm) and employed for photothermal spectroscopy. A combination of a wavelength division multiplexer (WDM), short-pass optical filter, and second photodetector (PDA) then allows for a simultaneous direct measurement of photons of different wavelengths traveling through the taper, revealing dramatically distinct spectral features, as shown in the bottom row of **Figure 3.3a**. At each WGM energy position lies a resonant line shape that is conspicuously different from the Fano antiresonance seen in the absorption spectra. Measurements on different AuNRs and

microresonators show these same phenomena (see Figure S1 in SI). High-resolution spectra over a full spectral range taken through the two channels also show distinct spectral features where the spectrally broad LSP resonance measured via photothermal absorption is replaced by a series of resonance “teeth” in the two-sided transmission spectra (see Figure S3 in SI). These distinct spectral behaviors are also robust over a range of pump laser modulation frequencies (Figure S4 in SI). The two-sided transmission signal is highly dependent on taper position relative to the microresonator, with certain positions rendering some WGMs inaccessible while other modes are viable channels for outcoupling photons to the taper (see Figures S8 and S12 in SI), as expected.[54] Taken together, adding a WDM-filtered detection channel enables one to realize the simultaneous measurement of absorption and two-sided transmission for a coupled LSP-WGM system using a single optical waveguide.

Main text: Modeling

The spectral features exposed by simultaneous absorption and transmission measurements can be well-understood through mathematical modeling of the various energy pathways available to the coupled LSP-WGM system. To that effect, we develop a coupled oscillator model which includes physically independent system parameters relevant to each dissipative process and, as will be shown, each spectral observable. While this model is derived from first principles (SI), simplifications informed by experimental results are made. For example, the distinct line shapes in transmission spectra indicate that the tapered fiber does not simply play a passive role in the

interrogation of the coupled LSP-WGM system. Instead, the propagating modes of the tapered fiber are coupled to the WGMs of the microresonator through the mutual overlap of their evanescent fields. Because this coupling is weak, it manifests itself in the LSP-WGM dynamics as a taper-induced loss mechanism and the dynamics of the fiber modes need not be explicitly considered. In addition, quantum fluctuations, while typically included in input-output theory as a manifestation of the fluctuation-dissipation theorem,[51] are ignored here as all excitations are in the many-quanta limit where classical effects dominate. Lastly, only a single WGM need be considered since the modes of the toroid are mutually orthogonal and therefore do not interact directly. Taking all of these considerations into account, the equations of motion for the LSP-WGM system may be written as

$$\begin{aligned} &m\ddot{x} + m\gamma_{0,\mathrm{NR}}\dot{x} + m\omega_0^2 x + g\sqrt{\frac{m}{V}}\dot{q} = \frac{2e^2}{3c^3}\dddot{x} + eE_{\mathrm{ext}}e^{-i\omega t} \\ &\frac{1}{V}\ddot{q} + \frac{1}{V}\left(\gamma_{1,\mathrm{NR}} + \gamma_{1,\mathrm{Rad}} + \gamma_{1,\mathrm{Fib}}\right)\dot{q} + \frac{1}{V}\omega_1^2 q - g\sqrt{\frac{m}{V}}\dot{x} = 0 \end{aligned} \qquad 3.1$$

where x and m are the oscillator amplitude and effective mass of the dipolar LSP along the AuNR's long axis, c is the speed of light, $E_{\mathrm{ext}}e^{-i\omega t}$ is the field of the pump laser incident on the AuNR, and the radiation reaction force (proportional to $\dddot{x}$ and e is the elementary charge) acting on the LSP has been included.[55] Where appropriate, the subscripts 0 and 1 are used to signify LSP and WGM parameters, respectively. On the second line, V is the mode volume of the WGM and q is related to its associated electric field by

$$\vec{E}(\vec{x},t) = -\frac{\sqrt{4\pi}}{V}\dot{q}(t)\vec{f}(\vec{x}), \tag{3.2}$$

where the mode function[56, 57] $\vec{f}(\vec{x})$ is a solution to a generalized form of the vector Helmholtz equation appropriate for an isolated WGM resonator. Finally, appearing in both equations of motion is a term proportional to the coupling strength, g, determined (up to scaling factors) by the projection of the WGM mode function onto the long axis of the AuNR at its center, $\vec{r}_0$,

$$g = e\sqrt{\frac{4\pi}{mV}}\vec{f}(\vec{r}_0)\cdot\hat{x}. \tag{3.3}$$

While the equations of motion (equation 3.1) are similar to those used in our previous work[31, 50], here we explicitly differentiate between the various physical processes which contribute to the decay of both the LSP and WGM excitations. Each distinct damping rate is labeled by γ with a subscript denoting the relevant dissipative pathway. The LSP dissipates energy via nonradiative absorption ($\gamma_{0,\mathrm{NR}}$) and radiation into the far field ($\gamma_{0,\mathrm{Rad}} = 2e^2\omega^2/3mc^3$), while the WGM can decay through energy transfer to the fiber ($\gamma_{1,\mathrm{Fib}}$) in addition to dissipative processes intrinsic to the WGM, including material absorption, bending loss, and surface inhomogeneity scattering. According to the model, $\gamma_{1,\mathrm{Fib}}$ depends upon the mutual overlap of evanescent fields of WGMs and fiber taper modes. Additionally, energy may be transferred from the WGM to LSPs of undriven AuNRs on the surface of the toroid which in turn can absorb and radiate. While these

taper-independent WGM decay pathways are each the result of physically distinct processes, all terminate in either heating the microresonator or liberating energy into the far-field via radiation, and therefore can be aggregated into a total nonradiative ($\gamma_{1,\mathrm{NR}}$) and radiative ($\gamma_{1,\mathrm{Rad}}$) damping rate.

Each dissipative pathway is associated with a distinct experimental observable; absorption measurements probe nonradiative dissipation, scattering measurements collect radiated energy in the far field, and the previously described two-sided transmission measurement detects energy transferred from the WGM to the tapered fiber. Accordingly, expressions for various cross-sections may be derived by computing the power dissipated in the steady state by the corresponding damping force in equation 3.1 and normalizing to the intensity of the pump laser incident on the AuNR (SI). Carrying out this procedure leads to the following expressions for the reduced absorption, scattering, and extinction (i.e., total) cross-sections

$$\frac{\sigma_{\mathrm{abs}}}{\sigma_{\mathrm{abs}}^{0}} = \frac{\tilde{\gamma}_{0,\mathrm{NR}}}{\gamma_{0,\mathrm{NR}}} F(\omega) \qquad \frac{\sigma_{\mathrm{scat}}}{\sigma_{\mathrm{scat}}^{0}} = \frac{\tilde{\gamma}_{0,\mathrm{Rad}}}{\gamma_{0,\mathrm{Rad}}} F(\omega) \qquad \frac{\sigma_{\mathrm{ext}}}{\sigma_{\mathrm{ext}}^{0}} = \frac{\tilde{\gamma}_{0,\mathrm{Tot}}}{\gamma_{0,\mathrm{Tot}}} F(\omega) \tag{3.4}$$

where the superscript 0 denotes the cross-section of the isolated LSP and

$$\tilde{\gamma}_{0,j}(\omega) = \gamma_{0,j} + \frac{\omega^2 g^2}{(\omega^2 - \omega_1^2)^2 + \omega^2 \gamma_{1,\mathrm{Tot}}^2} \gamma_{1,j} \tag{3.5}$$

is the WGM-dressed LSP damping rate where j indicates a particular decay pathway (nonradiative, radiative, or total). Each reduced cross-section scales with the function

$$F(\omega) = \left|\frac{q_{\mathrm{F}} + \epsilon}{\epsilon + i}\right|^2 \qquad 3.6$$

which depends on the scaled and shifted pump frequency $\epsilon(\omega) = (\omega^2 - \Omega^2)/\omega\Gamma$ where explicit forms for $\Omega(\omega)$ and $\Gamma(\omega)$ are given in the SI. In the limit where LSP damping dominates the coupled LSP-WGM dynamics $\left(\mathrm{i.e.}, \gamma_{0,\mathrm{Tot}} \gg \gamma_{1,\mathrm{Tot}}, g\right)$, the complex-valued function $q_{\mathrm{F}}(\omega) = (\Omega^2 - \omega_1^2 + i\omega\gamma_{1,\mathrm{Tot}})/\omega\Gamma$ becomes approximately constant over the spectral width of the WGM and can thus be identified as a complex generalization of the Fano asymmetry parameter,[31] while $F(\omega)$ becomes the familiar Fano line shape[50, 53, 58] describing an antiresonant effect at pump frequencies near the WGM resonant frequency.

Because the two-sided transmission measurement is unique to the LSP-WGM system and not of the LSP itself, it is not sensible to normalize the transmission cross-section to that of the bare LSP. Instead, it can be shown (SI) that it takes the form,

$$\sigma_{\mathrm{T}} = \frac{\gamma_{1,\mathrm{Fib}}}{\gamma_{1,\mathrm{Tot}}}\left(1 - \frac{\gamma_{0,\mathrm{Tot}}}{\tilde{\gamma}_{0,\mathrm{Tot}}}\right)\sigma_{\mathrm{ext}}. \qquad 3.7$$

This expression, while different in form from the other cross-sections previously discussed, can be intuitively understood by considering the pathway taken by the transmitted energy prior to its detection in the tapered fiber: the extinction cross-section σ_{ext} characterizes the total fraction of energy imparted into the LSP by the incident pump laser per unit time in the steady state, while the two preceding factors (from right-to-left) describe the fraction

of that energy that is transferred to the WGM and, finally, the fraction that is dissipated into the tapered fiber.

Main text: Analysis

While the above model alone yields a qualitative understanding of the physics underlying the coupled LSP-WGM system and the observables which probe its dissipative pathways, quantitative estimates of the parameters relevant to those observables may be obtained through a combination of theory and experimental data through least-squares fitting. Such a quantitative characterization of the system is compelling for a variety of reasons. An order-of-magnitude comparison between various parameters elucidates the breadth of timescales which play a role in the system dynamics, while an analysis of the coupling strength in relation to the dominant dissipative rates reveals where the system lies in the range of weak-to-strong coupling (our system is clearly in the weak coupling regime). In addition, an accurate parameter estimation is important for optimizing hybrid

cavity design to control light-matter interactions, such as for maximum Purcell enhancement.[31]

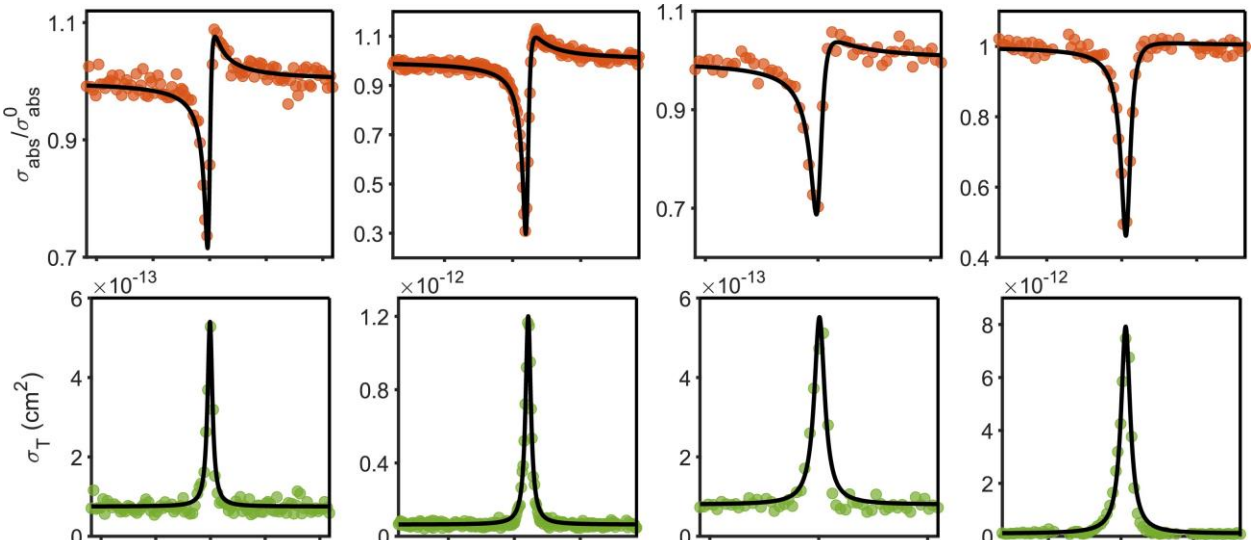

Figure 3.4 Simultaneous fits to reduced absorption cross-section (top) and transmission cross-section (bottom). Though relative energies are plotted here, absolute energies are used for further analysis.

Due to the multiple order-of-magnitude mismatch between LSP and WGM linewidths, both low- and high-resolution absorption spectral measurements are taken into consideration. The low-resolution scan characterizes the spectrally broad Lorentzian "envelope" of the LSP, while the high-resolution scan reveals spectrally narrow Fano line shapes in absorption[31, 50, 53, 58] and sharp resonance "teeth" in transmission, as discussed above. Parameter estimates are obtained through a two-step fitting procedure. First, LSP parameters (ω_0, $\gamma_{0,\mathrm{NR}}$, $\gamma_{0,\mathrm{Rad}}$) are extracted by fitting low-resolution absorption spectra to the bare LSP absorption cross-section

$$\sigma^0_{\mathrm{abs}}(\omega) = \frac{4\pi\omega^2 e^2 \hbar}{mc} \frac{\gamma_{0,\mathrm{NR}}}{(\omega^2 - \omega_0^2)^2 + \omega^2 \gamma^2_{0,\mathrm{Tot}}}. \qquad 3.8$$

Subsequently, remaining parameters (ω_1, $\gamma_{1,\mathrm{NR}}$, $\gamma_{1,\mathrm{Rad}}$, $\gamma_{1,\mathrm{Fib}}$, g), are obtained through simultaneous fitting of high-resolution absorption and two-sided transmission spectra to Eqs. (3.4) and (3.7) with LSP parameters bound within 95% confidence intervals. Notably, all fits are carried out on absolute measurements without artificial scaling parameters. Simultaneous fits over several spectral ranges that contain a large number of WGM resonances all show an excellent agreement between experimental measurements and the model, a few of which are shown in **Figure 3.4** and Figure S7 in SI.

The plasmon natural frequency (ω_0) and nonradiative damping rate ($\gamma_{0,\mathrm{NR}}$) obtained from fits vary minimally between different WGM resonances, as shown in Figure 5a. The stepwise trend of ω_1 results from the fact that individual, well-separated spectral windows are surveyed, each containing multiple WGM resonances. Likewise, a similar stepwise trend is observed for the frequency-dependent LSP radiative damping rate $\gamma_{0,\mathrm{Rad}}(\omega)$ which here is evaluated at $\omega = \omega_1$. Analyzed WGMs consist of those at resonant frequencies both higher and lower than the frequency of the LSP (ω_0). Cavity intrinsic ($\gamma_{1,\mathrm{NR}}$ and $\gamma_{1,\mathrm{Rad}}$) and taper-induced ($\gamma_{1,\mathrm{Fib}}$) loss rates are less than those contributed by the LSP by over three orders of magnitude. We calculate the global mean of individual damping rates obtained from the fitting for each parameter. As shown in **Table 3.1**, fits to simultaneous absorption and transmission measurements make it possible to extract a high dynamic range of damping rates spread over six orders of magnitude. The LSP damping rates are comparable to those reported by Refs[45, 59, 60] reported for single AuNRs, while WGM damping rates are in accordance with typical Q factors (~10^6) of higher-order

modes measured in toroidal microresonators with AuNRs deposited on the surface. As expected, the coupled LSP-WGM system is well within the weak coupling regime as the interaction energy g is multiple orders-of-magnitude smaller than the system's total damping rates ($\hbar g \sim 10^{-4}\ \mathrm{eV}, \hbar\gamma_{0,\mathrm{Tot}} \sim 10^{-2}\ \mathrm{eV}, \hbar\gamma_{1,\mathrm{Tot}} \sim 10^{-6}\ \mathrm{eV}$). $\gamma_{1,\mathrm{Fib}}$ is the smallest among WGM loss rates, suggesting the taper is under-coupled and can act as a weakly perturbative readout to examine those WGMs that interact with the LSP.

As seen by examining the standard deviation of the mean, the variation amongst LSP parameters is minimal in comparison to the WGM parameters. This is expected as all measurements were carried out for a single LSP with a well-defined resonance frequency and linewidth. In contrast, the mean and standard deviation of the mean for the WGM parameters compiles results across 12 distinct WGM resonances and variation is therefore expected. In particular, the fiber-induced loss rate $\gamma_{1,\mathrm{Fib}}$ and the coupling strength g depend crucially on the field profile of the particular WGM in question and therefore the standard deviation of the mean conveys important information about the range of attainable values for these parameters. Among all parameters, the most uncertain is the WGM radiative loss rate $\gamma_{1,\mathrm{Rad}}$. This is expected as we do not measure scattering and therefore do not directly probe the energy dissipated through radiative means. In other words, the absorption and two-sided transmission measurements provide sufficient information to extract the individual rates $\gamma_{1,\mathrm{NR}}$ and $\gamma_{1,\mathrm{Fib}}$, respectively, while the line shape in either observable may be used to determine the total linewidth $\gamma_{1,\mathrm{Tot}}$. The radiative rate $\gamma_{1,\mathrm{Rad}}$ is inferred through a combination of these independent

measurements along with the relation $\gamma_{1,\mathrm{Rad}} = \gamma_{1,\mathrm{Tot}} - \gamma_{1,\mathrm{NR}} - \gamma_{1,\mathrm{Fib}}$. A more direct determination of $\gamma_{1,\mathrm{Rad}}$ would be possible through a scattering measurement simultaneous with the absorption and transmission measurements.

In order to evaluate the sensitivity of each observable on the coupling strength and the various damping rates, we compute all derived observables using the global mean of all fit parameters and examine the effect of the parameters' variation upon that observable (SI), as shown in Figure 5b in SI. The LSP damping rates, particularly $\gamma_{0,\mathrm{NR}}$, dominate the contribution to σ_{abs}, σ_{scat}, and σ_{ext}. However, σ_{T} is more sensitive to the variations of WGM damping rates and coupling strength. Overall, through simultaneous measurement of absorption and transmission, we are able to fully describe this weakly coupled system even though its parameter space spans nearly nine orders of magnitude in energy. This capability provides a foundation for deterministic control and design of specific dissipative channels for specific purposes.

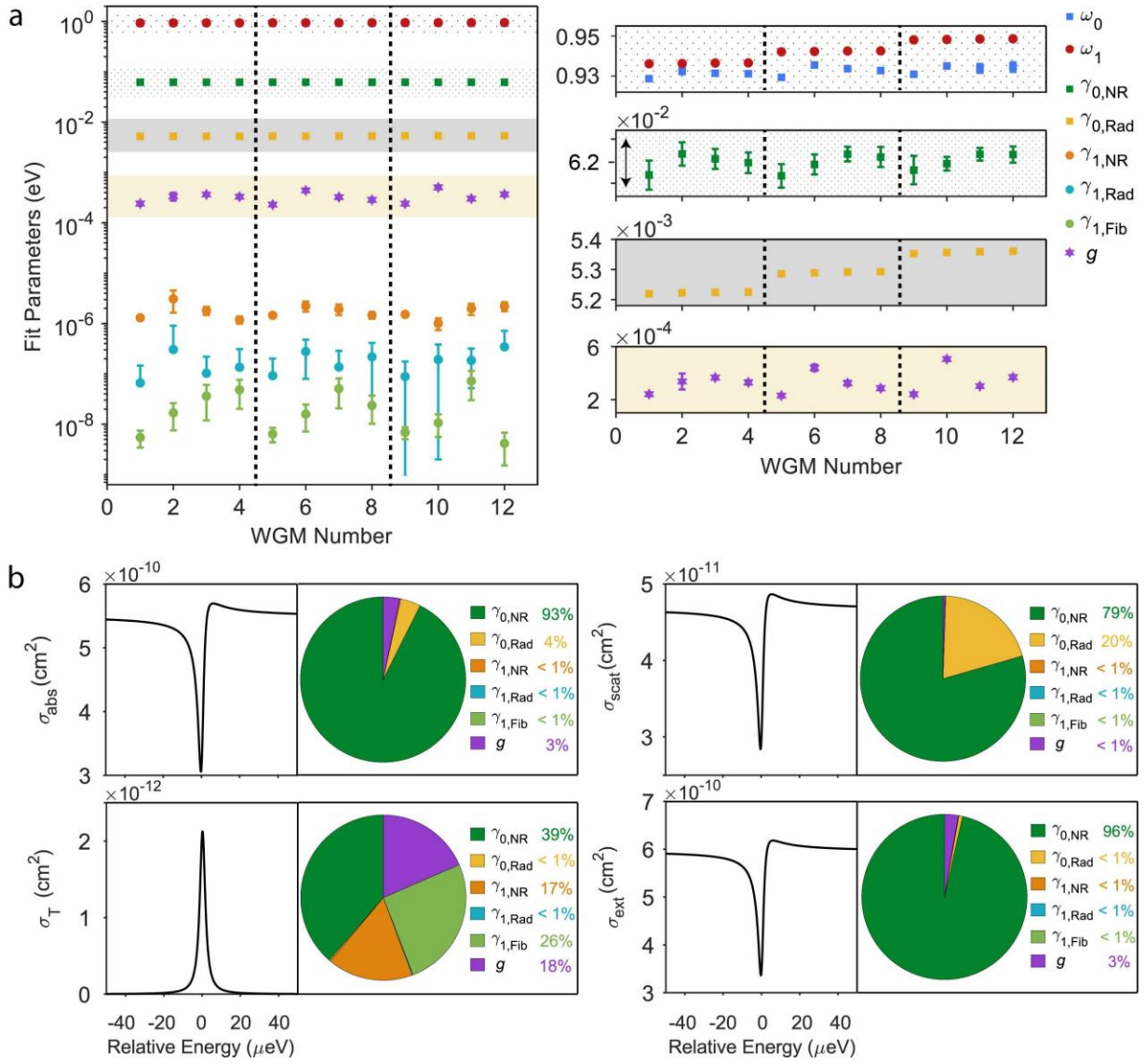

Figure 3.5 (a) All fit parameters in log scale (left side) obtained from simultaneous fits to experimental data in well-separated spectral windows indicated by dark dashed lines. Scaling these parameters between frequency and energy units is accomplished by an implicit factor of $\hbar$. Zoom-in plots in linear scale (right side) for better clarity. The arrow on the second panel indicates a range of $5 \times 10^{-6}\ eV$. (b) Computed spectra (left side) based on the global mean of all fit parameters and pie charts (right side) for the parameters' contributions to the corresponding cross-sections.

One example of an application would be to tailor far-field radiation by controlling the influence of the photonic environment on a single nanorod's polarizability. A similar

scheme was used in an array of nanorods coupled to a single WGM through backaction.[43] With the addition of a far-field scattering measurement and theoretical modeling, a complete accounting of every photon entering and exiting the system would be possible. As dictated by energy conservation, the sum of the powers scattered, absorbed, and transmitted must equal the laser power extinguished when averaged over an optical cycle. This conservation is made explicit through the sum rule obeyed by the observables in Eqs. (3.4) and (3.7),

$$\sigma_{\text{ext}}(\omega) = \sigma_{\text{abs}}(\omega) + \sigma_{\text{scat}}(\omega) + \sigma_{\text{T}}(\omega), \qquad 3.9$$

which can be derived by appealing to Newton's equations (SI). Nevertheless, even without a scattering measurement, it is possible to extract parameter values from absorption and transmission measurements and subsequently extrapolate the system's scattering behavior from the model. This method of determining system parameters can be combined with previously reported methods for tuning the plasmonic resonance based on thermal annealing[31] to exert unprecedented control over plasmonic-photonic mode mixing and energy flow.

Table 3.1 The mean and standard deviation of the mean for all fit parameters.

	$\hbar\omega_0$ (eV)	$\hbar\omega_1$ (eV)	$\hbar\gamma_{0,\text{NR}}$ (meV)	$\hbar\gamma_{0,\text{Rad}}$ (meV)	$\hbar g$ (meV)	$\hbar\gamma_{1,\text{NR}}$ (μeV)	$\hbar\gamma_{1,\text{Rad}}$ (μeV)	$\hbar\gamma_{1,\text{Fib}}$ (neV)
Mean	0.9326	0.9426	62.20249	5.293	0.332	1.74	0.18	26

S.D.	0.0001	0.0002	0.00009	0.002	0.004	0.04	0.02	1

In general, the emergent properties of cavity-matter systems are determined by the dissipation rates and couplings such as those quantitatively determined in this work. The balance of these parameters must often be precisely controlled in order to achieve certain functionality across a breadth of applications. For example, tunability of LSP and WGM resonance energies in a coupled plasmonic-photonic cavity is crucial for maximizing Purcell enhancement.[31] A perfect balance of gain and loss is imperative for creation of exceptional points in parity-time symmetric systems.[13, 61] To achieve strong cavity-matter coupling, a significant disparity between coupling and total loss is necessary.[62, 63] The ability to dial-in specific coupling strengths and resonance energies is a critical requirement for creation of nonlinear coupled cavities arrays for quantum simulation,[64-66] quantum error correction,[67] and optical signal processing.[68] Creation of routing systems in photonic circuits requires precise control of photon transfer rates between component cavities.[69] Realization of all these applications depends upon convenient experimental techniques, such as those presented here, to determine intrinsic system parameters across many timescales.

In summary, using a single tapered optical fiber, we demonstrate the simultaneous measurement of photothermal absorption and two-sided transmission from individual plasmonic nanorods coupled to an optical microresonator. These observables allow us to track down the distribution and dissipation of energy through multiple competing pathways. We also present a model of the coupled plasmonic-photonic system that we

use to fit the measured data and extract the damping parameters as well as the LSP-WGM coupling strength with a high dynamic range spanning up to nine orders of magnitude, fully describing the LSP-WGM dynamics in a weakly coupled system. These combined experimental and theoretical techniques may be useful for future spectroscopic investigation of weakly or strongly coupled plasmonic, excitonic, and photonic systems with dissipation and coupling spanning a wide range of timescales. This quantitative understanding is necessary to leverage light-matter interactions through manipulating specific dissipation channels and/or coupling for applications in quantum communication and quantum information science,[3-9] single-molecule detection,[70, 71] and cavity-controlled chemistry.[15-22]

Main text: Methods

Sample preparation. Toroidal microresonators were fabricated as described previously.[72] A vortexed stock solution of gold nanorods (25×256 nm^2, Nanopartz A12-25-1400) was diluted by 200 times in Millipore water. Prior to deposition onto resonators, the diluted solution was vortexed again. The solution was then drop-cast onto a chip of resonators and allowed to settle for 5 minutes before spinning for 1 minute at 3000 rpm.

Spectroscopic measurement. The previously described apparatus[31, 50, 52] is modified for simultaneous measurement of photothermal and two-sided transmission signal. A tunable laser (Newport TLB-6728) is used as the probe laser. Unless otherwise stated, a wavelength division multiplexer (Thorlabs, WD1350A, 1310 nm/1550 nm) is used to split two colors of photons (~1310 nm and ~1550 nm) co-propagating in a single-

mode fiber (SMF-28e+, Corning). The photons of two different colors are then measured by two photodetectors (PDA10CS, APD430C), respectively. A free-space pump beam (~1310 nm) from another tunable laser (Thorlabs TLK-L1300) is delivered through a high numerical aperture (NA) air objective (Nikon, 60X, NA 0.95). The pump beam is amplitude-modulated at kHz and results in heat dissipation from AuNR to the microresonator, which shifts WGM resonance. The photothermal signal is then de-modulated by a lock-in amplifier (Ametek, Signal Recovery 7265). The amount of resonance shift is related to the actual power absorbed by AuNR using COMSOL simulation and AuNR's photoluminescence quantum yield (assumed to be zero[73]). In contrast to photothermal measurement, the two-sided transmission photons (~1310 nm) are collected through the other port of WDM and passed through an optical filter (Edmund Optics, 1450 nm, 25 mm, OD 2 Short-pass filter) for blocking photons at ~1550 nm. The filtered transmitted photons are measured by the PDA photodetector. The transmission signal is then de-modulated by a second lock-in amplifier. The two lock-in amplifiers are synchronized and externally connected with a refence square wave at kHz from the same function generator. More details in SI.

Supporting Information. Information on (1) experimental details, including (i) experimental setup, (ii) data acquisition methods and (iii) investigation of pump laser modulation's effect on spectra. Also (2) modeling LSP-WGM interaction and derivation of cross-sections and other expressions. Also (3) data analysis, including (i) fitting details and extra simultaneous fits, (ii) examination of some WGM damping parameters'

dependence on taper relative position, (iii) method for evaluating contribution of LSP and WGM parameters to each observable, and (iv) characterization of angular structure of WGMs via transmission measurement.

Funding We acknowledge support from the National Science Foundation under awards CHE-1836482 (R.H.G.), CHE-1836506 (D.J.M), DMR-1610345 (R.H.G.) and CHE-1664684 (D.J.M.).

Author Contributions FP acquired data with help from HLN and RHG. KCS performed modeling and calculations with help from DJM. KCS and FP analyzed data with help from RHG and DJM. KAK fabricated the resonators. FP and KCS wrote the manuscript together with help from all co-authors. FP and KCS contributed equally to this work.

References

1. Purcell, E. M., "Spontaneous Emission Probabilities at Radio Frequencies." *Phys. Rev.* **1946**, *69*(681).

2. Goy, P., Raimond, J. M., et al., "Observation of Cavity-Enhanced Single-Atom Spontaneous Emission." *Phys. Rev. Lett.* **1983**, *50*(24): 1903-1906.

3. Li, Y.-H., Zhou, Z.-Y., et al., "Multiplexed entangled photon-pair sources for all-fiber quantum networks." *Phys. Rev. A* **2016**, *94*(4): 043810.

4. De Greve, K., Yu, L., et al., "Quantum-dot spin–photon entanglement via frequency downconversion to telecom wavelength." *Nature* **2012**, *491*: 421.

5. Imamog¯lu, A., Awschalom, D. D., et al., "Quantum Information Processing Using Quantum Dot Spins and Cavity QED." *Phys. Rev. Lett.* **1999**, *83*(20): 4204-4207.

6. Pellizzari, T., Gardiner, S. A., et al., "Decoherence, Continuous Observation, and Quantum Computing: A Cavity QED Model." *Phys. Rev. Lett.* **1995**, *75*(21): 3788-3791.

7. Zheng, S.-B. and Guo, G.-C., "Efficient Scheme for Two-Atom Entanglement and Quantum Information Processing in Cavity QED." *Phys. Rev. Lett.* **2000**, *85*(11): 2392-2395.

8. Kimble, H. J., "The quantum internet." *Nature* **2008**, *453*: 1023-1030.

9. Sillanpää, M. A., Park, J. I., et al., "Coherent quantum state storage and transfer between two phase qubits via a resonant cavity." *Nature* **2007**, *449*: 438-442.

10. Wang, D., Kelkar, H., et al., "Turning a molecule into a coherent two-level quantum system." *Nat. Phys.* **2019**, *15*(5): 483-489.

11. McKeever, J., Buck, J. R., et al., "Determination of the Number of Atoms Trapped in an Optical Cavity." *Phys. Rev. Lett.* **2004**, *93*(14): 143601.

12. Münstermann, P., Fischer, T., et al., "Dynamics of Single-Atom Motion Observed in a High-Finesse Cavity." *Phys. Rev. Lett.* **1999**, *82*(19): 3791-3794.

13. Peng, B., Özdemir, Ş. K., et al., "Parity–time-symmetric whispering-gallery microcavities." *Nat Phys* **2014**, *10*: 394.

14. Özdemir, Ş. K., Rotter, S., et al., "Parity–time symmetry and exceptional points in photonics." *Nat. Mater.* **2019**, *18*(8): 783-798.

15. Herrera, F. and Spano, F. C., "Cavity-Controlled Chemistry in Molecular Ensembles." *Phys. Rev. Lett.* **2016**, *116*(23): 238301.

16. Schäfer, C., Ruggenthaler, M., et al., "Modification of excitation and charge transfer in cavity quantum-electrodynamical chemistry." *Proc. Natl. Acad. Sci. U. S. A.* **2019**, *116*(11): 4883-4892.

17. Dunkelberger, A. D., Spann, B. T., et al., "Modified relaxation dynamics and coherent energy exchange in coupled vibration-cavity polaritons." *Nat. Commun.* **2016**, *7*: 13504.

18. Zhong, X., Chervy, T., et al., "Energy Transfer between Spatially Separated Entangled Molecules." *Angew. Chem. Int. Ed.* **2017**, *56*(31): 9034-9038.

19. Du, M., Ribeiro, R. F., et al., "Remote Control of Chemistry in Optical Cavities." *Chem* **2019**, *5*(5): 1167-1181.

20. Lather, J., Bhatt, P., et al., "Cavity Catalysis by Cooperative Vibrational Strong Coupling of Reactant and Solvent Molecules." *Angew. Chem. Int. Ed.* **2019**, *58*(ja): 1-5.

21. Thomas, A., George, J., et al., "Ground-State Chemical Reactivity under Vibrational Coupling to the Vacuum Electromagnetic Field." *Angew. Chem. Int. Ed.* **2016**, *55*(38): 11462-11466.

22. Thomas, A., Lethuillier-Karl, L., et al., "Tilting a ground-state reactivity landscape by vibrational strong coupling." *Science* **2019**, *363*(6427): 615-619.

23. Vahala, K. J., "Optical microcavities." *Nature* **2003**, *424*(6950): 839-846.

24. Srinivasan, K. and Painter, O., "Linear and nonlinear optical spectroscopy of a strongly coupled microdisk–quantum dot system." *Nature* **2007**, *450*(7171): 862-865.

25. Ohta, R., Ota, Y., et al., "Strong coupling between a photonic crystal nanobeam cavity and a single quantum dot." *Appl. Phys. Lett.* **2011**, *98*(17): 173104.

26. Lodahl, P., Mahmoodian, S., et al., "Interfacing single photons and single quantum dots with photonic nanostructures." *Rev. Mod. Phys.* **2015**, *87*(2): 347-400.

27. Hennessy, K., Badolato, A., et al., "Quantum nature of a strongly coupled single quantum dot–cavity system." *Nature* **2007**, *445*: 896.

28. Chen, Y., Ryou, A., et al., "Deterministic Positioning of Colloidal Quantum Dots on Silicon Nitride Nanobeam Cavities." *Nano Lett.* **2018**, *18*(10): 6404-6410.

29. Armani, D. K., Kippenberg, T. J., et al., "Ultra-high-Q toroid microcavity on a chip." *Nature* **2003**, *421*(6926): 925-928.

30. Gayral, B., Gérard, J. M., et al., "High-Q wet-etched GaAs microdisks containing InAs quantum boxes." *Appl. Phys. Lett.* **1999**, *75*(13): 1908-1910.

31. Thakkar, N., Rea, M. T., et al., "Sculpting Fano Resonances To Control Photonic–Plasmonic Hybridization." *Nano Lett.* **2017**, *17*(11): 6927-6934.

32. Doeleman, H. M., Verhagen, E., et al., "Antenna–Cavity Hybrids: Matching Polar Opposites for Purcell Enhancements at Any Linewidth." *ACS Photonics* **2016**, *3*(10): 1943-1951.

33. Shopova, S. I., Rajmangal, R., et al., "Plasmonic enhancement of a whispering-gallery-mode biosensor for single nanoparticle detection." *Appl. Phys. Lett.* **2011**, *98*(24): 243104.

34. Santiago-Cordoba, M. A., Boriskina, S. V., et al., "Nanoparticle-based protein detection by optical shift of a resonant microcavity." *Appl. Phys. Lett.* **2011**, *99*(7): 073701.

35. Boriskina, S. V. and Reinhard, B. M., "Spectrally and spatially configurable superlenses for optoplasmonic nanocircuits." *Proc. Natl. Acad. Sci. U. S. A.* **2011**, *108*(8): 3147-3151.

36. Shopova, S. I., Blackledge, C. W., et al., "Enhanced evanescent coupling to whispering-gallery modes due to gold nanorods grown on the microresonator surface." *Appl. Phys. B* **2008**, *93*(1): 183-187.

37. Ahn, W., Boriskina, S. V., et al., "Photonic–Plasmonic Mode Coupling in On-Chip Integrated Optoplasmonic Molecules." *ACS Nano* **2012**, *6*(1): 951-960.

38. Badolato, A., Hennessy, K., et al., "Deterministic Coupling of Single Quantum Dots to Single Nanocavity Modes." *Science* **2005**, *308*(5725): 1158-1161.

39. Englund, D., Fattal, D., et al., "Controlling the Spontaneous Emission Rate of Single Quantum Dots in a Two-Dimensional Photonic Crystal." *Phys. Rev. Lett.* **2005**, *95*(1): 013904.

40. Englund, D., Faraon, A., et al., "Controlling cavity reflectivity with a single quantum dot." *Nature* **2007**, *450*: 857.

41. Liu, J.-N., Huang, Q., et al., "Nanoantenna–Microcavity Hybrids with Highly Cooperative Plasmonic–Photonic Coupling." *Nano Lett.* **2017**, *17*(12): 7569-7577.

42. Solomon, G. S., Pelton, M., et al., "Single-mode Spontaneous Emission from a Single Quantum Dot in a Three-Dimensional Microcavity." *Phys. Rev. Lett.* **2001**, *86*(17): 3903-3906.

43. Ruesink, F., Doeleman, H. M., et al., "Controlling Nanoantenna Polarizability through Backaction via a Single Cavity Mode." *Phys. Rev. Lett.* **2018**, *120*(20): 206101.

44. Wang, P., Wang, Y., et al., "Single-Band 2-nm-Line-Width Plasmon Resonance in a Strongly Coupled Au Nanorod." *Nano Lett.* **2015**, *15*(11): 7581-7586.

45. Sönnichsen, C., Franzl, T., et al., "Drastic Reduction of Plasmon Damping in Gold Nanorods." *Phys. Rev. Lett.* **2002**, *88*(7): 077402.

46. Ruesink, F., Doeleman, H. M., et al., "Perturbing Open Cavities: Anomalous Resonance Frequency Shifts in a Hybrid Cavity-Nanoantenna System." *Phys. Rev. Lett.* **2015**, *115*(20): 203904.

47. Peng, P., Liu, Y.-C., et al., "Enhancing Coherent Light-Matter Interactions through Microcavity-Engineered Plasmonic Resonances." *Phys. Rev. Lett.* **2017**, *119*(23): 233901.

48. Srinivasan, K., Painter, O., et al., "Single quantum dot spectroscopy using a fiber taper waveguide near-field optic." *Appl. Phys. Lett.* **2007**, *91*(9): 091102.

49. Xiao, Y.-F., Liu, Y.-C., et al., "Strongly enhanced light-matter interaction in a hybrid photonic-plasmonic resonator." *Phys. Rev. A* **2012**, *85*(3): 031805.

50. Heylman, K. D., Thakkar, N., et al., "Optical microresonators as single-particle absorption spectrometers." *Nat. Photonics* **2016**, *10*: 788-795.

51. Gardiner, C. W. and Collett, M. J., "Input and output in damped quantum systems: Quantum stochastic differential equations and the master equation." *Phys. Rev. A* **1985**, *31*(6): 3761-3774.

52. Horak, E. H., Rea, M. T., et al., "Exploring Electronic Structure and Order in Polymers via Single-Particle Microresonator Spectroscopy." *Nano Lett.* **2018**, *18*(3): 1600-1607.

53. Fano, U., "Effects of Configuration Interaction on Intensities and Phase Shifts." *Phys. Rev.* **1961**, *124*(6): 1866-1878.

54. Lin, G., Qian, B., et al., "Excitation mapping of whispering gallery modes in silica microcavities." *Opt. Lett.* **2010**, *35*(4): 583-585.

55. Jackson, J. D., "Classical Electrodynamics (3rd ed.)." **1999** New York, John Wiley & Sons.

56. Vernooy, D. W., Furusawa, A., et al., "Cavity QED with high-Qwhispering gallery modes." *Phys. Rev. A* **1998**, *57*(4): R2293-R2296.

57. Dalton, B. J., Guerra, E. S., et al., "Field quantization in dielectric media and the generalized multipolar Hamiltonian." *Phys. Rev. A* **1996**, *54*(3): 2292-2313.

58. Miroshnichenko, A. E., Flach, S., et al., "Fano resonances in nanoscale structures." *Rev. Mod. Phys.* **2010**, *82*(3): 2257-2298.

59. Juvé, V., Cardinal, M. F., et al., "Size-Dependent Surface Plasmon Resonance Broadening in Nonspherical Nanoparticles: Single Gold Nanorods." *Nano Lett.* **2013**, *13*(5): 2234-2240.

60. Li, Z., Mao, W., et al., "Absorption Spectroscopy of Single Optically Trapped Gold Nanorods." *Nano Lett.* **2015**, *15*(11): 7731-7735.

61. Bender, C. M. and Boettcher, S., "Real Spectra in Non-Hermitian Hamiltonians HavingPTSymmetry." *Phys. Rev. Lett.* **1998**, *80*(24): 5243-5246.

62. Sanvitto, D. and Kéna-Cohen, S., "The road towards polaritonic devices." *Nat. Mater.* **2016**, *15*: 1061-1073.

63. Du, M., Martínez-Martínez, L. A., et al., "Theory for polariton-assisted remote energy transfer." *Chem. Sci.* **2018**, *9*(32): 6659-6669.

64. Greentree, A. D., Tahan, C., et al., "Quantum phase transitions of light." *Nat. Phys.* **2006**, *2*(12): 856-861.

65. Carusotto, I. and Ciuti, C., "Quantum fluids of light." *Rev. Mod. Phys.* **2013**, *85*(1): 299-366.

66. Majumdar, A., Rundquist, A., et al., "Design and analysis of photonic crystal coupled cavity arrays for quantum simulation." *Phys. Rev. B* **2012**, *86*(19): 195312.

67. Kerckhoff, J., Nurdin, H. I., et al., "Designing Quantum Memories with Embedded Control: Photonic Circuits for Autonomous Quantum Error Correction." *Phys. Rev. Lett.* **2010**, *105*(4): 040502.

68. Mabuchi, H., "Nonlinear interferometry approach to photonic sequential logic." *Appl. Phys. Lett.* **2011**, *99*(15): 153103.

69. Almeida, V. R., Barrios, C. A., et al., "All-optical control of light on a silicon chip." *Nature* **2004**, *431*(7012): 1081-1084.

70. Baaske, M. D., Foreman, M. R., et al., "Single-molecule nucleic acid interactions monitored on a label-free microcavity biosensor platform." *Nat. Nanotechnol.* **2014**, *9*: 933.

71. Dantham, V. R., Holler, S., et al., "Label-Free Detection of Single Protein Using a Nanoplasmonic-Photonic Hybrid Microcavity." *Nano Lett.* **2013**, *13*(7): 3347-3351.

72. Heylman, K. D. and Goldsmith, R. H., "Photothermal mapping and free-space laser tuning of toroidal optical microcavities." *Appl. Phys. Lett.* **2013**, *103*(21): 211116.

73. Link, S. and El-Sayed, M. A., "Spectral Properties and Relaxation Dynamics of Surface Plasmon Electronic Oscillations in Gold and Silver Nanodots and Nanorods." *J. Phys. Chem. B* **1999**, *103*(40): 8410-8426.

Chapter 4 Active control of plasmonic-photonic interactions in a microbubble cavity

Main text: Introduction

Tailoring light-matter interactions in resonant photonic structures has attracted tremendous attention recently for applications in cavity-controlled chemistry, quantum information science and sensing. There are multiple ways to achieve this control by either tuning systems' damping rates or coupling strength. Operating a light-matter system at low temperatures may reduce matter's damping rates substantially until they are lower than coupling strength.[1] However, tuning coupling strength is more attractive for photonic applications at room temperature, as demonstrated in exciton-polariton,[2] molecular vibration-polariton,[3] and plasmon-polariton systems,[4] where many molecular or excitonic modes are collectively, coherently coupled to cavity modes. A ultrasmall mode volume shown in plasmonic dimer nanocavity can largely contribute to the increase in coupling strength.[5] Inhomogeneous field distribution in this nanocavity results in multiple coupling regimes in a plasmon-emitter coupled system, from weak-coupling, intermediate-strong to strong-coupling.[6] Unfortunately, the coupling strength cannot be actively modulated in a controllable way because it totally depends on local features in the plasmonic nanostructure. Very few studies have been focused on directly modifying electromagnetic local density of states that are accessible to molecules and nanoparticles. In the

meantime, tailoring couplings at the single-molecule/particle level is meaningful for single-photon nonlinearities and quantum information processing.[7, 8]

Recently, coupled plasmonic-photonic systems have emerged as unique platforms for control of light-matter interactions because they may inherit ultrahigh Q-factor and ultrasmall mode volume from their component cavities, leading to strong Purcell enhancement[9, 10] and retaining near-field properties from the plasmonic component.[11] We have recently demonstrated a new way to pin down all system parameters that govern energy dissipation pathways in a coupled plasmonic-photonic cavity through simultaneous measurement of photothermal absorption and two-sided transmission.[12] Tailoring these system parameters, particularly couplings, are imperative to create a tunable multi-component photonic network for photonic applications in quantum communications and information science. Actively tuning the mode overlap between plasmons and photons would be of significance to understand plasmonic-photonic interactions at the single-particle level and then provide insights into optimal design in coupled systems. However, directly doping a WGM microcavity with plasmonic nanoparticles requires intricate fabrications and lacks the ability of active modulation in mode overlap. Instead, embedding nanoparticles with an index-matching medium promises to directly modify mode overlap in a both reversible and controllable way.

In this work we present a solvent-embedding approach to actively modulate plasmonic-photonic interactions, particularly couplings, in a microbubble cavity (**Figure 4.1**). In addition to altered localized surface plasmon (LSP) parameters, such as a redshift

in plasmon natural resonance and a slight decrease in total damping rate, plasmonic-photonic couplings in different coupled systems respond differently to the change in

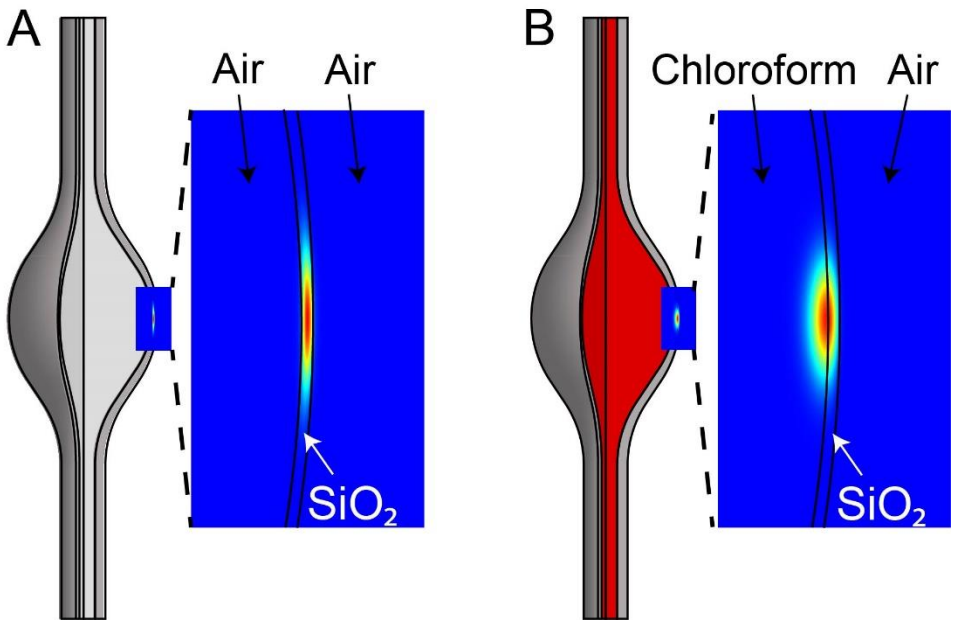

Figure 4.1 Schematic of active control via modifying interior dielectric environment in a microbubble cavity. The microbubble is either filled with air (**A**) or chloroform (**B**) in this work. The zoom-in field intensity profile for a fundamental mode shows a pronounced difference when the interior dielectric constant matches that in SiO_2.

dielectric environment. Our optical simulations agree well with our experimentally determined distribution in coupling strength, showing that both mode volume and mode overlap play important roles in shaping the distributions, where the contribution from an increased mode overlap may be largely counteracted by an increase in mode volume.

Main text: Embedding method

Optical microbubble cavities have been widely used for (bio)sensing,[13-15] lasing,[16] frequency comb generation,[17] and liquid-phase measurements[18] because of its attractive

properties, including ultrahigh Q-factors (~10^7), hollow structure, and subwavelength wall thickness. Recently, this photonic structure has enabled photothermal monitoring of reaction dynamics of gold nanorods in aqueous solution at the single-particle level.[18] An intriguing feature in this cavity is the tunability in mode properties which are highly depending on dielectrics inside and can be elegantly controlled. This tunability may lead to a very high thermo-optic coefficient, a figure of merit for applications in photothermal measurements, due to the large negative thermo-optic response in liquids (e.g., water and organic solvents),[14] while introducing minimal absorption loss to the cavity in visible or telecommunication bands.

In this demonstration chloroform was chosen to fill an ultrahigh-Q microbubble cavity because a chloroform-filled microbubble promises the maximum mode overlap in a plasmonic-photonic coupled system, as shown in **Figure 4.1**. Another consideration is that chloroform minimally absorbs light in both pump (1275-1355 nm) and probe (1550-1570 nm) spectral bands, posing very small loss to the Q-factors. After gold nanorods (AuNRs) were deposited as described previously,[18] remaining aqueous solution was removed and the cavity was flushed by flowing millipore water and then methanol and eventually the cavity was dry (**Method**). This treatment leaves AuNRs being exposed to the air inside the cavity. Single AuNRs were determined using photothermal imaging and polarization measurement. A photothermal map in **Figure 4.2A** shows that a few AuNRs are sparsely distributed in a microbubble cavity, and they are likely to be single nanorods as confirmed by polarization-dependence study. Subsequently, single-particle photothermal absorption spectroscopy was conducted for individual coupled plasmonic-

photonic systems. Upon the introduction of chloroform (**Method**), photothermal imaging (**Figure 4.2**) determines that the spatial location of individual AuNRs under study does not change at all, suggesting that chloroform neither washes away nor translates them. At the same time, polarization-dependence measurements (bottom panel of **Figure 4.2**) demonstrate that AuNRs' orientations don't change either. Both results indicate that introducing chloroform does not impact our coupled systems, rendering the change in spectral behavior solely attributable to the difference in optical modes and therefore different couplings under air-filled and chloroform-filled conditions. In addition to the potential increase in mode overlap, the similar dielectrics between chloroform and silica leads to increasing number of modes in radial direction (**Supporting Information**), adding certain number of whispering gallery modes that may interact with the LSP.

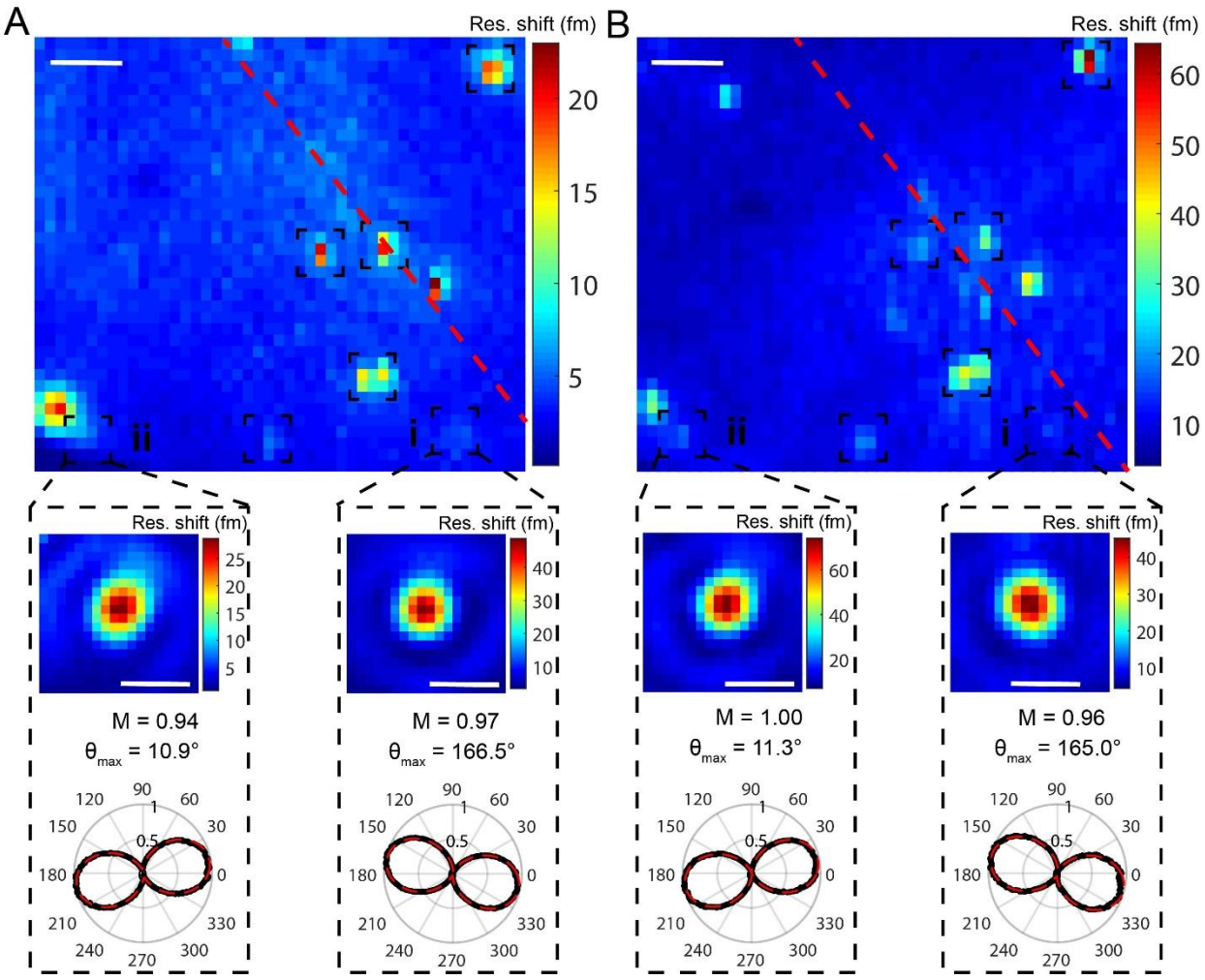

Figure 4.2 Fixation of single AuNRs on the interior surface of the microbubble. Both of spatial locations and orientations are not perturbed by filling the microbubble with chloroform, as evidenced by photothermal coarse (top) and fine (bottom) maps and polarization plots (object i and ii). The polar plots are fitted to $\cos^2(\theta)$ (red dashed line) for determination of the depth of modulation (M) and peak angle (θ_{max}). Each dashed square indicates a single AuNR. The red dashed line shows where the fiber taper is. The scale bars in coarse (fine) maps are 10 μm (2 μm).

Main text: Spectroscopic study

Photothermal absorption spectra at low-resolution, intermediate-resolution, and high-resolution were taken for each single AuNRs as described previously[12] to determine how dielectrics influences spectral signatures and consequently system parameters. The low-resolution spectra that capture LSP resonance demonstrate that plasmon natural frequency for most of single AuNRs under study is beyond our pump spectral band regardless of our chosen dielectrics, although an apparent red shift in LSP resonance is seen in one AuNR-microcavity coupled system (**Supporting Information: Figure 4.13**). The difficulty of determining the existence of the change in LSP resonance by comparing low-resolution spectra under air-filled and chloroform-filled conditions is remedied by our newly developed data fitting strategy (**Supporting Information**). Different from low-resolution spectra, intermediate-resolution spectra contain rich information about the plasmonic-photonic interaction, which is manifested by phenomenologically spectral signature, i.e., Fano antiresonance. The difference in number density of Fano antiresonance shown in intermediate-resolution spectra may imply that distinct dielectrics may exert an effect upon both couplings and mode density of microcavity. **Figure 4.3** shows that in one of AuNR-microcavity coupled system as presented in **Figure 4.2 (**object i**),** Fano number density barely changes (**Figure 4.3A**) upon the introduction of chloroform, whereas a drastic increase in Fano number density is observed in the other coupled system (**Figure 4.3B**). The scarcity of Fano antiresonance seen in this system under air-filled condition might be attributed to the fact that high-order polar WGMs with large mode

volumes (~3000 μm^3) interact with the LSP and the coupling strength is then reduced. When AuNRs are located closer to the center of the microcavity where tapered optical fiber likely resides (**Figure 4.2**), thus LSP may interact with fundamental or low-order polar WGMs and then Fano antiresonance is more likely to be seen unless LSP is orthogonal to transverse-electric polarization of WGMs. The increasing number of WGMs in radial direction, upon the introduction of chloroform, provides the possibility that a better mode overlap may outcompete the effect due to the increase in mode volume. This drastic difference is less seen for those AuNR-microcavity systems where AuNRs are located close to the center of the microcavity.

High-resolution spectra of Fano antiresonance are critical to extract all system parameters. Some of these spectra are shown in **Figure 4.3A** and **Figure 4.3B**, where minor difference in spectral lineshapes is observed between air-filled and chloroform-filled cases. We propose a new fitting method that treats high-resolution and low-resolution

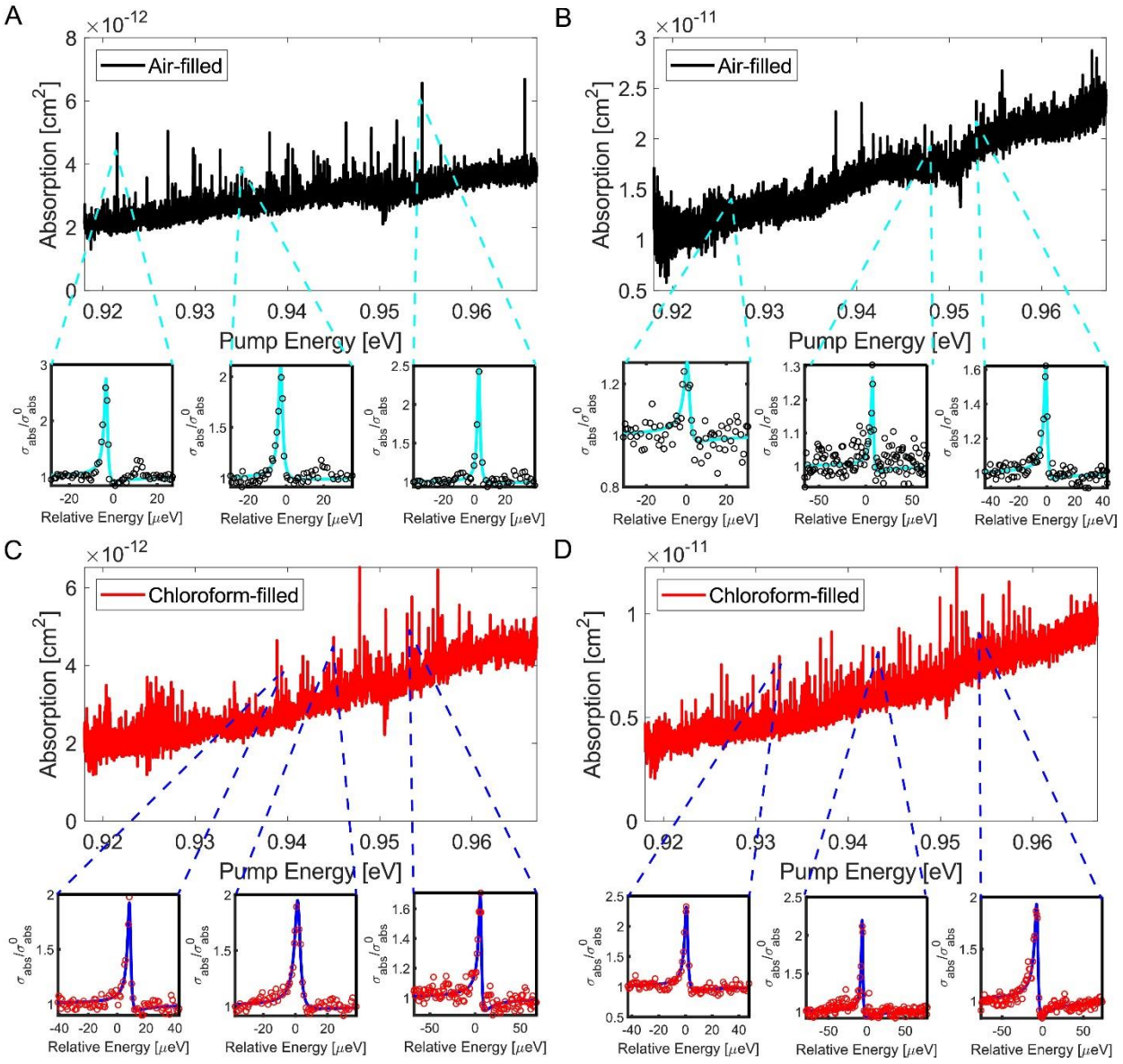

Figure 4.3 Intermediate-resolution and high-resolution absorption spectra of two single AuNRs in the air-filled (**A** and **C**) and chloroform-filled (**B** and **D**) microbubble. The two AuNRs are object i and ii in **Figure 4.2**. Fits (cyan and blue solid curves) to high-resolution spectra (black and red dots) are presented at different spectral locations.

absorption spectra simultaneously. A low-resolution spectrum that was previously used to determine LSP parameters (ω_0, $\gamma_{0,NR}$, $\gamma_{0,Rad}$) is combined with a high-resolution spectrum that contains the information about WGM parameters (ω_1, $\gamma_{1,NR}$, $\gamma_{1,Rad}$) and couplings in addition to LSP parameters. The combined spectra are then fitted to an objective function (G) in equation **4.1** shown below,

$$G(\omega) = \lambda f_1\left(\omega_0, \gamma_{0,NR}, \gamma_{0,Rad}; \omega\right) + f_2\left(\omega_0, \gamma_{0,NR}, \gamma_{0,Rad}, \omega_1, \gamma_{1,NR}, \gamma_{1,Rad}; \omega\right), \qquad 4.1$$

where $f_1 = \frac{4\pi\omega^2\hbar e^2}{cm}\frac{\gamma_{0,NR}}{\left(\omega^2-\omega_0^2\right)^2+\omega^2\gamma_{0,Tot}^2}$, e is the elementary charge, m is the effective mass, $\gamma_{0,Tot} = \gamma_{0,NR} + \gamma_{0,Rad}$, $f_2 = \frac{\sigma_{abs}}{\sigma_{abs}^0} = (1 + \frac{\omega^2 g^2}{\left(\omega^2-\omega_1^2\right)^2+\omega^2\gamma_{1,Tot}^2}\frac{\gamma_{1,NR}}{\gamma_{0,NR}})F(\omega)$, g is the coupling strength, $\gamma_{1,Tot} = \gamma_{1,NR} + \gamma_{1,Rad}$, and $F(\omega)$ is described previously. A global searching algorithm is utilized to minimize fitting error and avoid being trapped in local minima of G (**Supporting Information: Figure 4.9**).

Figure 4.4 presents bar plots of LSP parameters for different AuNRs and the effect of changing dielectrics on them, among which ω_0 and $\gamma_{0,Tot}$ under air-filled and chloroform-filled conditions are compared, respectively. ω_0 decreases in all the coupled systems under study with a difference of up to 70 meV, suggesting that a decrease in dielectric contrast induces a red shift in LSP resonance, which is consistent with the dependence of LSP resonance on dielectric environment commonly seen in literature.[19, 20] However, $\gamma_{0,Tot}$ does not vary significantly although a seemingly decreasing trend is seen in most of the AuNRs under study. Notably, filling the surrounding of plasmonic nanoparticles with water or other liquids may introduce a new channel for interfacial damping (e.g., electron-surface scattering damping[21]) mediated by solvent or solute

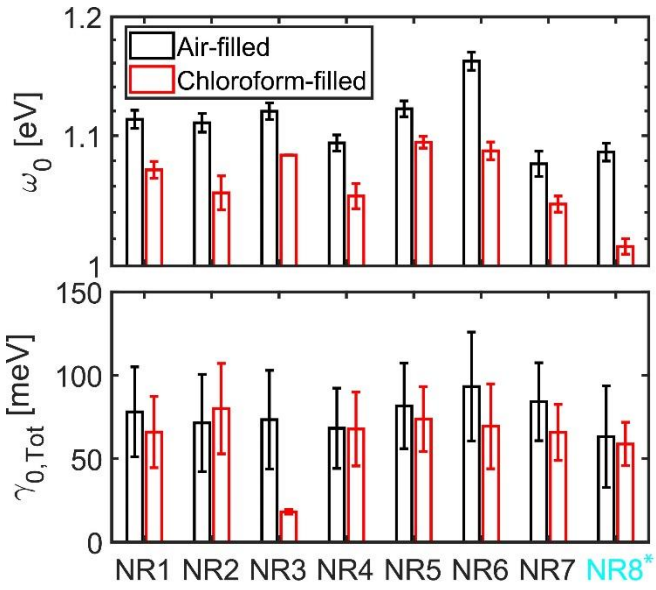

Figure 4.4 LSP parameters determined via simultaneous fits to high-resolution and low-resolution spectra. The y-axis is in log scale (Top panel) for clarity. NR1-7 are single AuNRs studied in one microbubble and NR8 highlighted in cyan is a single AuNR from a different microbubble.

molecules and result in an increase in $\gamma_{0,Tot}$. An enhanced radiative damping due to an increased surrounding dielectric constant can contribute to the increased total damping rates. But this contribution is unlikely in our case because radiative damping in our AuNRs (width: 25 nm, AR: 5) is a minor contributor and this increased radiative damping versus increasing dielectric constant has been typically observed in large nanoparticles.[22] However, the removal of ligands around AuNRs by chloroform likely occurs and therefore reduces interfacial damping caused by the ligands, which may vary from nanorod to nanorod.

Main text: Determining couplings and optical simulations

Our analysis gives rise to a statistical distribution of experimental coupling strength (g) for the interaction between a single LSP and a set of WGMs in each AuNR-microcavity coupled system. g reaches up to 7.5×10^{-4} eV in one of our studied coupled systems (**Supporting Information: Figure 4.11**), which is comparable to our estimated maximum value (6.7×10^{-4} eV) for a fundamental WGM. This value is less than $\gamma_{0,Tot}$ by about two orders of magnitude, confirming that our system still operates in the weak coupling regime even if the maximum mode overlap is achieved. The lowest determined coupling strength is approximately 1.0×10^{-4} eV, which is limited by our signal-to-noise ratio (SNR) in high-resolution spectra. **Figure 4.5A** shows that the distribution profile downshifts under chloroform-filled condition relative to that under air-filled condition in one coupled system (left panel), whereas the other system (right panel) exhibits a upshift. Correspondingly, the mean value of g decreases by a factor of 1.3 upon the introduction of chloroform in

the former system, whereas it increases by a factor of 1.4 in the latter, though the number density of Fano antiresonance under air-filled condition (**Figure 4.3B**) is smaller. Further examination of the rest of AuNR-microcavity coupled systems (**Supporting Information: Figure 4.11**) shows that the distribution profile can upshift, downshift, or barely change when chloroform fills the microbubble. Overall, the mean of g is not seen to change appreciably. Thus, simply comparing the mean of g or distribution profile is not very helpful to decipher the roles mode volume and mode overlap play in affecting g and its statistical distribution.

Thus, numerical optical simulations were conducted to reveal the contributions of mode volume and mode overlap to g. The simulations take into consideration all the WGMs from the eigen solutions regardless of mode volumes in a frequency range that matches our pump band in experiments. In contrast, the high-resolution spectra were measured within several finite spectral ranges of the entire pump band, because both taper-microcavity detachment due to mechanical instability and cavity-laser unlocking may occur during measurements, preventing all Fano signatures available from being completely surveyed. In addition, our SNR may limit only certain number of Fano signatures to be fitted and then analyzed for generating a statistical distribution. With the presence of the two limitations above, we postprocessed our simulated reduced g through both keeping the eigen modes that fall only within the finite spectral ranges and rejecting reduced g below minimum values determined in experiments. The expression of g is described in equation 4.2,

$$g = e\sqrt{\frac{4\pi}{mV}}J, \qquad 4.2$$

where $J = \sqrt{\frac{I(\overrightarrow{r_0})}{\max(I(\overrightarrow{r_0}))}}\cos(\theta)$, $I(\overrightarrow{r_0})$ is the field intensity at $\overrightarrow{r_0}$, and $\cos(\theta)$ determines AuNR's orientation to the transverse-electric polarization of a WGM. In addition to mode volume (V) and mode overlap (J) governed primarily by a specific WGM in the weak coupling regime, it contains an effective mass (m) term that originates from LSP character ($m = \frac{\gamma_{0,Rad}}{\omega_1^2}\frac{3c^3}{2e^2}$). To elucidate the effects of modifying mode volume and mode overlap by introducing chloroform, a reduced form of g ($g/\sqrt{\gamma_{0,Rad}/\omega_1^2}$) is obtained by rearranging equation 4.2 as a function of mode overlap (J), $\sqrt{V}$, and $\cos(\theta)$. J is spatially dependent on where single AuNRs are deposited on the interior surface relative to the equator of the microbubble. Since the mode volume in AuNRs is relatively small compared to that of WGMs in the microbubble, the LSP is treated as a point dipole. When the AuNR is just located in the maximum of field intensity of WGMs, J is equal to 1, i.e., maximum mode overlap is achieved. Otherwise, J decrease rapidly or reach a minimum when the AuNR is in a WGM node. Unfortunately, it is very difficult to precisely locate individual AuNRs on the interior surface relative to the equator of the microbubble. Instead, the interior surface is raster-scanned relative to the equator for each WGM in our simulations to work around this limitation. After applying the two constraints dictated by finite spectral measurement and SNR in experiments to our simulations, a distribution of $g/\sqrt{\gamma_{0,Rad}/\omega_1^2}$

is obtained at individual discrete spatial locations where a nanorod may reside. As shown in **Figure 4.5B** and **Figure 4.5C**, the behavior in the simulated distributions of $g/\sqrt{\gamma_{0,Rad}/\omega_1^2}$ resemble those in experimentally determined distributions for the two AuNRs when chloroform fills the microbubble, when they are simulated at the equator and 20 μm away from the equator along the microbubble stem axis. Simulations for other AuNRs deposited onto the same interior surface of the microbubble also agree well with experimental results at their corresponding locations (**Supporting Information: Figure 4.10**).

We further investigate the distribution of V, J, and $J/\sqrt{V}$ without the two constraints. The distribution profiles of V for air-filled and chloroform-filled microbubble are in two distinctive regimes, as shown in **Figure 4.6A**. In particular, V in chloroform-filled microbubble shows a bimodal distribution, centering at 4500 and 5800 μm^3. The fundamental and a few low-order modes in the chloroform-filled microbubble extend to the low-V area featuring most mode volumes in the air-filled microbubble. Overall, the

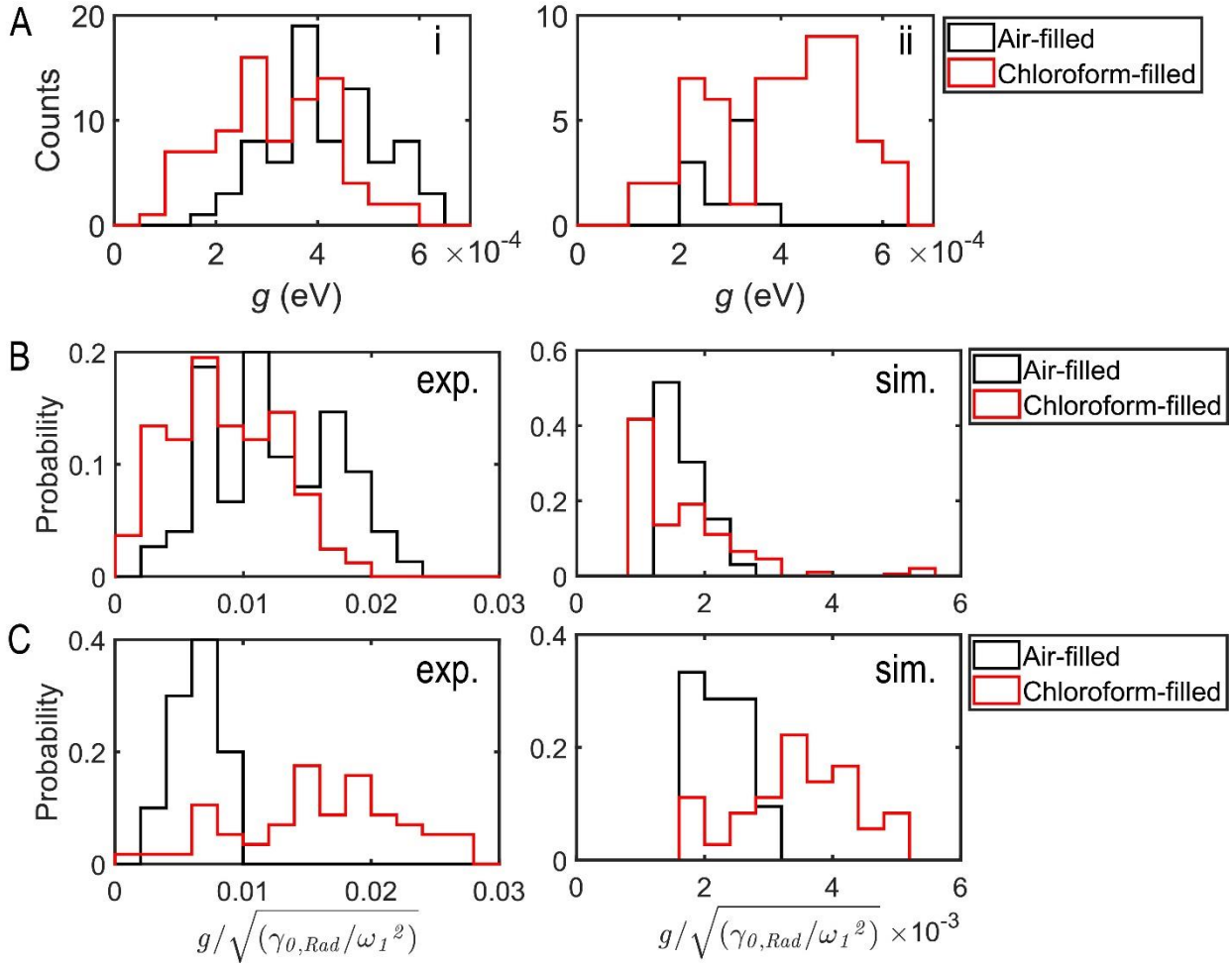

Figure 4.5 Distributions of g determined in experiments for two single AuNRs (**i** and **ii**) (**A**) and comparison of distributions for reduced g ($g/\sqrt{\gamma_{0,Rad}/\omega_1^2}$) between experiment and simulation for AuNR **i** (**B**) and AuNR **ii** (**C**).

mean of V increases by a factor of ~2. The distribution of J spreads more broadly in chloroform-filled microbubble (**Figure 4.6B**), whereas J exhibits a bimodal distribution in air-filled microbubble in which two peaks gradually merge as the spatial location moves away from the equator (Supporting Information). In the meantime, J piles up at the lower bound for both dielectric environments, suggesting plasmonic-photonic interaction would be very weak if a AuNR is far away from the equator. **Figure 4.6C** shows the distribution of $J/\sqrt{V}$, where the profile of air-filled microbubble is also bimodal like J, whereas the distribution gains certain contraction in chloroform-filled microbubble. Thus, the large mode volumes in chloroform-filled microbubble limit the contribution of mode overlap to the coupling strength. Decreasing V significantly while introducing small aggregates of AuNRs may result in a comparable g to $\gamma_{0,Tot}$. Additionally, the angle dependence of g

may be explored through photo-activated rotation of AuNRs to determine how it influences the distribution of g.

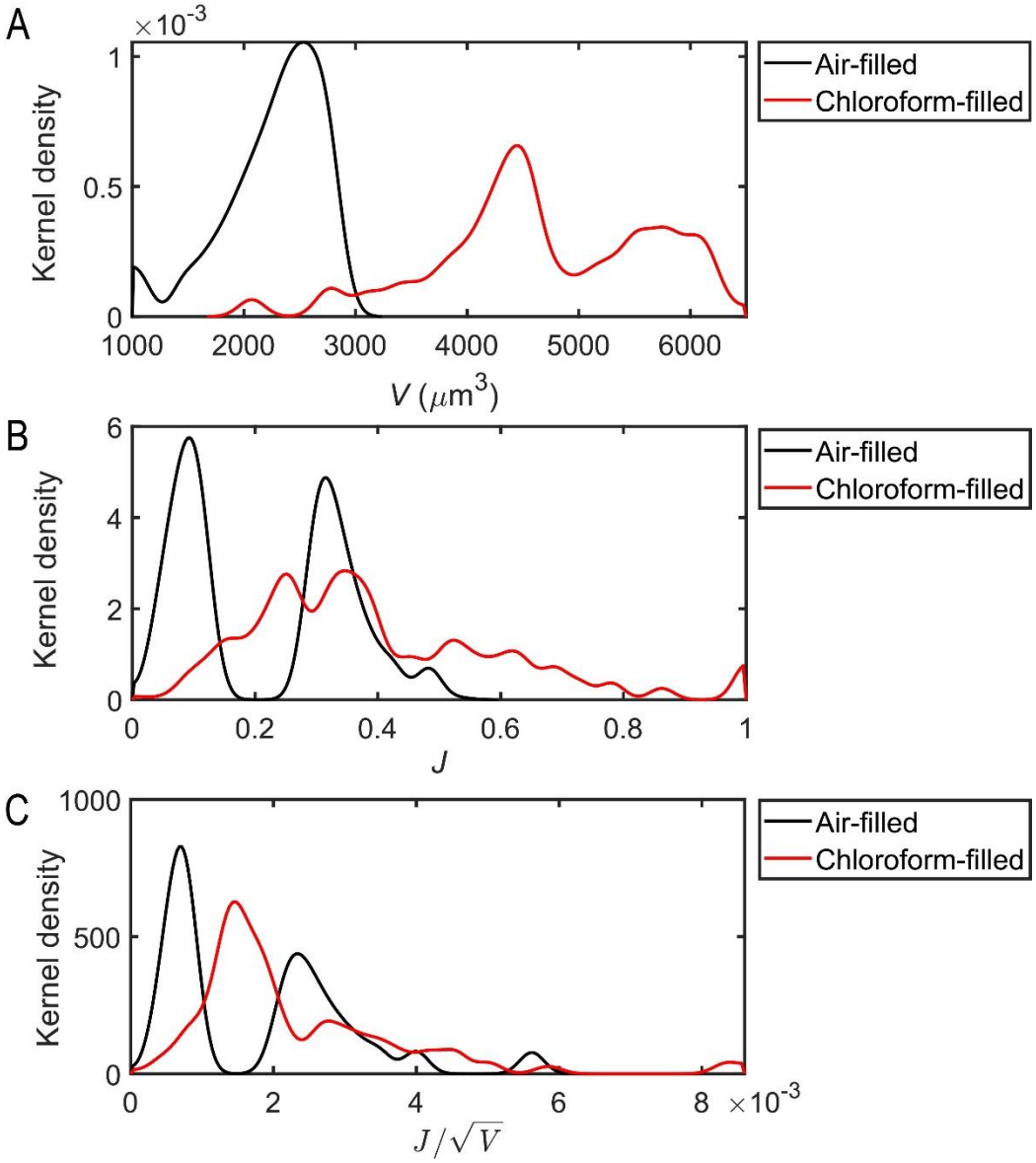

Figure 4.6 Kernel density distributions of V (**A**), J (**B**), and $J/\sqrt{V}$ (**C**). Distributions of J and $J/\sqrt{V}$ are presented only at the spatial location of 0 µm projected along the microbubble stem axis. The values of $J/\sqrt{V}$ are scaled by an implicit factor of 0.693.

Main text: Conclusion

We present a solvent-embedding method to actively control plasmonic-photonic interactions in a microbubble cavity. Changing the dielectric environment by filling the microbubble cavity with chloroform alters the systems parameters, ω_0 and g in particular. Our combined experimental determination and simulation reveal that both mode volume and mode overlap increase as the dielectric contrast decreases, influencing the change in g in a competing manner. Our simulated results agree well with experimentally determined distribution of reduced coupling strength. This agreement implies that spatial locations of AuNRs relative to mode profiles of WGMs may result in distinct distributions of g and LSP interacts with fundamental or low-order WGMs more strongly in chloroform-filled microbubble. The active control of the interaction provides new insight into the design of plasmonic-photonic sensors for biological applications and solution-phase studies. In addition, due to the existence of high-order axial modes in the microbubble cavity, this plasmonic-photonic coupled cavity, if employed with add-drop configuration may be candidate for constructing photonic networks.

Main text: Methods

Sample preparation. Microbubble cavities were fabricated as described previously.[23] The procedure for AuNRs deposition on the interior surface of a microbubble was adapted from the ref.[18] First, a diluted HCl solution (pH = ~1.3) prepared from a concentrated HCl (Sigma-Aldrich, ACS Grade) was flowed from one end of the microbubble using a Luer-Lock syringe assembly until about 10 drops came out from the

other end. Subsequently, a diluted CTAB solution prepared in HCl (100 μM, pH = ~1.3) was flowed in a similar way. The two steps turned the interior surface of the microbubble ready for binding AuNRs. Afterwards, a 250X diluted AuNRs solution was prepared from a stock AuNRs solution (25 × 256 nm^2, Nanopartz A12-25-1064) through a serial dilution using diluted CTAB solution. This diluted AuNRs solution was flowed through the microbubble until about 12 big drops came out. The microbubble was flushed by the diluted CTAB solution (100 μM, pH = ~1.3), diluted HCl (pH = ~1.3), and Millipore water to remove extra unbound AuNRs and excess CTAB. Finally, Millipore water was pushed out from the microbubble and taken away by flushing the microbubble with methanol (HPLC grade) for several minutes. The remaining methanol was removed and then the microbubble was dry overnight under ambient conditions. Regarding filling the microbubble with chloroform, after chloroform (HPLC grade) was flowed through the microbubble for several minutes, the two ends were sealed to retain chloroform inside by dipping them in a degassed sodium silicate solution three times and letting it dry in air.

Spectroscopic measurement. The previously described experimental setup was used to carry out spectroscopic characterization and polarization dependence study.[12, 24] A free-space pump beam is amplitude-modulated at 510 Hz for all the measurements. The resulting photothermal signal is demodulated by a lock-in amplifier (Ametek, Signal Recovery 7265). The absorption cross section shown in this work is obtained by relating the amount of resonance shift to the power absorbed by AuNR through finite-element method simulations in COMSOL Multiphysics. Note that our fitting method for determining

all system parameters is insensitive to exact determination of absorption cross section which is compromised by the difficulty of assigning mode identity in a microbubble cavity.

Optical simulations. All the simulations were run in COMSOL Multiphysics using Oxborrow's method.[25] First, the diameter and length of the microbubble used in experiments were determined from an optical image. And then, the wall thickness was estimated as described previously.[26, 27] These geometric parameters were used to create a model to solve for eigen values. The domain designated for air or chloroform medium has a refractive index of 1.0 or 1.43, respectively, and was updated accordingly. For a given azimuthal mode number, a set of eigen solutions were obtained and then exported along with field intensity data to compute reduced *g*. Note that only transverse-electric polarization modes were kept for further analysis.

Main text: Acknowledgements

We acknowledge support from the National Science Foundation under awards CHE-1836482 (R.H.G.), CHE-1836506 (D.J.M), and CHE-1664684 (D.J.M.). We are also grateful for the help of Paul McGuire from High-Performance Computing at the University of Wisconsin Madison on data analysis. Jonathan Ward is appreciated for helpful discussions.

Supporting information: the effect of changing dielectrics on mode spectrum

The effect of dielectric environment on mode spectrum of the microbubble is investigated by sweeping a probe laser (Newport TLB-6728) from 1550 to 1570 nm that

launches photons to the microbubble via evanescent coupling. The fiber taper is brought in contact with the microbubble to ensure stable coupling while mildly decreasing Q-factors. Afterwards, the taper is detached, and the probe laser is swept again so a mode spectrum can be normalized so that the profile of power spectrum in the probe laser can be removed. The mode spectrum is more congested than that in a microtoroid (**Figure 4.7 bottom panel**), but most of resonances are still well-resolved with Q-factors of 10^6-10^7. A mode spectrum is obtained again when chloroform fills the microbubble. As shown in the middle panel of **Figure 4.7**, the mode spectrum is even more congested, and some resonances have distorted lineshapes. Only a few resonances with Q-factors of middle 10^5 to low 10^6 are suitable for Pound-Drever-Hall locking.

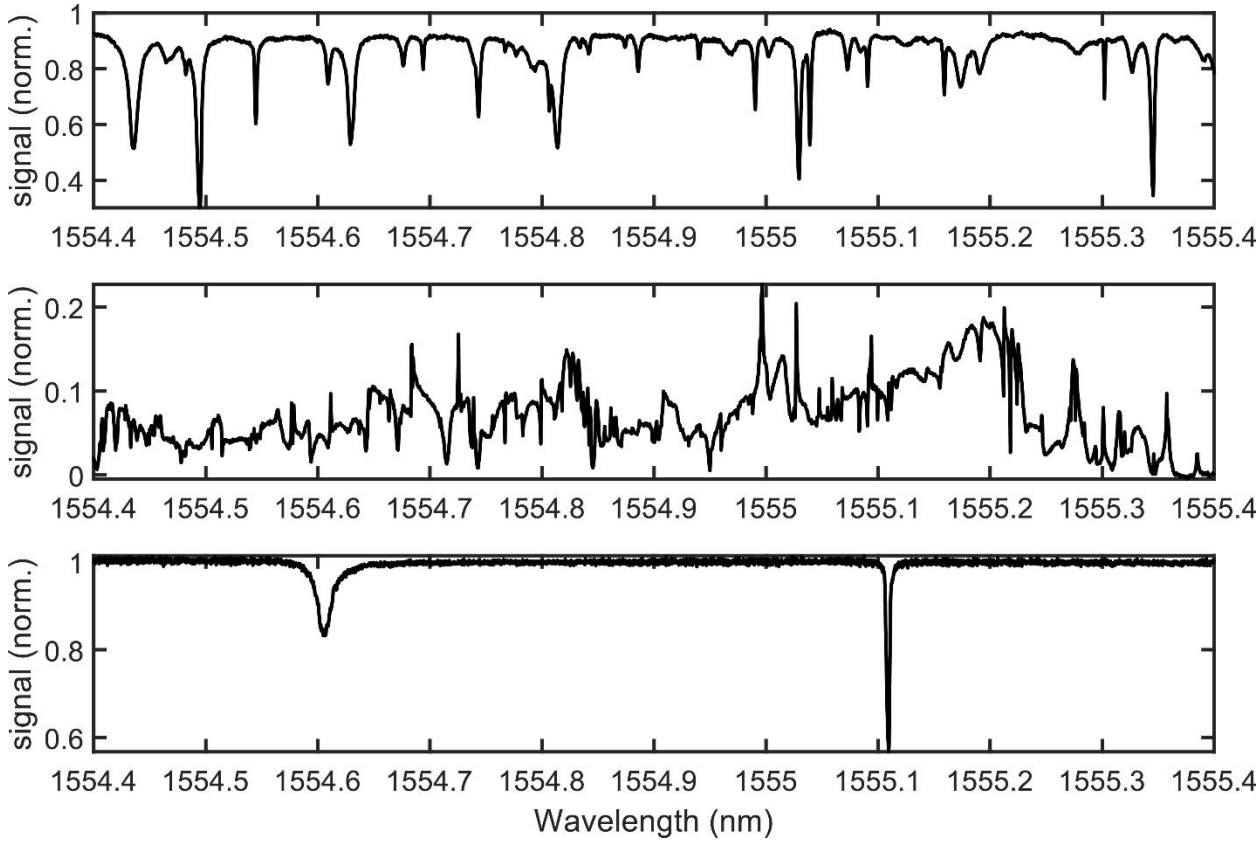

Figure 4.7 Mode spectra obtained for air-filled (**top**) and chloroform-filled (**middle**) microbubble and a microtoroid (**bottom**). The taper was in contact with the microbubble for the measurement of mode spectra in the microbubble, which may result in both strain-induced and absorption loss and consequently a lower baseline than 1. The effect is even pronounced in chloroform-filled microbubble due to absorption loss from bulk chloroform.

Supporting information: Optical images for air-filled and chloroform-filled microbubble

Optical images for air-filled and chloroform-filled microbubble are taken under a 10X objective (Nikon, air, NA = 0.25). Since the very similar refractive index between silica and chloroform results in much less reflection of light at the thin glass wall interface, the profile of chloroform-filled microbubble is easily discerned compared to air-filled

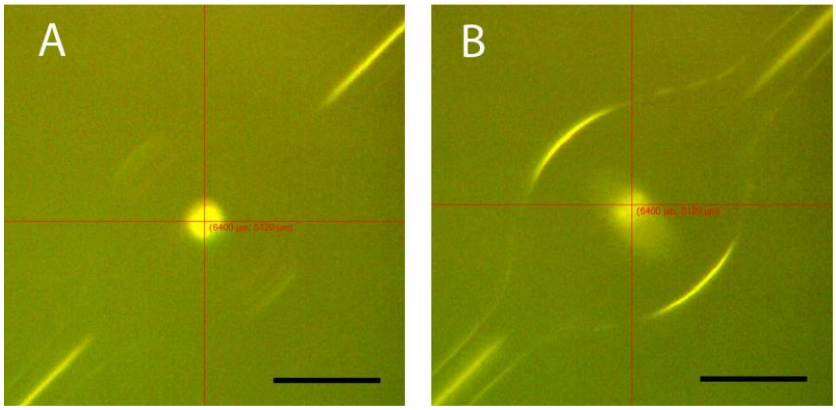

Figure 4.8 Optical images of the microbubble filled with air (**A**) and chloroform (**B**). The scale bar indicates 50 μm. The red cross guides the center of the microbubble.

microbubble (**Figure 4.8**). This striking comparison confirms that chloroform fills the whole microbubble and AuNRs are embedded in this index-matching medium.

Supporting information: Fitting method

Simultaneous fit of low-resolution and high-resolution spectra to equation 4.1 shown in main text is automated on a High-Performance Computing cluster. The weighting factor (λ) spanning from 0.2 to 50 is examined by iterating fitting to a few high-resolution spectra combined with a common low-resolution spectrum. In addition, each fit at a specific λ is iterated 50 times to investigate the robustness. The component fitting errors for low-resolution and high-resolution spectra versus both λ and fit iterations are presented in **Figure 4.9**. The fitting error for low-resolution spectra slows varies when λ is small and then decreases a lot as λ increases up to 50, whereas fitting of a high-resolution spectrum gains a large error. After gauging fitting errors and robustness for both low-resolution and high-resolution spectra, a universal weighting factor of $\lambda = 3$ is

chosen for all the fits. Note that fitting of some high-resolution spectra featuring narrow Fano signature become less robust when $\lambda > 3$.

A global searching algorithm in MATLAB is utilized to avoid trapping in local minima of the potential of the objective function. 3000 initial guesses of fitting parameters with feasible upper and lower bounds are generated from a normal distribution. Since

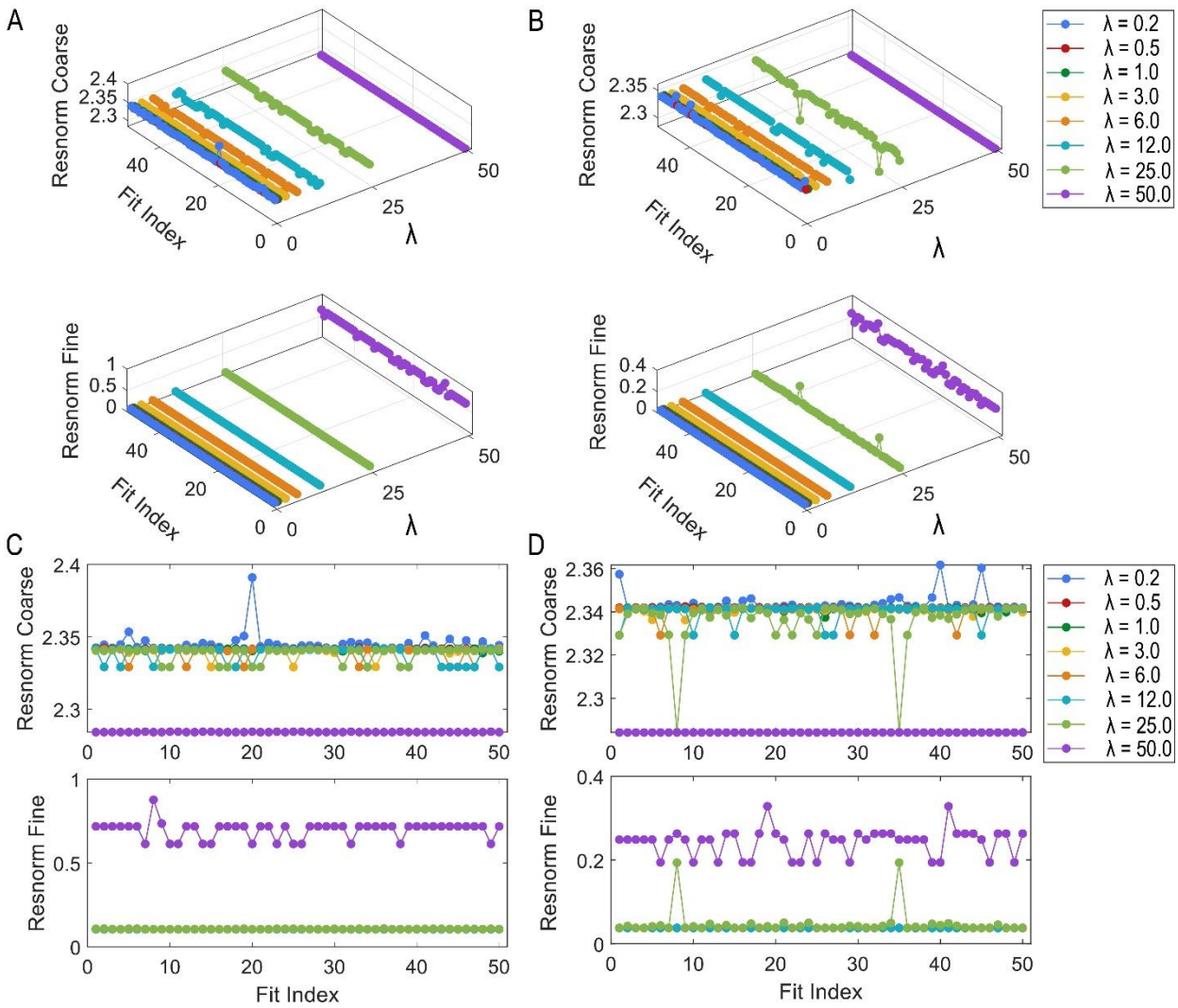

Figure 4.9 Analysis of fitting robustness. Resnorm coarse and fine are squared norm fitting errors obtained from least-square curve fit to low-resolution and high-resolution spectra, respectively. **C** (**D)** shows projected 2D plots from 3D plots in **A** (**B)**.

nonradiative damping is the main contributor to LSP total damping in our AuNRs and our Fano signatures are very narrow ($< 100\ \mu$eV), we apply two constraints to these initial guesses, i.e., $\gamma_{0,NR} > \gamma_{0,Rad}$ and $\hbar(\gamma_{1,NR} + \gamma_{1,Rad}) < 100\ \mu$eV. Afterwards, approximately 1500 guesses remain for fitting. Each fit is iterated 100 times to obtain the best fit with the lowest fitting error.

Supporting information: Optical simulations

The optical simulations presented in main text are carried out in frequency domain via COMSOL Multiphysics package. The microbubble model is constructed based on dimensions acquired from optical images shown in **Figure 4.8**. A weak-form expression method adapted from Oxborrow's model is used to solve for eigen modes at a specific azimuthal mode index. Only eigen frequencies fall within our experimental pump frequency band are retained. Spanning this index results in new sets of eigen values. The upper limit is determined so that the eigen frequency of the fundamental mode just falls within the upper bound of our pump laser frequency band in experiments. There is some uncertainty for defining the low limit because eigen modes with significantly large mode volume may span infinitely across our pump frequency band. The lower limit is obtained when most of eigen frequencies give rise to mode profiles with very large mode volumes. There are a smaller number of eigen modes in air-filled microbubble than that in chloroform-filled microbubble due to the thin glass wall (608 nm). The simulated data are postprocessed by rejecting transvers magnetic modes because they weakly interact with

LSP compared transverse electric modes. The two constraints described in main text that inherit experimental limitations are applied to compute reduced coupling strength.

We also compute mode overlap (J) and $J/\sqrt{V}$ without applying the two experimental constraints. In addition to the plots in main text, **Figure 4.10** shows the rest of them obtained at different spatial locations (5, 10 ,15, and 20 μm) that model the projected position of AuNRs on the interior surface along the microbubble stem axis.

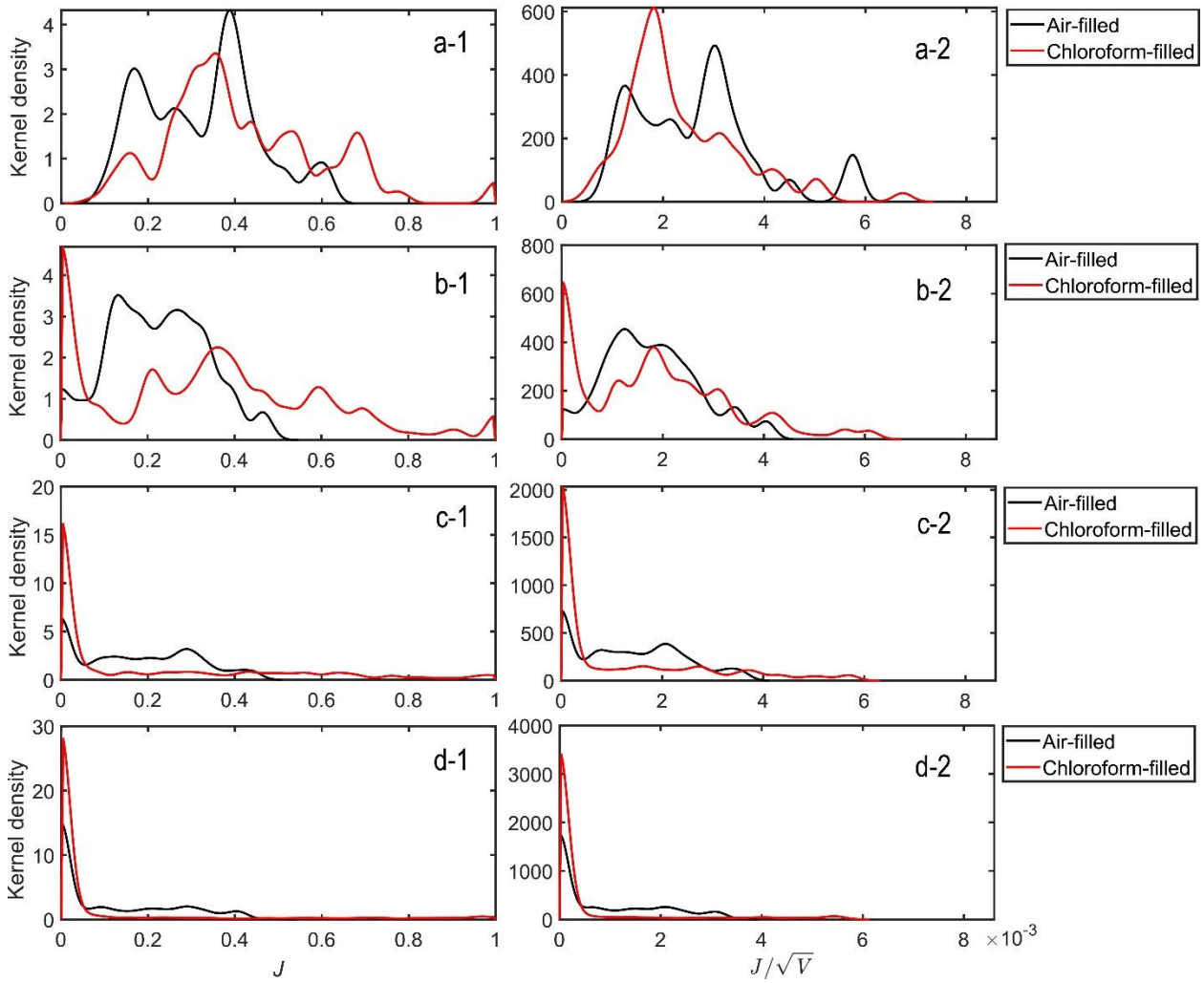

Figure 4.10 Kernel density plots of J and $J/\sqrt{V}$ at different simulated spatial locations along the microbubble stem axis. a-1 (a-2): 5 μm; b-1 (b-2): 10 μm; c-1 (c-2): 15 μm; d-1 (d-2): 20 μm.

Supporting information: Other results

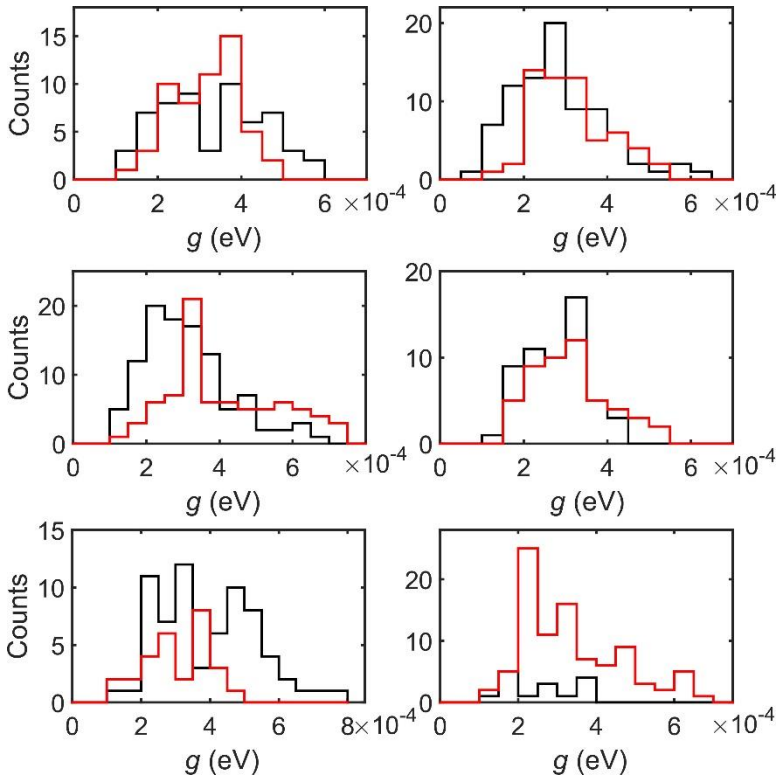

Figure 4.11 Experimentally determined distributions of g for the rest of single AuNRs. Black (red) histograms are obtained for air-filled (chloroform-filled) microbubble.

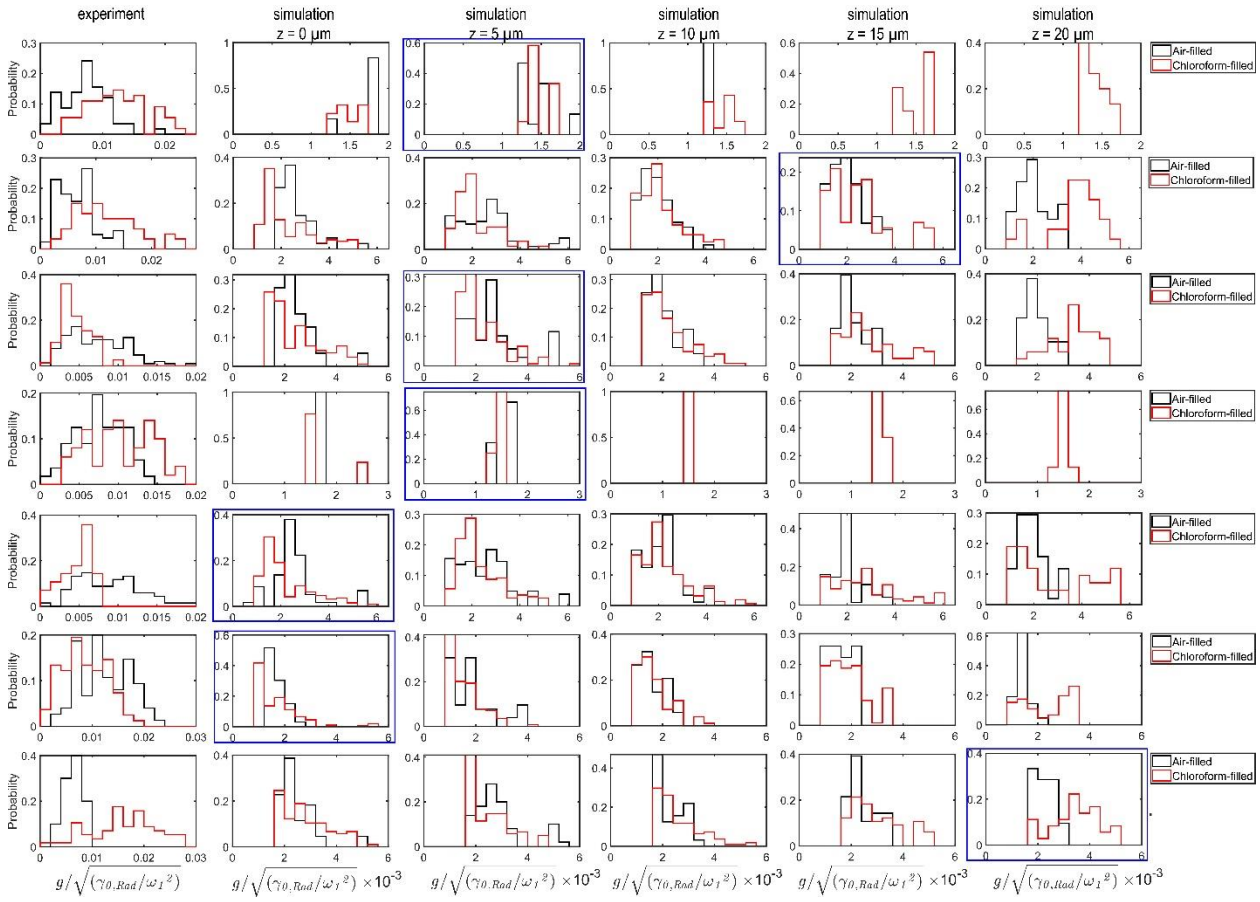

Figure 4.12 Probability distributions of experimental and simulated reduced g ($g/\sqrt{\gamma_{0,\mathrm{Rad}}/\omega_1^2}$) for different AuNRs at different simulated spatial locations along the microbubble stem axis (z: 0, 5 ,10, 15, and 20 µm). The blue rectangles highlight the most similar simulated distributions to experimental ones, respectively.

Table 4.1 Polarization dependence study of single AuNRs. * indicates AuNR associated with plots (object i and ii) shown in **Figure 4.2** and **Figure 4.3**.

	M_{Air}	$M_{Chloroform}$	$\theta_{max,Air}$ (º)	$\theta_{max,Chloroform}$ (º)
NR1	1.00	0.97	143.1	142.0
NR2	0.96	0.99	43.0	42.8
NR3	0.98	1.00	8.0	6.5
NR4	0.98	1.00	143.1	142.6
NR5	1.00	1.00	37.0	36.9
NR6*	0.97	0.96	166.5	165.0
NR7*	0.94	1.00	10.9	11.3

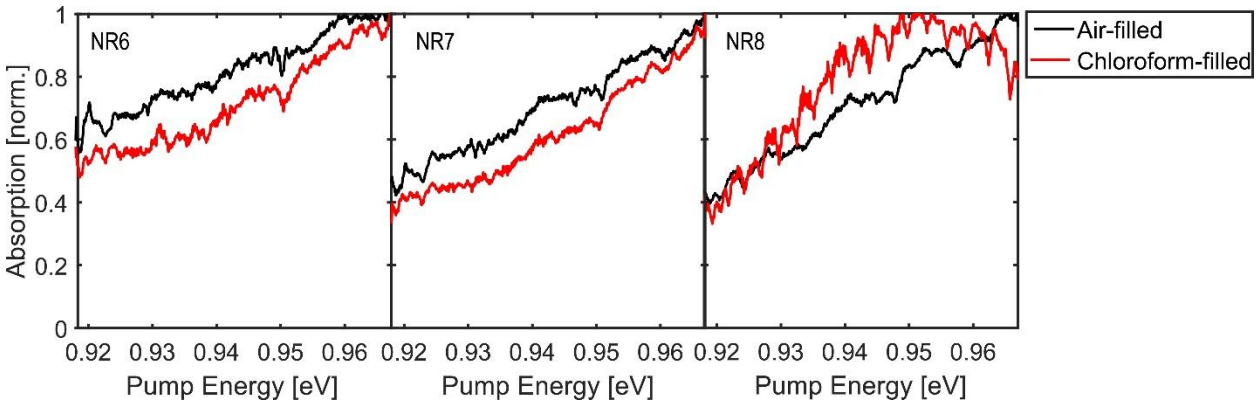

Figure 4.13 Low-resolution absorption spectra of single AuNRs under air-filled or chloroform-filled conditions. NR6 and 7 are object i and ii in **Figure 4.2** and **Figure 4.3**, respectively. NR8 is a single AuNR from a different microbubble.

References

1. Srinivasan, K. and Painter, O., "Linear and nonlinear optical spectroscopy of a strongly coupled microdisk–quantum dot system." *Nature* **2007**, *450*: 862.

2. Lidzey, D. G., Bradley, D. D. C., et al., "Strong exciton–photon coupling in an organic semiconductor microcavity." *Nature* **1998**, *395*(6697): 53-55.

3. Xiang, B., Ribeiro, R. F., et al., "Two-dimensional infrared spectroscopy of vibrational polaritons." *Proceedings of the National Academy of Sciences* **2018**, *115*(19): 4845-4850.

4. Min, B., Ostby, E., et al., "High-Q surface-plasmon-polariton whispering-gallery microcavity." *Nature* **2009**, *457*(7228): 455-458.

5. Santhosh, K., Bitton, O., et al., "Vacuum Rabi splitting in a plasmonic cavity at the single quantum emitter limit." *Nat. Commun.* **2016**, *7*(1): 11823.

6. Leng, H., Szychowski, B., et al., "Strong coupling and induced transparency at room temperature with single quantum dots and gap plasmons." *Nat. Commun.* **2018**, *9*(1): 4012.

7. Wang, D., Kelkar, H., et al., "Turning a molecule into a coherent two-level quantum system." *Nat Phys* **2019**.

8. Pscherer, A., Meierhofer, M., et al., "Single-Molecule Vacuum Rabi Splitting: Four-Wave Mixing and Optical Switching at the Single-Photon Level." *Phys. Rev. Lett.* **2021**, *127*(13): 133603.

9. Palstra Isabelle, M., Doeleman Hugo, M., et al. (**2019**). Hybrid cavity-antenna systems for quantum optics outside the cryostat? Nanophotonics. *8***:** 1513.

10. Doeleman, H. M., Dieleman, C. D., et al., "Observation of Cooperative Purcell Enhancements in Antenna-Cavity Hybrids." *ACS Nano* **2020**.

11. Conteduca, D., Dell'Olio, F., et al., "Rigorous design of an ultra-high Q/V photonic/plasmonic cavity to be used in biosensing applications." *Optics & Laser Technology* **2016**, *77*: 151-161.

12. Pan, F., Smith, K. C., et al., "Elucidating Energy Pathways through Simultaneous Measurement of Absorption and Transmission in a Coupled Plasmonic–Photonic Cavity." *Nano Lett.* **2020**, *20*(1): 50-58.

13. Yu, X.-C., Tang, S.-J., et al., "Single-molecule optofluidic microsensor with interface whispering gallery modes." *Proceedings of the National Academy of Sciences* **2022**, *119*(6): e2108678119.

14. Ward, J., Yang, Y., et al., "Liquid core microbubble resonators for highly sensitive temperature sensing." **2014**, SPIE.

15. Yang, Y., Ward, J., et al., "Optimization of whispering gallery modes in microbubble resonators for sensing applications." **2014**, SPIE.

16. Yang, Y., Lei, F., et al., "Tunable erbium-doped microbubble laser fabricated by sol-gel coating." *Opt. Express* **2017**, *25*(2): 1308-1313.

17. Yang, Y., Jiang, X., et al., "Four-wave mixing parametric oscillation and frequency comb generation at visible wavelengths in a silica microbubble resonator." *Opt. Lett.* **2016**, *41*(22): 5266-5269.

18. Hogan, L. T., Horak, E. H., et al., "Toward Real-Time Monitoring and Control of Single Nanoparticle Properties with a Microbubble Resonator Spectrometer." *ACS Nano* **2019**, *13*(11): 12743-12757.

19. Kelly, K. L., Coronado, E., et al., "The Optical Properties of Metal Nanoparticles: The Influence of Size, Shape, and Dielectric Environment." *J. Phys. Chem. B* **2003**, *107*(3): 668-677.

20. Hu, M., Novo, C., et al., "Dark-field microscopy studies of single metal nanoparticles: understanding the factors that influence the linewidth of the localized surface plasmon resonance." *J. Mater. Chem.* **2008**, *18*(17): 1949-1960.

21. Grigorchuk, N. I., "Radiative damping of surface plasmon resonance in spheroidal metallic nanoparticle embedded in a dielectric medium." *J. Opt. Soc. Am. B* **2012**, *29*(12): 3404-3411.

22. Hu, M., Chen, J., et al., "Correlated Rayleigh Scattering Spectroscopy and Scanning Electron Microscopy Studies of Au−Ag Bimetallic Nanoboxes and Nanocages." *J. Phys. Chem. C* **2007**, *111*(34): 12558-12565.

23. Yang, Y., Saurabh, S., et al., "High-Q, ultrathin-walled microbubble resonator for aerostatic pressure sensing." *Opt. Express* **2016**, *24*(1): 294-299.

24. Heylman, K. D., Thakkar, N., et al., "Optical microresonators as single-particle absorption spectrometers." *Nat. Photonics* **2016**, *10*: 788-795.

25. Oxborrow, M., "Traceable 2-D Finite-Element Simulation of the Whispering-Gallery Modes of Axisymmetric Electromagnetic Resonators." *IEEE Trans. Microwave Theory Tech.* **2007**, *55*(6): 1209-1218.

26. Henze, R., Seifert, T., et al., "Tuning whispering gallery modes using internal aerostatic pressure." *Opt. Lett.* **2011**, *36*(23): 4536-4538.

27. Cosci, A., Quercioli, F., et al., "Confocal reflectance microscopy for determination of microbubble resonator thickness." *Opt. Express* **2015**, *23*(13): 16693-16701.

Chapter 5 Single-particle photothermal imaging via inverted excitation through high-Q all-glass toroidal microresonators[l]

Main text: Abstract

Whispering-gallery mode (WGM) microresonators have recently been employed as platforms for label-free single-molecule and single-particle detection, imaging, and spectroscopy. However, innovations in device geometry and integration are needed to make WGM microresonators more versatile for biological and chemical applications. Particularly, thick device substrates, originating from wafer-scale fabrication processing, prevent convenient optical interrogation. In this work, we fabricate all-glass toroidal microresonators on a coverslip thickness (~170 μm) substrate, enabling excitation delivery through the sample, simplifying optical integration. Further, we demonstrate the application of this new geometry for single-particle photothermal imaging. Finally, we discover and develop simulations to explain a non-trivial astigmatism in the point spread function (PSF) arising from the curvature of the resonator.

---

[l] This chapter is adapted from the published manuscript as Knapper, K. A.*, Pan, F.*, et al., "Single-particle photothermal imaging via inverted excitation through high-Q all-glass toroidal microresonators." *Opt. Expr.* **2018**, *26*(19): 25020-25030. * Equal co-first authorship.

Main text: Introduction

Label-free measurements at the single-molecule and single-particle level can provide a powerful approach for understanding the dynamics and properties of biomolecules, catalysts, and nanomaterials by obviating the need for labelling, thus opening new targets to spectroscopic interrogation. Most single-molecule and single-particle measurements are based on photoluminescence (including fluorescence) [1], and while these methods are ideal when the target is emissive, new methods are required to study non-emissive targets, which comprise the vast majority of targets of interest.

A handful of room-temperature, label-free single-molecule and single-particle imaging experiments have been conducted using direct transmission [2-4], scattering [5] and ground state depletion [6], but robust application of these techniques remains a challenge. Photothermal techniques have been applied to indirectly measure the absorption of individual molecules [7, 8] and particles [9-12]. Detection of individual molecules in these experiments required signal enhancement from glycerol [7], a medium with a very high thermo-optic coefficient, with alternative media such as liquid crystals [10, 11] and super-critical xenon [13] providing even greater amplification. Alternatively, minute optical signals from single molecules or single particles can be amplified through micro and nanophotonic mechanisms. In particular, whispering gallery mode (WGM) resonators have been shown to be a powerful platform for label-free sensing [14-16], reaching the limit of detection of individual particles [17-22], viruses [17, 19, 23], proteins [24, 25], small molecules [26], and ions [27]. However, much of this work focuses solely on detection: adding in the

capacity for microscopy and spectroscopy opens a path toward the more powerful capabilities of identification and characterization of detected species.

We recently described a method for conducting single-particle absorption spectroscopy using a toroidal microresonator as the heart of the spectrometer [28]. The technique takes advantage of the phenomenal sensitivity of the resonator to small thermal changes in its local environment, even to the level of heat dissipated from a single nano-object upon photoexcitation [28, 29]. The microtoroid itself can be fabricated from silica on a silicon pillar and substrate [30], or it can be composed entirely of silica, an all-glass microtoroid [31], as seen in the scanning electron micrograph (SEM) in **Figure 5.1a**. To interrogate the resonator's local environment (**Figure 5.1d**) light from a tunable, communication-band laser is coupled to the resonator using a tapered optical fiber at specific resonant wavelengths which are a function of the refractive index of the material of the resonator [28, 31]. The refractive index of the toroid depends on the local temperature through the thermo-optic coefficient [32], such that temperature changes in the local environment shift the resonant wavelength, which is measured using the coupled tapered optical fiber. To perform imaging and spectroscopy, a second focused free-space beam excites nano-objects on the surface of the resonator, which dissipate heat upon relaxing from the excited state, shifting the resonance [29]. The pump beam can be scanned across the surface of the resonator to photothermally generate images [29, 31], tuned in wavelength to generate absorption spectra [28, 33, 34], and rotated in polarization direction to assess the polarization dependence and molecular ordering in single nano-objects [28, 34]. Pound-Drever-Hall (PDH) locking [35-38] of the probe beam to the resonance wavelength, while

amplitude modulating the pump beam, allows use of lock-in amplification. With this double modulation scheme, we achieve sensitivity down to a single attometer of resonant wavelength shift [28] and have used this technology to investigate the effect of successive morphological changes of gold nanorods in hybrid photonic-plasmonic systems [33] as well as the electronic properties and ordering of single conducting polymers [34]. Though the demonstrated responsivity of the toroidal microresonator spectrometer is more than sufficient to measure the shift from a single molecule [28], the photothermal background from the silicon pillar limits sensitivity in the visible region. This background can be reduced by using all-glass toroids for measurements in the visible region [31].

Main text: Fabrication and imaging setup

Even with these advancements, there are still barriers to robust application of our photothermal absorption spectrometer to a more complex condensed phase environment. One of the main challenges is the current, top-down geometry of the pump excitation delivery, where a fiber taper and high numerical aperture (NA) objective must be integrated in close proximity to the resonator, complicating device integration. Furthermore, delivering the pump beam through liquid can significantly distort the beam, and while water dipping objectives can be used, they are susceptible to fouling. An alternative geometry (**Figure 5.1d** and **Figure 5.1e**) delivering the pump excitation from the backside of the resonator, would eliminate both issues, as well as potentially allow for improved imaging resolution with the use of a higher NA oil immersion objective for pump delivery, and more convenient integration with microfluidics for sensing applications.

Backside excitation, however, is incompatible with the current all-glass toroid device chips because the substrate is substantially thicker (wafer thickness ~ 450 μm) than the working distance of typical high NA objectives. To address this issue, we have developed an all-glass toroidal microresonator on a coverslip-thickness (~170 μm) substrate (**Figure 5.1b**) and have demonstrated its use by photothermally imaging gold nanorods (AuNRs) using inverted excitation, with favorable comparison to our original geometry. We observe non-trivial alterations to the point spread function (PSF) due to the curvature of the resonator and can explain the origin of these effects using numerical simulations.

All-glass toroids were fabricated on standard thickness (~450 μm) quartz wafers according to a previously published procedure [31] and imaged via SEM (**Figure 5.1a**). Following furnace reflow, the device chips were polished from the underside of the substrate via chemical mechanical planarization (CMP) to a standard coverslip thickness of ~170 μm with an optical quality surface roughness (**Figure 5.1b**). Initial attempts to fabricate thin substrate all-glass toroids involved applying our all-glass toroid fabrication

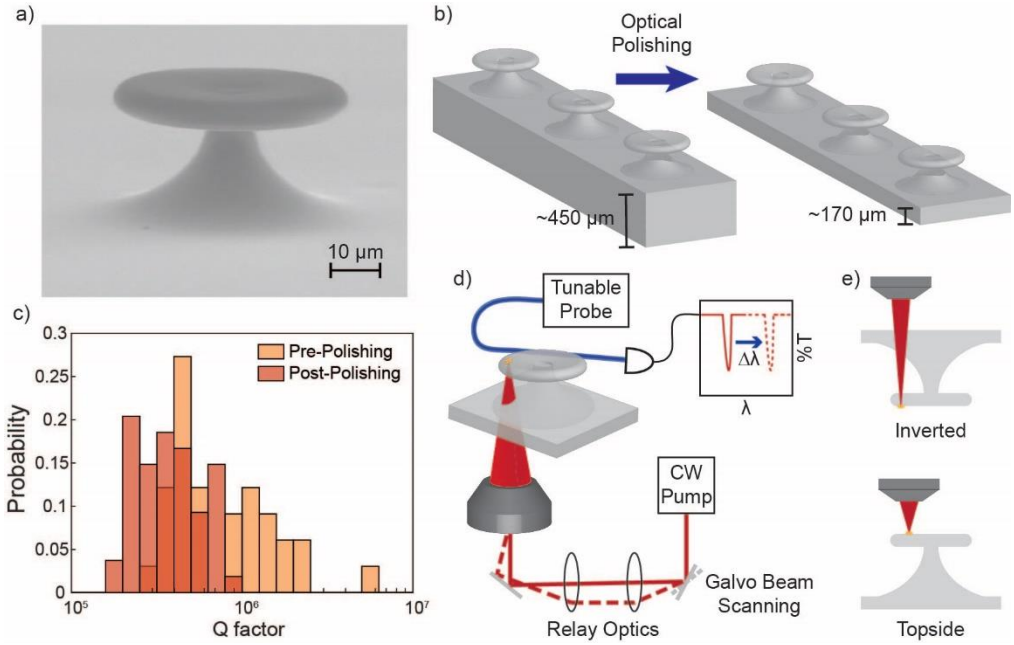

Figure 5.1 Imaging via inverted excitation with thin-substrate toroidal microresonators. (**a**) SEM image of an all-glass toroid. (**b**) Schematic of optical polishing. Device chips are secured from the front side and material is removed from the back via polishing until the substrate thickness is ~170 μm. (**c**) Comparison of toroid Q factors before and after polishing. A total of 87 resonances were measured: 33 resonances before polishing and 54 after polishing. (**d**) Integration of thin substrate toroids into photothermal imaging setup. Pump beam is delivered through the substrate and focused onto the toroid. Pump wavelength is 638 nm. (**e**) Schematic indicating the orientation differences between topside and inverted imaging.

scheme to coverslip thickness wafers, but this strategy was frustrated by stressed thermal expansion at the oxidation step and not pursued further.

Backside polishing requires securing the chip on the device side. To protect the resonators from damage during polishing, the chip was secured to the polisher with a thick coat of beeswax. Quality (Q) factors of toroids from polished chips were compared to those from pre-polished chips to assess whether damage to the resonators occurred during protection, deprotection, or other steps in the polishing process (**Figure 5.1c**). Pre-polished toroids had an average Q factor of 8.1×10^5 with highest Qs reaching mid-10^6. The average Q factor dropped to 4.1×10^5 after polishing, with the highest Q values reaching high-10^5, marking a tolerable decrease of approximately 50%, while successfully producing high-Q all-glass resonators on thin substrates suitable for imaging experiments. Conceptually, our work builds on other attempts to place high-Q resonators in more versatile geometries, including fabrication of toroids from organic [39] and biological materials [40, 41], free toroids [42], and transfer of resonators to flexible substrates [43].

Main text: Single-particle photothermal imaging

AuNRs were used as targets to test the capabilities of inverted imaging through thin substrate all-glass toroids (**Figure 5.1d** and **Figure 5.1e**). AuNRs were sparsely deposited via spincoating onto the surface of the microtoroid. Photothermal images were taken with topside and inverted excitation (**Figure 5.1e**). Large-area maps of the entire toroid at coarse resolution (**Figure 5.2**) confirm that objects (either single nanorods or

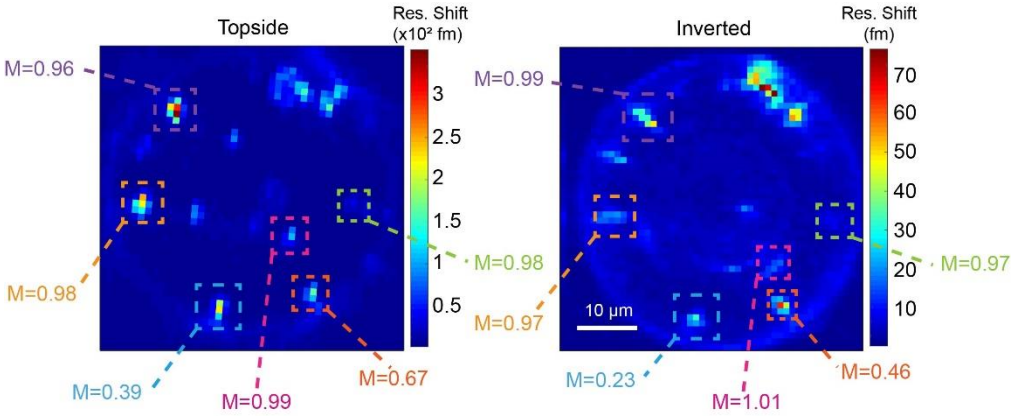

Figure 5.2 Comparison of photothermal imaging via topside and inverted excitation. Whole toroid maps were taken using topside (left) and inverted (right) excitation. Images reveal that nanorods maintain the same position on the toroid between the two excitation geometries, though variations in PSF size can manifest as minor shifts in the apparent position. The polarization dependence of the nanorods is also maintained. Modulation depths are given for the same objects for different excitation geometries, and are also largely unchanged. Image size: 50 µm x 50 µm. Topside image was rotated 5° to account for differences in chip placement between experiments.

small clusters) imaged in both modes are found at the same positions on the toroid with similar polarization modulation depth (M), equation 5.1:

$$I = I_{max}[1 - Msin^2(\theta - \theta_{max})]. \qquad 5.1$$

where I is the signal intensity (measured by the resonance shift), I_{max} is the maximum resonance shift, θ is the polarization angle of the incident light, and θ_{max} is the polarization angle of incident light where the maximum resonance shift occurs. High M values (near 1) indicate the presence of a single absorbing dipole, which suggests the target is likely a single nanorod. Four such cases are displayed in **Figure 5.2** with M values near one, confirming our ability to image single-particles with inverted excitation using thin-substrate all-glass toroids.

Main text: Low-resolution PSF characterization

Further investigation of single objects revealed an unexpected evolution of the PSF as a function of focal depth (**Figure 5.3**). Instead of observing a PSF that is radially symmetric about the object, spreads evenly, and decreases in intensity as the object is moved out of focus—as is normally observed in the planar imaging system that defines the usual topside excitation—the PSF acquired with inverted excitation was stretched in one way below the focus and stretched perpendicular to that above the focus (**Figure 5.3**). PSF stretching indicates the presence of astigmatism in the imaging optics, commonly observed in optical systems that are asymmetric around the optical axis [44-46]. However, the PSF stretching in our case occurs with radial symmetry around the resonator, as opposed to being along a fixed laboratory frame, as is typically observed with astigmatism originating from the microscope imaging optics. This feature, with

elongation direction dependent on the object's position on the microresonator, strongly suggests a role of the toroid itself in the imaging system.

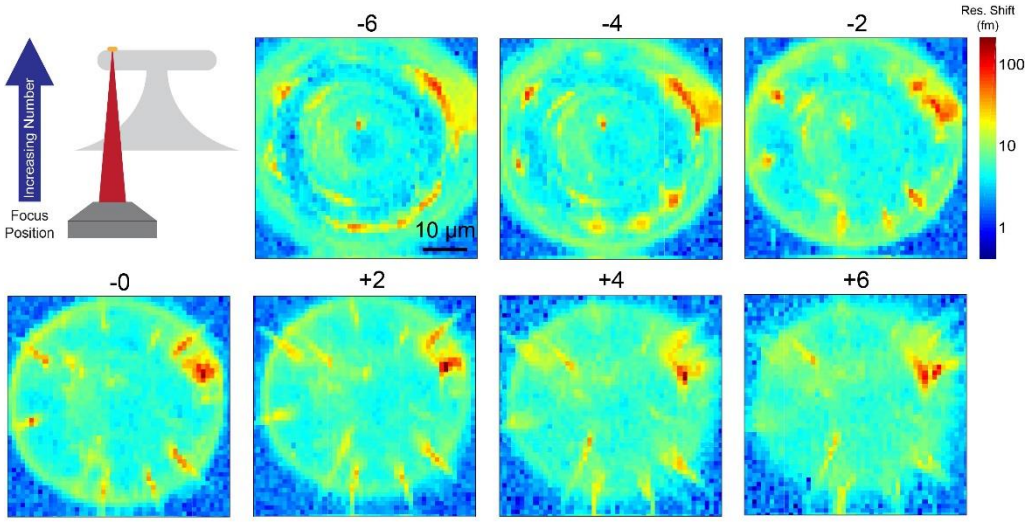

Figure 5.3 Focus progression of PSFs in whole toroid images. Whole toroid maps were taken on the same toroid at different objective positions. Increasing number indicates that the objective focus is moving toward the resonator with steps in units of µm. Image size: 50 µm x 50 µm.

Main text: Single nanorod PSF characterization

To better characterize the evolution of the astigmatism in the PSFs, individual nanorods were imaged at different focal positions by finely tuning the position of the objective along the optical axis using a piezo focus scanner (Mad City Labs, Nano-F100S). Additionally, photothermal images of AuNRs located at different radial positions on the surface of the toroid were taken to assess the impact of the changing pillar and rim curvature of the toroid on the PSF. Conspicuously, the PSF evolution is highly dependent on the nanorod's radial position on the resonator, with the beam distortion being more pronounced at positions near the rim and over the curved portion of the pillar, and virtually absent in the center of the toroid. Three representative sequences of finely resolved maps

provide snapshots of PSF evolution (**Figure 5.4**). The range captures the transition of the PSFs from being stretched in the direction parallel to the rim of the toroid to being stretched in the perpendicular direction, as observed in the large area maps. The object images sometimes reveal the presence of two “foci,” where each object shows two distinct signal intensity maxima as a function of the position on the optical axis (**Figure 5.4b**), further confirming astigmatism in the imaging system. Objects in the center of the toroid

exhibit minimal distortion of the PSF with focus, similar to those in planar optical systems (**Figure 5.4c**).

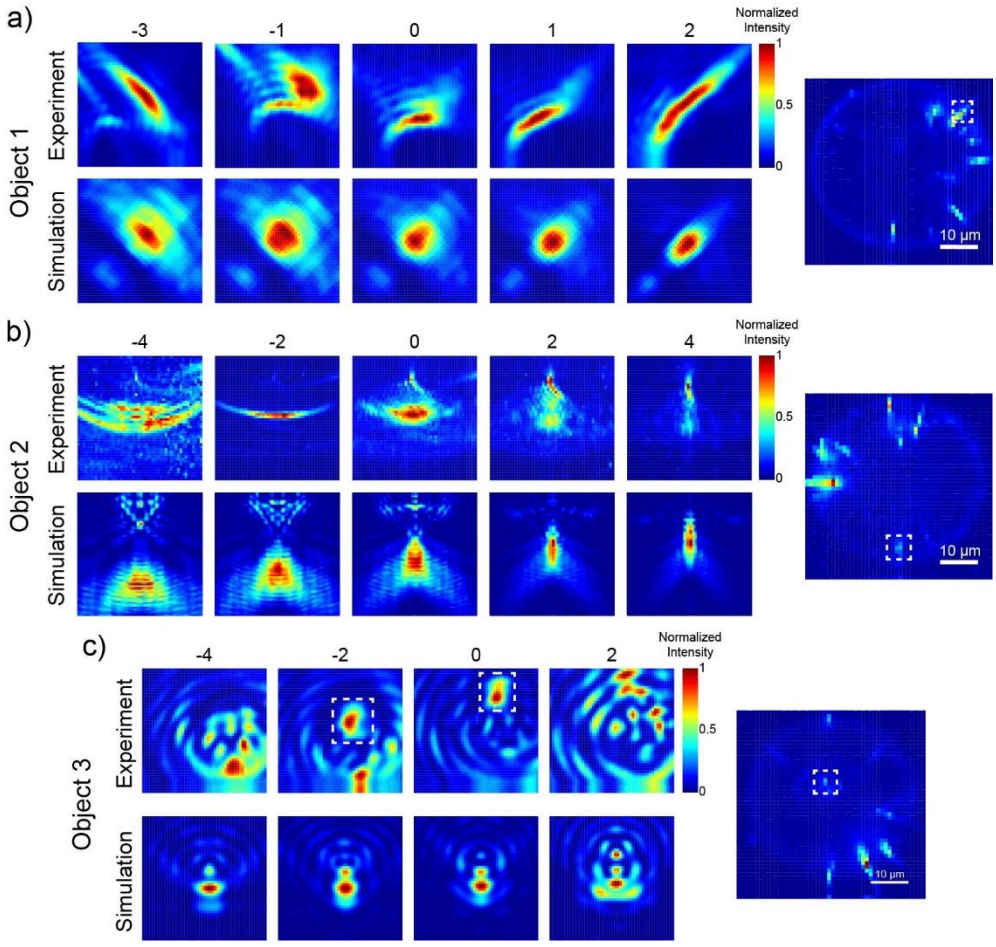

Figure 5.4 Experimental and simulated PSF evolution of single nanorods. A sequence of fine resolution images was taken at different objective positions along the optical axis. Two objects, with different positions relative to the toroid center, are displayed. The images are normalized with respect to their own maximum intensity for clarity and comparison. The M values of objects 1, 2 and 3 are 0.97, 0.95 and 0.97, respectively. The image sizes for object 1 and 3 are 5 μm x 5 μm, and for object 2, 12.5 μm x 12.5 μm. At right, whole toroid scans are shown to indicate object position. Note: PSF position changes in Object 3 (indicated by dashed white box) are due to taper drift over the course of the experiment.

Main text: Simulated ray-tracing analysis of astigmatism

The observed astigmatism and location-dependent PSF evolution can be attributed to the non-trivial geometry of the toroid pillar and rim. Rays propagate from the objective through the substrate, pillar, air, and disc to a tightly focused spot at the nanorod. The pillar and rim asymmetrically refract rays, resulting in differences in the beam profile at different radial positions of the toroid. To better understand the contribution of the toroid-induced refraction, we modeled a thin-substrate all-glass toroid via simulated ray-tracing (Zemax 13 Professional) to reproduce the PSFs observed in experiments. To directly model the experiment, a focused beam representing the illumination from the microscope objective would be scanned across the surface of the resonator. However, in this simulation scheme the AuNR would only interact with one point of the PSF. As the beam is scanned, the PSF changes rapidly, requiring many simulations for each beam position with respect to the AuNR. Instead, we employed the well-established and more efficient reverse ray tracing method, where rays are traced in reverse from the absorber to the source [47]. To apply this method, we treat the AuNR as a point source and trace the rays backwards, toward the objective. However, as the precise proprietary optical design of the objective is unknown, we trace rays to a space that is conjugate to the source, instead of through the objective and back to the source itself. In addition, since the microscope objective used in the experiment is corrected for use with a 170 μm thickness coverslip, spherical aberration exists on the objective side of the coverslip that compensates for the spherical aberration introduced by focusing

through the coverslip. To account for these factors, rays are traced backward through the resonator and coverslip, and then forward through the coverslip to the focal point of the objective in the absence of the resonator. The resulting PSF at this conjugate plane is then equivalent to the PSF detected by scanning the beam across the AuNR. A virtual image based on the Huygens PSF calculation was generated to produce a PSF that includes the effect of diffraction [48]. The distance between the stop plane and the conjugate image plane was tuned to mimic the location of the objective relative to the sample in experiments, producing a sequence of images varying in focal position on the optical axis.

These images were correlated to photothermal images, as seen in **Figure 5.4**. We see qualitative agreement in the elongation direction of the PSF, in the size of the PSF, and in the presence of lower intensity fringes. Specific to object 2 in **Figure 5.4b**, the simulation also contains the growth of a second, smaller area of high intensity and its eventual merging with the larger spot. This degree of qualitative agreement indicates that our simulation includes the essential details of the experiment: that the astigmatism arises from the toroid, and that our simulation method adequately explains the effect that the toroid curvature has on the PSF.

Though the qualitative trends are well-captured, there are some discrepancies between the experimental and simulated PSFs. The simulation achieves agreement in the elongation direction, however, it fails to produce the extremity of the elongation observed experimentally (**Figure 5.4a** and **Figure 5.4b**). Additionally, the simulated PSFs tend to be more circular than their experimental counterparts. These disagreements likely

arise from discrepancies between the simulated geometry and the physical experiment. Some degree of uncertainty in the resonator shape and dimensions as derived from SEM images, the mesh quality of the toroid model, and deviation of the beam profile from an ideal Gaussian may all be contributors to the observed differences. The dipole transition of the plasmon on the AuNR has a well-defined orientation, and in conjunction with the locally high numerical aperture from the toroid geometry, can also affect the shape of the PSF [49, 50], an effect that was also not included in our analysis. Nonetheless, as a qualitative model, our simulation demonstrates the essential experimental features, allowing additional analysis.

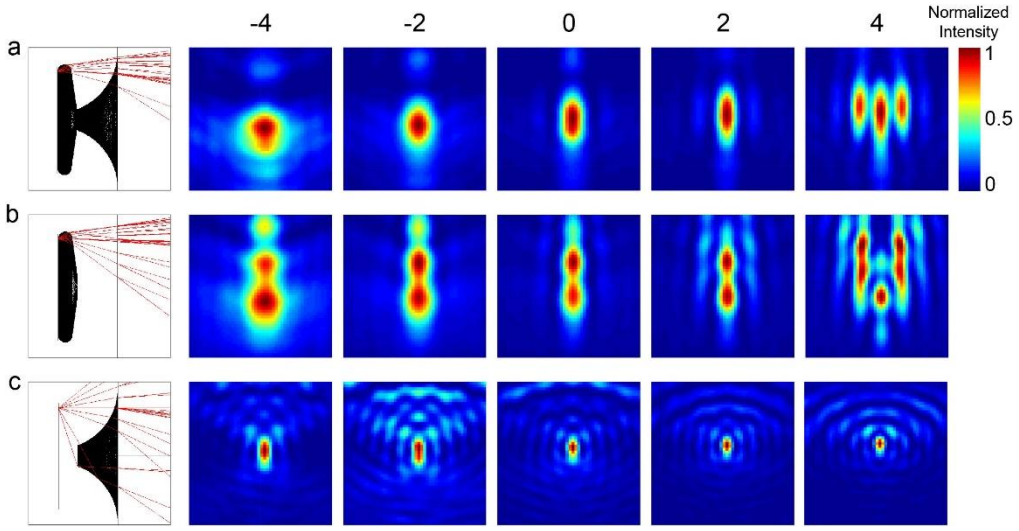

Figure 5.5 PSF evolution as a function of toroid component. Ray tracing simulations were performed for an object on the rim for a) complete toroid model, b) disc-only model, and c) pillar-only model. The focal position interval (columns) is 2 μm. The image size is 5 μm x 5 μm.

Main text: Toroid component analysis

Since both the pillar and rim contribute to the evolution of PSFs observed in experiments and simulation, ray-tracing through the pillar and disc separately can provide insight into the role of each element (**Figure 5.5**). The toroid was disassembled into the pillar and disc parts and the simulation was run on each piece. The results suggest that, in general, the rim plays a more significant role in inducing astigmatism than the pillar, because the PSF progression of the disc-only model more closely matches that of the whole toroid model (**Figure 5.5a** and **Figure 5.5b**). However, as the source moves closer to the center of the toroid, the contribution from the rim lessens and the contribution from the pillar becomes more important, as indicated by increasing similarity of the pillar-only PSF progression to the whole toroid PSF progression.

Main text: Conclusion

In summary, we have fabricated high-Q all-glass toroidal microresonators on a coverslip-thickness substrate and demonstrated their successful application for single-particle imaging with the excitation delivered through the substrate. Though astigmatism, arising from the curvature of the toroid, was observed in the imaging train, we present a method for simulating these PSF distortions that qualitatively agrees with the experimental observations. Understanding of the astigmatism induced by complex, asymmetrical structures, like the toroid pillar and rim, gained through our simulations provides insights for potentially correcting the experimental beam profile in future

applications through the insertion of a micro-cylindrical lens [51], aspherical lens [52], or adaptive optics. Further innovation on microresonator materials and geometry will enable microresonator sensing, microscopy, and spectroscopy to be integrated into an increasing number of analytical platforms.

Appendix A: Device fabrication details

All glass toroidal microresonators are fabricated according to published procedure [31]. Briefly, ~1 μm of polysilicon is deposited onto the surface of a quartz wafer via LPCVD (TYSTAR Poly Furnace). Discs in the polysilicon (60 μm) are patterned using photolithograpy and an anisotropic silicon etch (PlasmaTherm 770 ICP, SF_6 / O_2). The pillar is undercut by isotropically etching the quartz wafer using 6:1 BOE (buffered oxide etchant). Polysilicon discs are oxidized to thermal oxide in steam at 1050 °C (MRL Oxidation Furnace), producing an all glass structure. Discs are reflowed to remove residual surface roughness from etching in a high temperature furnace anneal (SentroTech, 1350 °C, 7-hour hold). Following the furnace reflow, device chips were polished from the backside via CMP by Brand Laser Optics (slurry: 500S, Eminess Technologies; Pad: SUBA 500, Eminess Technologies; Strasbaugh Eccentric Polisher).

Appendix B: Gold nanorod deposition and imaging

Toroid chips were rigorously cleaned using a solvent rinse, 10 min oxygen plasma clean (Unaxis 790 RIE, 200 W), and a standard RCA clean (piranha, 100 °C for 15 min;

SC-1, 75 °C for 15 min; SC-2, 75 °C for 15 min) to remove residual contamination from polishing process. AuNRs (40 x 80 nm, SPR: 650 nm, Nanopartz) are diluted 150x in Millipore 18 MΩ water and are deposited via spincoating (60 s at 3000 rpm). Photothermal imaging experiments were conducted with the double modulation technique described previously [28] using a 638 nm free space pump beam (FibreTec II, Blue Sky Research) focused with a Nikon 0.95 NA air objective (CFI Plan Apo Lambda 60x), amplitude modulated at 2.010 kHz, and a fiber coupled tunable probe beam (1520 – 1570 nm, Newport TLB-6728) [31]. The excitation spot size (FWHM) is 560 nm with topside excitation, and 870 nm (rim) or 750 nm (center) with inverted excitation. The incident power of the pump beam at the sample is 270 μW. The probe laser is actively locked to the resonance using PDH locking [28]. For mapping experiments, the PDH error slopes were between 42 V/fm and 94 V/fm, with corresponding Q factors of 2.5×10^5 to 4.5×10^5. The lock-in time constant is 100 ms. Individual nanorods are imaged by scanning the focused pump beam across the surface of the resonator using a gimbal-mounted scanning mirror, located at the conjugate plane of the back aperture of the objective. The polarization is adjusted at the sample using a motorized half-wave plate (AHWP10M-600, Thorlabs) immediately before the objective. Focus progression sequences are taken by tuning the focal position of the microscope with an objective piezo positioner (Nano-F100S, Mad City Labs).

Appendix C: Zemax ray-tracing analysis

A toroidal model was drawn in Solidworks 2017 according to dimensions estimated from SEM images and was imported into Zemax 13 Professional as a non-sequential

component (NSC). Rays are traced from the surface of the toroid at specific radial locations mirroring where the Au nanorods were imaged in experiments and propagated through the toroid and glass substrate. BK7 was chosen as the material of both toroid and substrate. To simplify the ray-tracing and avoid possible aberration correction, no paraxial lenses were used in the optical sequence. Instead, a standard type of stop plane was inserted before the image plane to act as the exit pupil plane. The relative focal position is controlled by tuning the negative thickness of the stop plane. An aperture type of object space NA with a value of 0.95 and a uniform apodization were used along with a telecentric object space. Huygens PSFs were calculated with a pupil sampling of 128 × 128, an image sampling of 256 × 256 and image delta of 0.1. Polarization and centroid options were selected. These settings give rise to images of 25.6 μm × 25.6 μm with a resolution of 0.1 μm. Simulation map intensity was normalized to better reproduce astigmatism as seen in experiments.

Funding

National Science Foundation (NSF) (DBI-1556241, DGE-1256259)

Acknowledgments

The authors would like to acknowledge Brand Laser Optics for CMP polishing of device chips. Device fabrication was carried out at the Wisconsin Center for Applied Microelectronics.

References

1. Moerner, W. E. and Fromm, D. P., "Methods of single-molecule fluorescence spectroscopy and microscopy." *Rev. Sci. Instrum.* **2003**, *74*(8): 3597-3619.

2. Celebrano, M., Kukura, P., et al., "Single-molecule imaging by optical absorption." *Nat. Photonics* **2011**, *5*(2): 95-98.

3. Devadas, M. S., Li, Z. M., et al., "Detection of single gold nanoparticles using spatial modulation spectroscopy implemented with a galvo-scanning mirror system." *Appl. Opt.* **2013**, *52*(32): 7806-7811.

4. Blancon, J. C., Paillet, M., et al., "Direct measurement of the absolute absorption spectrum of individual semiconducting single-wall carbon nanotubes." *Nat. Commun.* **2013**, *4*.

5. Piliarik, M. and Sandoghdar, V., "Direct optical sensing of single unlabelled proteins and super-resolution imaging of their binding sites." *Nat. Commun.* **2014**, *5*: 8.

6. Chong, S. S., Min, W., et al., "Ground-State Depletion Microscopy: Detection Sensitivity of Single-Molecule Optical Absorption at Room Temperature." *J. Phys. Chem. Lett.* **2010**, *1*(23): 3316-3322.

7. Gaiduk, A., Yorulmaz, M., et al., "Room-Temperature Detection of a Single Molecule's Absorption by Photothermal Contrast." *Science* **2010**, *330*(6002): 353-356.

8. Hou, L., Adhikari, S., et al., "Absorption and Quantum Yield of Single Conjugated Polymer Poly 2-methoxy-5-(2-ethylhexyloxy)-1,4-phenylenevinylene (MEH-PPV) Molecules." *Nano Lett.* **2017**, *17*(3): 1575-1581.

9. Yorulmaz, M., Nizzero, S., et al., "Single-Particle Absorption Spectroscopy by Photothermal Contrast." *Nano Lett.* **2015**, *15*(5): 3041-3047.

10. Parra-Vasquez, A. N. G., Oudjedi, L., et al., "Nanoscale Thermotropic Phase Transitions Enhancing Photothermal Microscopy Signals." *J. Phys. Chem. Lett.* **2012**, *3*(10): 1400-1403.

11. Chang, W. S. and Link, S., "Enhancing the Sensitivity of Single-Particle Photothermal Imaging with Thermotropic Liquid Crystals." *J. Phys. Chem. Lett.* **2012**, *3*(10): 1393-1399.

12. Cognet, L., Berciaud, S., et al., "Photothermal methods for single nonluminescent nano-objects." *Anal. Chem.* **2008**, *80*(7): 2288-2294.

13. Ding, T. N. X., Hou, L., et al., "Hundreds-fold Sensitivity Enhancement of Photothermal Microscopy in Near-Critical Xenon." *J. Phys. Chem. Lett.* **2016**, *7*(13): 2524-2529.

14. Foreman, M. R., Swaim, J. D., et al., "Whispering gallery mode sensors." *Advances in Optics and Photonics* **2015**, *7*(2): 168-240.

15. Heylman, K. D., Knapper, K. A., et al., "Optical Microresonators for Sensing and Transduction: A Materials Perspective." *Advanced Materials* **2017**, *29*(30).

16. Wade, J. H. and Bailey, R. C., "Applications of Optical Microcavity Resonators in Analytical Chemistry." *Annu. Rev. Anal. Chem.* **2016**, *9*: 1-25.

17. He, L. N., Ozdemir, K., et al., "Detecting single viruses and nanoparticles using whispering gallery microlasers." *Nat. Nanotechnol.* **2011**, *6*(7): 428-432.

18. Ozdemir, S. K., Zhu, J. G., et al., "Highly sensitive detection of nanoparticles with a self-referenced and self-heterodyned whispering-gallery Raman microlaser." *Proc. Natl. Acad. Sci. U.S.A.* **2014**, *111*(37): E3836-E3844.

19. Shao, L. B., Jiang, X. F., et al., "Detection of Single Nanoparticles and Lentiviruses Using Microcavity Resonance Broadening." *Adv. Mater.* **2013**, *25*(39): 5616-+.

20. Li, B. B., Clements, W. R., et al., "Single nanoparticle detection using split-mode microcavity Raman lasers." *Proc. Natl. Acad. Sci. U.S.A.* **2014**, *111*(41): 14657-14662.

21. Swaim, J. D., Knittel, J., et al., "Detection of nanoparticles with a frequency locked whispering gallery mode microresonator." *Appl. Phys. Lett.* **2013**, *102*(18).

22. Lu, T., Lee, H., et al., "High sensitivity nanoparticle detection using optical microcavities." *Proc. Natl. Acad. Sci. U.S.A.* **2011**, *108*(15): 5976-5979.

23. Vollmer, F., Arnold, S., et al., "Single virus detection from the reactive shift of a whispering-gallery mode." *Proc. Natl. Acad. Sci. U.S.A.* **2008**, *105*(52): 20701-20704.

24. Dantham, V. R., Holler, S., et al., "Label-Free Detection of Single Protein Using a Nanoplasmonic-Photonic Hybrid Microcavity." *Nano. Lett.* **2013**, *13*(7): 3347-3351.

25. Yu, W. Y., Jiang, W. C., et al., "Cavity optomechanical spring sensing of single molecules." *Nat. Commun.* **2016**, *7*.

26. Baaske, M. D., Foreman, M. R., et al., "Single-molecule nucleic acid interactions monitored on a label-free microcavity biosensor platform." *Nature Nanotechnology* **2014**, *9*(11): 933-939.

27. Baaske, M. D. and Vollmer, F., "Optical observation of single atomic ions interacting with plasmonic nanorods in aqueous solution." *Nature Photonics* **2016**, *10*(11): 733-+.

28. Heylman, K. D., Thakkar, N., et al., "Optical microresonators as single-particle absorption spectrometers." *Nature Photonics* **2016**, *10*(12): 788-+.

29. Heylman, K. D., Knapper, K. A., et al., "Photothermal Microscopy of Nonluminescent Single Particles Enabled by Optical Microresonators." *J. Phys. Chem. Lett.* **2014**, *5*(11): 1917-1923.

30. Armani, D. K., Kippenberg, T. J., et al., "Ultra-high-Q toroid microcavity on a chip." *Nature* **2003**, *421*(6926): 925-928.

31. Knapper, K. A., Heylman, K. D., et al., "Chip-Scale Fabrication of High-Q All-Glass Toroidal Microresonators for Single-Particle Label-Free Imaging." *Adv. Mater.* **2016**, *28*(15): 2945-2950.

32. Heylman, K. D. and Goldsmith, R. H., "Photothermal mapping and free-space laser tuning of toroidal optical microcavities." *Appl. Phys. Lett.* **2013**, *103*(21).

33. Thakkar, N., Rea, M. T., et al., "Sculpting Fano Resonances To Control Photonic-Plasmonic Hybridization." *Nano Lett.* **2017**, *17*(11): 6927-6934.

34. Horak, E. H., Rea, M. T., et al., "Exploring Electronic Structure and Order in Polymers via Single-Particle Microresonator Spectroscopy." *Nano Letters* **2018**.

35. Black, E. D., "An introduction to Pound-Drever-Hall laser frequency stabilization." *Am. J. Phys.* **2001**, *69*(1): 79-87.

36. Weng, W. L., Anstie, J. D., et al., "Refractometry with Ultralow Detection Limit Using Anisotropic Whispering-Gallery-Mode Resonators." *Phys. Rev. Applied* **2015**, *3*(4).

37. Carmon, T., Kippenberg, T. J., et al., "Feedback control of ultra-high-Q microcavities: application to micro-Raman lasers and microparametric oscillators." *Opt. Express* **2005**, *13*(9): 3558-3566.

38. Barnes, J. A., Gagliardi, G., et al., "Absolute absorption cross-section measurement of a submonolayer film on a silica microresonator." *Optica* **2014**, *1*(2): 75-83.

39. Armani, A. M., Srinivasan, A., et al., "Soft lithographic fabrication of high Q polymer microcavity arrays." *Nano Lett.* **2007**, *7*(6): 1823-1826.

40. Xu, L. H., Jiang, X. F., et al., "High-Q silk fibroin whispering gallery microresonator." *Opt. Express* **2016**, *24*(18): 20825-20830.

41. Yilmaz, H., Pena-Francesch, A., et al., "Structural Protein-Based Whispering Gallery Mode Resonators." *ACS Photonics* **2017**, *4*(9): 2179-2186.

42. Hossein-Zadeh, M. and Vahala, K. J., "Free ultra-high-Q microtoroid: a tool for designing photonic devices." *Opt. Express* **2007**, *15*(1): 166-175.

43. Chen, Y., Lin, H. T., et al., "Heterogeneously Integrated Silicon Photonics for the Mid-Infrared and Spectroscopic Sensing." *Acs Nano* **2014**, *8*(7): 6955-6961.

44. Turunen, J., "Astigmatism in laser beam optical systems." *Appl. Opt.* **1986**, *25*(17): 2908-2911.

45. Massey, G. A. and Siegman, A. E., "Reflection and Refraction of Gaussian Light Beams at Tilted Ellipsoidal Surfaces." *Appl. Opt.* **1969**, *8*(5): 975-978.

46. Arnaud, J. A. and Kogelnik, H., "Gaussian Light Beams with General Astigmatism." *Appl. Opt.* **1969**, *8*(8): 1687-1693.

47. Daly, J. C., "SOLAR CONCENTRATOR FLUX DISTRIBUTIONS USING BACKWARD RAY TRACING." *Appl. Opt.* **1979**, *18*(15): 2696-2699.

48. Goodman, J. W., "Introduction to Fourier optics." **1968** San Francisco, McGraw-Hill.

49. Dickson, R. M., Norris, D. J., et al., "Simultaneous imaging of individual molecules aligned both parallel and perpendicular to the optic axis." *Phys. Rev. Lett.* **1998**, *81*(24): 5322-5325.

50. Betzig, E. and Chichester, R. J., "Single Molecules Observed by near-Field Scanning Optical Microscopy." *Science* **1993**, *262*(5138): 1422-1425.

51. Hasan, M. N., Haque, M.-U., et al., "Deastigmatism, circularization, and focusing of a laser diode beam using a single biconvex microlens." *Opt. Eng.* **2016**, *55*(9): 7.

52. Xiao-qun, Z., Ngoi Kok Ann, B., et al., "Single aspherical lens for deastigmatism, collimation, and circularization of a laser beam." *Appl. Opt.* **2000**, *39*(7): 1148-1151.

Chapter 6 Two-dimensional palladium-nanosheet intercalated with gold-nanoparticle for plasmon-enhanced electrocatalysis[l]

Main text: Abstract

Plasmon-enhanced electrocatalysis holds great promise for converting solar energy into chemical energy by efficiently harvesting photons for electrocatalytic reactions. Here, we report a unique two-dimensional (2D) “Egg Waffle”-like heterostructure, i.e., gold nanoparticle intercalated in a palladium nanosheet (AuNP-in-PdNS), effectively interfacing Au NPs with a 2D Pd for greatly enhancing electrocatalytic activity under optical illumination. A considerable electrocatalytic enhancement, i.e., a small overpotential of 19 mV (i.e., 4-fold decrease) at the current density of 10 mA cm^{-2} for hydrogen evolution reaction and improved oxygen reduction reaction with half-wave potential of 0.882 V, is achieved on 2D AuNP-in-PdNS heterostructure due to excitation of the localized surface plasmon resonance (LSPR). The unique heterostructure and strongly enhanced localized field intensity under LSPR excitation could result in hot

---

[l] This chapter is adapted from the published manuscript as Ding, J.*, Wang, F.*, Pan, F.*, et al., "Two-Dimensional Palladium Nanosheet Intercalated with Gold Nanoparticles for Plasmon-Enhanced Electrocatalysis." *ACS Catal.* **2021**, *11*(21): 13721–13732. * Equal co-first authorship.

electrons concentrated on the surface of Pd NSs and direct transfer of plasmonic energy to metal-absorbate complexes, manifesting as a reduction of the apparent activation barrier in the electrocatalysis. This study provides insight into both the design of efficient electrocatalysts and the distinct role of LSPR excitation in plasmon-enhanced electrocatalysis.

Main text: Introduction

Plasmon-enhanced catalysis has recently emerged as a thrilling field where solar energy is efficiently harvested to drive chemical transformations for energy conversion.[1-3] The excitation of collective oscillations of free conduction electrons, also known as localized surface plasmon resonances (LSPRs), results from strong visible light-matter interactions in plasmonic nanomaterials (Au, Ag or Cu). These LSPRs give rise to strongly enhanced light absorption and localized electromagnetic field intensity, facilitating energy and electron transfer during reactions. Nevertheless, these plasmonic nanomaterials alone catalyze only limited types of reactions under light illumination. A variety of bimetallic nanostructures that combine plasmonic metals and catalytic metals (palladium, platinum, rhodium, etc.),[4] such as antenna-reactor,[5-10] core-shell structure,[11-14] and alloys,[15-17] have been reported and exhibited excellent performance in catalysis. The created electromagnetic hotspots underpin improved chemical kinetics and reaction rates

seen in different catalytic reactions.[6, 18-22]

In particular, plasmon-enhanced electrocatalysis, in which the excitation of LSPRs is coupled with an applied potential to improve catalysts' selectivity and activity, offers an opportunity to lower the activation barrier for chemical conversions and constitutes a critical strategy for sustainable production of fuels or value-added chemicals. Some typical electrochemical reactions, such as carbon dioxide reduction,[23] oxygen reduction[24, 25] and hydrogen evolution reactions,[26, 27] are promoted by the plasmons. Unfortunately, the inherent chemical inertness of common plasmonic noble metals (e.g., Au or Ag)[28] constrains their wide applications in electrocatalysis. To remedy this situation, various supported structures, combining plasmonic nanostructured metals with efficient electrocatalysts, have been established.[24, 25, 29, 30] Indeed, important and often surprising structure-function relationships in recent studies have begun to imply that the two-dimensional (2D) nature of the electrocatalyst is important.[24, 30, 31] Ultrathin 2D nanostructures are attractive to mingle with plasmonic metals for providing a versatile and effective platform for electrocatalysis with abundant active sites to adsorb species, high specific surface area, and fast electron transport. But most commonly reported structures are plasmonic nanostructures decorated on the surface of the 2D electrocatalysts.[24, 30] On one hand, these heterostructures potentially limit the contact between the reactants

and the catalytically active sites, preventing catalytic performance from further being improved. On the other hand, strongly enhanced electromagnetic field may not be fully utilized because the field polarized in certain directions favorably enhances charge excitations and concentrates hot carriers in the areas away from some catalytically active sites. Thus, a powerful new strategy for maximizing electrocatalytic activity would be to interface plasmonic nanoparticles with 2D electrocatalysts.

Here, we report a novel 2D heterostructure with gold nanoparticles intercalated in a palladium nanosheet (AuNP-in-PdNS) to enhance electrocatalytic activity under the LSPR excitation. A facile wet-chemical method that combines seed growth, galvanic replacement, and assembly in one step (denoted as SGA method), was developed to synthesize the 2D AuNP-in-PdNS heterostructure (**Figure 6.1a**), which demonstrate an “Egg Waffle”-like structure. This heterostructure, which features ultrathin (~1.4 nm) PdNS wrapping Au NPs, integrates all the advantages of 2D nanostructures with plasmonic effect offered by Au NPs for boosting electrocatalysis. Specifically, we investigated its electrocatalytic activity in the hydrogen evolution reaction (HER) and oxygen reduction reaction (ORR) under light illumination, showing strongly enhanced reduction of H^+ to H_2 and O_2 reduction by leveraging the simultaneous LSPR excitation of Au NPs intercalated in Pd NS. Conspicuously lowered overpotential, increased limiting current density,

accelerated kinetics, and wavelength-dependent catalytic enhancement are observed. Our electromagnetic simulations shed light upon the underlying mechanism of plasmonic enhancement, underscoring the importance of plasmon-enhanced absorption and unique plasmonic modal properties in AuNP-in-PdNS along with favorable interband transitions in Pd NS. These attributes significantly contribute to efficient hot-carrier generation in the Pd NS that wrap Au NP and possibly mediate a direct transfer of plasmonic energy to the metal-absorbate complex while activating a new desorption pathway in the HER, both of which synergistically enable the apparent activation barrier to substantially decrease from

9.43 kJ mol^{-1} to 7.29 kJ mol^{-1}.

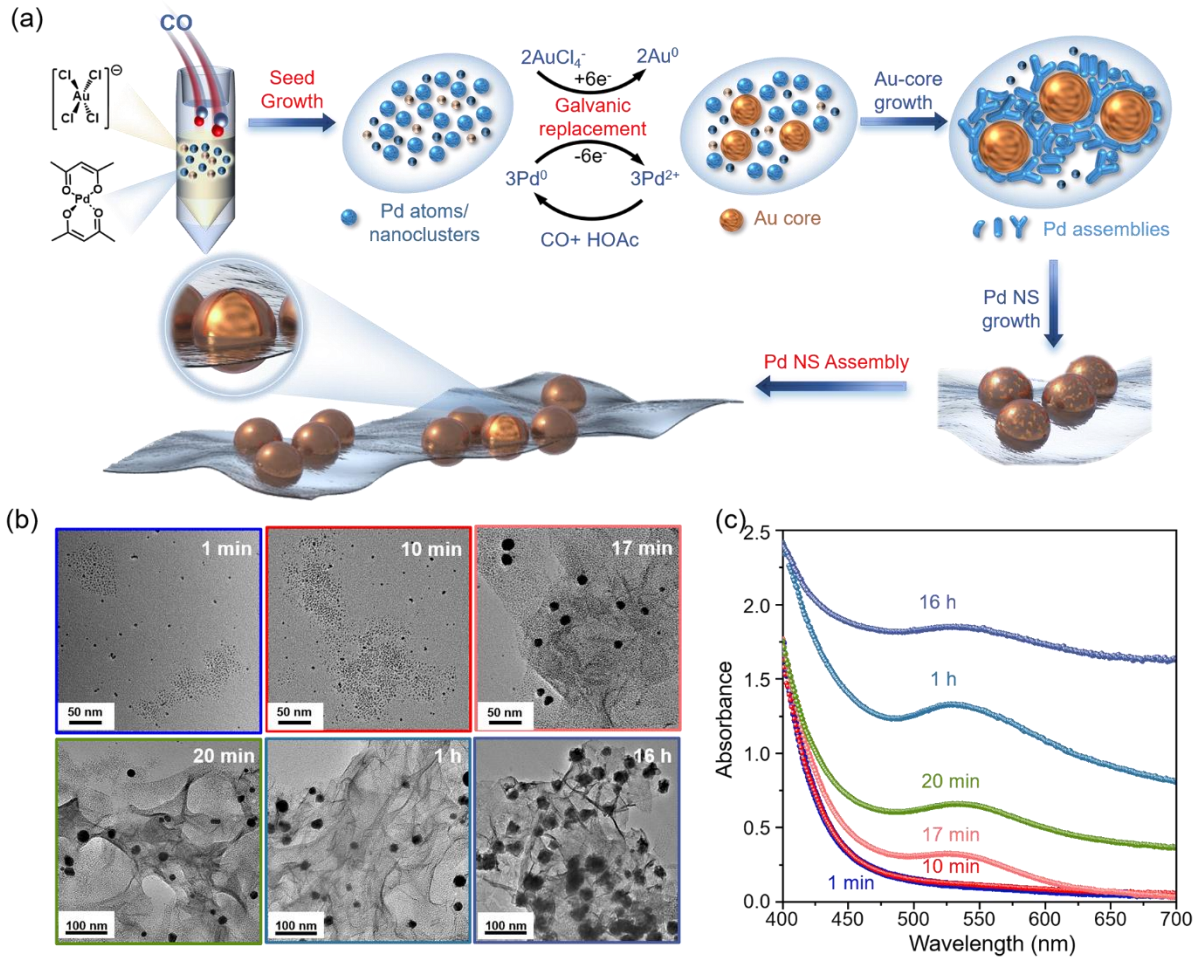

Figure 6.1 Synthesis of 2D AuNP-in-PdNS heterostructure. (**a**) Schematic illustration for the formation process, including seed-growth, galvanic replacement and assembly steps, of 2D AuNP-in-PdNS heterostructure. (**b**) Ex-situ TEM characterization of the intermediates extracted at different reaction times (1, 10, 17, 20, 60 min, and 16 h) during the synthesis process, clearly showing the formation of 2D Au0.15NP-in-PdNS heterostructure. (**c**) Corresponding UV-Vis absorption spectra of the intermediate solutions shown in **b**.

Main text: Synthetic method and formation mechanism of 2D AuNP-in-PdNS heterostructure.

To date, some 2D nanostructures based on Au or Pd NSs have been created by means of several synthetic strategies including seeded growth, organic ligand-assisted growth, and crystal phase transformation.[32-34] Typically, multiple steps of pre-preparation, surface modification of supports, and in-situ growth/immobilization of metals are involved in these conventional protocols. Here, we developed a spontaneously combined seed growth-galvanic replacement-assembly (named as SGA) method for constructing the AuNP-in-PdNS heterostructure. All reactants, including metal precursors ($Pd(acac)_2$ and $HAuCl_4{\cdot}xH_2O$) and solvent (acetic acid), were simultaneously added into a reactor vessel, followed by bubbling CO gas to initiate the synthesis. The reaction was conducted at room temperature under surfactant-free conditions without any reductant or stabilizer (see Methods section for detailed information). An intriguing feature lies in that the Au NPs are not coated on the surface of Pd NS but buried within the body of Pd NS (detailed structural characterization is shown later). As illustrated in **Figure 6.1a**, the Pd^0 atoms/nanoclusters acting as seeds were first formed when introducing CO gas through the coordination reaction, after which the subsequent galvanic replacement between Pd^0 and Au^{3+} was spontaneously driven to obtain Au NPs due to the more positive reduction potential (1.50

V) of Au^{3+}/Au^{0} than that of Pd^{2+}/Pd^{0} (0.915 V).[35] The simultaneous galvanic replacement and assembly processes finally gave rise to the formation of the 2D AuNP-in-PdNS heterostructure. In comparison, there was no product observed if only $HAuCl_4 \cdot xH_2O$ was added, whereas the Pd NSs could be formed if only $Pd(acac)_2$ was introduced during the synthesis (see Supporting Information for detailed information, Figure S1), concluding the necessity of the specific coordination reaction among $Pd(acac)_2$, acetic acid and CO for building the 2D architecture.[36, 37] The control studies on other reaction conditions, including the choice of metal precursors (see SI for detailed information, Figures S2a,b), the usage of CO or acetic acid (see SI for detailed information, Figures S2c,d), and participation of water (see SI for detailed information, Figures S2e,f), also further verify this finding. Meanwhile, employing both precursors with various ratios of Au^{3+} to Pd^{2+} (denoted as *x*) produces similar 2D heterostructures. By tuning *x* (i.e., 0.05, 0.10, 0.15, 0.20, 0.50, 1.0 and 2.0), a series of 2D heterostructured samples (denoted as Au_xNP-in-PdNS) with a similar lateral size (around 2 μm) were obtained. From the scanning electron microscopy (SEM, Figure S3 in SI) and transmission electron microscopy (TEM, Figure S4 in SI) images, the size of Au NPs increases from 13.6 nm to 45.7 nm when *x* increases from 0.05 to 0.50, but there is no significant change in the thickness (~ 1.4 nm) of the Pd NS (Figure S5 in SI). If $x > 1.0$, no intact Pd NS but conspicuous aggregation of Au NPs

is observed (Figures S4f, g in SI). The composition obtained from inductively coupled plasma optical emission spectrometry (ICP-OES) was very close to the theoretical ratios of Au to Pd after the galvanic-replacement step (Table S1 in SI). To further unravel the reaction mechanism, taking the synthesis of $Au_{0.15}$NP-in-PdNS as an example, the reaction was monitored by characterizing a series of aliquots of the reaction solution via both *ex-situ* TEM and UV-Vis absorption spectroscopy at specific reaction time points (see SI for detailed information, Figure S6 and S7). **Figure 6.1b** presents the corresponding TEM images, including generation of Pd atoms/nanoclusters as seeds (i.e., seed growth), replacement of Pd seeds for producing Au NPs (i.e., galvanic replacement), and Pd NS formed surrounding the Au NP (i.e., assembly). The gradually growing absorption peak at ~530 nm and its slightly redshift observed in UV-Vis spectra (**Figure 6.1c** and Figure S7a in SI) within 20 minutes in the reaction indicates the formation of Au NP; while, after 20 minutes, the overall ascending absorption envelope suggests the formation of Pd NS around the Au NP (Figure S7b in SI). Based on these characterizations, the formation mechanism is proposed as follows: i) first, the preferential coordination reaction of three reactants (Pd^{2+} ions, CO and acetic acid) rapidly gave rise to Pd atoms/nanoclusters as seeds/nucleation sites (within 1 minute), enabling subsequent galvanic replacement between Pd atoms and Au^{3+} ions for Au NP production;

ii) then, the size of Au NP kept growing, which is suggested by gradually growing and slightly redshift LSPR absorption feature at ~530 nm within 20 minutes (**Figure 6.1c** and Figure S7a in SI), until all of Au^{3+} ions were consumed with repeated reduction of Pd^{2+} ions and replacement; iii) Pd atoms/nanoclusters were continuously generated around the Au NP, and finally assembled into Pd NS (Figure S8) along the [111] direction with the help of the CO confinement effect,[38] which is indicated by increasing absorbance in the whole absorption envelope seen in the formation process of the heterostructures (**Figure 6.1c** and Figure S7b in SI).

Figure 6.2a displays a TEM image of the as-obtained 2D $Au_{0.15}$NP-in-PdNS heterostructure, demonstrating lots of spherical NPs (about 15 nm in diameter) intercalated in the body of ultrathin Pd NSs with an interesting “Egg Waffles”-like morphology. To acquire more detailed structural information, high-angle annular dark-field scanning transmission electron microscopy (HAADF-STEM) was employed. As shown in **Figure 6.2b**, the Au NP core (marked in red line) is buried in the ultrathin Pd NS shell (marked in blue line). A clear lattice spacing of 0.225 nm observed upon and around the Au NP core suggests the Pd NS with the (111)-facet was formed (Figure S8 in SI). Meanwhile, both the line-scan profile across a single Au NP by energy dispersive X-ray spectroscopy (EDX) (**Figure 6.2c**) and EDX mapping images at different magnifications

(**Figure 6.2d** and Figure S9 in SI) show that Au NPs are intercalated within the body of Pd NS, further confirming the formation of the 2D AuNP-in-PdNS heterostructure. The X-ray diffraction (XRD) and X-ray photoelectron spectroscopy (Figure S10 and S11 in SI)

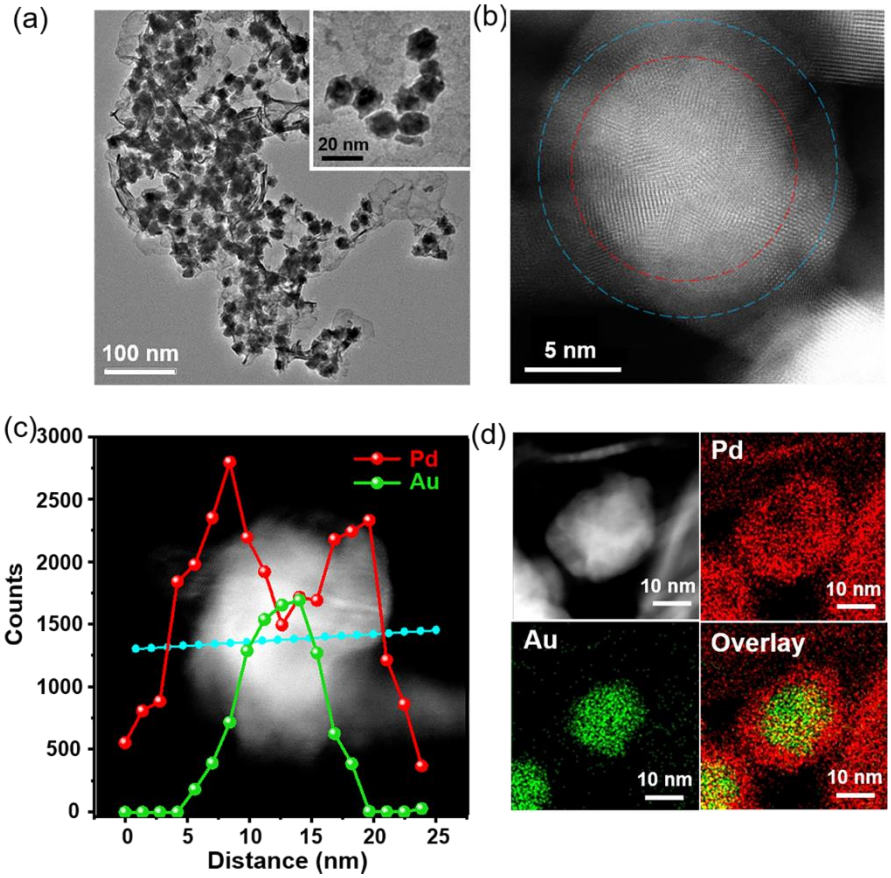

Figure 6.2 Structural characterization of the 2D Au0.15NP-in-PdNS heterostructure. (**a**) TEM images under different magnifications. (**b**) A HAADF-STEM image collected around one Au NP. The red and blue circles represent the Au-Pd interface and Pd NS shell, respectively. (**c**) An EDX line-scanning profile across a single Au NP intercalated in Pd NS, clearly showing that Au atoms dominate in the middle and Pd atoms are around Au-core. (**d**) Corresponding EDX mapping images of Pd and Au elements, further confirming the Au NP intercalated in Pd NS.

verify the co-existence of separate Au and Pd phases instead of alloyed Au-Pd

nanostructure.

Main text: Plasmon-enhanced hydrogen evolution and oxygen reduction on Au_xNP-in-PdNS.

Given Pd NS's two-dimensional (2D) nature that provides a large catalytic surface area and plasmon-driven processes induced by optical plasmon-excitation of Au NPs in the 2D AuNP-in-PdNS heterostructure, we investigated the electrocatalytic activity of Au_xNP-in-PdNS under light illumination. First, the hydrogen evolution reaction (HER) is focused on here due to its promising activity in palladium based materials and one-electron process during the electrochemical reaction.[39] The electrochemical measurements were conducted in a typical three-electrode system in acidic $HClO_4$ solution (1 M, pH ≈ 0.09), where the Au_xNP-in-PdNS (x = 0.05, 0.10, 0.15, 0.20, 0.50, 1.0 and 2.0) catalyst was drop-casted on a rotating disk electrode (RDE) acting as the working electrode (see Methods section for detailed information), and a Xenon light lamp was utilized as light source to irradiate the working electrode surface (Figure S12 and S13 in SI). In comparison, the commercial Pt/C and Pd/C catalysts were also tested under the same condition. Polarization curves (**Figure 6.3a** and Figure S14 in SI) show a superior HER performance with an overpotential of 19.0 mV at the current density of 10 mA cm^{-2} (i.e., η_{10}) for the $Au_{0.50}$NP-in-PdNS catalyst under light illumination. It is noted that the

geometric surface area (0.196 cm^2) of RDE is used to normalize current densities in all electrochemical measurements if they are not specified. Even the current density normalized by electrochemical surface areas (ECSA) of the various electrocatalyst, the $Au_{0.50}$NP-in-PdNS still demonstrate the best performance (Figure S16 in SI). Compared to the control experiment under dark condition (72.4 mV of η_{10}), a four-fold decrease is achieved. In other words, an overpotential decrement (i.e., the difference of η_{10} between dark and light illumination conditions) of 53.4 mV is obtained, suggesting a considerable enhancement in hydrogen evolution. Notably, the catalytic activity of $Au_{0.50}$NP-in-PdNS under light illumination outperforms the benchmark of Pt/C (**Figure 6.3a**) and other reported catalysts (Table S3 in SI) in acidic media. The smaller overpotential for HER on Pd NS, compared with other structures (Table S2 in SI), also indicate the improved activity of two-dimensional structure. A much lower Tafel slope of 37 mV dec^{-1} and a smaller charge transfer resistance (R_{ct}, 21.7 Ω) (Figures S15 and S17, Table S6 in SI) are found in the $Au_{0.50}$NP-in-PdNS catalyst under light illumination than those (79 mV dec^{-1} and 108.9 Ω) under dark condition, revealing improved kinetics of HER. Clearly, the obvious decrease in the Tafel slope from 79 to 37 mV dec^{-1}, which is very close to the value (34 mV dec^{-1}) in the Pt/C catalyst, suggests that Volmer-Tafel mechanism dominates under light illumination with Tafel desorption as the limiting step. The continuous

chronopotentiometry test (Figure S18 in SI) by alternating dark and light illumination signifies an additional photopotential (or photocharging) experienced by the electrode,[27] resulting in accelerated rate of electron transfer from the $Au_{0.50}$NP-in-PdNS electrocatalyst to protons in solution. This result is consistent with the reduced charge-transfer resistance and lowered overpotential. A much higher H_2 gas evolution rate (15.0 μmol min^{-1}) under light illumination than that (13.0 μmol min^{-1}) under dark suggests the plasmon-enhanced HER (Figure S19c in SI). Meanwhile, the unchanged polarization curves after 10000 cyclic voltammetry sweep cycles (Figure S20 in SI) suggest that this catalyst still preserves a superior stability through long-term measurements under light illumination.

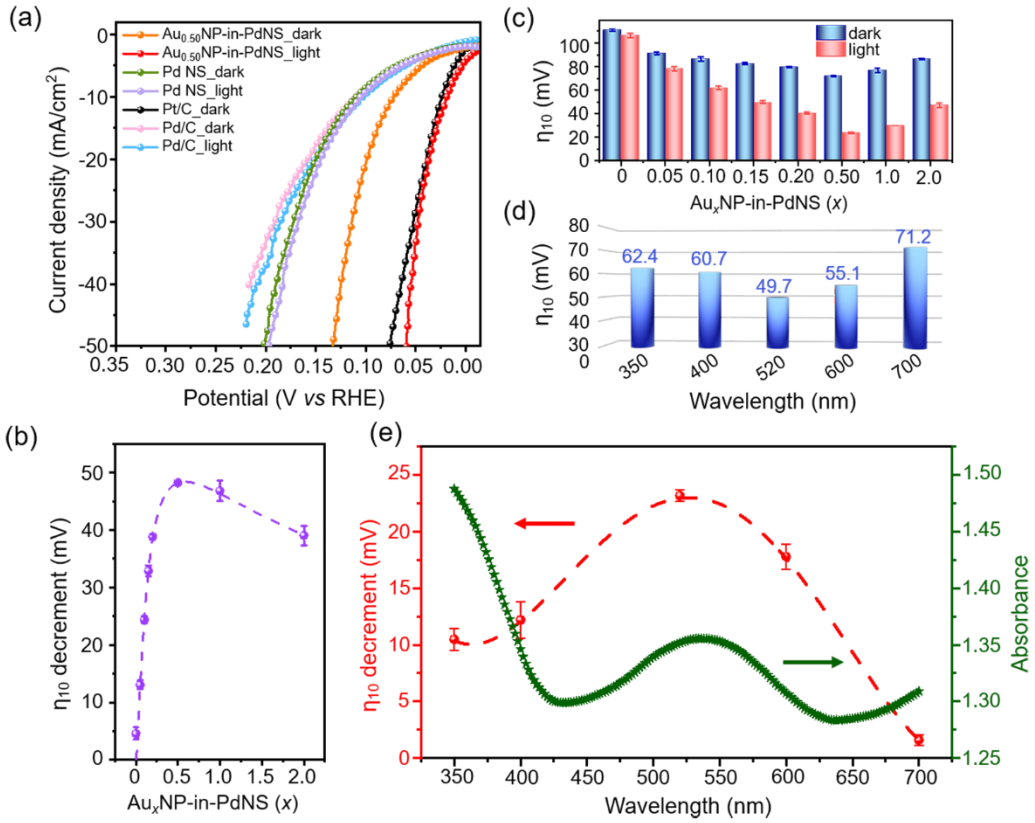

Figure 6.3 Plasmon-enhanced hydrogen evolution reaction electrocatalysis on 2D AuNP-in-PdNS heterostructure at room temperature. (**a**) Polarization curves collected on the Au0.50NP-in-PdNS electrode at the scan rate of 10 mV s-1 under Xenon light illumination (200 mW cm-2) and dark conditions. In comparison, the commercial 20%wt Pt/C and Pd/C were also tested under the same condition. (**b**) The η10 decrement, i.e., the difference of the overpotential at 10 mA cm-2 between under dark and Xenon light illumination conditions, for various AuxNP-in-PdNS electrodes. (**c**) The η10 values collected from the various AuxNP-in-PdNS electrodes under dark (green) and light illumination (yellow) conditions. (**d**) Wavelength-dependent η10 values collected from Au0.50NP-in-PdNS electrode, showing a smallest η10 at 520 nm. (**e**) Wavelength-dependent η10 decrement (red) before and after light illumination obtained on the Au0.50NP-in-PdNS electrode, along with a UV-Vis absorption spectrum of the catalyst (dark green). Data are presented as the mean of three independent experiments and error bars signify standard errors. The same light intensity of 16.8 mW cm-2 was utilized for the measurements in **d-e**.

In addition, various Au_xNP-in-PdNS electrocatalysts exhibited different HER

performance under light illumination, showing a strong dependence on the AuNP size. From **Figure 6.3a-c**, $Au_{0.50}$NP-in-PdNS leads to the largest overpotential decrement (with the average value of 48.3 ± 0.2 mV) under light illumination compared with the other catalysts (e.g., 38.9 ± 0.5 mV and 46.8 ± 1.8 mV for $Au_{0.20}$NP-in-PdNS and $Au_{1.0}$NP-in-PdNS, respectively). When the content of Au NP is dramatically increasing (like in $Au_{1.0}$NP-in-PdNS and $Au_{2.0}$NP-in-PdNS), the degradation in HER performance is observed probably due to the aggregation of Au NPs and rarely intact Pd NS (Figure S4 in SI). We hypothesize that the improved apparent catalytic activity of Au_xNP-in-PdNS ($x \leq 0.5$) is caused by the LSPR being excited on the Au NPs intercalated in Pd NSs under light illumination. We then studied the electrocatalytic HER of $Au_{0.50}$NP-in-PdNS at various wavelengths of light illumination with the same light intensity of 16.8 $mWcm^{-2}$. In **Figure 6.3d**, the smallest overpotential (η_{10} = 49.7 ± 1.1 mV) is observed at 520 nm, showing the best catalytic activity. Furthermore, η_{10} decreases at different wavelengths (350, 400, 520, 600 and 700 nm) demonstrating a non-monotonic curve (the red curve in **Figure 6.3e**) that is strongly correlated to the LSPR line shape in the UV-Vis absorption spectrum[40] of $Au_{0.50}$NP-in-PdNS (the green plot in **Figure 6.3e**). This correlation lends support to our hypothesis that LSPR effectively enhances electrocatalytic HER activity of 2D AuNP-in-PdNS heterostructures.

To further demonstrate the plasmon-enhanced electrocatalysis on 2D AuNP-in-PdNS heterostructures, we also study its oxygen reduction reaction (ORR) activity. The ORR performance of AuNP-in-PdNS heterostructures, compared with that of Pt/C (20 wt%), was evaluated in O_2-saturated alkaline solution (0.1 M KOH). In Figure S21 and S22 in SI, $Au_{0.50}$NP-in-PdNS exhibits the best ORR performance with both increased half-wave potential ($E_{1/2}$) of 0.882 V and limiting current density (j_L) of 7.5 mA/cm^2 under light illumination than those (0.871 V and 6.1 mA) under dark condition, further verifying plasmonic enhancement in electrocatalytic activity (Table S4 in SI). Moreover, the ORR performance of 2D $Au_{0.50}$NP-in-PdNS outperforms that of Pt/C benchmark, resulting in the low overpotential and superior mass transfer for ORR on this 2D heterostructure.

Main text: Electromagnetic simulations of Au_xNP-in-PdNS

In order to elucidate how the LSP effectively enhances the electrocatalytic activity, we performed electromagnetic simulations of the plasmonic effect for the Au_xNP-in-PdNS heterostructure using the finite-difference time-domain method (see SI for detailed information). Au_xNP-in-PdNS (x =0.05, 0.20, 0.50, 1.0) core-shell structures that match corresponding Au NP sizes (D_{core} = 14, 18, 30 and 46 nm) determined for Au_xNP-in-PdNS catalysts (Figure S4 in SI) were simulated to reduce the computation cost without affecting the essence of the plasmonic effect in play. Given the electronic transitions

typically are activated at higher photon energies close to bulk plasmon resonances, here, the quantum-sized effect on the dielectric functions that has been demonstrated in Ag[41] and Au[42] nanoparticles and thin films[42, 43] was not considered in the simulations. A theoretical model based on Mie theory was employed for calculating absorption spectra and local field distribution. First, we theoretically examined the effect of Au NP size on the LSPR in a series of Au_xNP-in-PdNS core-shell models (**Figure 6.4a**, bottom). The LSPR peak shows a redshift and its line shape becomes more pronounced as Au NP size becomes larger (**Figure 6.4a**, bottom). The simulated absorption spectra nicely capture the absorption feature in the 500-600 nm wavelength spectral window of the experimental absorption spectra (**Figure 6.4a**, top), though the line shapes in the experimental spectra are broader, likely due to the polydispersity of the Au NPs. This agreement confirms that the LSP is being excited on various Au_xNP-in-PdNS catalysts. The feature is further verified by an absorption spectrum of pure Au NPs (D_{core} = 30 nm) shown in Figure S23 (SI) and thus is attributed to optical excitations of Au NP's LSPR. This plasmon-enhanced absorption in the visible range increases the efficiency of harvesting visible light for photo-electrocatalytic reactions. The larger the Au NP size, the stronger the absorption. This trend agrees well with the observation that electrocatalytic activity becomes better as *x* increases from 0 to 0.5 (**Figure 6.3b**). However, as Au NP size further increases, the

electrocatalytic reaction with a certain catalyst loading amount (≥ 0.102 mg cm^{-2}) likely operates in a light-limited regime where all the photons are either absorbed or scattered and thus a decrease in electrocatalytic activity is consistent with the higher scattering cross section (see the blue plot in **Figure 6.4b** and Figure S24 in SI, and SI for detailed information). In addition, the aforementioned conspicuous aggregation of Au NPs and rarely intact Pd NS, especially in $Au_{1.0}$NP-in-PdNS and $Au_{2.0}$NP-in-PdNS, will somehow hinder the electrocatalytic activity. Thus, all these factors likely contribute to the opposite size-dependent trend observed in **Figure 6.3b** when x > 0.5. In other words, an optimal Au NP size (i.e. D_{core} = 30 nm) and the intact morphology of 2D $Au_{0.50}$NP-in-PdNS heterostructure give rise to the highest catalytic activity.

The two-dimensional field enhancement profiles in **Figure 6.4c** shows that the electromagnetic field of Au_xNP-in-PdNS core-shell structure is concentrated at the outer surface of Pd NS-shell upon excitation. The local field maximum (hot spot) is very different from that in other core-shell systems (like Au-Ag core-shell)[44] where energy is concentrated at both the outer surface of the shell and the core-shell interface. Meanwhile, a larger Au NP results in a higher field enhancement factor with an increase from 12-fold up to 26-fold (the red plot in **Figure 6.4b**), which is consistent with size-dependence of plasmon-enhanced absorption observed in **Figure 6.4a** at the LSPR wavelengths (~530

nm). However, this correlation might break down when interband transitions are largely involved and thus contribute to absorption heavily. Our calculations show that both field enhancement and the LSPR feature become less pronounced when Au NP is wrapped by Pd, and they are further weakened when the Pd-shell is thicker (Figures S25 and S26 in SI). Nevertheless, in our novel 2D heterostructures Pd-shell (~1.4 nm thickness) minimally wraps the Au NP and thus minimally undermines the plasmonic response while still introducing the indispensable catalytic compartment. When $Au_{0.50}$NP-in-PdNS core-shell nanostructures aggregate into a dimer, tetramer, or even a chain shown in the inset of **Figure 6.2a**, the plasmonic field enhancement further increases by over two orders of

magnitude and LSPR gains more redshifts (**Figure 6.4d**, Figures S27 and S28 in SI).

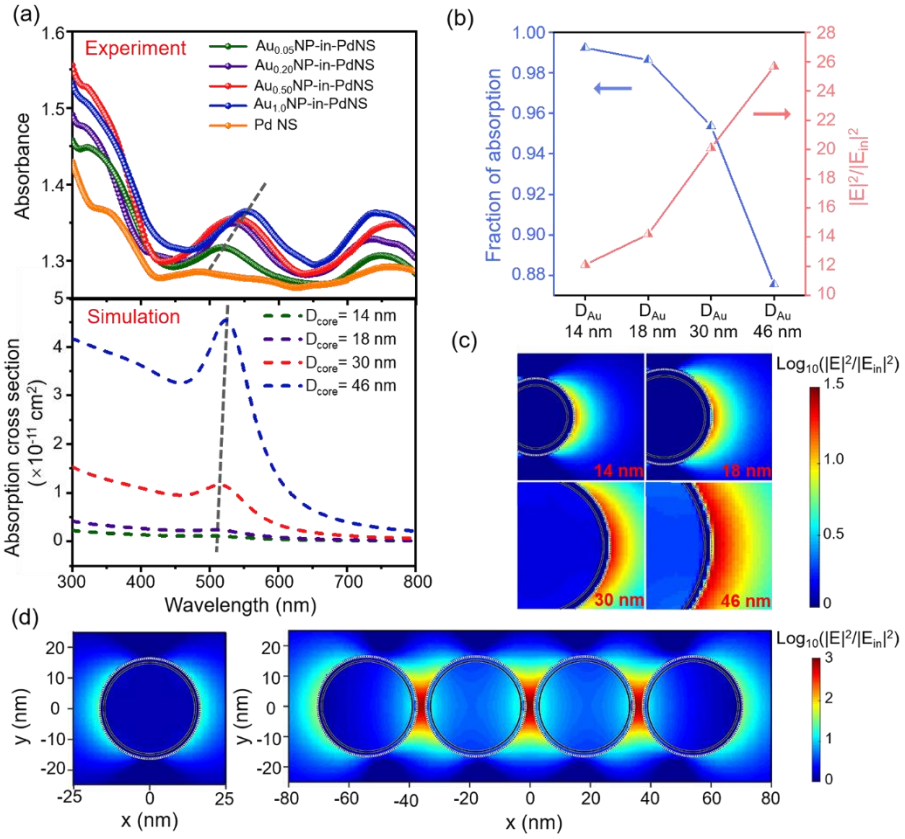

Figure 6.4 Electromagnetic simulations for AuxNP-in-PdNS heterostructure. (**a**) Experimental absorption spectra (top) for a series of AuxNP-in-PdNS heterostructure combined with pure Pd NS, and simulated absorption spectra (bottom) for corresponding AuxNP-in-PdNS core-shell nanostructures. (**b**) Calculated fraction of absorption and maximum field enhancement factors for the AuxNP-in-PdNS core-shell nanostructures at the wavelength of 548 nm. (**c**) Two-dimensional field enhancement profiles for the AuxNP-in-PdNS core-shell nanostructures, where the interface between Au-core and Pd-shell is marked by a black circle and the outer surface of Pd shell marked by white dashed line. (**d**) Comparison of field enhancement profiles between a single and aggregated Au0.50NP-in-PdNS nanostructures.

Regarding the spacing between $Au_{0.50}$NP-in-PdNS nanostructures, when it shrinks from

20 nm down to 1 nm, the field enhancement factor increases by three orders of magnitude (Figure S29 in SI). Although the spacing between Au NPs in our catalysts might vary from one to another, the collective plasmonic effect tremendously contributes to increased fraction of absorbed photons and stronger field enhancement[45, 46] and subsequently enhances electrocatalytic activity.

Main text: Mechanism discussion

Plasmons can decay via radiative and nonradiative pathways following excitation.[3, 47, 48] Among nonradiative dissipation pathways, hot charge carriers are generated through interband and/or intraband transitions and then collide with other carriers, forming the hot Fermi-Dirac distribution.[3] On the one hand, interband transitions occur in Au at short wavelengths (≤ 600 nm) through both direct excitations and indirect excitations via Landau damping of plasmons[49, 50]. Intraband transitions assisted by phonons or confined surface modes slightly contribute to generating the hot carriers in Au. On the other hand, interband transitions in Pd are favorable over intraband transitions across the entire visible frequency range because of its unfilled d-band intersecting the Fermi level. Thus, interband transitions in both Au and Pd at the LSPR wavelengths are preferential pathways for generating hot carriers. Although the relatively low ratio in the imaginary part of Pd and Au at LSPR wavelengths[51] indicates that plasmon energy more likely dissipates

through indirect excitation of interband transitions in Au, the presence of the unique modal feature in our Au-Pd heterostructure and resulting intense field favor charge excitations which are proportional to the intensity of the local electric field[52] and hot carriers being concentrated on hot spots of the Pd surface. Eventually, the carrier density on the surface of the Au_xNP-in-PdNS increases due to hot-carrier generation and transfer mediated by the LSP, facilitating the participation of hot carriers in electrochemical hydrogen evolution process in the wavelength range of LSPR (**Figure 6.3e**). Meanwhile, benefiting from the abundant active sites and high specific surface area of the ultrathin 2D Pd NSs, these hot carriers can efficiently transport and be exploited for accelerating HER and ORR processes with a much smaller overpotential.

Notwithstanding, direct excitations of interband transitions in both Au and Pd indeed occur and dominate the process of hot-carrier generation at wavelengths close to ultraviolet region,[53] manifesting as rapidly increasing absorption as the wavelength decreases (**Figure 6.4a**). When direct excitations of interband transitions are activated at short wavelengths (< 400 nm) beyond LSPR, hot carriers are directly generated in both Au and Pd, and then transferred to the catalytic surface for electrochemical conversions. Similar behavior is also observed on the Au nanoparticles for HER when the electrodes are illuminated at higher photon energies.[27] Although these interband transitions

contribute to improved electrocatalytic activity, hot carriers are more vulnerable to a variety of dissipation pathways such as electron-electron, electron-phonon scattering, and charge recombination when they migrate through the Au-Pd interface toward the catalytic sites. This behavior is evidenced by a moderately gained but still smaller overpotential decrement at 350 nm for HER (**Figure 6.3e**). The overpotential decrement might increase again as interband transitions in both Au and Pd via direct excitation contribute more to hot-carrier generation. As indirect and direct excitations taper off at long wavelengths (> 650 nm), hot-carrier generation is no longer efficient thus leading to a very small overpotential decrement at 700 nm. Taken together, the maximum overpotential decrement observed under Xenon light illumination within the wavelength range from 320 nm to 780 nm mainly results from hot-carrier generation through both indirect excitation of interband transitions in Pd mediated by LSPRs and direct excitation of interband transitions in Au and Pd. In addition to favorable hot-carrier generation in AuNP-in-PdNS, a direct energy transfer mediated by LSP decay is possible because of high LSP field intensity and the existence of the electronic states on the Pd surface that might hybridize with states in the chemisorbed hydrogen atoms on the Pd surface.[54, 55]

Based on the discussion above, we specifically propose a tentative mechanism for plasmon-enhanced HER performance that takes into account both the generation of hot

carriers (or indirect energy transfer) and direct energy transfer mediated by LSP decay.[3] The LSP exerts a strong impact on both hydrogen absorption (Volmer step) and desorption (Tafel step) steps in the HER through the involvement of indirect and direct transfer of plasmonic energy. As shown in **Figure 6.5a**, the hot carriers, which are readily involved in the proton reduction, are generated on the Pd surface due to both unique modal feature of Au_xNP-in-PdNS structure and favorable interband transitions in Pd. The effectively cathodic photocharging[56] on the 2D Pd NS improves the kinetics of interfacial electron transfer to protons in the electrolyte. The hydrogen atoms chemisorbed on the Pd surface after the Volmer step result in newly hybridized Pd-H states. These states may enable direct momentum-conserved excitations of electrons mediated by the LSP decay like other plasmonic systems featuring absorbate/metal hybridized states,[57, 58] providing a new channel to pass the plasmonic energy directly to the Pd-H complex at the interface and then activating a new reaction path in the desorption process. To clearly elucidate the mechanism of intrinsic plasmon-enhanced HER, we plot reaction free energy profiles under thermodynamic equilibrium (or with zero applied potential) in **Figure 6.5b**. Regarding the reaction free energy profiles between dark (**Figure 6.5b**, blue) and light illumination (**Figure 6.5b**, red) conditions, the initial state under light is much closer to the first transition state (TS_1) due to the hot-electron involvement, making the Volmer step

kinetically favorable. The Pd-H complex (H_{ad}) formed in the Volmer step has a lower free energy than that of the initial state because of a negative absorption free energy of H on Pd surface under dark condition.[59] A direct energy transfer from the LSP to H_{ad} promotes H_{ad} from the ground state to an excited state and therefore modifies the desorption reaction pathway. The energy barrier (ΔG_a), i.e. energy difference between H_{ad} and the second transition state (TS_2), is lowered when H_{ad} is in the excited state (**Figure 6.5b**, red). The Tafel slope (< 120 mV dec^{-1}) of $Au_{0.50}$NP-in-PdNS under light illumination suggests that the desorption step is kinetically limiting.[60] Thus, the direct energy transfer

mechanism may play a vital role in lowering ΔG_a of the intrinsic electrocatalytic HER.

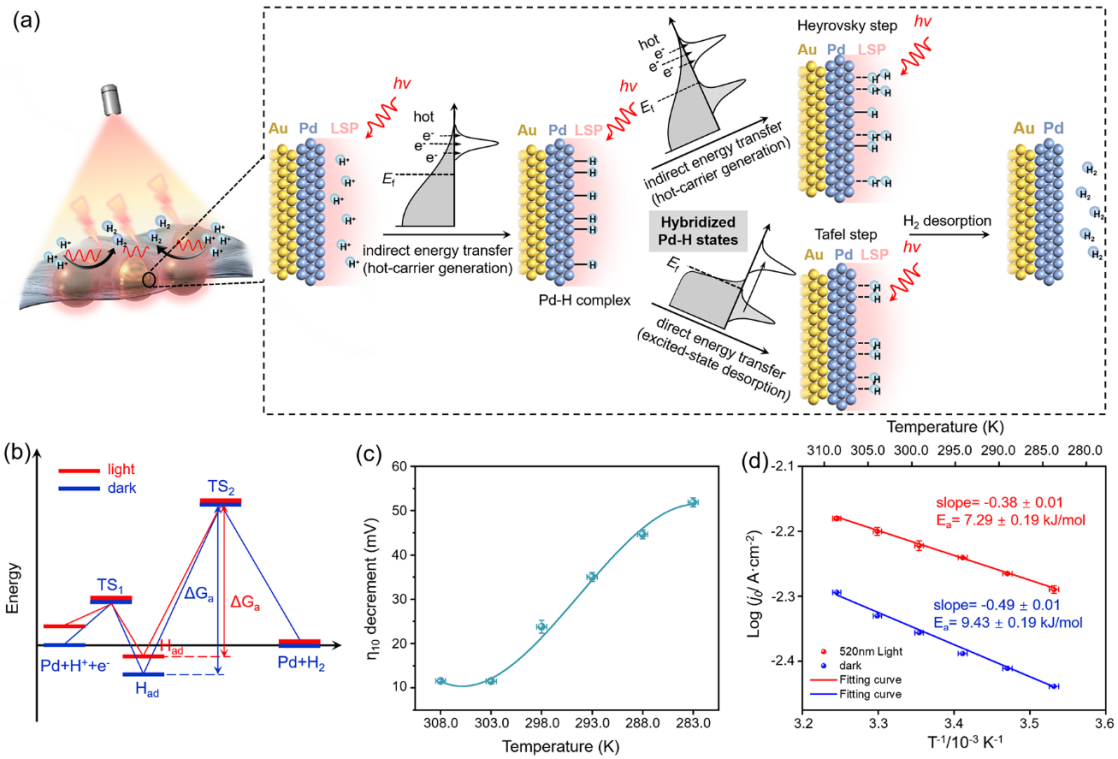

Figure 6.5 Proposed mechanism for the plasmon-enhanced hydrogen evolution reaction. (**a**) Schematic of indirect and direct transfer of plasmonic energy for generating hot carriers and promoting excited-state desorption in hydrogen evolution steps, respectively. The hot electrons from the hot Fermi-Dirac distribution transfer to protons forming Pd-H complexes in the Volmer step. The chemisorbed hydrogen atoms desorb from Pd surface forming H2 either via the electron transfer resulting from the hot Fermi-Dirac distribution or by exciting Pd-H complexes due to direct transfer of plasmonic energy. (**b**) Proposed reaction free energy profiles of HER at equilibrium under dark (blue) and light illumination (red) conditions. (**c**) Temperature-dependent η10 decrement obtained on Au0.50NP-in-PdNS electrode under light illumination (520 nm, 21.6 mW cm-2) and dark conditions. (**d**) Arrhenius plots of jo for 2D Au0.50NP-in-PdNS heterostructure electrocatalyst over the range of temperature from 283±0.5 K to 308±0.5 K with an interval of 5 K, from which apparent activation energies are calculated based on their slopes under dark (blue) and 520 nm (21.6 mW cm-2) light illumination (red) conditions.

The photothermal effect resulting from hot-carrier thermalization via both electron-phonon scattering in the catalyst and phonon-phonon scattering at the interface between the catalyst and the surrounding medium may affect electrocatalytic reactions by increasing the local temperature.[61] Thus, we explored temperature-dependent behavior by measuring HER polarization curves of $Au_{0.50}$NP-in-PdNS at temperatures ranging from 283 K to 308 K (Figure S30 in SI) under 520 nm light illumination and dark conditions (Figure S31 and S32 in SI). η_{10} increases when the temperature decreasess from 308 K to 283 K under both light illumination and dark conditions (Figure S33 in SI), revealing the typical Arrhenius behavior.[54] Interestingly, the plasmonic enhancement of the HER is much more striking at a lower temperature, evidenced by monotonically increasing η_{10} decrement as temperature drops from 308 K to 283 K (with 51.9 mV decrement) (**Figure 6.5c**). This behavior likely indicates that the photothermal contribution is minimal in the plasmon-enhanced HER, becaue the heat generated through relaxation of hot electrons leads to a temperature increase of 1.96×10^{-6} K on the surface of the catalyst given the low illumination intensity (21.6 mW cm^{-2}) and high thermal conductivity of Pd NS.[61-63] Such small increase in temperature would not contribute significantly to the large η_{10} decrement at the low temperature. Based on the polarization curves, the exchenge current density (j_o) and Tafel slopes were calculated through the Tafel equation (η= a +

blg*j*, where a is the intercept obtained through fitting the linear part of the Tafel plot, b is the Tafel slope, η is the overpotential and j_0 is obtained when η= 0). In Figure S34 (SI), j_0 decreases as the temperature decreases under both dark and 520 nm light illumination conditions. Moreover, using the values of j_o obtained under both conditions over the temperature range of 283-308 K and Arrhenius equation, we determined the apparent activation energies (E_a)[54] for the HER (see Experimental section for detailed information). E_a decreases from 9.43 kJ mol^{-1} under dark to 7.29 kJ mol^{-1} under light illumination (**Figure 6.5d**), further substantiating that the LSP excited on the Au NPs efficiently reduces the energy barrier for the HER.

Main text: Conclusions

We present a novel synthetic method in this work that enables plasmonic Au NPs to be intercalated in the ultrathin 2D electrocatalytic Pd NS. This heterostructure with size tunability in Au NPs effectively interfaces LSPRs with the 2D electrocatalyst's abundant active sites and fast charge-carrier transport properties for efficiently enhancing electrocatalytic activity. The decreased overpotential (η_{10}) for electrocatalytic hydrogen evolution and increased half-wave potential and limiting current density for oxygen reduction are achieved on 2D AuNP-in-PdNS heterostructure under light illumination. The strong correlation between wavelength-dependent electrocatalytic activity and the LSPR

line shape implies that the LSPR excitation on Au NPs plays a key role in promoting hydrogen evolution and oxygen reduction performance. Relying on the electromagnetic simulations, we found plasmon-enhanced absorption and unique plasmonic modal property in AuNP-in-PdNS along with favorable interband transitions in Pd NSs, are of paramount importance to enhance the electrocatalytic performance. These attributes favorably give rise to hot-carrier generation in 2D Pd NSs and mediate transfer of electron and plasmonic energy for lowering the reaction energy barrier. More importantly, 2D AuNP-in-PdNS heterostructure will be also promising to act as electrocatalyst for carbon dioxide reduction or organic electrochemical reactions. This study provides a new avenue for rational design of efficient plasmon-enhanced electrocatalysts and highlights the distinct role of LSPR excitation in plasmon-enhanced electrocatalysis.

Main text: Experimental section

Materials. The chemicals were directly used without further purification−$Pd(acac)_2$ (Alfa Aesar, 99% purity), $HAuCl_4$ (Alfa Aesar, 99.9% metals basis purity), acetic acid (Innochem, 99.5% purity), acetone (Beijing Chemical Works, ≥99.5% purity), ethanol (Beijing Chemical Works, 99.7% purity), $HClO_4$ (Acros, ca. 70% solution in water), Nafion solution (Aldrich, 5 wt% in lower aliphatic alcohols and water), isopropanol (Beijing Chemical Works, absolute, ≥99.7% purity), commercial Pt/C (Alfa Aesar, Platinum, 20%

on carbon black) and Pd/C (Aldrich, 10% Pd basis). The ultrapure water (18.2 MΩ) purified from Millipore were used in all experiments.

Synthesis of Au_xNP-in-PdNS. 2D Au_xNP-in-PdNS heterostructure was synthesized through a facile wet-chemical method combining a three-step process of seed growth, galvanic replacement, and self-assembly (SGA). Au_xNP-in-PdNS with various *x* ratios were synthesized by tuning the mass of $HAuCl_4$ against $Pd(acac)_2$, keeping the $HAuCl_4$: $Pd(acac)_2$ molar ratios of 0.05, 0.10, 0.15, 0.20, 0.50, 1.0 and 2.0, in 10 mL acetic acid. For instance, when synthesizing $Au_{0.05}$NP-in-PdNS, 15.2 mg of $Pd(acac)_2$ and 125 µL 20 mM $HAuCl_4$ solution were simultaneously dissolved in 10 ml of acetic acid; then, CO gas bubbled the solution at the speed of 200 mL min^{-1} for 30 min, followed by incubation under sealed conditions for 24 h. The obtained precipitant was collected after high-speed centrifugation and thoroughly washed with acetone and ethanol. Finally, the various Au_xNP-in-PdNS samples were dispersed in ethanol solvent with the concentration of 1 mg mL^{-1} for further usage.

Synthesis of Pd NSs. The Pd NS catalyst was prepared according to the previous report[37] with minor modification. Typically, $Pd(acac)_2$ (15.2 mg, 5 mmol) was dissolved in 10 mL of acetic acid to form a homogeneous solution. Subsequently, CO gas was introduced by bubbling at the speed of 200 mL min^{-1} for 30 min, followed by incubation

under sealed conditions for 24 h. The obtained precipitant was separated by centrifugation and thoroughly washed with acetone and ethanol. The Pd NSs were dispersed in ethanol with the concentration of 1 mg mL^{-1}.

Materials Characterization. The morphologies of Au_xNP-in-PdNS were characterized on transmission electron microscopy (TEM, FEI Tecnai G2 F20), aberration-corrected high-resolution transmission electron microscopy (JEM ARM200F) at 200 kV equipped with energy-dispersive X-ray (EDX) analysis, and scanning electron microscopy (SEM, Hitachi S-4800). The X-ray powder diffraction (XRD, Bruker D8 Focus) was used to determine the crystal structure of 2D Au_xNP-in-PdNS. The inductively coupled plasma optical emission spectroscopy (ICP–OES) analysis was carried out on the Thermo Scientific iCAP 6300 to confirm the exact composition of various Au: Pd ratios of 2D Au_xNP-in-PdNS heterostructure. The X-ray photoelectron spectroscopy (XPS) analysis was performed on Thermo Fisher ESCALAB 250Xi to further study the composition of various Au_xNP-in-PdNS. UV-Vis absorption spectra were collected from a Multimode Plate Reader (PerkinElmer EnSpire).

Electrode preparation. For working electrode preparation, drop-casted catalyst powders were prepared on a rotating disk electrode (RDE, Pine Research Instrumentation) made of glass carbon disk (with a geometric area of 0.196 cm^2). Prior to

electrode preparation, the RDE was polished with 1, 0.3, 0.05 μm alumina suspensions on a polishing cloth successively, thoroughly rinsed with Milli-Q water and ethanol, briefly sonicated in ethanol for less than 30 s, and dried under ambient condition. Au_xNP-in-PdNS and Pd NS catalyst inks were prepared by suspending 500 μL 1.0 mg mL^{-1} pre-prepared solution and 20 μL 5 wt% Nafion solution in 1.48 mL isopropanol via sonication for 0.5 h. 80 μL of catalyst ink was then drop-casted onto the RDE and dried under ambient conditions to form a uniform catalyst film with fixed catalyst loading of 0.102 mg cm^{-2}. As comparison, the Pd/C and Pt/C catalyst inks were prepared by suspending 500 μL 1.0 mg mL^{-1} pre-pared solution, in which 0.5 mg 20 wt% Pd/C and Pt/C commercial powder were pre-dispersed in 0.5 mL ethanol, and 20 μL 5 wt% Nafion solution in 1.48 mL isopropanol via sonication for 0.5 h. To prepare Pd/C and Pt/C electrodes, 80 μL ink was then drop-casted onto the RDE and dried under ambient conditions to form a uniform catalyst film with the same catalyst loading of 0.102 mg cm^{-2}. The carbon paper electrode with $Au_{0.50}$NP-in-PdNS catalyst was prepared and tested to determine the H_2 evolution. For the corresponding electrode preparation, the $Au_{0.50}$NP-in-PdNS catalyst ink was drop-casted on the carbon paper, which is successively cleaned in the ethanol, acetone, DI water, and then dried.

Main text: Plasmon-enhanced Electrocatalysis Measurements.

Plasmon-enhanced hydrogen evolution reaction (HER) Measurements. All electrochemical measurements were conducted in an undivided three-electrode cell connected to an electrochemical workstation (Princeton Applied Research Parstat. MC, US). For the convenience of light illumination, a quartz cell was utilized during the measurement. A graphite rod and a saturated calomel electrode (SCE, saturated KCl) electrode were used as the counter and reference electrodes, respectively. The 1.0 M $HClO_4$ (pH ≈ 0.09) was utilized as acidic electrolyte. Prior to each measurement, the electrolyte solution was purged and saturated with N_2 gas. A home-made cell system (Figure S12) was applied to achieve the photo-enhanced hydrogen evolution reaction (HER) measurements with the help of a 300 W Xenon lamp. The various monochromatic light was controlled with a cut-off filter of different wavelength (λ = 350 nm, 400 nm, 520 nm, 600 nm, and 700 nm) under fixed light intensity of 16.8 mW cm^{-2}. All experiments were performed isothermally, i.e., keeping the temperature of reference electrode and working electrode same and varied from 308 to 283 K at 5 K interval. At the same time, the temperatures in the bulk electrolyte and the area around 5 mm away from the electrode surface were measured using a Digital Thermometer (Anymetre PT3001). The measured temperatures are presented in the Table S5. During the measurement, a

home-made three-electrode cell equipped with water bath was utilized and the temperature of the electrolyte was accordingly measured with a thermometer (Figure S12a in SI). Finally, all potentials were corrected to the reversible hydrogen electrode (RHE) scale after i*R*-correction at the same temperature according to the Nernst Eq 6.1,

$$V_{vs\ RHE} = V_{vs\ SCE} + E^{\theta}_{SCE,T} + \frac{2.3025RT}{F}pH, \qquad 6.1$$

where *R* is the universal gas constant (R= 8.314 K^{-1} mol^{-1}), T (K) is the temperature, F is the Faraday constant (96485.3 J mol^{-1}) and $E^{\theta}_{SCE,T}$ is the standard electrode potentials at different temperature. Linear scan voltammetry (LSV) at 5 mV s^{-1} were recorded on different electrodes, which were vigorous rotated at 1600 rpm. For stability evaluation of $Au_{0.50}$NP-in-PdNS electrode, the continuous chronopotentiometry test at 10 mA cm^{-2} and 10000 cyclic voltammetry sweep cycles were conducted under dark and Xenon light illumination. The series resistance (R_s) and charge transfer resistance (R_{ct}) over the different conditions was measured by electrochemical impedance spectroscopy (EIS, Figure S15 in SI). Based on the exchange current density (j_o) at different temperatures, the apparent activation energies for the hydrogen evolution on $Au_{0.50}$NP-in-PdNS electrode under dark and 520 nm light illumination (21.6 mW cm^{-2}) were determined according to the Arrhenius equation

$$d(logj_0) = -\frac{E_a}{2.3R}\, d\left(\frac{1}{T}\right), \qquad 6.2$$

where E_a is the apparent activation energy for hydrogen evolution on catalyst, j_0 is the exchange current density. For testing the produced H_2 in the plasmon-enhanced HER measurement, a sealed H-type electrolyzer (Figure S19a in SI) was utilized. The prepared carbon paper electrode acted as the working electrode. The produced H_2 gas was analyzed using an on-line gas chromatograph (Shimadzu GC-2014) equipped with a thermal conductivity detector, a Molsieve 5 Å column and a flame ionization detector.

Plasmon-enhanced oxygen reduction reaction (ORR) Measurements. The electrochemical properties were measured by a three-electrode cell that was composed of a glassy-carbon rotating disk electrode (RDE) with the area of 0.196 cm^2 as the working electrode, along with the $Hg/HgO/OH^-$ reference electrode (1M KOH) and platinum-wire counter electrode in 0.1 M KOH electrolyte. Prior to each measurement, the electrolyte solution was purged with oxygen for 30 min to saturate and then bubble it continuously. The measurements were conducted at a scan rate of 10 mV s^{-1} and a rotation rate of 1600 rpm, respectively. The photo-enhanced oxygen reduction reaction (ORR) was measured at ~25 ^oC under 300 W Xenon lamp using a home-made cell system. During the measurement, a home-made three-electrode cell equipped with water bath was

utilized and the temperature of the electrolyte was accordingly measured with a thermometer (Figure S12a in SI). Finally, all potentials were corrected to the reversible hydrogen electrode (RHE) scale by i*R*-correction according to the Nernst equation (6.3) at the same temperature,

$$V_{vs\,RHE} = V_{vs\,Hg/HgO} + E^{\theta}_{Hg/HgO,T} + 0.059pH, \qquad 6.3$$

where $E^{\theta}_{Hg/HgO,T}$ is the standard electrode potential at 25 ^{o}C.

Main text: Electromagnetic simulations

The optical properties of Au_xNP-in-PdNS heterostructure were simulated using the finite-difference time-domain (FDTD) method. All the models were established and implemented in the package of FDTD solutions (Lumerical, Inc.). The AuNP was modeled as a sphere with different diameters (14 nm, 18 mm, 30 nm, or 46 nm) and with refractive index taken from the material database of CRC[64]. The Pd NS that wraps the AuNP was modeled as an etched sphere surrounding the AuNP-sphere with different thicknesses (1.5 nm, 6 nm, or 12 nm) and with refractive index taken from the material database of Palik[65]. Total-field/scattered-field light source conditions were employed throughout all the simulations. The incident field injected along z-axis was polarized along x-axis and wavelength range was set from 300 nm to 800 nm. Water was chosen as the background

medium with a refractive index of 1.33. The non-uniform mesh was used in the simulation region. A mesh sweeping converging test was run to choose proper mesh sizes for individual components in the simulation region. The absorption and scattering spectra (not shown) were calculated based on the Mie theory within the formalism of total-field/scattered-field. The fraction of absorption was calculated as a ratio of the total photon energy being absorbed to the sum of the total energy being absorbed and scattered by the electrocatalysts under broadband illumination of the Xenon lamp. The electromagnetic field distributions in the x-y plane were obtained at each wavelength via the standard Fourier transform, but only the field enhancement profiles at the LSPR wavelength are shown in the main text and Supporting Information.

Main text: Acknowledgements

This work is supported by the Strategic Priority Research Program of the Chinese Academy of Sciences (XDB36000000), the National Key R&D Program of China (Nos. 2021YFE0112600 and 2018YFA0703700), National Natural Science Foundation of China (Nos. 21805057 and 61625401), and the National Science Foundation (USA, CHE-1856518). F.W, P.Y and N. G acknowledges the support from CAS Key Laboratory of Nanosystem and Hierarchical Fabrication.

References

1. Zhang, Y., He, S., et al., "Surface-Plasmon-Driven Hot Electron Photochemistry." *Chem Rev* **2018**, *118*(6): 2927-2954.

2. Corson, E. R., Creel, E. B., et al., "Important Considerations in Plasmon-Enhanced Electrochemical Conversion at Voltage-Biased Electrodes." *iScience* **2020**, *23*(3): 100911.

3. Aslam, U., Rao, V. G., et al., "Catalytic conversion of solar to chemical energy on plasmonic metal nanostructures." *Nat. Catal.* **2018**, *1*(9): 656-665.

4. Sytwu, K., Vadai, M., et al., "Bimetallic nanostructures: combining plasmonic and catalytic metals for photocatalysis." *Advances in Physics: X* **2019**, *4*(1): 1619480.

5. Sytwu, K., Vadai, M., et al., "Driving energetically unfavorable dehydrogenation dynamics with plasmonics." *Science* **2021**, *371*(6526): 280-283.

6. Vadai, M., Angell, D. K., et al., "In-situ observation of plasmon-controlled photocatalytic dehydrogenation of individual palladium nanoparticles." *Nat Commun* **2018**, *9*(1): 4658.

7. Wang, C., Yang, W.-C. D., et al., "Endothermic reaction at room temperature enabled by deep-ultraviolet plasmons." *Nat. Mater.* **2020**.

8. Li, K., Hogan, N. J., et al., "Balancing Near-Field Enhancement, Absorption, and Scattering for Effective Antenna–Reactor Plasmonic Photocatalysis." *Nano Lett.* **2017**, *17*(6): 3710-3717.

9. Swearer, D. F., Zhao, H., et al., "Heterometallic antenna-reactor complexes for photocatalysis." *Proc. Natl. Acad. Sci. U. S. A.* **2016**, *113*(32): 8916-8920.

10. Robatjazi, H., Zhao, H., et al., "Plasmon-induced selective carbon dioxide conversion on earth-abundant aluminum-cuprous oxide antenna-reactor nanoparticles." *Nat Commun* **2017**, *8*(1): 27.

11. Engelbrekt, C., Crampton, K. T., et al., "Efficient Plasmon-Mediated Energy Funneling to the Surface of Au@Pt Core–Shell Nanocrystals." *ACS Nano* **2020**, *14*(4): 5061-5074.

12. Xu, P., Lu, W., et al., "Efficient Hydrolysis of Ammonia Borane for Hydrogen Evolution Catalyzed by Plasmonic Ag@Pd Core–Shell Nanocubes." *ACS Sustain. Chem. Eng.* **2020**, *8*(33): 12366-12377.

13. Huang, H., Zhang, L., et al., "Unraveling Surface Plasmon Decay in Core-Shell Nanostructures toward Broadband Light-Driven Catalytic Organic Synthesis." *J. Am. Chem. Soc.* **2016**, *138*(21): 6822-6828.

14. Aslam, U., Chavez, S., et al., "Controlling energy flow in multimetallic nanostructures for plasmonic catalysis." *Nat. Nanotechnol.* **2017**, *12*(10): 1000-1005.

15. Sarina, S., Zhu, H., et al., "Enhancing Catalytic Performance of Palladium in Gold and Palladium Alloy Nanoparticles for Organic Synthesis Reactions through Visible Light Irradiation at Ambient Temperatures." *J. Am. Chem. Soc.* **2013**, *135*(15): 5793-5801.

16. Lin, S.-C., Hsu, C.-S., et al., "Edgeless Ag–Pt Bimetallic Nanocages: In Situ Monitor Plasmon-Induced Suppression of Hydrogen Peroxide Formation." *J. Am. Chem. Soc.* **2017**, *139*(6): 2224-2233.

17. Zheng, Z., Tachikawa, T., et al., "Plasmon-Enhanced Formic Acid Dehydrogenation Using Anisotropic Pd–Au Nanorods Studied at the Single-Particle Level." *J. Am. Chem. Soc.* **2015**, *137*(2): 948-957.

18. Christopher, P., Xin, H., et al., "Singular characteristics and unique chemical bond activation mechanisms of photocatalytic reactions on plasmonic nanostructures." *Nat Mater* **2012**, *11*(12): 1044-1050.

19. Robatjazi, H., Bahauddin, S. M., et al., "Direct Plasmon-Driven Photoelectrocatalysis." *Nano Lett.* **2015**, *15*(9): 6155-6161.

20. Gargiulo, J., Berté, R., et al., "From Optical to Chemical Hot Spots in Plasmonics." *Acc. Chem. Res.* **2019**, *52*(9): 2525-2535.

21. Cortés, E., Xie, W., et al., "Plasmonic hot electron transport drives nano-localized chemistry." *Nat. Commun.* **2017**, *8*: 14880.

22. Zhou, L., Swearer, D. F., et al., "Quantifying hot carrier and thermal contributions in plasmonic photocatalysis." *Science* **2018**, *362*(6410): 69-72.

23. Creel, E. B., Corson, E. R., et al., "Directing Selectivity of Electrochemical Carbon Dioxide Reduction Using Plasmonics." *ACS Energy Lett.* **2019**, *4*(5): 1098-1105.

24. Shi, F., He, J., et al., "Plasmonic-Enhanced Oxygen Reduction Reaction of Silver/Graphene Electrocatalysts." *Nano Lett.* **2019**, *19*(2): 1371-1378.

25. Zheng, Z., Xie, W., et al., "Platinum electrocatalysts with plasmonic nano-cores for photo-enhanced oxygen-reduction." *Nano Energy* **2017**, *41*: 233-242.

26. Guo, X., Li, X., et al., "Plasmon-enhanced electrocatalytic hydrogen/oxygen evolution by Pt/Fe–Au nanorods." *J. Mater. Chem. A* **2018**, *6*(17): 7364-7369.

27. Wilson, A. J., Mohan, V., et al., "Mechanistic Understanding of Plasmon-Enhanced Electrochemistry." *J. Phys. Chem. C* **2019**, *123*(48): 29360-29369.

28. Hammer, B. and Norskov, J. K., "Why gold is the noblest of all the metals." *Nature* **1995**, *376*(6537): 238-240.

29. Shang, B., Cui, X., et al., "Lattice -Mismatch-Induced Ultrastable 1T-Phase MoS(2)-Pd/Au for Plasmon-Enhanced Hydrogen Evolution." *Nano Lett.* **2019**, *19*(5): 2758-2764.

30. Shi, Y., Wang, J., et al., "Hot electron of Au nanorods activates the electrocatalysis of hydrogen evolution on MoS2 nanosheets." *J. Am. Chem. Soc.* **2015**, *137*(23): 7365-7370.

31. Wang, S. S., Jiao, L., et al., "Boosting Electrocatalytic Hydrogen Evolution over Metal-Organic Frameworks by Plasmon-Induced Hot-Electron Injection." *Angew. Chem. Int. Ed. Engl.* **2019**, *58*(31): 10713-10717.

32. Zhang, Z., Liu, Y., et al., "Submonolayered Ru Deposited on Ultrathin Pd Nanosheets used for Enhanced Catalytic Applications." *Adv. Mater.* **2016**, *28*(46): 10282-10286.

33. Ge, J., He, D., et al., "Atomically Dispersed Ru on Ultrathin Pd Nanoribbons." *J. Am. Chem. Soc.* **2016**, *138*(42): 13850-13853.

34. Fan, Z., Huang, X., et al., "Surface modification-induced phase transformation of hexagonal close-packed gold square sheets." *Nat. Commun.* **2015**, *6*: 6571.

35. Bratsch, S. G., "Standard Electrode Potentials and Temperature Coefficients in Water at 298.15 K." *J. Phys. Chem. Ref. Data* **1989**, *18*(1): 1-21.

36. Yin, X., Warren, S. A., et al., "A Motif for Infinite Metal Atom Wires." *Angew. Chem. Int. Ed.* **2014**, *53*(51): 14087-14091.

37. Yin, X., Liu, X., et al., "Hanoi Tower-like Multilayered Ultrathin Palladium Nanosheets." *Nano Lett.* **2014**, *14*(12): 7188-7194.

38. Huang, X., Tang, S., et al., "Freestanding palladium nanosheets with plasmonic and catalytic properties." *Nat Nanotechnol* **2011**, *6*(1): 28-32.

39. Chen, A. and Ostrom, C., "Palladium-Based Nanomaterials: Synthesis and Electrochemical Applications." *Chem. Rev.* **2015**, *115*(21): 11999-12044.

40. Yu, Y., Wijesekara, K. D., et al., "Quantifying Wavelength-Dependent Plasmonic Hot Carrier Energy Distributions at Metal/Semiconductor Interfaces." *ACS Nano* **2019**, *13*(3): 3629-3637.

41. Scholl, J. A., Koh, A. L., et al., "Quantum plasmon resonances of individual metallic nanoparticles." *Nature* **2012**, *483*(7390): 421-427.

42. Liu, G., "Electron surface scattering and quantum finite-size effect on dielectric and optical properties of thin gold films." *Superlattices Microstruct.* **2019**, *125*: 322-329.

43. Zhang, G., Yu, M., et al., "Quantum Size Effects on Dielectric Constants and Optical Absorption of Ultrathin Silicon Films." *IEEE Electron Device Lett.* **2008**, *29*(12): 1302-1305.

44. Zhang, C., Chen, B.-Q., et al., "Surface Plasmon Resonance in Bimetallic Core–Shell Nanoparticles." *J. Phys. Chem. C* **2015**, *119*(29): 16836-16845.

45. Yu, G., Qian, J., et al., "Collective excitation of plasmon-coupled Au-nanochain boosts photocatalytic hydrogen evolution of semiconductor." *Nat. Commun.* **2019**, *10*(1): 4912.

46. Halas, N. J., Lal, S., et al., "Plasmons in Strongly Coupled Metallic Nanostructures." *Chem. Rev.* **2011**, *111*(6): 3913-3961.

47. Sönnichsen, C., Franzl, T., et al., "Drastic Reduction of Plasmon Damping in Gold Nanorods." *Phys. Rev. Lett.* **2002**, *88*(7): 077402.

48. Pan, F., Smith, K. C., et al., "Elucidating Energy Pathways through Simultaneous Measurement of Absorption and Transmission in a Coupled Plasmonic-Photonic Cavity." *Nano Lett.* **2020**, *20*(1): 50-58.

49. Sundararaman, R., Narang, P., et al., "Theoretical predictions for hot-carrier generation from surface plasmon decay." *Nat. Commun.* **2014**, *5*(1): 5788.

50. Kim, Y., Smith, J. G., et al., "Harvesting multiple electron–hole pairs generated through plasmonic excitation of Au nanoparticles." *Nat. Chem.* **2018**, *10*(7): 763-769.

51. Chavez, S., Aslam, U., et al., "Design Principles for Directing Energy and Energetic Charge Flow in Multicomponent Plasmonic Nanostructures." *ACS Energy Lett.* **2018**, *3*(7): 1590-1596.

52. Christopher, P. and Moskovits, M., "Hot Charge Carrier Transmission from Plasmonic Nanostructures." *Annu. Rev. Phys. Chem.* **2017**, *68*(1): 379-398.

53. Sarina, S., Zhu, H. Y., et al., "Viable photocatalysts under solar-spectrum irradiation: nonplasmonic metal nanoparticles." *Angew. Chem. Int. Ed. Engl.* **2014**, *53*(11): 2935-2940.

54. Marković, N. M., Grgur, B. N., et al., "Temperature-Dependent Hydrogen Electrochemistry on Platinum Low-Index Single-Crystal Surfaces in Acid Solutions." *J. Phys. Chem. B* **1997**, *101*(27): 5405-5413.

55. Vadai, M., Angell, D. K., et al., "In-situ observation of plasmon-controlled photocatalytic dehydrogenation of individual palladium nanoparticles." *Nat. Commun.* **2018**, *9*(1): 4658.

56. Kim, Y., Dumett Torres, D., et al., "Activation Energies of Plasmonic Catalysts." *Nano Lett.* **2016**, *16*(5): 3399-3407.

57. Boerigter, C., Campana, R., et al., "Evidence and implications of direct charge excitation as the dominant mechanism in plasmon-mediated photocatalysis." *Nat. Commun.* **2016**, *7*(1): 10545.

58. Yan, J., Jacobsen, K. W., et al., "First-principles study of surface plasmons on Ag(111) and H/Ag(111)." *Phys. Rev. B* **2011**, *84*(23): 235430.

59. Jaramillo, T. F., Jørgensen, K. P., et al., "Identification of active edge sites for electrochemical H2 evolution from MoS2 nanocatalysts." *Science* **2007**, *317*(5834): 100-102.

60. Conway, B. E. and Tilak, B. V., "Interfacial processes involving electrocatalytic evolution and oxidation of H2, and the role of chemisorbed H." *Electrochim. Acta* **2002**, *47*(22): 3571-3594.

61. Wang, F., Li, C., et al., "Plasmonic Harvesting of Light Energy for Suzuki Coupling Reactions." *J. Am. Chem. Soc.* **2013**, *135*(15): 5588-5601.

62. Huschka, R., Zuloaga, J., et al., "Light-Induced Release of DNA from Gold Nanoparticles: Nanoshells and Nanorods." *J. Am. Chem. Soc.* **2011**, *133*(31): 12247-12255.

63. Baffou, G., Quidant, R., et al., "Nanoscale Control of Optical Heating in Complex Plasmonic Systems." *ACS Nano* **2010**, *4*(2): 709-716.

64. Haynes, W. M. and Boulder, "CRC Handbook of Chemistry and Physics, 95th Edition, Online edition."

65. Palik, E., "Handbook of Optical Constants of Solids: Index, Vol. 3." **1988**.

Chapter 7 Unfinished projects

Introduction

This chapter presents two unfinished projects during my Ph.D. career, i.e., single-particle absorption spectroscopy of a synthetic conductive polymer and enhancing plasmonic-photonic interactions using a polymer-embedding method. The first project is an addendum to the two published papers[1, 2] aiming at correlating electronic structure to high conductivity of conjugated polymers using single-particle photothermal absorption spectroscopy. The second project presents a different method from solvent-embedding method described in **Chapter 4**, using a polymer matrix to directly modulate LSP-WGM mode overlap on a microtoroid. The first project is divided into two parts, centering around breaking PEDOT-S aggregates and control of doping level, while the second project shows my effort to increase the thickness of polymer layer without degrading Q-factors too much.

Project 1: Breaking PEDOT-S aggregates

Poly(3,4-ethylenedioxythiophene) sulfonate, or PEDOT-S, a member of polythiophene polymer family, has been investigated in this study due to its single-component backbone without the involvement polystyrene sulfonate (PSS), like PEDOT:PSS, and comparable conductivity to PEDOT:PSS.[3, 4] PEDOT-S is water-soluble due to a sodium sulfonate side chain along the backbone and self-doped as synthesized.

Unfortunately, this polymer is more dispersed with a polydispersity index of 3.24, suggesting a wide distribution of polymer aggregates in aqueous solution.[4]

PEDOT-S sample was prepared as previously described and then spin-coated onto microtoroids.[1, 2] Photothermal absorption spectroscopy and polarization study of individual PEDOT-S particles were carried out one at a time. The resulting absorption spectra are flat like those of PEDOT:PSS (**Figure 7.1**).[1, 2] We can thus average absorption cross sections over the whole pump spectral range to represent the particle size as previously described. The mean of cross sections ranges from 10^{-13} to 10^{-11} cm^2 for the pristine PEDOT-S (**Figure 7.2**), higher than 1.02×10^{-15} cm^2 predicted for a single PEDOT-S polymer chain when the degree of polymerization is 16.

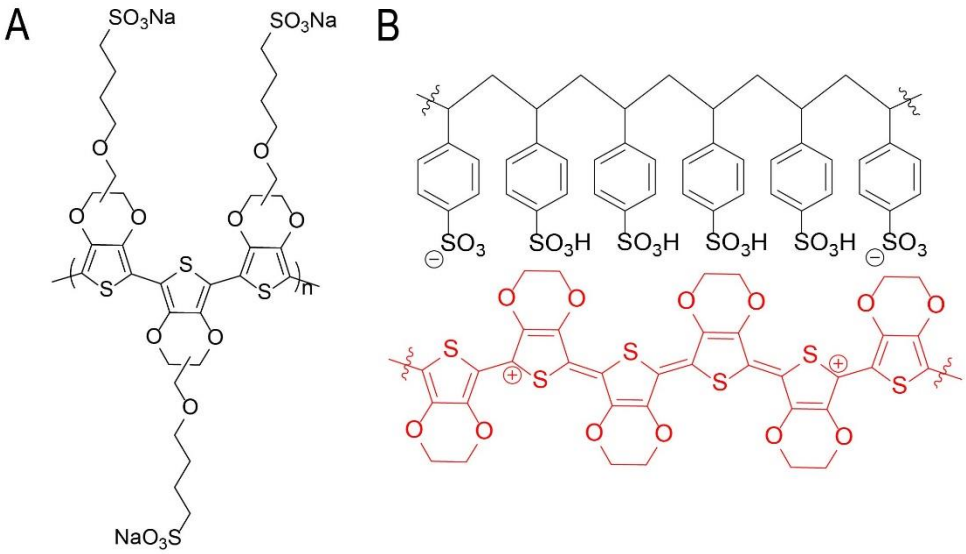

Figure 7.1 Molecular structure of PEDOT-S (**A**) and PEDOT:PSS (**B**) .

When a diluted PEDOT-S solution is sonicated, the lowest of cross section is 5.0×10^{-15} cm^2. Alternatively, a diluted PEDOT-S sample is boiled at 100º in a flask under N_2 flowing condition to break aggregates. Interestingly, the color of PEDOT-S aqueous

solution turned bluer (**Figure 7.3)**, suggesting that sample might degrade. In addition to the long-tailed bipolaron absorption feature above 1200 nm, a bulk UV-Vis-NIR

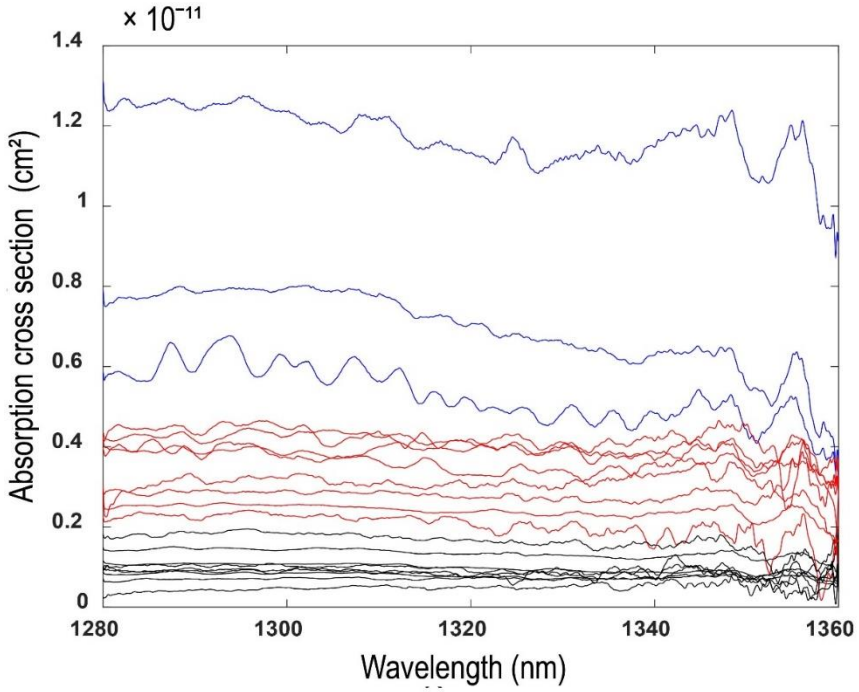

Figure 7.2 Absorption spectra of PEDOT-S measured by single-particle absorption spectroscopy. Three sets of spectra (blue, red, and black) are sorted according to their averaged cross sections.

absorption spectroscopy of the boiled sample exhibits two shoulders at 600 and 900 nm, which are attributed to the absorption of neutral and polaron species in PEDOT-S, respectively.[5] The change in absorption spectra suggests that PEDOT-S might be de-doped in an aqueous solution at high temperatures.

Project 1: pH control of doping level in PEDOT-S

Crispin's group has shown that doping level can be tuned by treating PEDOT-Tos film with inorganic solutions at different pH.[6] A basic treatment leads to a smaller number of bipolarons and thus de-dope PEDOT, whereas an acidic treatment does the other way

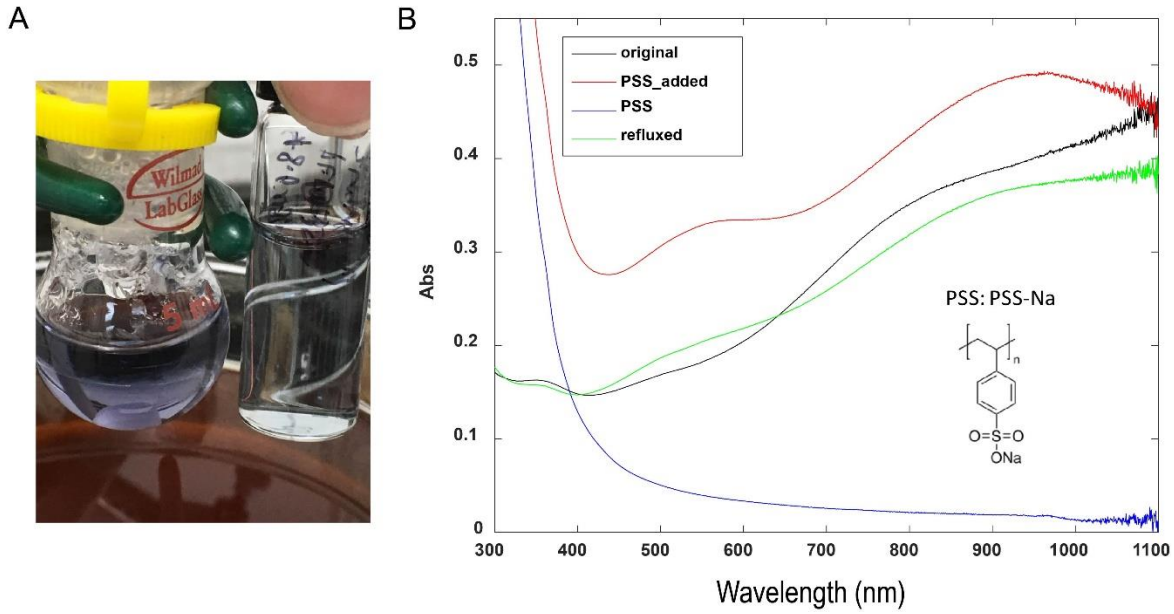

Figure 7.3 Thermal treatment of PEDOT-S solution. The solution in the flask is bluer after treatment at 100º than that in the vial (**A**). The absorption spectrum of this sample (green, **B**) shows a rising feature at 600 and 900 nm like the shoulders for the sample (red) treated with PSS-Na (inset), which is attributable to absorption by neutral and polaron species in PEDOT-S. The absorption spectrum of PSS-Na is shown as control.

around. When the doping level of PEDOT decreases, bipolaron species turn into neutral and polaron species and then neutral species dominate in PEDOT-S. The similar pH effect on the absorption spectra of PEDOT-S is observed in our ensemble measurement using UV-Vis-NIR absorption spectroscopy (**Figure 7.4**). A de-doping mechanism is proposed in **Figure 7.4B**, where protons are extracted from PEDOT and then charged species are neutralized.

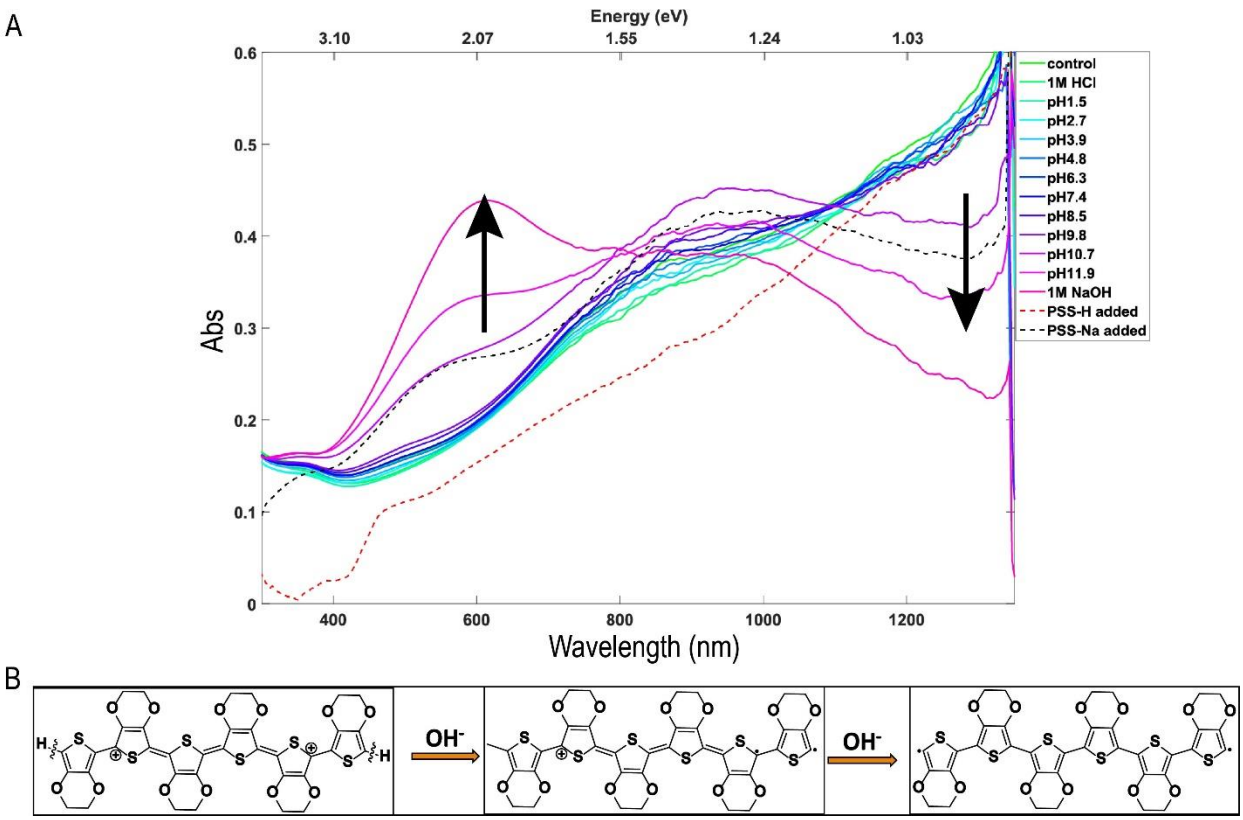

Figure 7.4 pH control of doping level in PEDOT-S. As pH increases, absorption features at 600 and 900 nm are rising, whereas absorption beyond 1200 nm decreases (**A**). A proposed de-doping mechanism is shown in **B**.

We then investigate this pH control at the single-particle level. A basic treatment (0.01 M NaOH aqueous solution) of PEDOT-S polymer deposited on microtoroids, however, washes away PEDOT-S, suggesting that the affinity of PEDOT-S to the silica surface might be unstable under basic condition. An organic base may be an option to mildly de-dope PEDOT-S without destroying the affinity. Alternatively, acidic or basic PSS, i.e., PSS-H or PSS-Na, was mixed with PEDOT-S sample during sample preparation and co-deposited onto microtoroids, providing an acidic or basic local environment for PEDOT-S, respectively. Three different sets of PEDOT-S sample were studied, i.e.,

pristine PEDOT-S, PEDOT-S:PSS-Na, and PEDOT-S:PSS-H. The correlation between the depth of modulation and particle size is presented in a scatter density plot and then fitted to a logistic function as previously described[1] to extract the degree of ordering (**Figure 7.5**). Surprisingly, the lone parameter at 50% falloff of oligomer alignment decreases in both PEDOT-S:PSS-Na and PEDOT-S:PSS-H samples, suggesting that the introduction of PSS likely breaks long-range ordering. The doping level increases through acidic treatment and bipolaron density thus increases, leading to an increase in absorption cross section and apparent particle size. However, PSS effect may compete with the increase in particle size.

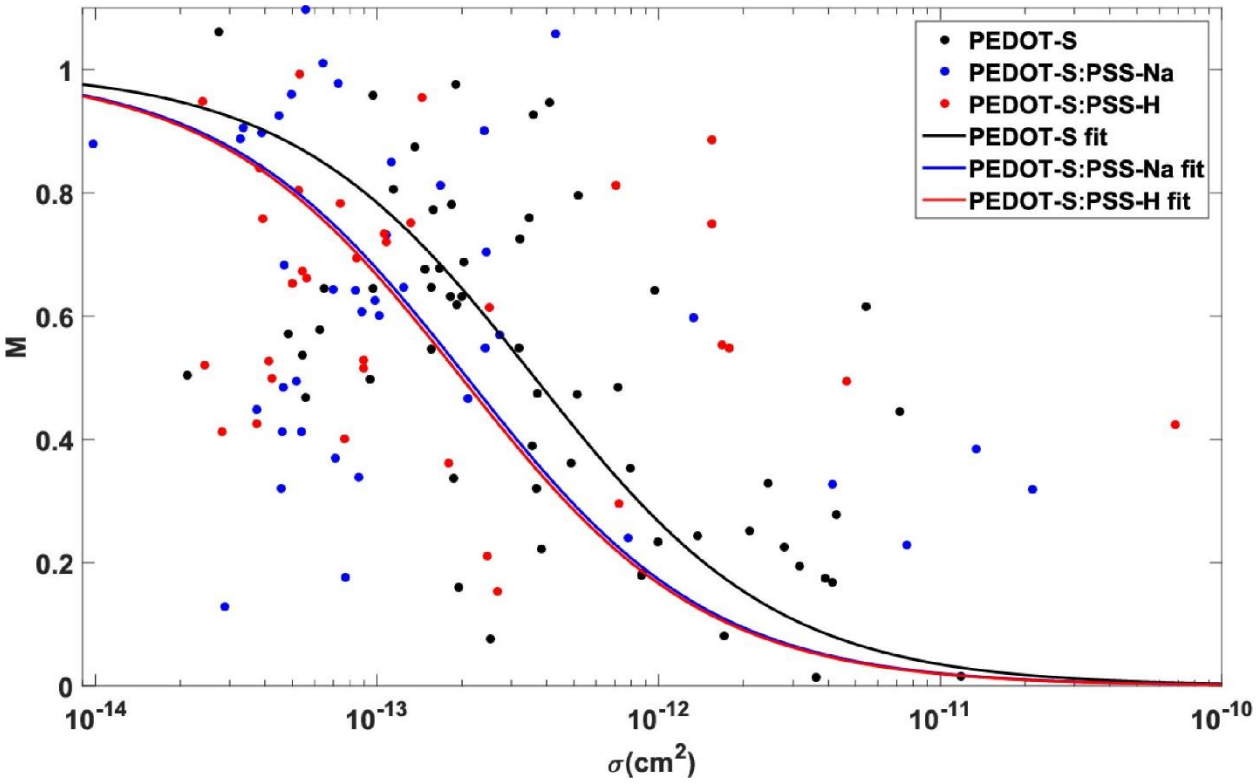

Figure 7.5 Correlation of electronic structure to ordering of chromophores. The density distribution is fitted to a logistic function as described previously. The lone parameter at 50% falloff is $10^{-12.44}$ (black, PEDOT-S), $10^{-12.68}$ (blue, PEDOT-S:PSS-Na), $10^{-12.7}$ (red, PEDOT-S:PSS-H).

Project 2: PDMS coating

Polydimethylsiloxane (PDMS), which is widely used in optical lithography, is chosen for coating microtoroids due to its low absorption loss in near-infrared spectral range and similar refractive index to silica. Commercial PDMS sample contains two component reagents (A and B). The mixing ratio of A and B affects how fast PDMS solidifies from liquid phase from a few hours up to 24 hours. In addition, heating the mixture sample can accelerate solidification and may turn PDMS into solid within 1 hour or so at 100º.[7] PDMS has been used for improving thermo-optic property of microcavities (microtoroid[7, 8] and microsphere[9]) because it has a large negative thermo-optic coefficient (-1.8×10^{-4} K^{-1}) compared to silica (5.5×10^{-7} K^{-1}). A thermal sensitivity of 0.151 nm/K in PDMS-coated microtoroid has been demonstrated when the coating thickness is about 1.5 um.[8] The method used in this work is a droplet-wetting technique.[7, 8] A microtoroid chip on a nano-positioning stage is controlled to approach a PDMS droplet until the droplet blasts and then spreads along the peripheral ring of the silica disk due to low surface tension, while some portion of PDMS droplet remains on the center of the disk (**Figure 7.6A**). One droplet of PDMS may result in a layer of approximately a few hundred nm onto the silica microtoroid, while the thickness can be estimated empirically. Unlike

spin-coating technique, this method provides certain control of both coating thickness through choosing droplet size and selectivity over which microtoroid to coat on a chip.

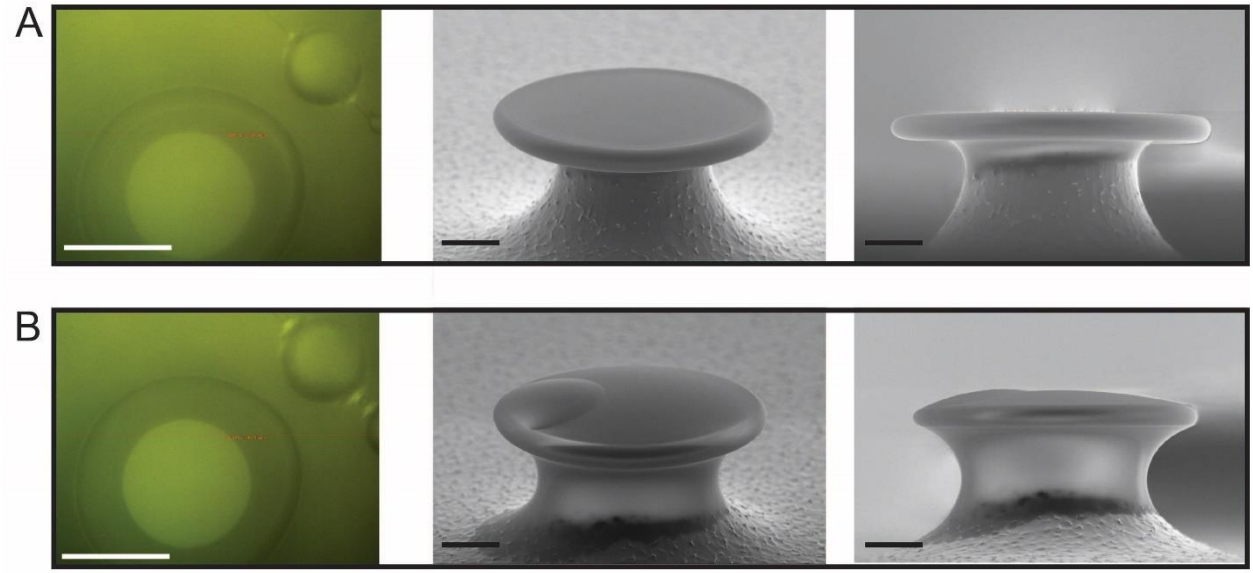

Figure 7.6 PDMS coating of a microtoroid via droplet-wetting method. Optical images for the first (**A**) and second (**B**) run on the same microtoroid are shown along with scanning electron micrographs (top and side views). The white scale bar is 25 μm and black scale bar is 10 μm.

A tapered optical fiber which does not have high transmission efficiency as a tapered one for photothermal measurements, is fabricated using the same heat-pull method. A freshly mixed PDMS sample is gently transferred to this taper by a fiber tip. Consequently, a string of droplets is formed on the taper and ready for coating. Typically, the droplets' viscosity gradually increases within the first 45 minutes and then coating became difficult as the droplet may stop spreading due to high viscosity. As shown in **Figure 7.7**, field intensity profile gradually shifts from silica to PDMS layer. When PDMS layer is ~1.25 μm, the interface gains a maximum field intensity. To achieve the desired thickness, the coating is expected to be repeated on the same toroid about 5 times.

Unfortunately, Q-factors dropped rapidly from middle 10^6 to $<10^4$ after the third or fourth run of coating. Although a blueshift in one or two low-Q (low 10^5) resonances is seen, suggesting a negative thermo-optical property in the PDMS-coated microtoroid, the remaining high-Q resonances still exhibit a redshift. The large pillar may trap certain

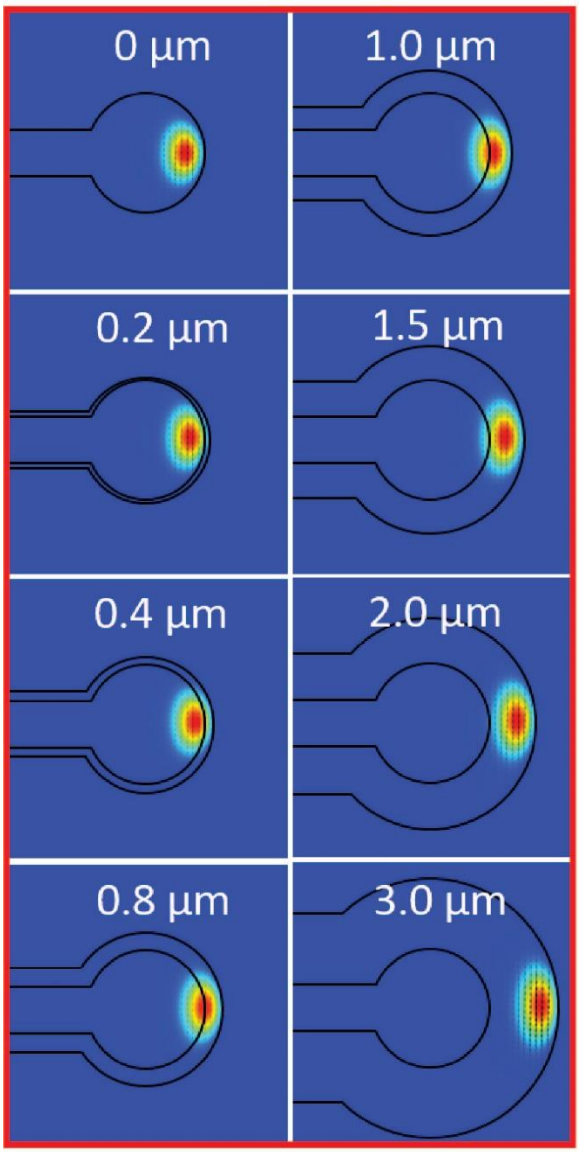

Figure 7.7 Field intensity profiles as a function of the thickness of PDMS layer. The fundamental transverse-electric (TE00) mode is simulated.

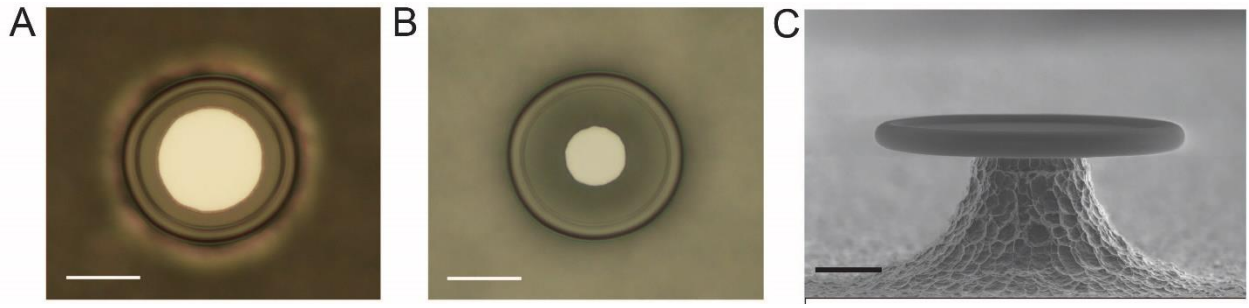

Figure 7.8 Narrowing pillar via XeF_2 etching. Pillar is narrowed by a factor of 2.5 by comparing optical images taken before and after etching (**A** and **B**). Pillar's surface becomes rough after etching (**C**). The white scale bars in optical images (**A** and **B**) are 20 µm and black scale bar on SEM image (**C**) is 10 µm.

amount of PDMS liquid, as seen in scanning electron micrographs (SEM), which leads to light leakage and decreased Q-factors. XeF_2 dry etching is applied to reflowed microtoroids to narrow the pillars down to 12 µm at the junction of silica disk and silicon top (**Figure 7.8**). Although a homogeneous layer is obtained even after 5 times coating, Q-factors still drops quickly and then microtoroids would be unusable. A plausible reason might be that pristine microtoroids only have modest Q-factors around middle 10^6 instead

of 10^7 or 10^8, which may not survive from repeated PDMS coating. In addition, imaging via SEM is not suitable for examining coating performance because electrons can degrade PDMS layer, as shown in **Figure 7.9**.

Project 2: Optical simulations of PDMS-coated microtoroid

Introducing a material with a large negative thermo-optic and thermo-expansion properties to the silica microtoroid impacts thermal response of the hybrid microcavity and consequently photothermal measurement. An adjustment in the relationship between resonance shift and absorbed heat is needed to get accurate absorbance based on the newly hybrid microcavity. A thorough understanding of this relationship can be obtained from a series of combined electromagnetic and thermal simulations as described previously.[1, 10, 11] Note that only fundamental transverse-electric mode (TE00) is studied

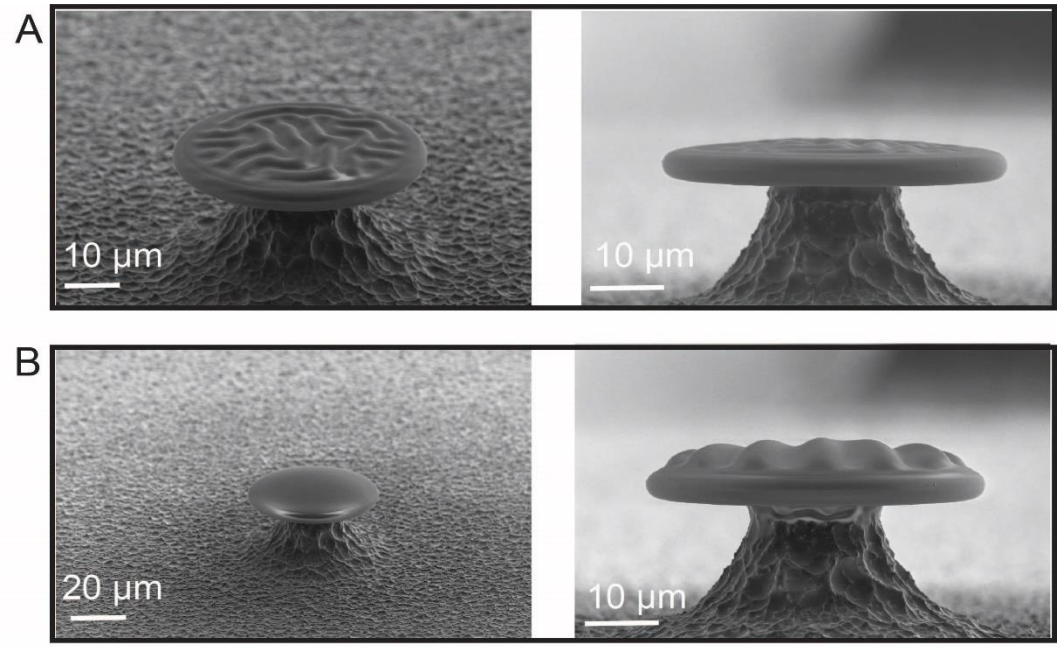

Figure 7.9 Scanning electron micrographs for PDMS-coated, etched microtoroid. The first (**A**) and second (**B**) run of coating on the same microtoroid (top and side views).

in these simulations. As the material layer increases, overall thermo-optic coefficient of the hybrid microcavity first decreases down to 0 at a thickness of ~0.4 μm (transition point 1, or TP1), and then is overtaken by the negative thermo-optic component of PDMS, as seen in **Figure 7.10**. When PDMS layer continues to increase further, thermal expansion begins contributing to a positive thermal response. Thus, the most negative thermal response ($\frac{d\lambda}{dT}$) is seen at a thickness of 2.2 μm (transition point 2, or TP2), after which the response is turning over and may reach an asymptotic limit where a mode profile primarily resides in the PDMS medium as shown in **Figure 7.7**. Between TP1 and TP2, the electric field intensity is maximized at the interface at our desired thickness of 1.25 μm where energy is equally partitioned between the two media. The trend is slightly different in high-order modes and gains negative thermo-optic component from PDMS at a thinner layer. This expectation is consistent with both our observation of the blueshift in low-Q

resonances (high-order modes) and high-Q resonances (potentially fundamental mode) and measurements by He et al.[7]

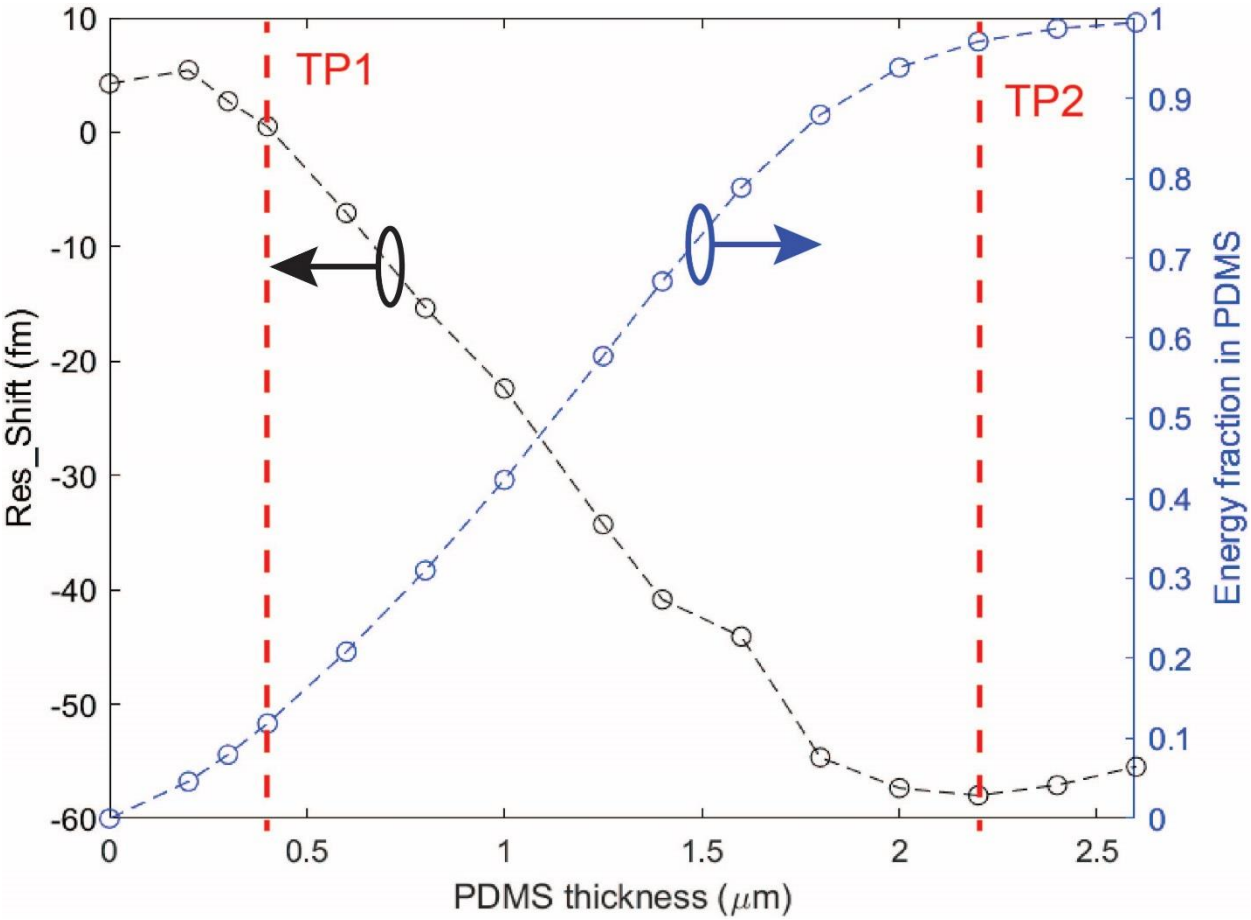

Figure 7.10 Resonance shift (black) and energy fraction (blue) in PDMS as a function of the thickness of PDMS layer. Transition point 1 (TP1) and transition point 2 (TP2) are marked. A pillar diameter of 15 μm and a point heat source of 10 nW on the microtoroid rim are used in simulations. Only resonance shift at the steady state is obtained at each thickness.

References

1. Horak, E. H., Rea, M. T., et al., "Exploring Electronic Structure and Order in Polymers via Single-Particle Microresonator Spectroscopy." *Nano Lett.* **2018**, *18*(3): 1600-1607.

2. Rea, M. T., Pan, F., et al., "Investigating the Mechanism of Post-Treatment on PEDOT/PSS via Single-Particle Absorption Spectroscopy." *J. Phys. Chem. C* **2019**, *123*(51): 30781-30790.

3. Persson, K. M., Karlsson, R., et al., "Electronic Control of Cell Detachment Using a Self-Doped Conducting Polymer." *Adv. Mater.* **2011**, *23*(38): 4403-4408.

4. Karlsson, R. H., Herland, A., et al., "Iron-Catalyzed Polymerization of Alkoxysulfonate-Functionalized 3,4-Ethylenedioxythiophene Gives Water-Soluble Poly(3,4-ethylenedioxythiophene) of High Conductivity." *Chem. Mater.* **2009**, *21*(9): 1815-1821.

5. Massonnet, N., Carella, A., et al., "Improvement of the Seebeck coefficient of PEDOT:PSS by chemical reduction combined with a novel method for its transfer using free-standing thin films." *J. Mater. Chem. C* **2014**, *2*(7): 1278-1283.

6. Khan, Z. U., Bubnova, O., et al., "Acido-basic control of the thermoelectric properties of poly(3,4-ethylenedioxythiophene)tosylate (PEDOT-Tos) thin films." *J. Mater. Chem. C* **2015**, *3*(40): 10616-10623.

7. He, L., Xiao, Y.-F., et al., "Compensation of thermal refraction effect in high-Q toroidal microresonator by polydimethylsiloxane coating." *Appl. Phys. Lett.* **2008**, *93*(20): 201102.

8. Li, B.-B., Wang, Q.-Y., et al., "On chip, high-sensitivity thermal sensor based on high-Q polydimethylsiloxane-coated microresonator." *Appl. Phys. Lett.* **2010**, *96*(25): 251109.

9. Li, B.-B., Xiao, Y.-F., et al., "Low-threshold Raman laser from an on-chip, high-Q, polymer-coated microcavity." *Opt. Lett.* **2013**, *38*(11): 1802-1804.

10. Heylman, K. D., Thakkar, N., et al., "Optical microresonators as single-particle absorption spectrometers." *Nat. Photonics* **2016**, *10*: 788-795.

11. Pan, F., Smith, K. C., et al., "Elucidating Energy Pathways through Simultaneous Measurement of Absorption and Transmission in a Coupled Plasmonic–Photonic Cavity." *Nano Lett.* **2020**, *20*(1): 50-58.

Chapter 8 Mingling a nanoscopic world with a microscopic world

Introduction

This chapter is intended to explain my graduate research to non-scientific audiences and is supported by the Wisconsin Initiative for Science Literacy at UW-Madison. I would like to thank Prof. Bassam Shakhashiri, Elizabeth Reynolds, and Cayce Osborne for their constructive feedback and encouragement. Science should be approachable to everyone. Thus, I hope my research to be both understandable and appealing to a broad readership. In the meantime, it is extremely rewarding that this chapter sparks people's interest in new sciences and passion for exploring interdisciplinary subjects which may revolutionize our understanding about our world from tiny particles to grand universe. My research revolves around plasmonics, photonics, and their interactions. I hope to use this chapter to explain a few critical concepts in these topics. What are plasmons, photons, and the media that host them? How do we understand and control interactions between them?

Plasmons and their media

Let's first get to know plasmons. We can think of a plasmon like a child in a swing moving back and forth (**Figure 8.1A**). But eventually this kiddo will stop at a moment when he is not pushed any more. A plasmon is very like this child but is a cloud of electrons (or

negatively charged tiny particles) moving back and forth around an origin. This cloud is moving periodically at a certain frequency when it is driven by light irradiation (an electric field), as seen in **Figure 8.1B**, and will stop soon after this external irradiation ends.

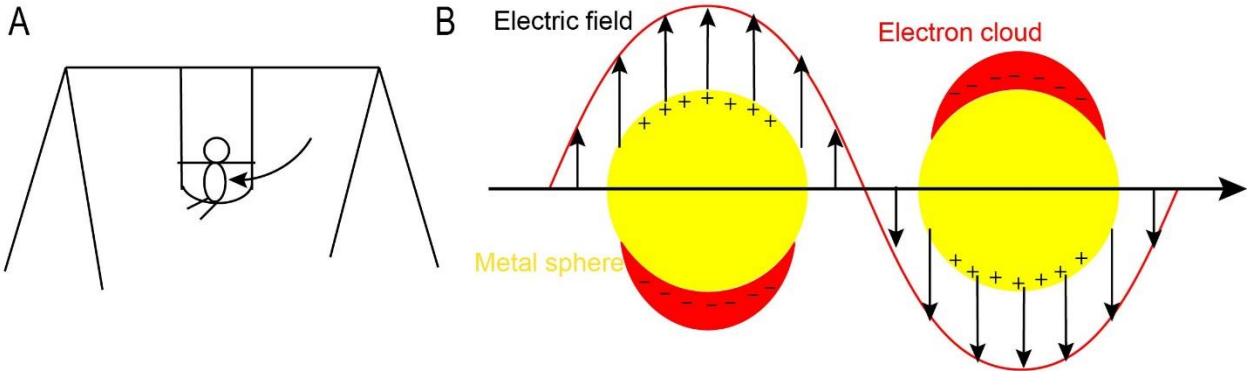

Figure 8.1 Understanding oscillation and plasmon. (**A**) A child is pushed to swing. (**B**) A plasmon (oscillation of electron cloud) in a metal is generated by an electric field.

How do we generate the plasmon? Since it is a cloud of electrons that move periodically, a matter that generates this plasmon must have electrons, specifically, electrons that can move freely with very little friction. Metals, like gold, silver, and aluminum, host such free electrons. However, to have free electrons oscillate back and forth in one of these metals, we must make it extremely small, about a few hundred nanometers (~10^{-7} m), which we cannot see with our eyes. However, when this metal is tiny, plasmons are produced by light of only certain colors (like red light). Since light is also a wave, a formal description for the color of light is frequency or wavelength. We call this condition under which a plasmon is produced a resonant condition. Just like when I want to push a swinging kiddo at a different speed, I would have to fight against the already moving swing. Plasmons must be in harmony with light at a specific frequency.

Now I would like to briefly talk about some important properties of plasmons, which are important to understanding interactions when plasmons mingle with photons in the following discussion. First, the oscillation of free electrons will have a very short lifetime, less than 10^{-13} s. You can think of it this way: after it is generated, a plasmon is already gone before you can blink your eyes. Although it recedes so rapidly, it can be localized in an extremely finite volume, for instance, a few hundred cubic nanometers, due to its tiny physical size.

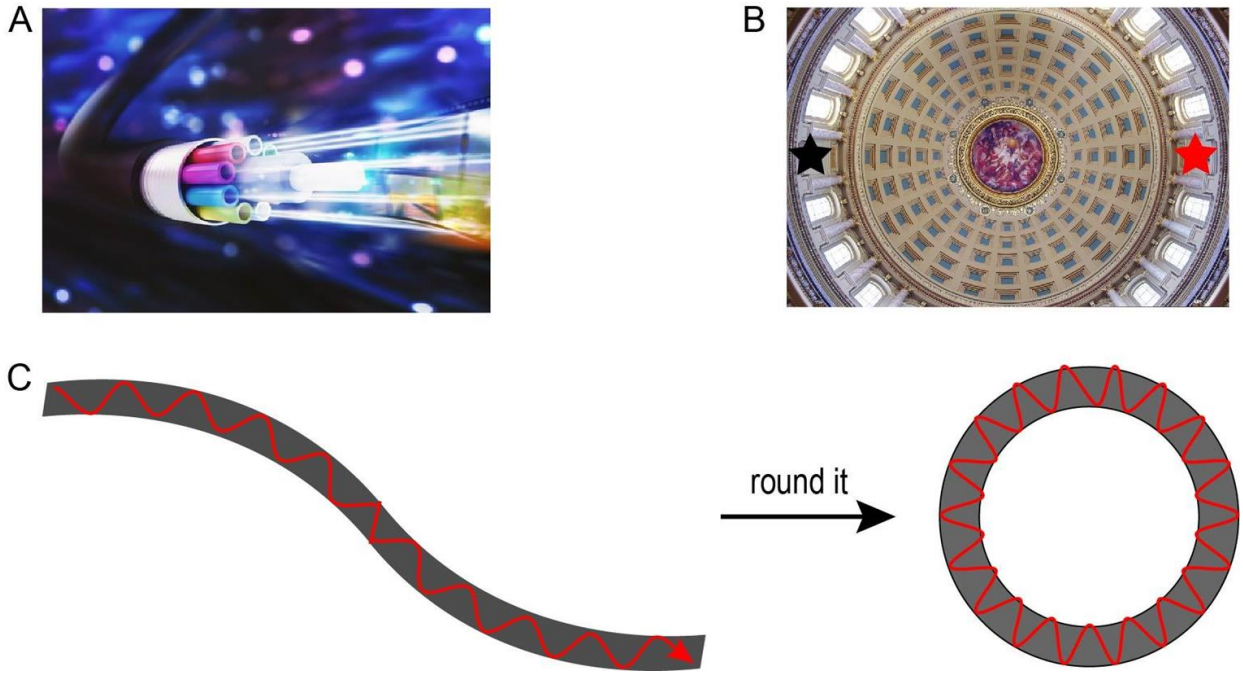

Figure 8.2 Whispering-gallery waves and microcavities. (**A**) The whispering produced at the position of the black star can be heard at the position of the red star. (**B**) Optical fibers. (**C**) A whispering-gallery cavity is equivalent to a rounded optical fiber.

Photons and whispering-gallery-mode microcavities

Now we have some idea about how a plasmon can act like a particle (a cloud of electrons) and a wave (oscillating behavior). This dual property is exactly like light, or a

photon. In daily life, photons are everywhere, for instance, that's why you can read my thesis on a screen. It is because your screen is lighting up and emitted photons are perceived by your eyes. As I just mentioned, a photon is traveling like both a sound wave and a ball. Unlike a sound wave, which must travel in a medium, a photon can travel even in a vacuum where there is no air at all. Also, the photon can travel in a material, for instance, an optical fiber (**Figure 8.2A**), which transmits encoded information at the speed of light. That's the reason why we have internet and are connected to the world.

My research interrogates the behavior of photons propagating in such materials, like silicon oxide, that make the core of optical fibers. We make a unique structure of silicon oxide so that photons can stay inside it for a very long time or have a long lifetime, such as a few tens of microseconds (10^{-5} s). Although it might still sound very short, this lifetime is way longer than that of a plasmon. Now the question is what kind of structure can keep photons traveling so long. Researchers were inspired by sound waves propagating in the whispering gallery of St Paul's Cathedral and invented an optical analog. We can find a similar structure in the State Capitol of Wisconsin (**Figure 8.2B**). Let me use this structure to briefly explain how a sound wave propagates in it. When I stand at a spot along this peripheral ring and then whisper, you can hear my voice at any spot as long as you are still close to this ring, even far from me. We call this type of propagation whispering-gallery waves or whispering-gallery modes. The structure we use for photons is very like this whispering gallery or we think of it like a closed loop of an optical fiber (**Figure 8.2A and Figure 8.2C**). We can imagine that photons are traveling in this loop repeatedly up to millions of round trips under certain circumstances. One

condition for keeping my whispering propagating along this ring so that you can hear clearly is that I must whisper at certain frequencies, i.e., my sound must be resonant with this structure. We call this resonant structure a cavity. Likewise, light only at certain frequencies can travel in such a whispering-gallery-mode cavity. If a cavity has a larger size or a larger diameter, then the resonant frequencies would be smaller, or wavelength would be longer. Photons tend to travel a longer distance per period (the interval of time between successive occurrences in a wave) to finish one circulation under this condition. This cavity is not empty but filled with material. Our lab makes a chip of such whispering-gallery-mode cavities whose size is around 50 micrometers ($5*10^{-5}$ m). One such microcavity is presented in **Figure 8.3A**. We can see a disk made of silica sit on top of a pillar made of silicon, or a microscopic “mushroom”, as visualized by the scanning electron micrograph. This mushroom is sensitive to humidity, pressure, and temperature because a change in external conditions can affect the frequency of light propagating within this cavity. We can make several sensors out of this mushroom and even transform them into portable devices. Such a device can be incorporated in a mobile phone so that

one can obtain information about relative humidity and temperature in a room conveniently.

Whispering-gallery-mode microcavity as a tiny thermometer

We can use this whispering-gallery-mode microcavity as a tiny thermometer in an experiment and then determine absorption ability of molecules or how many photons are absorbed per second by a molecule, like any dye molecule you can imagine. To understand how this temperature sensor works, let's recall the resonant condition. Only photons (light) at certain frequencies can travel in this microcavity. Fortunately, we can change this resonant condition by tweaking the local temperature because one of the optical properties in this microcavity, refractive index (the ratio of the velocity of light in a vacuum to its velocity in a specific medium, here the microcavity), linearly depends on

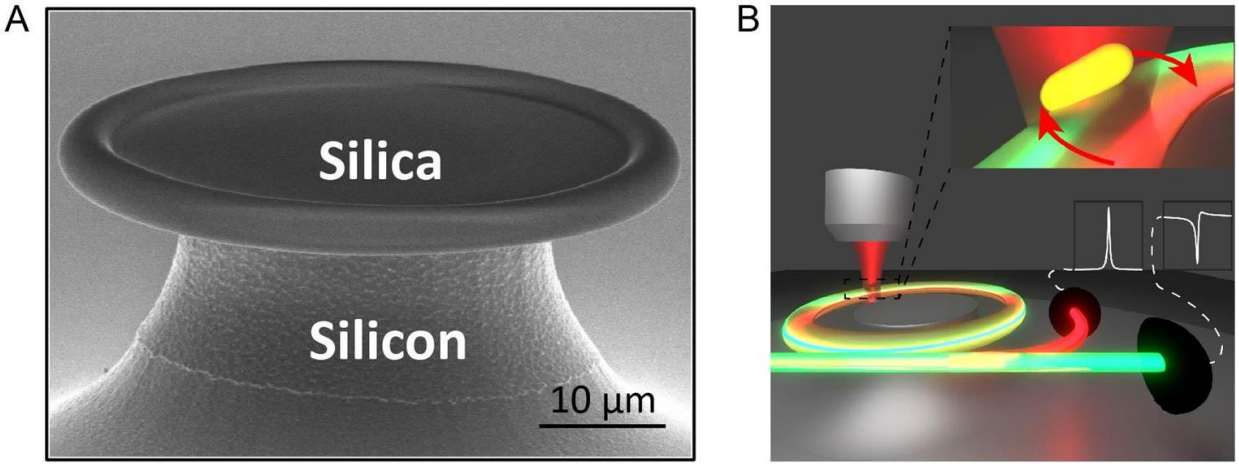

Figure 8.3 A whispering-gallery microcavity and my experimental scheme. (**A**) A scanning electron micrograph of a microtoroid cavity. The scale bar is 10 micrometers (10^{-5} m). (**B**) A mingled system is illuminated by a laser beam (red cone) and energy is redistributed within the system. The whole information about this energy redistribution process is perceived by the two photoreceivers (black hemispheres) as two distinct spectral signatures (white curves in the two boxes). A gold nanorod (yellow glowing rod, inset) is on the surface of the whispering-gallery microcavity shown in **A**.

temperature. When the local temperature increases, the refractive index will increase and only photons at a shorter wavelength (or higher frequency) can travel in the microcavity now. I track the change in wavelength in my experiments when the refractive index changes. Thus, I can use this microcavity as a tiny thermometer to sense a change in temperature. The temperature change I can measure here is very minute, even below 10^{-6} K. This capability allows me to determine how many photons are absorbed by a single molecule per second. When I shine light upon a single molecule, the molecule absorbs a certain amount of light and eventually converts this energy into heat, which results in a change in the local temperature. I finally obtain the number of photons being absorbed by this molecule per second by measuring the change in temperature. If a gold nanorod that hosts a plasmon sits on the microcavity, I can certainly determine the number of photons being absorbed by this nanorod per second while a plasmon is generated. I use this powerful tool to glean important information about how energy is redistributed and dumped upon light irradiation in a mingled system that hosts plasmons and photons in its components.

What we learn from a mingled system

I lay out a foundation for understanding plasmons, photons, and cavities as well as how to determine absorption ability in a gold nanorod in the previous sections. Now let's see what will happen when we mingle plasmons and photons together. We can consider that plasmons exist in a nanoscopic cavity (in a length scale of 10^{-7} m) while photons are in a microscopic cavity (in a length scale of 10^{-5} m). When we bring them

together, it is interesting to see how plasmons and photons communicate with each other and whether their own behavior will be influenced by this communication. This understanding has significant implications for creating highly sensitive assessment tools even better than the whispering-gallery-mode microcavity itself for biological applications and building optical networks for communication and information storage. In my research, I attach a single gold nanorod that can host a plasmon to the surface of a whispering-gallery-mode microcavity that can host photons. The photons in this microcavity can either come from energy conversion between plasmons and photons due to the communication between the two worlds or be launched into the system through an optical fiber. I use the whispering-gallery-mode microcavity for two purposes, one as a tiny thermometer for measuring photons absorbed by the mingled system per second, the other as a component microcavity for mingling with the gold nanorod (**Figure 8.3B**). Note that these two purposes are not interfering with each other. I tightly focus a laser beam through an objective lens to a very small area (10^{-12} m^2), as represented by the red cone shown in **Figure 8.3B**, which illuminates the gold nanorod (yellow glowing rod, inset) on top of the whispering-gallery microcavity (**Figure 8.3A**). This illumination generates plasmons in the gold nanorod and then plasmons may convert into photons propagating in the microcavity. An optical fiber that is brought close to this mingled system captures photons leaking out from the system. I use photon receivers (black hemispheres in **Figure 8.3B**) to measure these leaking photons and convert them into an electrical signal that I can read on my computer, like how our retinas perceive incoming light and converts it into an electrical signal sensed by our nerves and then finally processed by our brains.

Ultimately, by analyzing the spectral signatures (white curves) shown in **Figure 8.3B,** I paint a full picture of energy flow in both the nanoscopic and microscopic world. I find that although energy is exchanged between these two worlds, the exchange rate is slower than the rates that plasmons and photons dump energy to their local environment. These two worlds primarily operate on their own but occasionally communicate with each other.

To make them connect more closely, I then invented a new method to manipulate the interaction between plasmons and photons. Instead of using the mushroom-shaped microcavity shown in **Figure 8.3A**, I choose a bubble-shaped microcavity like an extremely small soap bubble (~10^{-4} m), another member of the whispering-gallery-mode microcavity family. This microcavity has a hollow structure so that I can flow a variety of liquids through the microcavity to modify the refractive index inside the microcavity. This property governs how photons travel in this microcavity, just like that a chopstick looks bent in a glass bottle filled with water. When the microcavity is just filled with air, photons

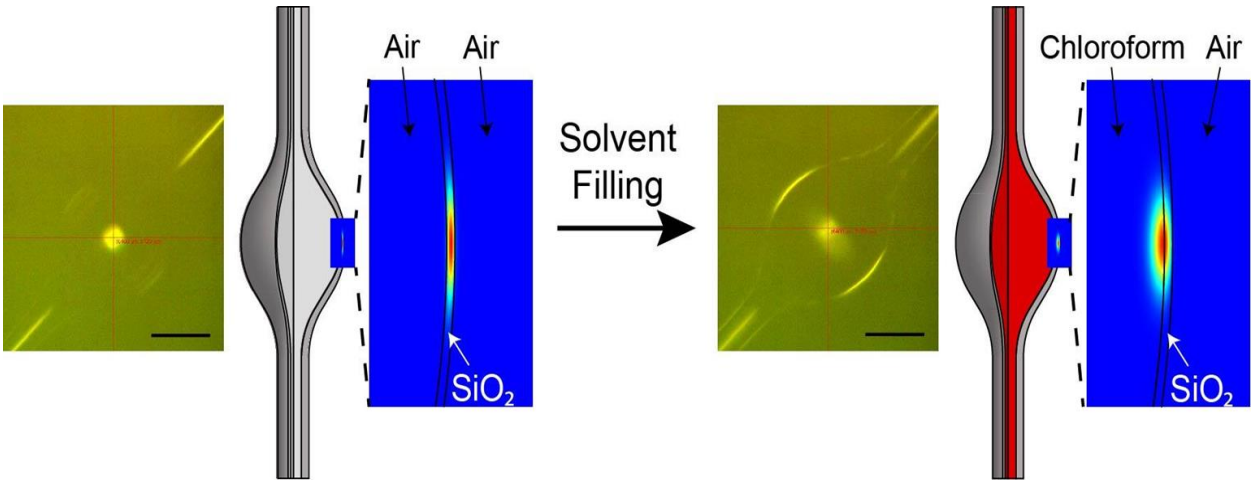

Figure 8.4 Optical difference between a bubble-shape microcavity filled with air and an organic solvent. Optical image, microbubble geometry, and false color image for electromagnetic field are shown in sequence under each filling condition. The black scale bar is 50 micrometers.

primarily propagate inside the thin glass (SiO_2) wall, as shown in the false color image of the electromagnetic field on the left (**Figure 8.4**). Note that when a photon travels in a vacuum or specific medium, it results in a specific pattern of electromagnetic field distribution. If we look at the air-filled microbubble in a microscope (optical images in **Figure 8.4**), we barely see the profile of the microbubble. When illuminating light is reflecting at the air-glass interface many times due to the high contrast in refractive indices between air (1.0) and glass (1.45), we will see the image get blurred. By contrast, when a liquid, for instance, chloroform, fills the microbubble, there is a striking difference. First, we can see the profile of the microbubble much more clearly in the optical image. The reason is that there is a very small contrast between the filling medium (1.43) and glass (1.45) and reflection at the interface is largely eliminated. We can experiment with this behavior by watching the difference before and after filling a glass bottle with water. In the meantime, the electromagnetic field also populates the filling medium, acting like there is no difference between the glass and the liquid (**Figure 8.4**).

How does this filling enhance the communication between plasmons and photons? When a gold nanorod is sitting on the surface of an interior glass wall and we then fill the microbubble with a liquid (chloroform), we will see that the liquid totally immerses the gold nanorod. As I show the electromagnetic field in the liquid-filled microbubble in **Figure 8.4**, we observe the most intense electromagnetic field at the interface, which is exactly where the gold nanorod may sit. When photons are traveling in such a microbubble, plasmons are more likely to interact strongly with photons because they are closer to each other. When we flow a different liquid which has an even higher refractive index than glass, we

will see that the electromagnetic field favors the liquid now and plasmons will interact less with photons again. Basically, by changing the refractive index inside the microbubble, we can control the communication between plasmons and photons. The control of this interaction will provide insight into the rational design of new sensors that can better harness the advantages of plasmons and photons.

Understanding this mingled system provides the knowledge about which knob we need to tweak for getting an even better system. For instance, like the communication between plasmons and photons I presented above, we can tweak this parameter to create a strongly interacted system so that the transformation between plasmons and photons is easier to occur. In the meantime, an elegant control over the mingled system leads to a more sensitive tool for studying molecules and materials. One application might be to create new sensors and imaging tools for detection and measurement of single molecules. Researchers might use this diagnostic tool to determine the size of different viruses or tiny particles and even identify different proteins in solutions. Also, when we anchor a substrate (a molecule that can attract specific proteins) onto this mingled system, we can examine binding behavior of proteins to the substrate at the single-molecule level. This knowledge is important to design new drugs for curing diseases. One day we may transform this mingled system into a portable device for field experiments to sense air quality because our mingled system responds very sensitively to low-concentration particulates in the air.

Outlook and future directions

I present a framework throughout my thesis that captures a few exciting elements revolving around light-matter interactions in plasmonics, photonics, and their coupled systems. The goal is to provide readers the frontier of control of light-matter interactions through engineering local DOS using plasmonic nanocavity, photonic microcavity, and their coupled cavity, which underpins the applications in photocatalysis, emission control, (bio)sensing, and single-molecule spectroscopy. While I am wrapping up my graduate study, I envision several future directions that interested readers may pursue in this interdisciplinary area.

New optical microcavities toward strongly coupled systems

The two optical microcavities that are involved in my thesis work, albeit showing ultrahigh Q-factors, have complicated mode structures, which makes the assignment of mode identity very difficult, particularly in the microbubble cavity. Although a statistical treatment of mode analysis sheds light upon LSP-WGM couplings, understanding and controlling the interaction between a single optical mode and a single LSP is more intriguing. Microring or 1D PC cavities, because of geometric confinement of mode around $\left(\frac{\lambda}{2n}\right)^3$ and much clean mode spectrum, are attractive candidates for making strongly coupled plasmonic-photonic systems, which may assist in entering strong coupling regime. In addition, it is relatively easier to embed quantum emitters or

plasmonic nanoparticles with index-matching materials (PDMS or PMMA) using standard optical lithography methods.

Dark-field scattering measurement

I demonstrate a simultaneous measurement of photothermal absorption and two-sided transmission using a single optical fiber in a plasmonic-photonic coupled cavity in Chapter 3. However, we have not provided a far-field scattering measurement through the same experimental design. In the meantime, it is interesting to see if a scattering spectrum would be dressed with Fano signatures like our absorption spectrum. Interferometric scattering method where scattered light is interfered with a reference light (here reflected light) on a detector, may be a way to measure this scattering signal from large background scattering due to the curvature of a microtoroid. Adding an InGaAs camera or point detector to the current setup may serve this goal because the high-NA objective focuses pump beam to diffraction limit and collect both reflected and scattered light. An absolute scattering cross section might be obtained by taking into consideration collection efficiency of detection optics and the cone angle of collection defined by the numerical aperture of the objective. Alternatively, a dark-field scattering method may reject some portion of background scattering. In this setup, a pump laser beam is delivered through a reflective, dark-field objective and scattered light from the coupled cavity is collected by an inner lens compound nested inside the objective barrel. One limitation is that only scattering is measured.